UC San Diego

UC San Diego Electronic Theses and Dissertations

Title

Dynamic metasurface antennas for next-generation wireless communications

Permalink

https://escholarship.org/uc/item/7x35w5pq

ISBN

9798173723529

Author

Carlson, Joseph Michael

Publication Date

2026-11-03

Peer reviewed|Thesis/dissertation

eScholarship.org Powered by the California Digital Library
University of California

UNIVERSITY OF CALIFORNIA SAN DIEGO

Dynamic metasurface antennas for next-generation wireless communications

A dissertation submitted in partial satisfaction of the
requirements for the degree Doctor of Philosophy

in

Electrical Engineering (Communication Theory and Systems)

by

Joseph Michael Carlson

Committee in charge:

Professor Robert W. Heath, Jr., Chair
Professor Richard Averitt
Professor Nuria González-Prelcic
Professor Daniel Sievenpiper

2026

Copyright

Joseph Michael Carlson, 2026

All rights reserved.

The Dissertation of Joseph Michael Carlson is approved, and it is acceptable in quality and form for publication on microfilm and electronically.

University of California San Diego

2026

DEDICATION

To my wife, Sierra, for being there with me every step of the way.

TABLE OF CONTENTS

Dissertation Approval Page iii

Dedication iv

Table of Contents v

List of Figures ix

List of Tables xvii

Acknowledgements xviii

Vita xxi

Abstract of the Dissertation xxiv

Chapter 1 Introduction 1
1.1 Large antenna arrays for next-generation wireless communications 1
1.2 Dynamic metasurface antennas 4
1.3 Challenges in DMA-based communication 6
1.3.1 Beamforming and codebook design 7
1.3.2 Wideband communications and DMA element modeling 8
1.3.3 Interference mitigation and source localization 8
1.3.4 DMA element design optimization 9
1.4 Summary of contributions 10
1.5 Organization 11
1.6 Notation 11

Chapter 2 Hierarchical codebook design with dynamic metasurface antennas for energy-efficient arrays 13
2.1 Overview 13
2.2 Introduction 13
2.2.1 Prior work 14
2.2.2 Problem formulation 17
2.2.3 Contributions 17
2.3 System model 19
2.3.1 DMA element model 20
2.3.2 Communication and signal model 23
2.4 DMA mapping design 24
2.4.1 DMA mapping 26
2.4.2 Mapping optimization 27
2.5 DMA design and hardware implementation 30
2.5.1 DMA design 31

2.5.2 Power consumption and component loss model 33
2.5.3 DMA hierarchical codebook 35
2.6 Results 38
2.6.1 Impact of phase rotation optimization 39
2.6.2 DMA with wide beam patterns 42
2.6.3 DMA steering accuracy 44
2.6.4 DMA coverage 44
2.6.5 Spectral efficiency 47
2.6.6 Energy efficiency 49
2.7 Conclusions 49
2.7.1 Proof of Lemma 1 51

Chapter 3 Wideband dynamic metasurface antenna performance with practical design characteristics 53
3.1 Overview 53
3.2 Introduction 53
3.2.1 Prior work 54
3.2.2 Contributions 57
3.3 System model 59
3.3.1 MISO-OFDM signal model 59
3.3.2 Wideband beamforming gain and spectral efficiency 60
3.4 DMA channel and beamformer model 61
3.4.1 Channel and waveguide model 62
3.4.2 Frequency-selective DMA beamforming model 64
3.4.3 Frequency-selective Lorentzian constraint 65
3.4.4 Approximation of the polarizability angle and center-frequency DMA beamforming 68
3.5 Beamforming gain approximation for a DMA-based wideband communication system 69
3.5.1 Impact of frequency selectivity 71
3.5.2 Impact of tuning bandwidth 72
3.5.3 Impact of waveguide attenuation 73
3.6 DMA successive beamforming algorithm 75
3.6.1 DMA center-frequency beamforming algorithm 75
3.6.2 DMA successive beamforming algorithm 75
3.7 Data rate and spectral efficiency results 78
3.7.1 Simulation setup and design considerations 78
3.7.2 Validation for the DMA beamforming gain approximation 80
3.7.3 Simulation results for the approximation and successive DMA beamformer 83
3.7.4 Impact of DMA element spacing and damping factor 85
3.7.5 Impact of multipath on DMA beamforming performance 88
3.8 Conclusions and future work 92
3.8.1 Proof of Lemma 2 92
3.8.2 Proof of Lemma 3 93

3.8.3 Proof of Lemma 4 . . . 94
3.8.4 Proof of Lemma 5 . . . 95
3.8.5 Proof of Lemma 6 . . . 95
3.8.6 Proof of Lemma 7 . . . 97

Chapter 4 Advanced array processing for nullsteering and DOA estimation with dynamic metasurface antennas . . . 99
4.1 Overview . . . 99
4.2 Introduction . . . 99
4.2.1 Prior work . . . 101
4.2.2 Contributions . . . 103
4.3 DMA model and beamforming . . . 105
4.3.1 DMA weights . . . 105
4.3.2 Beam pattern . . . 109
4.3.3 Relationship to the Lorentzian constraint . . . 110
4.3.4 Mutual coupling in DMAs . . . 112
4.4 Beam pattern prediction with machine learning . . . 113
4.5 DOA estimation with DMAs . . . 118
4.6 Adaptive nullsteering with DMAs . . . 125
4.7 Conclusion . . . 131

Chapter 5 A sub-6 GHz dynamic metasurface antenna design for improved gain and cross-polarization isolation . . . 134
5.1 Overview . . . 134
5.2 Introduction . . . 134
5.3 DMA architecture and meta-atom design methodology . . . 138
5.3.1 Polarizability and effective weight model . . . 138
5.3.2 REMA design methodology . . . 140
5.4 Final REMA design . . . 145
5.4.1 Meta-atom comparison . . . 147
5.4.2 Array integration and beamsteering simulations . . . 150
5.5 Prototype fabrication and measurement results . . . 156
5.5.1 REMA single-element measurements . . . 156
5.5.2 Array beam pattern measurements . . . 158
5.5.3 Wideband beam pattern measurements . . . 160
5.5.4 Comparison with prior-art DMAs . . . 161
5.6 Conclusions and future work . . . 165

Chapter 6 Conclusions . . . 167
6.1 Key takeaways . . . 167
6.2 Future work . . . 169
6.2.1 Multi-user MIMO . . . 169
6.2.2 Integration with the tri-hybrid architecture . . . 170
6.2.3 Real-time wireless testbed . . . 171

6.2.4 The cost and benefit of DMAs 172

Bibliography 175

LIST OF FIGURES

Figure 1.1. Diagrams of the (a) digital, (b) analog, and (c) hybrid precoding architectures for wireless communication systems. The digital architecture achieves the highest performance but requires a dedicated RF chain per antenna, increasing power consumption and hardware cost. The analog architecture uses a single RF chain with a network of phase shifters, reducing cost and complexity at the expense of performance. The hybrid architecture combines a smaller number of RF chains with analog phase shifters, offering a balance between the two. 3

Figure 1.2. Design and structure of the DMA. A DMA consists of multiple sub-wavelength meta-atoms etched onto the upper conductor of a waveguide. Integrated, tunable components, like varactor diodes, provide beamforming capabilities with low power consumption. 5

Figure 1.3. The guided-wave propagation in a DMA. The waveguide is excited from one end, and each metamaterial element radiates a fraction of the guided wave as it propagates. The lower plot shows the field along the waveguide, which advances in phase and decays in amplitude from element to element, so each element is excited differently. 5

Figure 1.4. The main research problems addressed in this dissertation. A DMA offers an energy-efficient way to build a large antenna array, but using it in a practical wireless communication system requires new models, algorithms, and hardware designs. We develop these across the four areas shown, which form the basis of Chapters 2–5. 7

Figure 2.1. Visualization of an entire DMA with D waveguides and L radiating slot elements per waveguide. 20

Figure 2.2. Analog beamforming transmitter architecture for (a) a typical phased antenna array and (b) the DMA. Typical analog implementations enable precoding with phase shifters, while DMAs use reconfigurable components. 25

Figure 2.3. Applying a phase rotation to the desired weights results in a new set of mapped weights onto the Lorentzian-constrained weights. We can leverage this to achieve greater beamforming gain with the DMA. 31

Figure 2.4. Simulated results for the Lorentzian-constrained weights of the designed DMA in HFSS using (2.18). We find that the DMA accurately achieves the Lorentzian-constrained weights defined in (2.2). 33

Figure 2.5. Antenna efficiency simulation results for (a) layer 2, (b) layer 3, and (c) layer 4. We find in layers 2 and 3 that the phase rotation optimization can make a significant difference in the overall antenna efficiency by configuring the weights to maximize the output power of the DMA. 41

Figure 2.6. Simulated beam patterns for the second hierarchical codebook layer using (a) Euclidean modulation and (b) Euclidean modulation with optimized phase rotation. The vertical, dashed lines at $\phi \in [-60^\circ, 0^\circ, 60^\circ]$ represent the desired angular range for each beam pattern. We see that the phase rotation optimization leads to beam patterns with larger realized gain. 43

Figure 2.7. (a) Desired versus simulated steering angle for the fourth hierarchical codebook layer and (b) steering angle error for each codeword. All mapping methods enable accurate beamsteering compared to the phased array. 45

Figure 2.8. Coverage analysis of simulated beam patterns for the hierarchical codebook layers. We find that the brute-force search provides the best coverage of the mapping techniques for the DMA. 46

Figure 2.9. Simulated results with the DMA and phased array for (a) spectral efficiency and (b) energy efficiency. We find that the DMA outperforms a traditional passive phased array due to the significant transmit power attenuation for the high-resolution phase shifter. While the active phased array provides the highest spectral efficiency, its large power consumption makes it the least energy-efficient option. 50

Figure 3.1. Architecture of a DMA as a leaky-wave uniform linear array of antenna elements. Varactor diodes are integrated into each antenna element to enable low-power beamforming with the use of an external controller. 60

Figure 3.2. Lorentzian-constrained weight distribution for the DMA elements compared with unit-amplitude weights. We find that the Lorentzian-constrained weights allow for a total phase range of $[-\pi, 0]$. 67

Figure 3.3. We plot the validation for the (a) weight fill term, (b) leakage term, and (c) frequency-selectivity term using the DMA approximation against the center-frequency beamformer. We find that the weight fill and leakage terms provide an accurate model to approximate the wideband DMA performance, while the frequency-selectivity term is accurate at small signal bandwidths and becomes less accurate as the signal bandwidth increases. 81

Figure 3.4. We plot spectral efficiency in (a) and data rate in (b) as a function of the signal bandwidth. We find that spectral efficiency decreases with signal bandwidth due to the noise power term and increased frequency-selectivity of the DMA elements. We also see that the successive algorithm provides better data rates and spectral efficiency than the center-frequency beamformer. 84

Figure 3.5. Spectral efficiency as a function of the steering angle ϕ_{t}. As the steering angle varies, the spectral efficiency does not change significantly for both the center-frequency beamformer and the successive beamformer. 85

Figure 3.6. Maximum data rate results comparing the center-frequency beamforming and DMA successive algorithm. The DMA successive algorithm allows for larger data rates and signal bandwidths as it can better configure the DMA elements for a wideband frequency-selective scenario. 86

Figure 3.7. DMA element spacing analysis for spectral efficiency. As the approximation predicts, smaller DMA element spacing leads to lower frequency-selectivity and higher spectral efficiency. As DMAs are impacted more by the beam-squint effect than phased arrays, it is important to minimize DMA element spacing to mitigate beam-squint. 86

Figure 3.8. Data rates for the center-frequency beamformer and different damping factors. We show that larger damping factors lead to improved data rates due to the lower impact of frequency-selectivity. 87

Figure 3.9. Spectral efficiency results for a multipath channel environment with $N_{\mathsf{ele}} = 6$ elements per subarray and $N_{\mathsf{rf}} = 4$ subarrays. We find that the proposed DMA successive beamforming algorithm outperforms both the baseline DMA center-frequency beamforming method and the hybrid architectures. This is due to the flexible algorithm design that adapts to the DMA and channel frequency-selectivity, dense DMA element spacing, and high component loss from passive phase shifters for the hybrid architecture. . . . 90

Figure 3.10. Average spectral efficiency for a multipath channel environment as a function of the number of channel paths. We find that the proposed DMA successive beamforming algorithm provides the best performance across every number of channel paths. 91

Figure 4.1. Overview of the DMA-based communication system for DOA estimation and adaptive nullsteering. The DMA receiver determines the location of various sources, and steers a beam toward the target user while placing nulls at the directions of interferers. The weight vector $\mathbf{w}$ is generated to configure the DMA elements connected to a single RF chain. 106

Figure 4.2. RMSE for (a) full pattern reconstruction and (b) null regions for 300 test beam patterns. The ML model achieves a median RMSE of 1.11 dB across the full pattern and 2.67 dB in null regions, compared to 4.85 dB and 7.08 dB for the analytical model. 116

Figure 4.3. Comparison of (a) beam patterns and (b) element weights for the HFSS simulation, ML prediction, and analytical model. The analytical model produces sidelobe errors and a spurious null near -22° absent from the HFSS pattern. The ML model applies small corrections to the analytical weights, closely reproducing the HFSS ground truth. 117

Figure 4.4. Null-scan beam patterns for the DMA-based DOA estimation algorithm with $C = 81$ configurations across $\theta \in [-40^\circ, 40^\circ]$ at 1° intervals. Each configuration places a deep null at a distinct angle while maintaining relatively flat gain elsewhere. 119

Figure 4.5. Detection probability versus number of sources for the DMA null-scanning method and MUSIC with $L = 80$ time-averaging samples. The null-scanning method approaches the detection probability of MUSIC at both low and high SNR. 122

Figure 4.6. DOA estimation RMSE versus SNR for the DMA null-scanning method and MUSIC with $K = 1$ to 4 sources and $L = 80$ samples. The DMA achieves sub-degree RMSE above -10 dB SNR for all cases. 123

Figure 4.7. Angular resolution of the DMA null-scanning method for $K = 2$ equal-power sources. The 1° null spacing enables near-perfect resolution for sources separated by 3° or more, even at 0 dB SNR. 124

Figure 4.8. Detection probability versus number of time-averaging samples L for $K = 1$ to 4 sources at SNR $= 10$ dB. Increasing L suppresses cross-term noise, with diminishing returns beyond $L \approx 100$. 124

Figure 4.9. Example nullsteering beam pattern with a main beam at -20° and three simultaneous nulls. The ML-predicted pattern closely matches the HFSS-simulated ground truth, with nulls accurately placed at the desired locations. 128

Figure 4.10. HFSS nullsteering results for the 3-null cases showing (a) beam gain and (b) null depth. The DMA consistently achieves close to the desired beam gain of $D^{\mathsf{dB}}_{\mathsf{beam}} = 8$ dBi and null depth of $D^{\mathsf{dB}}_{\mathsf{null}} = -20$ dBi across all tested beam patterns. 129

Figure 4.11. Nullsteering accuracy for the 3-null case showing (a) a scatter plot of the desired vs. actual null angle and (b) the null angle error. The null accuracy remains within $\pm 1^\circ$ of error for the majority of cases. 130

Figure 4.12. Beam gain as a function of the number of simultaneous nulls for the 20 random nullsteering scenarios. The beam gain decreases gradually as additional nulls consume degrees of freedom in the DMA weight optimization. 131

Figure 4.13. Nullsteering performance as a function of the number of simultaneous nulls for the (a) achieved null depth at the actual null locations and (b) angular error between desired and actual null locations. The null depth and accuracy remain relatively constant for up to 3 nulls, while 4 nulls introduce greater uncertainty and shallower null depths. 132

Figure 5.1. Topology of the typical square meta-atom and the proposed REMA. Both meta-atoms are etched onto the upper conductor of a substrate-integrated waveguide, with the guided TE_{10} mode propagating vertically in the figure. The varactor bridges the outer gap. 138

Figure 5.2. Examples for the different candidate DMA designs that we compare to finalize the REMA geometry with the best tradeoff between radiation efficiency and tuning range. 143

Figure 5.3. Simulated $|S_{12}|$ in linear scale for the eight REMA candidate designs, each tuned to land its resonance at 5.9 GHz (solid) and 6.1 GHz (dashed). The varactor capacitance spread required to achieve this detuning reflects each design's tuning sensitivity. 144

Figure 5.4. Tuning sensitivity S_{tune} versus radiation efficiency at 6 GHz for the eight candidate designs. We find that there is a distinct tradeoff between radiation efficiency and tuning sensitivity when we compare the eight designs. We choose design 7 (D7) for our final, proposed element due to its favorable radiation efficiency and sufficient tuning sensitivity with the selected varactor diode. 145

Figure 5.5. Element response versus waveguide height and slot offset at $c_{\mathsf{var}} = 0.10\,\text{pF}$, for (a) the resonant frequency and (b) the $|S_{12}|$ dip at each design's own resonance. Increasing the waveguide height lowers the resonant frequency and weakens the coupling between the REMA and the SIW, while increasing the slot offset raises the resonant frequency and strengthens the coupling. . 146

Figure 5.6. Peak co- and cross-polarized element directivity over $\theta \in [-40^\circ, +40^\circ]$ vs. waveguide height and slot offset at three swept varactor capacitances. Increasing the slot offset helps to improve the cross-polarization isolation at the lower varactor capacitance values. 147

Figure 5.7. Geometry of the proposed REMA, the coplanar waveguide feed, and the substrate-integrated waveguide, with labeled dimensions corresponding to the values in Table 5.1. 148

Figure 5.8. Simulated co- and cross-polarized element patterns at the lowest, 6 GHz-resonant, and highest swept capacitances for both the REMA and the square meta-atom. The REMA provides a higher co-polarized directivity compared with the square meta-atom, at the cost of a smaller beamwidth, and also yields better cross-polarization isolation. 150

Figure 5.9. Simulated radiation efficiency versus varactor capacitance at 6 GHz for the REMA and the square meta-atom. The proposed REMA provides an increase in the overall radiation efficiency, especially at lower varactor capacitance values. 151

Figure 5.10. The simulated electric and magnetic polarizabilities for the (a) square meta-atom and the (b) proposed REMA. We find that the REMA favors electric-dipole radiation, while the square meta-atom favors magnetic-dipole radiation. 152

Figure 5.11. Comparison of the current densities and electric fields for the square meta-atom and proposed REMA. 153

Figure 5.12. Simulated co- and cross-polarized beam patterns of the 8-element (a) square and (b) REMA array at 6 GHz, steered from -60° to $+60^\circ$ in 10° steps. The REMA array sustains a higher co-polarized peak and a lower cross-polarized level within the $\pm 30^\circ$ scan range, while both arrays roll off beyond $\pm 30^\circ$ due to the element pattern. 154

Figure 5.13. Simulated co- and cross-polarized realized gain at the desired steering angle for the REMA and square meta-atom arrays at 6 GHz. Within the -30° to 30° scan range, the proposed REMA provides an average co-polarized gain improvement of 3.2 dBi over the square meta-atom, and an average cross-polarization isolation improvement of 11.2 dB. 155

Figure 5.14. Isometric layout of the 4-layer printed circuit board for the fabricated REMA. Layers 1 and 2 consist of the REMA elements, CPW, and SIW, while layer 4 holds the biasing traces. A 1.524 mm thick Rogers 4003C substrate is used between layers 1 and 2, and layers 3 and 4, where pre-preg holds layers 2 and 3 together. 157

Figure 5.15. Fabricated 8-element DMA prototype mounted in the anechoic chamber. The array is fed through the CPW-to-microstrip-to-SIW transition, and the bias-stub network on the back side is connected to the control hardware. . . 158

Figure 5.16. Measured, de-embedded $|S_{12}|$ of the fabricated REMA across the varactor bias voltage sweep (0–15 V). As we tune the varactor diodes with the bias voltage, the resonant frequency of the REMA varies between 5.5 and 6.25 GHz. 159

Figure 5.17. Measured Lorentzian-constrained beamforming weight using (5.3), drawn at four frequencies from 5.85 to 6 GHz with the bias voltage as the curve parameter. The measured Lorentzian constraint matches closely to the theoretical curve (grey), and the wide tuning range allows for a sufficient antenna weight range across multiple frequencies. 160

Figure 5.18. Simulated (dashed) and measured (solid) co-polarized element realized gain of the single-element REMA at 6 GHz, with the simulated varactor capacitance matched to the resonant frequency of each measured bias voltage by color. The measured patterns track the simulated patterns across the tuning range, which validates the Lorentzian polarizability model and the bias-voltage-to-capacitance mapping used to configure the array. 161

Figure 5.19. Measured co- (solid) and cross-polarized (dotted) beam patterns of the fabricated 8-element array at 6 GHz, steered from -60° to $+60^\circ$ in 10° steps. The measured realized gain stays between 7.9 and 9.4 dBi within the $\pm 30^\circ$ scan range, and the cross-polarized level remains more than 20 dB below the co-polarized peak at each commanded angle. 162

Figure 5.20. Measured co- and cross-polarized realized gain of the fabricated 8-element REMA array at 6 GHz versus commanded steering angle from -60° to $+60^\circ$. The array averages 24.7 dB of cross-polarization isolation within the $\pm 30^\circ$ scan range and rolls off at wider angles due to the element pattern. . . 163

Figure 5.21. Measured beam patterns of the fabricated array at four frequencies from 5.85 to 6.00 GHz, steered to $+20^\circ$, with (a) a single bias configuration optimized for the full bandwidth and (b) a separate bias configuration optimized at each frequency. The dotted vertical line marks the commanded steering target. Single-bias operation maintains the peak gain over a roughly 100 MHz band, while per-frequency optimization recovers an additional 2.2 dBi at 6 GHz. 164

Figure 6.1. Overview of the tri-hybrid architecture using DMAs. To manage the signal processing with three layers of configuration, a joint analog, digital, and DMA precoder or combining algorithm is necessary. 171

Figure 6.2. Hardware setup for a potential DMA-based wireless testbed with the fabricated DMA array on the left and a USRP radio on the right. 173

LIST OF TABLES

Table 2.1. Parameters for the modeled DMA based on [1] 33

Table 2.2. Power consumption and component loss in the transmitter architecture model. 36

Table 2.3. Notation used to represent simulation results. 39

Table 3.1. Summary of DMA model parameters incorporated into the beamforming algorithm design 77

Table 5.1. Geometric parameters of the proposed REMA and CPW-to-SIW feed. 149

Table 5.2. Comparison with prior-art DMA prototypes. 162

ACKNOWLEDGEMENTS

The PhD is a difficult journey, and I could not have done it without the support of family and friends. First, I would like to thank the WSIL group, Ryan, Nitish, Ibrahim, Arnaud, Nima, and Jaebum, for all of the wonderful times throughout these years. The random chats, arguing over coffee and tea, and research discussions all made the PhD so much more fruitful. I will always look back fondly on hanging out with everyone at FAH. I'd also like to give a special shout-out to Nitish and Ryan. For Nitish, we went through countless classes, homework assignments, and projects together, collaborated on research, moved across the country, traveled to conferences, and many other things. I'm very grateful to have had such a great friend to start and end the PhD with. For Ryan, your guidance and friendship as an older student in the group was really impactful on my first three years at NC State. I will always be thankful for your help during those times.

Second, I would like to thank all of the friends and family that have been by my side throughout the PhD. My parents have always been so supportive of me in whatever I wanted to do. I am truly so grateful for all of the love and encouragement they have given me during the PhD, especially since I moved far and then farther away. Next, I am very lucky to have had amazing friends across multiple states through the PhD. Moving to a new state without any connections is hard, so I am extra thankful for all of the friends I've met in both North Carolina and California. Whether it was a game night, beach volleyball, or going out to dinner, I have had so many wonderful, fun memories over the last five years that I will always remember. My #1 supporter, however, has been my beautiful wife Sierra. You have been there for me since day 1, and it is not an understatement to say that I could not have done the PhD without you. Your love and support has gotten me through so many of the challenges of the PhD, and I am so happy to have had you there to celebrate all of the successes. I truly cannot thank you enough for all that you've done.

Third, I would like to thank the research mentors that have guided me throughout my PhD journey. I probably would not have pursued a PhD if it wasn't for my undergraduate research

advisor, Dr. Matilde D'Arpino, encouraging me to do so. I learned and grew so much under your mentorship, and I am very thankful for all of the amazing opportunities and support that I had at CAR. Next, I'd like to thank Prof. Rodrigo Castellanos for all of his help at NC State. I came in basically knowing nothing about wireless communications, and our frequent meetings and research discussions were crucial to my growth as a researcher and understanding how to be a PhD student. Lastly, I would of course like to thank my advisor, Prof. Heath. I know that picking the right students to be in the group is not easy, especially ones that did not have significant wireless communication experience. I am very thankful to have joined the lab, gotten to learn under your mentorship, and grow into a capable wireless researcher. In particular, I'd like to thank you for tailoring the PhD to the interests of different students, as well as giving us many unique research opportunities throughout the PhD. I truly loved getting to work on dynamic metasurface antennas, and I am so happy to have gotten to work on actual hardware and fabricated designs. My final prototype made the entire PhD experience feel very rewarding, and I'm thankful for you encouraging me to pursue that direction of work. Moreover, I really enjoyed getting to attend many conferences, present my research findings, and meet with collaborators. These experiences were both extremely valuable and fun, and made all of the research effort feel worth it.

Lastly, I would like to thank God for his steadfast love and pursuit of my soul. Whether I knew it or not, He guided me every step of the way throughout the PhD. This dissertation is a reflection of His goodness and grace, and nothing could have been completed here without Him. I hope that the work herein glorifies His name, and His son, Jesus Christ, whom He sent down to Earth 2,000 years ago.

Chapter 2, in full, is a reprint of the material as it appears in J. Carlson, M. R. Castellanos, and R. W. Heath, "Hierarchical Codebook Design With Dynamic Metasurface Antennas for Energy-Efficient Arrays," *IEEE Transactions on Wireless Communications*, vol. 23, no. 10, pp. 14790–14804, 2024. The dissertation author was the primary investigator and author of this paper.

Chapter 3, in full, is a reprint of the material as it appears in J. M. Carlson, N. V. Deshpande,

M. R. Castellanos, and R. W. Heath, "Wideband Dynamic Metasurface Antenna Performance With Practical Design Characteristics," *IEEE Transactions on Wireless Communications*, vol. 25, pp. 4674–4690, 2026. The dissertation author was the primary investigator and author of this paper.

Chapter 4, in full, has been submitted for publication of the material as it may appear in J. Carlson and R. W. Heath, "Advanced array processing for null steering and DOA estimation with dynamic metasurface antennas," submitted to *IEEE Transactions on Wireless Communications*. The dissertation author was the primary investigator and author of this paper.

Chapter 5, in full, has been submitted for publication of the material as it may appear in J. Carlson, S. Keshmiri, M. F. Imani, and R. W. Heath, "A sub-6 GHz dynamic metasurface antenna design for improved gain and cross-polarization isolation," submitted to *IEEE Transactions on Antennas and Propagation*. The dissertation author was the primary investigator and author of this paper.

VITA

2021	Bachelor of Science in Engineering Physics, The Ohio State University
2023	Master of Science in Electrical and Computer Engineering, North Carolina State University
2026	Doctor of Philosophy in Electrical Engineering (Communication Theory and Systems), University of California San Diego

PUBLICATIONS

Journals

J. Carlson, S. Keshmiri, M. F. Imani and R. W. Heath, "A sub-6 GHz dynamic metasurface antenna design for improved gain and cross-polarization isolation," submitted to *IEEE Transactions on Antennas and Propagation*.

J. Carlson and R. W. Heath, "Advanced array processing for null steering and DOA estimation with dynamic metasurface antennas," submitted to *IEEE Transactions on Wireless Communications*.

N. V. Deshpande, **J. Carlson**, S. Yang, M. Akrout, A. Gonzalez, M. R. Castellanos, T. Ratnarajah, C.-B. Chae and R. W. Heath, "Signal Processing Foundations of Reconfigurable Antennas in the Tri-Hybrid MIMO Architecture," submitted to *npj Wireless Technology*.

L. Han, H. Yin, R. W. Heath and **J. Carlson**, "Power Scaling Law of Superdirective Multi-User Beamforming in Compact Arrays," in *IEEE Transactions on Communications*, vol. 74, pp. 3659–3673, Jan. 2026.

R. W. Heath, **J. Carlson**, N. V. Deshpande, M. R. Castellanos, M. Akrout and C.-B. Chae, "The Tri-Hybrid MIMO Architecture," in *IEEE Wireless Communications*, vol. 33, no. 1, pp. 199–206, Feb. 2026.

J. Carlson, N. V. Deshpande, M. R. Castellanos and R. W. Heath, "Wideband Dynamic Metasurface Antenna Performance With Practical Design Characteristics," in *IEEE Transactions on Wireless Communications*, vol. 25, pp. 4674–4690, 2026.

J. Carlson, M. R. Castellanos and R. W. Heath, "Hierarchical Codebook Design With Dynamic Metasurface Antennas for Energy-Efficient Arrays," in *IEEE Transactions on Wireless Communications*, vol. 23, no. 10, pp. 14790–14804, Oct. 2024.

Conference proceedings

M. Akrout, **J. Carlson** and R. W. Heath, "Modeling and Integration of Dynamic Metasurface Antennas with Clustered Channel Models," in *Proc. ICASSP 2026 - 2026 IEEE International Conference on Acoustics, Speech and Signal Processing (ICASSP)*, Barcelona, Spain, May 2026, pp. 21576–21580.

J. Carlson, S. Keshmiri, M. F. Imani and R. W. Heath, "Design optimization of dynamic metasurface antenna elements for beamforming capabilities," in *Proc. 2026 European Conference on Antennas and Propagation (EuCAP)*, Dublin, Ireland, Apr. 2026, to be published.

J. Carlson and R. W. Heath, "Tri-hybrid combining for interference mitigation in mobile ad hoc networks," in *Proc. 2025 59th Asilomar Conference on Signals, Systems, and Computers*, Pacific Grove, CA, USA, Oct. 2025, pp. 599–603.

J. Carlson, N. V. Deshpande and R. W. Heath, "Interference-resistant reconfigurable antenna arrays via dynamic metasurface antennas," in *Proc. MILCOM 2025 - 2025 IEEE Military Communications Conference (MILCOM)*, Los Angeles, CA, USA, Oct. 2025, pp. 466–471.

N. V. Deshpande, I. Kilinc, **J. Carlson** and R. W. Heath, "Frequency-reconfigurable ad hoc networks with dynamic metasurface antennas," in *Proc. MILCOM 2025 - 2025 IEEE Military Communications Conference (MILCOM)*, Los Angeles, CA, USA, Oct. 2025, pp. 460–465.

N. V. Deshpande, **J. Carlson**, M. R. Castellanos and R. W. Heath, "Frequency-Selective Beamforming with Dynamic Metasurface Antennas," in *Proc. ICC 2025 - IEEE International Conference on Communications*, Montreal, QC, Canada, June 2025, pp. 602–607.

J. Carlson, N. V. Deshpande, M. R. Castellanos and R. W. Heath, "A Wideband Beamforming Algorithm for Dynamic Metasurface Antennas Under Realistic Constraints," in *Proc. ICC 2025 - IEEE International Conference on Communications*, Montreal, QC, Canada, June 2025, pp. 3922–3927.

J. Carlson, N. V. Deshpande, M. R. Castellanos and R. W. Heath, "Analysis of dynamic metasurface antennas under matching network constraints," in *Proc. 2024 58th Asilomar Conference on Signals, Systems, and Computers*, Pacific Grove, CA, USA, Oct. 2024, pp. 614–618.

J. Carlson, M. R. Castellanos and R. W. Heath, "Dynamic metasurface antennas for energy-efficiency MISO communications," in *Proc. GLOBECOM 2023 - 2023 IEEE Global Communications Conference*, Kuala Lumpur, Malaysia, Dec. 2023, pp. 7502–7507.

M. R. Castellanos, **J. Carlson** and R. W. Heath, "Energy-Efficient Tri-Hybrid Precoding with Dynamic Metasurface Antennas," in *Proc. 2023 57th Asilomar Conference on Signals, Systems, and Computers*, Pacific Grove, CA, USA, Oct. 2023, pp. 1625–1630.

J. Carlson, M. R. Castellanos and R. W. Heath, "Wideband Reflected Gain Analysis for Intelligent Reflecting Surface-Aided Communication," in *Proc. 2022 IEEE Globecom Workshops (GC Wkshps)*, Rio de Janeiro, Brazil, Dec. 2022, pp. 55–60.

ABSTRACT OF THE DISSERTATION

Dynamic metasurface antennas for next-generation wireless communications

by

Joseph Michael Carlson

Doctor of Philosophy in Electrical Engineering (Communication Theory and Systems)

University of California San Diego, 2026

Professor Robert W. Heath, Jr., Chair

Large antenna arrays have become foundational to modern wireless communication systems, providing the array gain and spectral efficiency needed to meet growing user demand across new frequency bands. Increasing the number of antennas, however, also raises the power consumption, cost, and physical footprint of the hardware. Reconfigurable antennas have emerged as a way to add flexibility to the array while keeping power and cost low, enabling more energy-efficient systems. Among these, the dynamic metasurface antenna (DMA) is a particularly promising candidate, achieving low-power, reconfigurable beamforming through an array of tunable radiating elements. The DMA, however, is subject to physical constraints not present in conventional phased arrays, such as a restricted set of achievable beamforming weights. These

constraints can degrade the performance and are not yet fully understood in the current literature.

In this dissertation, we develop new models, beamforming algorithms, and an improved element design that address these limitations and make the DMA a feasible option for modern wireless communication systems. First, we design a hierarchical codebook that exploits the unique weight properties of the DMA to enable energy-efficient, limited-feedback beamforming. Next, we extend our analysis to the wideband regime, deriving a closed-form approximation of the DMA beamforming gain over large bandwidths and proposing a successive beamforming algorithm that improves wideband performance. We then move beyond single-beam beamforming to address interference mitigation and source localization. We develop a more accurate DMA element model that accounts for the scattering within the waveguide and train a machine learning model to capture the mutual coupling between elements, achieving accurate and consistent nullsteering in electromagnetic simulations. Finally, we improve the DMA element itself, proposing a rotated elliptical meta-atom that achieves higher gain, radiation efficiency, and cross-polarization isolation than conventional square elements, and we fabricate the element and an array prototype to demonstrate its beamforming capabilities through measurements.

Chapter 1

Introduction

Wireless communication systems continue to evolve toward larger antenna arrays. By combining many antennas, these arrays form directional beams that improve data rates and allow a base station to serve many users at once, which has made them a core technology in fifth-generation (5G) and sixth-generation (6G) systems [2, 3, 4]. Building large arrays, however, is challenging. As the number of antennas grows, so does the power consumption, hardware complexity, and cost of the array [5, 6]. Designing an array that scales to a large number of antennas while remaining power-efficient and low-cost is therefore a central challenge for next-generation wireless systems. In this dissertation, we study dynamic metasurface antennas (DMAs) as an energy-efficient way to build large arrays, and we develop the models, algorithms, and hardware needed to use them in practical wireless communication systems.

1.1 Large antenna arrays for next-generation wireless communications

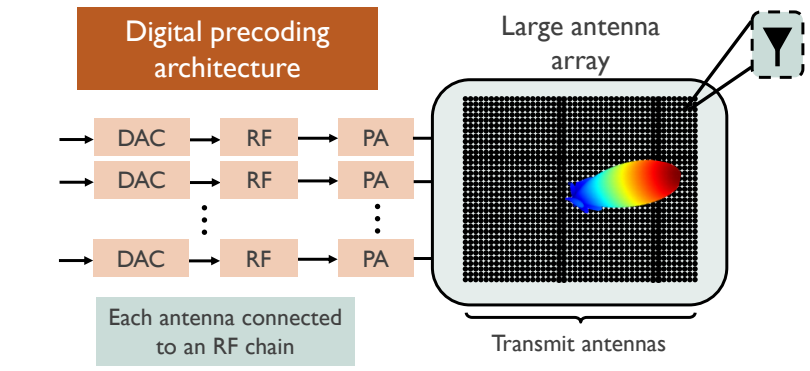
Large antenna arrays improve wireless performance through two main mechanisms. The first is beamforming gain, where the array adjusts the phase and amplitude of the signal at each antenna so that the individual contributions add coherently in the direction of the intended user. As the number of antennas and aperture size grows, the resulting beam becomes narrower and the array gain increases, which raises the received signal strength and suppresses energy radiated

toward unintended directions. The second mechanism is spatial multiplexing. The number of streams that can be supported grows with the number of antennas, so a larger array can serve more users or carry more data without using additional bandwidth [7]. These mechanisms are the foundation of massive multiple-input multiple-output (MIMO) [8], where a base station with far more antennas than users serves them simultaneously with high spectral and energy efficiency [9].

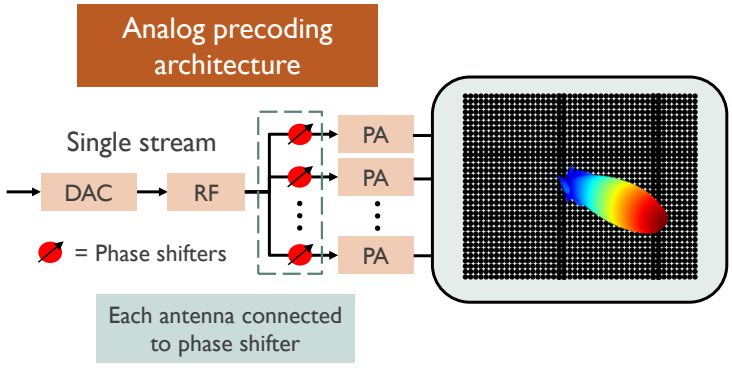
The main drawback of a large array is the cost of its radio hardware. A fully digital array offers the most flexibility, since it connects a dedicated radio frequency (RF) chain to every antenna and can control the signal at each element independently, as shown in Fig. 1.1a. Each RF chain, however, contains data converters, mixers, filters, and amplifiers, whose power and cost add up quickly as the array grows [10]. The data converters are especially demanding, since the power drawn by an analog-to-digital or digital-to-analog converter grows with both its sampling rate and resolution, and therefore with the signal bandwidth [11]. Because a fully digital array needs one RF chain per antenna, its power consumption and cost scale with the number of antennas, which makes the architecture impractical for the very large arrays envisioned for next-generation systems [12].

Hybrid and analog beamforming architectures, shown in Figs. 1.1b and 1.1c, reduce this cost by connecting a small number of RF chains to the array through a network of phase shifters [13, 14, 15]. A range of hybrid precoding designs has been developed for large arrays [16, 17, 18]. However, these architectures still consume significant power, since the phase shifters and associated power dividers introduce insertion loss and consume power that scales with the size of the array [19, 20]. Switch-based, lens-based, and subarray alternatives have been proposed to further reduce this cost [21, 22, 23], but for very large arrays the power and hardware of the analog beamforming network remain a fundamental limitation.

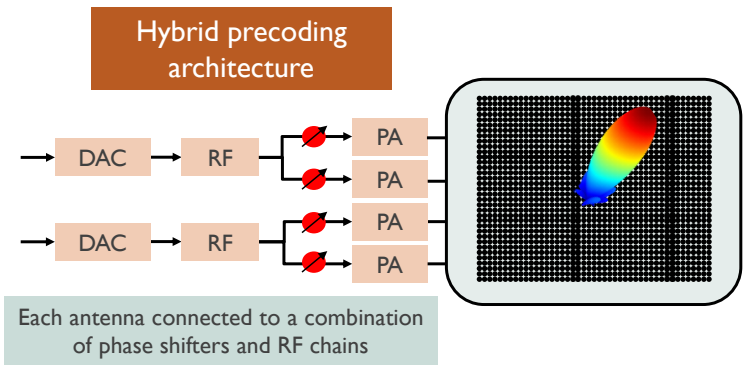
These limitations motivate the search for array architectures that scale to a large number of elements while keeping power consumption and cost low. One approach is to replace power-hungry active components, such as phase shifters, with low-power reconfigurable elements



(a)



(b)



(c)

Figure 1.1. Diagrams of the (a) digital, (b) analog, and (c) hybrid precoding architectures for wireless communication systems. The digital architecture achieves the highest performance but requires a dedicated RF chain per antenna, increasing power consumption and hardware cost. The analog architecture uses a single RF chain with a network of phase shifters, reducing cost and complexity at the expense of performance. The hybrid architecture combines a smaller number of RF chains with analog phase shifters, offering a balance between the two.

integrated directly into the antenna. Reconfigurable antennas tune their radiation characteristics through inexpensive tunable components, providing a path toward dense, energy-efficient arrays [24, 25, 26]. A related line of work uses reconfigurable surfaces and metasurfaces to shape the wireless propagation environment itself [27, 28]. Among transmit-side architectures, the dynamic metasurface antenna has emerged as a particularly promising energy-efficient array [29]. We introduce the DMA and its operating principles in the following section.

1.2 Dynamic metasurface antennas

Metasurfaces are engineered planar structures composed of subwavelength resonant elements that shape electromagnetic waves with a thin, low-profile aperture [30, 31, 32]. When the individual elements are made electronically tunable, the surface becomes a programmable aperture whose radiation can be reconfigured in real time [33]. The dynamic metasurface antenna applies this principle to build a reconfigurable transmit and receive array [34, 29]. A DMA consists of a waveguide, or a set of waveguides, on which a dense array of metamaterial radiating elements is etched, as shown in Fig. 1.2. As the guided wave propagates, each element leaks a controllable fraction of the energy into free space, so that the DMA behaves as a tunable leaky-wave antenna [35]. Unlike a phased array, where each antenna is fed independently, a DMA feeds all of its elements from a single guided wave. As the wave travels along the waveguide, it advances in phase and loses amplitude as each element radiates part of its energy, so every element is excited by a field of different amplitude and phase, as shown in Fig. 1.3. The excitation of a given element therefore depends on its position along the waveguide and on the elements that precede it, which the DMA beamforming model must capture to predict the radiated pattern.

Each radiating element is loaded with a low-power tunable component, such as a varactor diode, that shifts the element's resonant frequency and thereby controls the amplitude and phase of the field it radiates [1, 36]. By tuning every element, the DMA forms and steers beams without the phase shifters, attenuators, or per-element RF chains used in conventional arrays. Because the

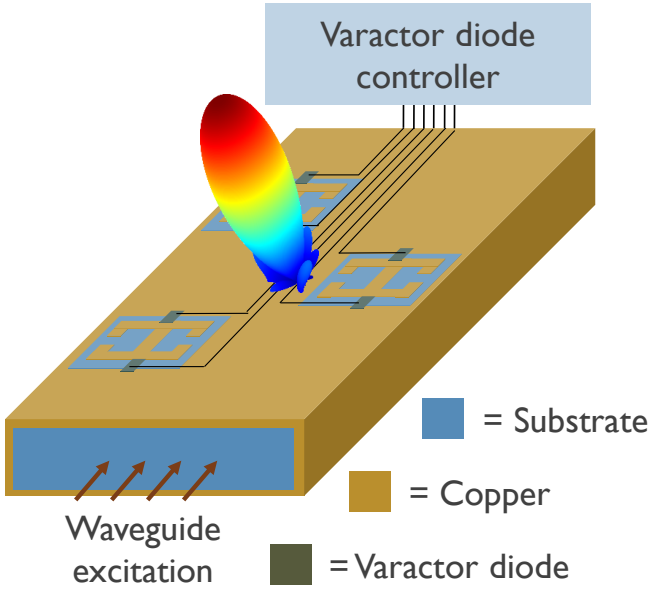


Figure 1.2. Design and structure of the DMA. A DMA consists of multiple sub-wavelength meta-atoms etched onto the upper conductor of a waveguide. Integrated, tunable components, like varactor diodes, provide beamforming capabilities with low power consumption.

tunable components draw little power and the elements can be packed at subwavelength spacing on a planar substrate, a DMA forms a large, dense aperture at low power, cost, and profile [29]. These properties first made DMAs attractive for microwave imaging, radar, and sensing [37, 38], and more recently for energy-efficient beamforming in wireless communications [39, 40, 41].

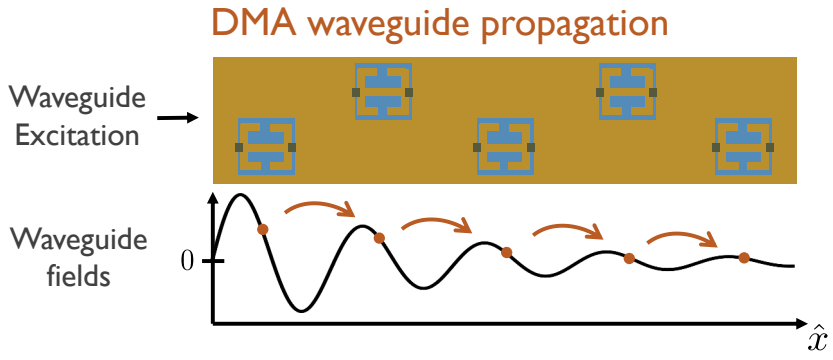


Figure 1.3. The guided-wave propagation in a DMA. The waveguide is excited from one end, and each metamaterial element radiates a fraction of the guided wave as it propagates. The lower plot shows the field along the waveguide, which advances in phase and decays in amplitude from element to element, so each element is excited differently.

The reconfigurability of a DMA element comes at the cost of a constrained beamforming response. The radiation of each tunable element is modeled as a dipole whose polarizability follows a Lorentzian resonance [42]. As a result, the amplitude and phase of each effective beamforming weight are coupled and confined to a circle in the complex plane, a relationship known as the Lorentzian constraint. This differs from the unit-modulus, freely tunable phase assumed for ideal phase shifters, and it means that beamforming algorithms designed for conventional arrays cannot be applied directly to DMAs. Accurately capturing this constraint, together with the waveguide propagation and the frequency-selective element response, is essential to predict and optimize DMA performance.

DMAs should also be distinguished from the closely related reconfigurable intelligent surfaces (RIS) that have received significant recent attention [27, 28]. An RIS is a passive surface placed in the propagation environment that reflects impinging waves, whereas a DMA is an active antenna with a dedicated RF feed that transmits and receives as part of the transceiver. The DMA is therefore a direct, low-power replacement for the antenna array and its analog beamforming network, rather than an additional element in the channel. Despite these advantages, using a DMA in a practical wireless system raises several challenges that arise from the DMA's physical structure and its constrained, frequency-selective response, which we discuss next.

1.3 Challenges in DMA-based communication

While DMAs offer an energy-efficient alternative to conventional arrays, realizing their potential in a wireless communication system raises challenges that stem from the Lorentzian-constrained, frequency-selective, and hardware-dependent nature of the DMA. In this dissertation, we address four of these challenges, corresponding to the four thrusts in Fig. 1.4, which we outline below and which form the basis of the technical chapters that follow.

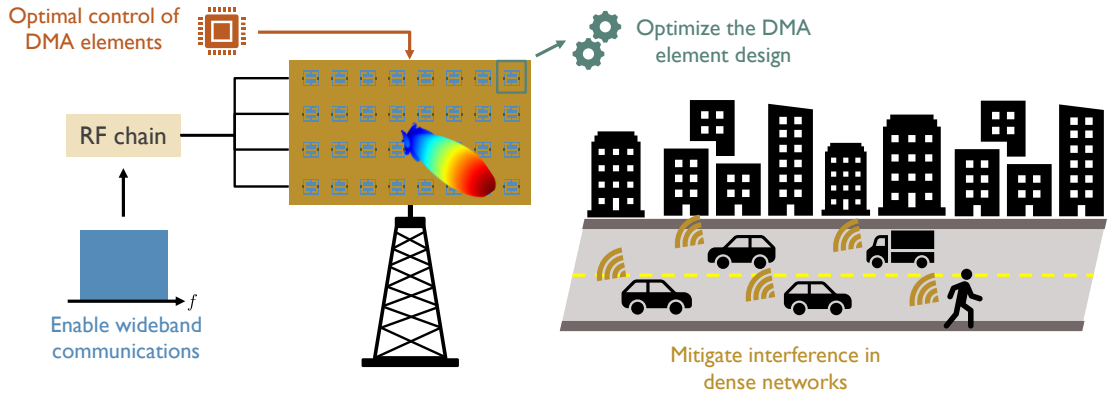


Figure 1.4. The main research problems addressed in this dissertation. A DMA offers an energy-efficient way to build a large antenna array, but using it in a practical wireless communication system requires new models, algorithms, and hardware designs. We develop these across the four areas shown, which form the basis of Chapters 2–5.

1.3.1 Beamforming and codebook design

Conventional beamforming relies on codebooks of predetermined beam patterns, such as the discrete Fourier transform codebooks and the hierarchical beam-training codebooks used for initial access in modern cellular standards [43]. These codebooks assume unit-modulus weights with freely tunable phase, which a DMA cannot realize. Since the Lorentzian constraint couples the amplitude and phase of every element, a desired beamformer must be mapped onto the constrained DMA weights, reducing beamforming gain and steering accuracy [34]. The wide beams required at the coarse layers of a hierarchical codebook are particularly difficult, since they are normally formed by deactivating elements, which a DMA must instead approximate within its constrained response. Designing practical codebooks for DMAs, and quantifying the energy efficiency they achieve relative to a phased array that must drive power-hungry phase shifters, is therefore an important open problem. We address this challenge in Chapter 2, where we design a hierarchical codebook for DMAs and analyze the resulting spectral and energy efficiency against a realistic phased array.

1.3.2 Wideband communications and DMA element modeling

Most analyses of DMAs assume a narrowband signal, yet next-generation systems operate over wide bandwidths where the physical characteristics of the DMA become significant. The Lorentzian resonance of each tunable element is inherently frequency-selective, so the amplitude and phase of the effective beamforming weights vary across the band and a configuration that is optimal at one frequency is suboptimal at others. Two further design characteristics compound this effect. The waveguide attenuates the guided wave as power leaks out along its length, imposing a frequency-dependent amplitude taper across the elements, and the tunable components can only shift the element resonance over a limited range. These effects are negligible for narrowband signals but have a large impact on the achievable beamforming gain and spectral efficiency as the bandwidth grows, similar to how beam squint degrades conventional wideband arrays [44]. Characterizing wideband DMA performance under these practical design characteristics, and designing beamforming algorithms that account for the frequency-selectivity, remains largely unexplored. We address this challenge in Chapter 3, where we analyze the wideband beamforming gain and spectral efficiency of DMAs under element frequency-selectivity, waveguide attenuation, and limited tuning range, and propose a beamforming algorithm that improves the wideband performance.

1.3.3 Interference mitigation and source localization

Beyond steering a single beam, practical systems must suppress interference by placing spatial nulls and localize sources by estimating their directions of arrival (DOA). These array-processing tasks are well established for conventional arrays through adaptive nulling [45] and subspace methods such as MUSIC [46], but they are difficult for DMAs for three reasons. First, the Lorentzian constraint limits the patterns a DMA can form, making deep, accurately placed nulls hard to achieve. Second, a DMA typically connects its many elements to a single radio frequency chain, which precludes forming the full array covariance matrix that subspace DOA

estimators require. Third, the analytical DMA model does not fully capture mutual coupling and internal waveguide scattering, so the patterns it predicts deviate from those of a fabricated device. As a result, accurate nullsteering and single-chain DOA estimation with DMAs has not yet been demonstrated. We address this challenge in Chapter 4, where we develop array processing methods that place accurate nulls for interference mitigation and estimate the directions of arrival of multiple sources through a single DMA array.

1.3.4 DMA element design optimization

The performance of a DMA depends not only on its beamforming algorithm but also on the design of the radiating element, which most analyses assume to be ideal. In practice, the element geometry, the integrated tunable component, the radiation efficiency, and the resonant-frequency tuning range all determine the amplitude and phase that each element can radiate [35, 36]. These element-level factors become especially important at sub-6 GHz, where most existing DMAs have not been designed to operate. Most prototypes instead target frequencies of 10 GHz and above, and the few sub-6 GHz designs use binary tuning that supports only a small number of fixed beams rather than continuous beamsteering. Designing a continuously-tunable element at sub-6 GHz is difficult for two reasons. First, the element must grow in size at lower frequencies while the varactor and substrate do not, which increases the loss near the tuning component and the coupling to the waveguide, reducing the radiation efficiency. Second, the element must maintain strong isolation between its two polarizations to support the dual-polarized antennas used in modern base stations. A DMA element that achieves high radiation efficiency, gain, and cross-polarization isolation at sub-6 GHz has not been demonstrated in prior work. We address this challenge in Chapter 5, where we propose a rotated elliptical element designed to radiate as an electric dipole, and fabricate an eight-element prototype at sub-6 GHz.

1.4 Summary of contributions

The overall goal of this dissertation is to make dynamic metasurface antennas a practical, energy-efficient solution for next-generation wireless communication. To this end, we develop signal models, beamforming and array processing algorithms, and element designs that account for the limitations of the DMA, and we evaluate them with realistic electromagnetic simulations and channel models. The specific contributions of this dissertation are summarized as follows.

- **Hierarchical codebook design with dynamic metasurface antennas for energy-efficient arrays.** In Chapter 2, we propose a phase-rotation optimization that enhances the DMA beamforming gain and design a hierarchical codebook that exploits the Lorentzian zero-weight to form the wide beams required for beam training. Using a detailed power-consumption and channel model, we show that the DMA outperforms a passive phased array in both spectral and energy efficiency and achieves roughly twice the energy efficiency of an active phased array.

- **Wideband dynamic metasurface antenna performance with practical design characteristics.** In Chapter 3, we develop a wideband DMA signal model that captures element frequency-selectivity, waveguide attenuation, and limited resonant-frequency tuning, derive a closed-form approximation of the wideband beamforming gain, and propose a successive beamforming algorithm. We show that the approximation accurately predicts performance and that the proposed algorithm improves the wideband spectral efficiency over a baseline, particularly as the signal bandwidth grows.

- **Advanced array processing for nullsteering and DOA estimation with dynamic metasurface antennas.** In Chapter 4, we develop a machine learning model that bridges the analytical DMA model and its true electromagnetic response, and use it to place accurate nulls and to estimate directions of arrival through a single RF chain. The proposed methods achieve a low median pattern-prediction error for modeling accuracy, allow up to

three simultaneous nulls with a 10-element DMA, and attain direction-of-arrival estimation approaching that of conventional MUSIC.

- **A sub-6 GHz dynamic metasurface antenna design for improved gain and cross-polarization isolation.** In Chapter 5, we propose and characterize a novel DMA element design tailored to sub-6 GHz bands, which improves the radiation characteristics relevant to beamforming. We find that the fabricated eight-element array prototype provides consistent and accurate beamsteering within a $\pm 30^\circ$ scan range, maintaining a high realized gain and cross-polarization isolation when compared with prior varactor-based DMA designs.

1.5 Organization

The remainder of this dissertation is organized as follows. In Chapter 2, we present the hierarchical codebook design for DMAs and analyze the resulting spectral and energy efficiency. In Chapter 3, we develop the wideband DMA signal model, derive the beamforming-gain approximation, and propose the successive beamforming algorithm. In Chapter 4, we develop the array processing methods for nullsteering and direction-of-arrival estimation with a single RF chain. In Chapter 5, we present the improved DMA element design for sub-6 GHz communication. Finally, Chapter 6 summarizes the dissertation and discusses directions for future work.

1.6 Notation

Throughout this dissertation, we use the following notation. A bold capital letter $\mathbf{A}$ denotes a matrix, a bold lowercase letter $\mathbf{a}$ denotes a vector, and a script letter $\mathcal{A}$ denotes a set. We write $\mathbf{A}^\mathsf{T}$, $\mathbf{A}^\mathsf{c}$, and $\mathbf{A}^*$ for the transpose, conjugate, and conjugate transpose of $\mathbf{A}$, respectively. We denote the nth entry of a vector $\mathbf{a}$ by a_n, the vectorization of a matrix $\mathbf{A}$ by $\mathrm{vec}(\mathbf{A})$, and the diagonal matrix with diagonal entries $a_0, \ldots, a_{N-1}$ by $\mathrm{diag}(a_0, \ldots, a_{N-1})$. For a complex number a, we use $\mathrm{Re}\{a\}$ and $\mathrm{Im}\{a\}$ to denote its real and imaginary parts, $|a|$ its magnitude, and $\angle a$ its phase. We denote the Hadamard (elementwise) product by $\odot$ and the Frobenius norm of a

vector $\mathbf{a}$ by $\|\mathbf{a}\|_{\mathsf{F}}$. We write $a \sim \mathcal{CN}(\mu, \sigma^2)$ to indicate that a is a circularly symmetric complex Gaussian random variable with mean μ and variance σ^2. Finally, $O(\cdot)$ denotes the big O notation.

Chapter 2

Hierarchical codebook design with dynamic metasurface antennas for energy-efficient arrays

2.1 Overview

In this chapter, we propose a codebook design for an 8-element dynamic metasurface antenna array. Leveraging the unique ”zero”-weight in the Lorentzian constraint, we generate wide and narrow beams using the DMA to create a hierarchical codebook. Then, with a realistic power consumption model, we simulate the DMA in a real-world wireless communication scenario to characterize the energy efficiency benefits that DMAs obtain over active and passive phased array architectures.

2.2 Introduction

DMAs are a type of reconfigurable antenna that form densely-packed energy-efficient arrays [34]. The DMA consists of slots in a waveguide that radiate power from an initial waveguide excitation, forming a leaky-wave slot antenna. DMAs leverage metasurface technology in their slotted element design to enable tight spacing, and reconfigurable components to perform low-power beamforming. Unlike a traditional antenna that has a fixed radiation pattern, a DMA has an adaptive radiation pattern tuned through the reconfigurable component. This differs

from a conventional radio frequency (RF) system, where antennas are connected to separate beamforming hardware like analog phase-shifters [47]. Although DMAs have desirable features from a power consumption and adaptive beamforming perspective [1, 34], further research is needed to analyze the benefits and drawbacks of DMAs in a MIMO wireless system.

2.2.1 Prior work

Large antenna arrays have been proposed in massive MIMO and millimeter wave (mmWave) systems as a method to increase spectral efficiency [8, 9, 20]. Scaling the number of antennas increases the spatial multiplexing capabilities of the system to achieve higher data rates and also allows for radiated energy to be focused very precisely towards desired users [9]. The increased flexibility, control and directivity of the radiation pattern is vital to compensate for path-loss in mmWave systems [13, 48] and generally provides more energy-efficient communication as less radiated energy is wasted in undesired directions [7]. Despite these advantages, a main challenge in realizing large antenna arrays is the associated increase in power consumption, hardware footprint and overall cost [5, 10].

Hybrid and analog precoding can decrease the power consumption for an array by reducing the number of radio frequency (RF) chains from conventional digital precoding [23, 15, 17]. Hybrid precoding has been analyzed for multiple different analog and digital precoding architectures to reduce power consumption, such as partially- [18] and fully-connected phase shifter systems [21] and subarray architectures [23]. However, scaling hybrid and analog precoding for large antenna arrays will still consume significant amounts of power through active phase shifters. Instead of concentrating on the transmitter hardware, DMAs have been proposed as a solution to decrease system power consumption by beamforming with the adaptive antenna radiation pattern [35]. Since DMAs enable beamforming with low-power low-profile reconfigurable components, transmitter hardware components and power consumption can be significantly reduced for large antenna arrays.

DMAs are a type of reconfigurable antenna, which generally operate by tuning the

resonant frequency of individual elements to elicit a desired radiated amplitude and phase for beamforming [24, 25]. A common reconfigurable antenna design is to modify conventional antennas, like dipole or patch antennas, with a reconfigurable component [49, 50, 51]. More complex designs involve physically change the antenna geometry via mechanical devices [52] and using materials like ferrites [53] or liquid crystal [54] to alter the radiated response of the antenna. We focus on the DMA implementation of reconfigurable antennas over other designs as DMAs typically provide higher radiation efficiency and leverage metasurface technology to allow for dense arrays due to the tightly spaced elements [29]. The dense energy-efficient arrays made possible through DMAs makes them a great candidate to enable the large antenna arrays required for massive MIMO and mmWave systems.

A key challenge in enabling beamforming using a DMA is the element weight constraint. DMA element weights have a limited phase range of $[-\pi, 0]$, whereas typical phase shifters provide the full $[0, 2\pi]$ phase coverage [34, 35]. The DMA element weight phases are also coupled to a unique amplitude curve that varies from 0 to 1 with the phase. Prior work has studied DMAs to overcome the DMA weight limitation and enable single-beam beamforming. For desired weights given by unit-amplitude complex-valued weights, the DMA beamforming method proposed in [55, 34] maps the desired weights to the DMA weights with two formulations for minimizing the Euclidean distance of the DMA weights and minimizing the phase difference. Results with a simulated DMA show that both mapping techniques allow for the DMA beam pattern to be steered in a desired direction with a high degree of accuracy in spite of the limited DMA phase range. A physical DMA prototype has also been developed in [1] to use the mapping techniques experimentally and verify their effectiveness for beamsteering. Additional studies have focused on DMA array processing to surpress grating lobes by applying phase shifts to each waveguide [56] and to minimize side lobes through an optimization algorithm of the reconfigurable controls [57]. The foundational work on DMAs in [34, 35, 55, 1] provides methods and results to overcome the beamforming weight limitations imposed by DMA elements, showing the potential for DMAs to create low-power, energy-efficient, reconfigurable arrays.

Recent studies have developed precoding and signal processing algorithms for MIMO with DMAs as well [39, 40, 41, 58]. The precoding studies largely model DMAs as an antenna array with constrained beamforming weights introduced by the DMA characteristics. The waveguide architecture of DMAs is modeled by integrating the waveguide electromagnetic field propagation into the wireless channel. Through this DMA model, prior work has developed ways to optimize the DMA weights for uplink and multi-user MIMO-OFDM scenarios [39, 40]. An algorithm has been developed to tune the DMA weights in a DMA-based precoding architecture to maximize energy efficiency in a multi-user MIMO system [41]. A hybrid DMA architecture has been proposed to combine digital precoding with DMA-based precoding [58]. The DMA hybrid precoder was then designed to maximize spectral efficiency via a joint optimization of the digital and DMA weights. While useful for developing signal processing algorithms for DMAs, the aforementioned DMA model places assumptions on the DMA to ignore mutual coupling, element perturbation of the waveguide feed, and other physical non-idealities of the DMA [39, 40, 41, 58]. Additional research is needed to incorporate realistic DMA constraints into the precoder design to obtain algorithms that work in practice.

Energy efficiency is a key metric of performance for MIMO systems due to the large amount of integrated circuitry [59, 60]. Despite the power consumption savings made possible by DMAs, there is still limited work comparing a DMA transmitter architecture to that of analog, digital or hybrid precoding architectures. The power consumption and component loss of the RF front end is heavily dependent on the transmitter architecture and MIMO application, making the development of an accurate hardware model a difficult task. Prior work on MIMO energy efficiency has implemented a realistic power consumption model to derive an expression for the optimal number of transmit antennas per base station to maximize energy efficiency [61, 62], and show that energy efficiency is maximized for hundreds of antenna per base station in a multi-user environment [63]. Additional research places emphasis on the hardware power consumption for different precoding architectures. A tradeoff between spectral and energy efficiency for active and passive phase shifters was analyzed in [11, 19], and switches have been shown to

provide channel estimation performance equal to or better than phase shifters [21]. The insights from [61, 63] stress the importance of large arrays for energy-efficient MIMO communications, and the hardware models in [11, 21, 19] provide a valuable baseline for comparing the power consumption of different MIMO precoding architectures. We will build upon these studies to analyze a DMA transmitter architecture compared to an analog precoding architecture.

2.2.2 Problem formulation

In this work, we analyze the power consumption and achievable rate of realistic DMAs with practical limitations. We examine the ability of DMAs to provide high antenna efficiency and beamsteering accuracy compared to phased arrays. We use electromagnetic simulations of DMAs, practical power consumption models, and a realistic channel generator to obtain accurate energy efficiency results that incorporate all of the characteristics of a DMA-based transmitter. We then compare the spectral and energy efficiency results of the DMA with both active and passive phased array architectures using patch antennas. We find that the DMA outperforms the passive phased array architecture in spectral and energy efficiency due to the high component loss of passive phase shifters. Compared to the active phased array, the DMA provides lower spectral efficiency but greater energy efficiency because of the varactor diode power consumption savings. Additionally, to improve the beamforming of the DMA, we introduce a phase rotation optimization technique that increases the DMA beamforming gain with the restricted Lorentzian-constrained weights.

2.2.3 Contributions

In this chapter, we integrate a codebook design with DMAs to analyze the resulting spectral and energy efficiency in a realistic wireless simulation environment. First, we propose a novel method for enhancing the beamforming gain of DMAs through an optimal phase rotation of the desired weights prior to mapping. We then apply this proposed mapping technique to a hierarchical codebook. Despite the widespread use of codebooks in current wireless standards

[64, 65], there are no studies that investigate codebook design for DMAs. Moreover, we use the hierarchical codebook to present new methods for generating wide beamwidth beam patterns with the DMA. While much of the DMA signal processing literature uses DMA models that ignore aspects like mutual coupling and element perturbation of the waveguide, we simulate a DMA to obtain realistic beam patterns in the electromagnetic simulation software HFSS. This allows us to account for the constraints and effects imposed by the physical DMA design that are not included in typical DMA models. Furthermore, we use the HFSS measurements and channel generation software QuaDRiGa to model a DMA-based MIMO system for spectral efficiency analysis. We apply QuaDRiGa with DMAs to account for channel effects like scattering, polarization, and path loss. Many current studies have implemented a simple multi-path channel model that does not account for these effects [58, 39, 41, 40]. Lastly, we integrate a detailed transmitter architecture to determine the power consumption savings of DMAs compared to a typical phased array. Prior work has analyzed energy efficiency with a DMA model that assumes perfect channel state information and unconstrained precoding [41]. We incorporate simulated DMA results from a realistic DMA design applying the hierarchical codebook design and limited feedback precoding. We use these calculations to establish the tradeoff in DMA performance with power consumption through the resulting spectral and energy efficiency. We summarize the contributions of this chapter as follows:

- We propose a novel method to enhance DMA single-beam beamforming gain via an optimized phase rotation prior to mapping. The proposed approach provides beam patterns with increased antenna efficiency, realized gain, spatial coverage, and steering accuracy compared with state-of-the-art methods.

- We leverage the ability to turn off DMA elements to create a hierarchical codebook. DMA beam patterns obtained from computational electromagnetics software demonstrate that the proposed codebook can achieve wide beamwidths while still maintaining adequate radiated power.

- We use a realistic power consumption model and channel model simulator to compare a DMA system and a practical phased-array with patch antennas in terms of the spectral and energy efficiency. While the patch antenna array with active phase shifters produces greater spectral efficiency, the DMA provides the best energy efficiency due to the power consumption savings in the reconfigurable varactor diodes.

This chapter is organized as follows: In Section 2.3, we discuss the operation of the DMA and how to incorporate its radiation characteristics into the signal model. We then establish a MISO-OFDM signal model for use with the DMA, integrating the DMA characteristics into the beamformer and channel model. Next, in Section 2.4, we describe the DMA mapping techniques implemented in [55] and propose a novel method to enhance the DMA beamforming gain via a phase rotation of the desired weights prior to mapping. In Section 2.5, we discuss the physical DMA design and transmitter architecture used to create DMA beam patterns and analyze power consumption. This section also details the hierarchical codebook design. In Section 2.6, we present results for the simulated DMA in HFSS with the hierarchical codebook design and power consumption model. We analyze the ability of the DMA to produce wide beamwidths, the coverage of the DMA hierarchical codebook through multiple mapping techniques, and the spectral and energy efficiency results for the DMA compared to a realistic phased array. Lastly, we summarize the key findings and results for this work in Section 2.7.

2.3 System model

We consider a single-user MISO-OFDM system with DMAs at the transmitter. We take an individual DMA to consist of a planar array with N_{T} total radiating elements. The DMA comprises D waveguides and L radiating elements per waveguide such that $N_{\mathsf{T}} = DL$, as shown in Fig. 2.1. The DMA is assumed to have reconfigurable elements that allow for changes to their radiated amplitude and phase. For a total of K subcarriers, we define the kth subcarrier wireless channel $\mathbf{h}[k]$ between the transmit and receive antennas to be an $N_{\mathsf{T}} \times 1$ matrix [23].

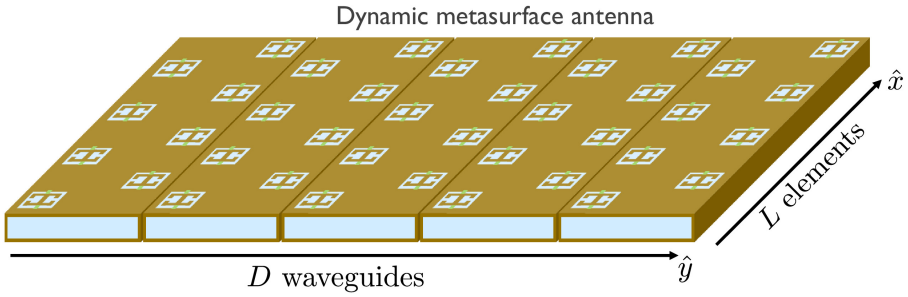


Figure 2.1. Visualization of an entire DMA with D waveguides and L radiating slot elements per waveguide.

2.3.1 DMA element model

We now discuss the general operation of the DMA to integrate its characteristics into the signal model. DMAs operate as a leaky-wave slot antenna, where each antenna element consists of a waveguide slot that radiates power [34]. The integration of reconfigurable components is the key enabling technology for energy-efficient beamforming with DMAs. The reconfigurable components operate by changing the resonant response of the individual DMA elements, which shifts their radiated amplitude and phase [39]. Changing the resonance of the DMA element requires altering its capacitance and/or inductance. This can be achieved in a variety of ways. Examples include integrating a varactor diode to tune the DMA element capacitance, or using a liquid crystal to tune the effective permittivity of the substrate [66]. In our work, we focus on the varactor diode implementation. Using varactor diodes is consistent with the physical DMA models in [1, 34]. The varactor diode capacitance range limits the resonant frequency tuning of the DMA. Adjusting the DMA element resonant frequency through varactor diodes leads to a controllable radiated phase and amplitude, enabling beamforming for the DMA.

We now examine how to integrate the DMA element models in [34, 1] into a DMA precoding framework. DMA elements are typically modeled as magnetic dipole radiators whose magnetic polarizability α_{M} dictates the radiated amplitude and phase [1, 34]. As DMA element geometry mimics a complimentary electric-LC resonator, we can relate the DMA element frequency response to a simple LC circuit. The inductance and capacitance for the circuit are

determined by the element geometry and the varactor diode value. For a DMA element, we let F be the coupling factor and γ be the damping factor. We also define ω as the angular frequency and ω_0 as the resonant angular frequency. The LC circuit model describes the magnetic polarizability as [1]

$$\alpha_{\mathsf{M}}(\omega) = \frac{F\omega^2}{\omega_0^2 - \omega^2 + \mathrm{j}\omega\gamma}. \tag{2.1}$$

The varactor diode can alter (2.1) by changing the resonant frequency ω_0, altering the amplitude and phase of the polarizability at a specific frequency.

Next, we discuss how to translate the magnetic dipole model to beamforming weights. For a DMA, the radiated fields are related by the dipole moment η of each DMA element [1]. For the magnetic polarizability $\alpha_{\mathsf{M}}(\omega)$ and waveguide magnetic field m, the dipole moment is given as $\eta = \alpha_{\mathsf{M}}(\omega)m$ [1]. Since the waveguide magnetic field is fixed, tuning $\alpha_{\mathsf{M}}(\omega)$ via the reconfigurable component allows for control of the radiated field through the DMA element dipole moment. Therefore, the tunable magnitude and phase of the magnetic polarizability can be thought of as the beamforming weights for a DMA precoding architecture. The integration of a varactor diode works to tune the resonant frequency ω_0 of the magnetic polarizability in (2.1). At a center angular frequency ω_{c}, these tuning states can create different radiated amplitude and phases with $\alpha_{\mathsf{M}}(\omega_{\mathsf{c}})$, where ω_0 is controlled by the varactor diode. We can normalize $\alpha_{\mathsf{M}}(\omega_{\mathsf{c}})$ by the factor $\frac{F\omega_0}{\gamma}$ to model the available DMA beamforming weights as Lorentzian-constrained weights given by [58, 55]

$$\mathcal{Q} = \left\{ -\frac{\mathrm{j} + e^{\mathrm{j}\varphi}}{2} : \varphi \in [0, 2\pi] \right\}. \tag{2.2}$$

The normalization by $\frac{F\omega_0}{\gamma}$ is such that the highest magnitude weight value coincides with desired weights at $-1\mathrm{j}$. The normalization makes it easier to compare the DMA weights to conventional unit-norm beamforming vectors and enables the mapping methods developed in [55], as discussed in Section 2.4. Given the limited DMA weights, we define the feasible DMA beamforming set $\mathcal{F}_{\mathsf{DMA}} = \left\{ \mathbf{f} = [f_1, \ldots, f_{N_{\mathsf{T}}}]^T : f_i \in \mathcal{Q}, i = 1, \ldots, N_{\mathsf{T}} \right\}$ as the set of all vectors of length N_{T} whose elements satisfy the constraint for $\mathcal{Q}$.

The DMA waveguide affects signal propagation, so we incorporate its effect in the channel model. The electric and magnetic fields within the waveguide have a sinusoidal distribution that also effects the radiation characteristics of each DMA element. As the electromagnetic fields propagate down the waveguide, the reference wave becomes attenuated due to the radiation of energy through the DMA slots and a waveguide attenuation constant. We assume there to be an attenuation $\bar{\alpha}$ which denotes the average attenuation of the waveguide fields due to the radiated power and losses [34]. This attenuation constant can be calculated with the polarizability results, as described in [34]. In our work, however, we will use simulation results to obtain the DMA beam patterns, which will inherently account for the waveguide attenuation in the electromagnetic simulations.

We now define the DMA waveguide model. For a waveguide propagation constant β, element position $x_{d,\ell}$ representing the dth waveguide and ℓth element, and assuming a unit-amplitude reference wave, the waveguide magnetic field at each DMA element is modeled as [58]

$$m_{d,\ell} = e^{-(\mathrm{j}\beta+\bar{\alpha})x_{d,\ell}}. \tag{2.3}$$

We define $\mathbf{m} \in \mathbb{C}^{DL\times 1}$ as the vectorized waveguide magnetic field values. We assume that the bandwidth is narrow enough such that the propagation constant β does not change significantly with frequency, allowing us to approximate $\mathbf{m}$ as frequency-flat. The propagation constant of the DMA waveguide introduces an inherent phase advance into the DMA system. Therefore, the DMA weights must be tuned both to steer the beam in a desired direction, and to counteract this phase advance.

The Lorentzian-constrained weights and waveguide model highlight the main tradeoff for enabling wireless communications with DMAs. DMAs offer an energy-efficient solution to beamforming via low-power reconfigurable components. The limited weights and grating lobes from the waveguide phase advance, however, often lead to decreased beamforming gain and

beamsteering accuracy compared to phased arrays [56, 1]. In the next section, we will integrate these parameters into a MISO signal model.

2.3.2 Communication and signal model

Next, we describe the MISO precoding architecture for implementation with a DMA. We first define the single-stream MISO-OFDM received signal $y[k]$ for Gaussian-distributed noise $n[k] \sim \mathcal{N}_{\mathbb{C}}(0,1)$, wireless channel $\mathbf{h}[k]$ from transmit antenna n_{T} to the single receiver, beamformer $\mathbf{f}$, transmitted symbol $s[k]$ and signal-to-noise ratio (SNR) ρ as [23]

$$y[k] = \sqrt{\rho}\mathbf{h}^*[k]\mathbf{f}s[k] + n[k]. \tag{2.4}$$

In the DMA architecture, the beamformer $\mathbf{f}$ will consist of the DMA beamforming weights, whose frequency response can be taken as a bandpass filter given the LC circuit model. It has been shown that the quality factor for the DMA element frequency response typically results in an approximately equal gain across frequency for a narrowband waveguide excitation [39]. Therefore, we assume that the bandwidth is small enough such that we can approximate the beamformer $\mathbf{f}$ as frequency-flat. As our goal is to investigate the use of DMAs for codebook design, we assume $\mathbf{f}$ to belong to a set of codewords in a codebook $\mathcal{F} \subseteq \mathcal{F}_{\mathsf{DMA}}$ for beamforming. For the codebook $\mathcal{F}$, the spectral efficiency optimized by the codeword selection assuming a known channel is then given as [67]

$$C\left(\rho|\{\mathbf{h}[k]\}_{k=1}^{K}\right) = \underset{\mathbf{f}\in\mathcal{F}}{\operatorname{argmax}} \frac{1}{K}\sum_{k=1}^{K}\log_2\left(1+\rho|\mathbf{h}^*[k]\mathbf{f}|^2\right). \tag{2.5}$$

We choose to investigate codebook designs for DMAs as codebooks are practical, low-complexity, and widely used in current standards [64, 65]. This topic also has not been studied in literature with DMAs like [58, 41, 39]. Therefore, we implement a hierarchical codebook design with DMAs in this chapter to help close the gap in literature and compare against current beamforming

methods with phased arrays.

We compare a typical analog precoding architecture to a DMA precoding architecture in Fig. 2.2 for a single-stream scenario. Using analog beamforming with phase shifters, an $N_{\mathsf{T}} \times 1$ beamformer $\mathbf{f}_{\mathsf{PS}}$ contains weight information to control each antenna. For a DMA beamformer $\mathbf{f}_{\mathsf{DMA}}$, however, we use the integrated varactor diode to alter the radiated amplitude and phase instead of phase shifters. The DMA beamforming weight information is translated to the varactor diode voltage control for beamforming via a weight-to-voltage mapping. The elements of the DMA beamformer $\mathbf{f}_{\mathsf{DMA}}$ are restricted by the Lorentzian-constrained weights $\mathcal{Q}$, while the elements of the phased array beamformer $\mathbf{f}_{\mathsf{PS}}$ lie on the complex unit circle.

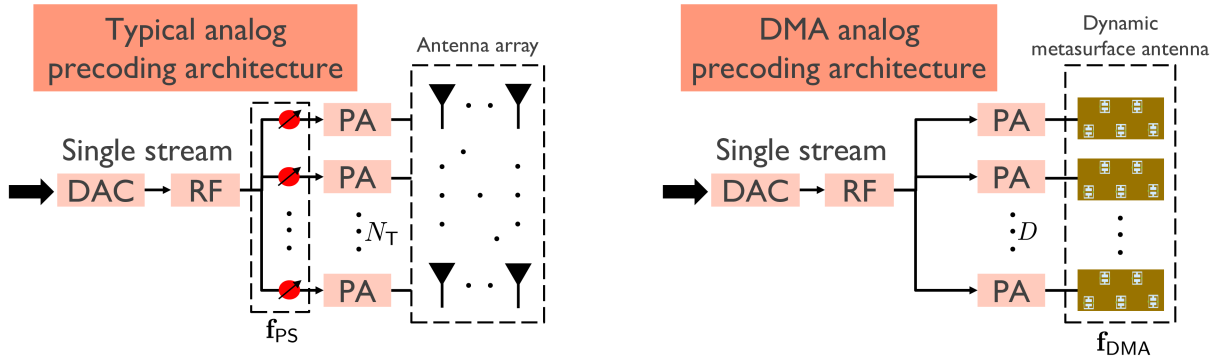
We also must integrate the effects of the DMA waveguide into the wireless channel for the DMA. The DMA waveguide introduces an additional phase term due to the phase advance of the waveguide field propagation for the dth waveguide and ℓth element as $m_{d,\ell} = e^{-\mathrm{j}\beta x_{d,\ell}}$. The input signal to the DMA then propagates through the DMA waveguide and is radiated out through the DMA elements to become a part of the wireless channel for this DMA element $h_{d,\ell}[k]$, yielding $h_{d,\ell}[k]m_{d,\ell}$. To account for this effect for all DMA elements, we multiply the wireless channel $\mathbf{h}[k]$ by its corresponding phase advance $\mathbf{m}$ to result in the effective channel

$$\mathbf{h}_{\mathsf{eff}}[k] = \mathbf{h}[k] \odot \mathbf{m}. \tag{2.6}$$

Therefore, the DMA element weights need to be set both to steer the beam and counteract the waveguide phase advance to create a high-gain beam in a desired direction. In the next section, we examine methods for setting the DMA weights developed in prior work [34, 55].

2.4 DMA mapping design

We now discuss mapping techniques that enable DMA beamforming. We formulate the DMA mapping problem by defining each DMA element to have a specified weight $q_{d,\ell}$, where the weight values are limited by the Lorentzian constraint $q_{d,\ell} \in \mathcal{Q}$. The desired weights



(a) (b)

Figure 2.2. Analog beamforming transmitter architecture for (a) a typical phased antenna array and (b) the DMA. Typical analog implementations enable precoding with phase shifters, while DMAs use reconfigurable components.

$w_{d,\ell}$ are assumed to lie on the complex unit circle so that $|w_{d,\ell}| = 1$. These weights mimic a typical phased array implemented with unit-amplitude phase shifters. Mapping then takes the desired weight $w_{d,\ell}$ and finds a corresponding Lorentzian-constrained weight $q_{d,\ell}$ that is close to the desired weight with respect to a metric. The individual DMA weight values form the overall DMA weight matrix $\mathbf{Q}$, and the desired weights form $\mathbf{W}$. We can then define the DMA beamformer as $\mathbf{f}_{\mathsf{DMA}} = \mathsf{vec}(\mathbf{Q})$. In a similar fashion, we define $\mathbf{f}_{\mathsf{PS}} = \mathsf{vec}(\mathbf{W})$ to represent the desired beamformer with phase shifters for beamforming. Thus, we specify the DMA analog beamformer in the same way as a typical array but with the additional Lorentzian-constrained weights.

The DMA beamformer $\mathbf{f}_{\mathsf{DMA}}$ is found by mapping the desired beamformer $\mathbf{f}_{\mathsf{PS}}$ onto the DMA weights given by $\mathcal{Q}$, also accounting for the waveguide channel effects. We define the effective desired weight $\tilde{w}_{d,\ell}$ that counteracts the waveguide phase advance as

$$\tilde{w}_{d,\ell} = w_{d,\ell} m^*_{d,\ell}. \tag{2.7}$$

We then use this new weight for mapping to find $\mathbf{f}_{\mathsf{DMA}}$. While there are multiple mapping methods presented in literature, we focus here on the two mappings that were found to provide the highest

beamforming gain and steering accuracy: Euclidean modulation and Lorentzian-constrained modulation [55]. We summarize these mapping techniques as follows, based on the work in [55, 34]. We also develop a novel method for creating larger beamforming gains through a phase rotation of the desired weights.

2.4.1 DMA mapping

Euclidean modulation is a mapping that involves minimizing the Euclidean distance between the effective desired weights and DMA weights. For the weight $\tilde{w}_{d,\ell}$, we can formulate the optimal weight $q_{d,\ell}^{\mathsf{EM}}$ for Euclidean modulation (EM) by setting [1]

$$q_{d,\ell}^{\mathsf{EM}} = \underset{q_{d,\ell} \in \mathcal{Q}}{\operatorname{argmin}} \, |q_{d,\ell} - \tilde{w}_{d,\ell}|^2. \tag{2.8}$$

This can be determined through a brute-force search algorithm, or formulaically as described in the following lemma:

Lemma 1. *For the desired weight $\tilde{w}_{d,\ell}$, the weight $q_{d,\ell} \in \mathcal{Q}$ that minimizes $|q_{d,\ell} - \tilde{w}_{d,\ell}|^2$ is given by $q_{d,\ell}^{\mathsf{EM}} = -\frac{\mathsf{j}+e^{\mathsf{j}(\angle(2\tilde{w}_{d,\ell}+\mathsf{j})-\pi)}}{2}$.*

Proof. See Appendix.

Under ideal conditions that assume no waveguide attenuation and a theoretical DMA model, prior work has shown that Euclidean modulation suffers from increased grating lobes and lower directivity due to the non-uniform phase differences between elements [1].

Lorentzian-constrained modulation allows for the DMA weights to be determined in a formulaic manner similar to the array factor. The desired weight phase $\angle\tilde{w}_{d,\ell}$ is substituted into the Lorentzian-constrained weight equation to calculate the Lorentzian-constrained (LC) modulation weights as [34]

$$q_{d,\ell}^{\mathsf{LC}} = -\frac{\mathsf{j} - e^{\mathsf{j}\angle\tilde{w}_{d,\ell}}}{2}. \tag{2.9}$$

The Lorentzian-constrained modulation provides a nearly constant phase difference between DMA elements as it minimizes the distance between the weight phase values [34], whereas Euclidean modulation minimizes the distance between desired and Lorentzian-constrained weights. Further details regarding the Euclidean and Lorentzian-constrained modulation techniques can be found in [34, 1].

While Lorentzian-constrained modulation provides greater beamforming gain and accuracy than Euclidean modulation [55], there is still limited work comparing these mapping techniques with realistic DMA designs. Moreover, these mappings techniques have not been optimized when considering non-ideal DMA characteristics, such as element perturbation of the waveguide. We will develop an optimization method to maximize the theoretical beamforming gain through a phase rotation of the desired weights in the following section.

2.4.2 Mapping optimization

We now introduce a novel technique of applying a phase rotation to the desired precoder $\mathbf{f}_{\mathsf{PS}}$ to maximize beamforming gain with current mapping techniques. Normally, adding an arbitrary phase rotation ζ to the antenna weights does not change the final beamforming gain or radiation pattern so that $\mathbf{f}_{\mathsf{PS}} \equiv \mathbf{f}_{\mathsf{PS}} e^{\mathsf{j}\zeta} \; \forall \; \zeta \in [0, 2\pi)$, where $\equiv$ indicates that the two quantities are equivalent in terms of beamforming gain. Applying a phase rotation to the desired weights, though, will result in a mapping onto different Lorentzian-constrained weights. We demonstrate the phase rotation mapping by decomposing the Lorentzian-constrained modulation with a phase rotation into its real and imaginary parts as $q_{d,\ell}^{\mathsf{LC}}(\zeta) = \frac{1}{2}\left[\cos\left(\angle(\tilde{w}_{d,\ell} e^{\mathsf{j}\zeta})\right) + \mathsf{j}\left(\sin\left(\angle(\tilde{w}_{d,\ell} e^{\mathsf{j}\zeta})\right) - 1\right)\right]$. The magnitude and phase for the Lorentzian-constrained weight are then given by

$$\begin{aligned} |q_{d,\ell}^{\mathsf{LC}}(\zeta)| &= \sqrt{\frac{1}{4}\left[\cos\left(\angle(\tilde{w}_{d,\ell} e^{\mathsf{j}\zeta})\right)^2 + \left(\sin\left(\angle(\tilde{w}_{d,\ell} e^{\mathsf{j}\zeta})\right) - 1\right)^2\right]} \\ &= \sqrt{\frac{1 - \sin\left(\angle(\tilde{w}_{d,\ell} e^{\mathsf{j}\zeta})\right)}{2}}, \end{aligned} \tag{2.10}$$

$$\angle q_{d,\ell}^{\mathsf{LC}}(\zeta) = \arctan\left(\frac{\sin\left(\angle(\tilde{w}_{d,\ell}e^{\mathsf{j}\zeta}) - 1\right)}{\cos\left(\angle(\tilde{w}_{d,\ell}e^{\mathsf{j}\zeta})\right)}\right). \tag{2.11}$$

We find in (2.10) and (2.11) that each phase rotation ζ leads to a unique complex value for the resulting DMA weight magnitude and phase. Therefore, the set of mapped weights from a phase rotation will correspond to a new radiation pattern with differences in the beamwidth, beamforming gain and steering accuracy. We further illustrate this phase rotation in Fig. 2.3.

We now formulate the phase rotation optimization problem to maximize the DMA beamforming gain. Let $q_{d,\ell}^{\mathsf{EM}}(\zeta)$ be the Euclidean mapping of the weight $\tilde{w}_{d,\ell}$ rotated by angle ζ as

$$q_{d,\ell}^{\mathsf{EM}}(\zeta) = \underset{q\in\mathcal{Q}}{\operatorname{argmin}} |q - \tilde{w}_{d,\ell}e^{\mathsf{j}\zeta}|^2. \tag{2.12}$$

For the total DMA weight matrix $\mathbf{Q}^{\mathsf{EM}}(\zeta)$ and desired weight matrix $\tilde{\mathbf{W}}$, we then define the vectorized Euclidean modulation beamformer as $\boldsymbol{q}^{\mathsf{EM}}(\zeta) = \mathsf{vec}(\mathbf{Q}^{\mathsf{EM}}(\zeta))$ and desired beamformer $\tilde{\boldsymbol{w}} = \mathsf{vec}(\tilde{\mathbf{W}})$. The optimal phase rotation that maximizes the beamforming gain for Euclidean modulation is

$$\hat{\zeta}^{\mathsf{EM}} = \underset{\zeta\in[0,2\pi)}{\operatorname{argmax}} |(\boldsymbol{q}^{\mathsf{EM}}(\zeta))^*\tilde{\boldsymbol{w}}e^{\mathsf{j}\zeta}|^2. \tag{2.13}$$

Similarly, let $q_{d,\ell}^{\mathsf{LC}}(\zeta)$ be the Lorentzian-constrained mapping of the weight $\tilde{w}_{d,\ell}$ rotated by angle ζ as

$$q_{d,\ell}^{\mathsf{LC}}(\zeta) = -\frac{\mathsf{j} - e^{\mathsf{j}\angle\left(\tilde{w}_{d,\ell}e^{\mathsf{j}\zeta}\right)}}{2}. \tag{2.14}$$

Then, the optimal phase rotation for Lorentzian-constrained modulation is given by

$$\hat{\zeta}^{\mathsf{LC}} = \underset{\zeta\in[0,2\pi)}{\operatorname{argmax}} |(\boldsymbol{q}^{\mathsf{LC}}(\zeta))^*\tilde{\boldsymbol{w}}e^{\mathsf{j}\zeta}|^2. \tag{2.15}$$

The phase rotation ζ will affect the beamforming gain for both mapping techniques by changing the phase difference and amplitude of all element weights. Therefore, testing different configurations

of the DMA weights with the phase rotation will allow for increased beamforming gain with the optimal phase rotation. Importantly, we incorporate the phase rotation to configure the DMA weights to have greater amplitude values in the Lorentzian-constrained weight distribution. The new amplitude of the weights allows for a higher radiated power per element, which can increase the antenna efficiency and beamforming gain of the DMA. We provide a thorough analysis of the phase rotation optimization in Section 2.6.

While this problem formulation may theoretically yield the phase rotation that maximizes beamforming gain, the practical experimental measurement results may differ due to the waveguide attenuation. To implement the mapping methods for beamforming, we use (2.3) and assume $\bar{\alpha} = 0$ such that only the phase advance of the waveguide is counteracted. This allows for the DMA weights to be configured around the desired phase, but will lead to inaccurate beamforming gain results due to the neglected attenuation factor. To overcome this challenge, we implement a brute-force search with electromagnetic simulations of a DMA to find the optimal phase rotation that maximizes beamforming gain in a desired direction, and leave the development of a sophisticated beamforming gain model for future work. Using electromagnetic simulation results ensures that the attenuation is accounted for in the codebook simulations.

We formulate the phase rotation optimization problem through a brute-force search of electromagnetic simulations as follows. We restrict the phase rotation ζ to be a part of the set $\mathcal{Z} = \left\{\frac{2\pi(0)}{Z}, \frac{2\pi(1)}{Z}, \ldots, \frac{2\pi(Z-2)}{Z}, \frac{2\pi(Z-1)}{Z}\right\}$, which describes the Z discrete phase rotations possible. For all $\zeta \in \mathcal{Z}$, we calculate the LC and EM mapped weights as $q_{d,\ell}^{\mathsf{LC}}(\zeta) = -\frac{\mathsf{j}-e^{\mathsf{j}\angle(\tilde{w}_{d,\ell}e^{\mathsf{j}\zeta})}}{2}$, $q_{d,\ell}^{\mathsf{EM}}(\zeta) = -\frac{\mathsf{j}+e^{\mathsf{j}(\angle(2\tilde{w}_{d,\ell}e^{\mathsf{j}\zeta}+\mathsf{j})-\pi)}}{2}$. We then perform electromagnetic simulations to extract the resulting DMA beam pattern gain as a function of its azimuth angle ϕ, denoted as $v(\zeta, \phi)$. At the desired beamsteering angle ϕ_0, we find the phase rotation that maximizes beamforming gain as $\hat{\zeta}(\phi_0) = \underset{\zeta\in\mathcal{Z}}{\operatorname{argmax}}\, v(\zeta, \phi_0)$. The optimized DMA weights are then given by

$$\hat{q}_{d,\ell}^{\mathsf{LC}}(\phi_0) = -\frac{\mathsf{j} - e^{\mathsf{j}\angle(\tilde{w}_{d,\ell}e^{\mathsf{j}\hat{\zeta}(\phi_0)})}}{2}, \tag{2.16}$$

$$\hat{q}_{d,\ell}^{\mathsf{EM}}(\phi_0) = -\frac{\mathsf{j} + e^{\mathsf{j}(\angle(2\tilde{w}_{d,\ell}e^{\mathsf{j}\hat{\zeta}(\phi_0)}+\mathsf{j})-\pi)}}{2}. \tag{2.17}$$

We implement this optimization to compare against the typical mapping techniques and enhance system performance.

The brute-force phase rotation optimization provides an additional methodology for enhancing the beamforming gain of DMAs. Moreover, given a specific DMA design, the brute-force phase rotation optimization can be completed offline and implemented into any real-time system with the saved varactor values for different beam patterns. The Z discrete phase rotations determines the tradeoff between increased resolution in the resulting beam patterns for different phase rotations, and offline computation time due to electromagnetic simulations of the DMA. Therefore, the value of Z for the brute-force search should be chosen large enough as to enable a thorough search through the different phase rotations to obtain varying beam patterns, but also small enough such that offline computational time is saved. For our simulations, we chose $Z = 12$ to yield discrete phase rotations by 30°, and further discuss how the beam patterns vary with phase rotations in Section 2.6. Once the offline optimization has configured the DMA weights, we will use these weights to develop a codebook based on simulation results from a realistic DMA. Thus, we now discuss the design of the DMA and its simulated radiation characteristics.

2.5 DMA design and hardware implementation

Although DMAs are motivated as an energy-efficient solution to large, MIMO arrays, there is limited work modeling their total power consumption and incorporating realistic DMA designs into the precoding architecture. In this section, we develop a DMA design based on previous work that we will use to simulate codebook beam patterns. Furthermore, we establish a transmitter power consumption model for both the DMA and a typical phased antenna array for energy efficiency comparisons.

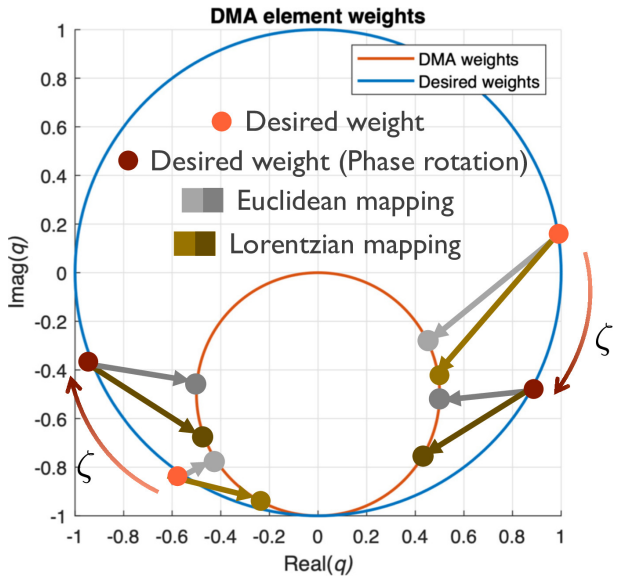


Figure 2.3. Applying a phase rotation to the desired weights results in a new set of mapped weights onto the Lorentzian-constrained weights. We can leverage this to achieve greater beamforming gain with the DMA.

2.5.1 DMA design

We now discuss the design of the DMA and details of the simulation process. Since the purpose of this chapter is to analyze codebook designs for DMAs, we choose to modify a previously-established DMA rather than develop our own. This allows for an analysis of the proposed DMA system model with DMAs that have been tested experimentally. We leave the joint optimization of a new DMA design and the proposed system model for future work.

We use and modify the DMA design from [1]. The element geometry for this design is depicted in Fig. 2.1, consisting of a complimentary electric-LC resonator [1]. We use a hollow waveguide design to increase the DMA radiation efficiency. Each antenna element is loaded with two controllable varactor diodes. We choose to analyze a DMA with $L = 8$ elements per waveguide, and $D = 5$ waveguides as it fits well with the binary hierarchical codebook we will discuss shortly. We can then design the DMA element to meet a radiated power performance requirement given the $D \times L$ array. With $L = 8$ DMA elements per waveguide, we need to ensure that the DMA is capable of radiating out all the input power from the excited waveguide.

Power not radiated out through the DMA elements will be absorbed at the end of the waveguide, resulting in low radiation efficiency. Additionally, radiating too much power through the first initial elements will cause the end elements to radiate nearly no power. It is important to design the DMA such that most or all of the elements are radiating out power to ensure an efficient antenna. We tune the amount of radiated power associated with each Lorentzian-constrained weight in the DMA element design via its geometry. We also offset the DMA elements from the center of the waveguide as another method to control the radiated power [1]. We alter the design in [1] to achieve a maximum element radiated power of around 40% of the input power through trial and error, corresponding to the Lorentzian-constrained weight of $-1\mathrm{j}$. Table 2.1 shows important specifications for the designed DMA, and we leave further details of the DMA design process and specific features of this DMA to be found in [1].

We model and simulate the designed DMA in the electromagnetic simulation software HFSS. We represent the varactor diodes as lumped elements and change the capacitance to vary the resonant frequency of the DMA elements. After simulating the characteristics of a single DMA element, we calculate the magnetic polarizability associated with each varactor diode value through the resulting S-parameters, waveguide dimensions a, b, and waveguide propagation constant β as [1]

$$\alpha_{\mathsf{M}}(\omega) = -\frac{\mathrm{j}ab}{\beta}\left(1 + S_{11}(\omega) - S_{21}(\omega)\right). \tag{2.18}$$

Next, we normalize the simulated α_{M} values such that the highest magnitude weight value corresponds with the weight $-1\mathrm{j}$. This is equivalent to normalizing by the factor $\frac{F\omega_0}{\gamma}$ discussed in Section 2.3. We show the resulting weights in Fig. 2.4. We chose discrete varactor diode values for the simulation, and interpolate the data to calculate the achievable weight-to-capacitance mapping for all varactor diode values. We find that the simulated DMA weights match very closely to the theoretical Lorentzian-constrained weights, which validates the beamforming model. Furthermore, we see that there is a small weight gap near the zero-weight for the simulated results. This is due to the realistic tuning constraints of a varactor diode, and will be further

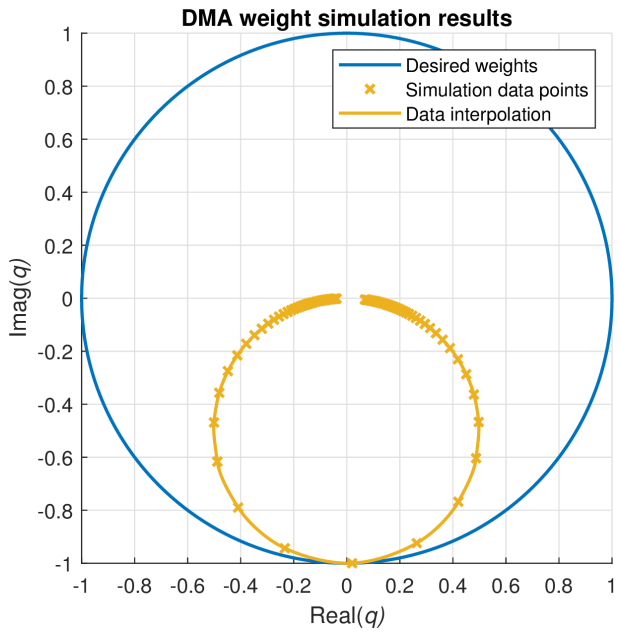


Figure 2.4. Simulated results for the Lorentzian-constrained weights of the designed DMA in HFSS using (2.18). We find that the DMA accurately achieves the Lorentzian-constrained weights defined in (2.2).

Table 2.1. Parameters for the modeled DMA based on [1] .

Elements per waveguide	L	8
Number of waveguides	D	5
Element spacing in x direction	d_{x}	5 mm
Element spacing in y direction	d_{y}	10 mm
Operating wavelength	λ	20 mm
Operating frequency	f_0	15 GHz

analyzed in Section 2.6 for its impact on the DMA beam patterns.

2.5.2 Power consumption and component loss model

We define power consumption models for the DMA and typical phased antenna array. We analyze scenarios for an analog MISO architecture as described in Section 2.3. We use these power consumption models to analyze the energy efficiency of the DMA compared to a phased array. Fig. 2.2 shows the transmitter architecture for the phased array and DMA [11]. Here, we assume a fully-connected architecture so that each antenna element is connected to its own phase shifter [21].

Next, we define a power consumption model for the two beamforming cases. We denote the power consumption for the individual components in the transmitter architecture as follows: let P_{LO} for the local oscillator, P_{PA} for all power amplifiers, P_{DAC} for the digital-to-analog converter as a function of the bit resolution b_{DAC} and sampling frequency F_{s}, P_{PS} for the phase shifter, and P_{VAR} for the varactor diode. We assume a single-stream scenario with only one RF chain. Putting these components together, we define the power consumption model for the typical phased array P_{ANT} and DMA P_{DMA} as [11]

$$P_{\mathsf{ANT}} = P_{\mathsf{LO}} + P_{\mathsf{PA}} + 2P_{\mathsf{DAC}}(b_{\mathsf{DAC}}, F_{\mathsf{s}}) + P_{\mathsf{RF}} + N_{\mathsf{T}}P_{\mathsf{PS}}, \tag{2.19}$$

$$P_{\mathsf{DMA}} = P_{\mathsf{LO}} + P_{\mathsf{PA}} + 2P_{\mathsf{DAC}}(b_{\mathsf{DAC}}, F_{\mathsf{s}}) + P_{\mathsf{RF}} + N_{\mathsf{T}}P_{\mathsf{VAR}}. \tag{2.20}$$

Additional information regarding this power consumption model can be found in [11]. We list the specific power consumption values used for each component in Table 2.2 [11]. The study context for [11] looks at the power consumption for RF components in the mmWave frequency regime, where the selected components operate at around $50 - 60$ GHz. DMAs are currently being studied for their use in mmWave communications to decrease the overall system power consumption from the integrated varactor diodes [58, 29]. While the modified DMA design for our architecture operates at 15 GHz, we incorporate the power consumption model in [11] to study the comparison between DMAs vs. typical phased arrays for mmWave communications. We leave the development of a DMA design that operates at higher frequencies for future work. Furthermore, it is important to note that the power amplifier consumption is dependent on the actual transmit power P_{T} as $P_{\mathsf{PA}} = \frac{P_{\mathsf{T}}}{\eta_{\mathsf{PA}}}$, where η_{PA} is the power amplifier efficiency. We also note that the difference in these power consumption models is the phase shifter versus varactor diode power consumption.

We integrate the loss of the RF components through a reduction in the transmit power from the initial input power P_{IN}. As described in [11], we implement the total loss through an

N_{A}-way power divider with static loss $\bar{L}_{\mathsf{D}}$ as $L_{\mathsf{D}} = \bar{L}_{\mathsf{D}}\lceil \log_2 N_{\mathsf{A}} \rceil$. We also denote the static loss due to phase shifters for each element by L_{PS}. The system transmit power can then be defined as

$$P_{\mathsf{T}} = \frac{P_{\mathsf{IN}}}{L_{\mathsf{D}} L_{\mathsf{PS}}}. \tag{2.21}$$

For the phased array, the power divider will have $N_{\mathsf{A}} = \frac{N_{\mathsf{T}}}{2}$ (see Section 2.6), while for the DMA the power divider will have $N_{\mathsf{A}} = D < \frac{N_{\mathsf{T}}}{2}$. Moreover, with no phase shifters attached to the DMA, there will be no loss from L_{PS} for the DMA case, and we assume a lossless waveguide excitation component. We analyze the effects of this transmit power loss in Section 2.6.

Lastly, as the goal of this work is to analyze the energy efficiency of the DMA compared to the phased array, we define the energy efficiency as a function of the spectral efficiency in (2.5) for the DMA C_{DMA} and phased array C_{ANT} as [41]

$$\eta_{\mathsf{DMA}} = \frac{C_{\mathsf{DMA}}}{P_{\mathsf{DMA}}}, \tag{2.22}$$

$$\eta_{\mathsf{ANT}} = \frac{C_{\mathsf{ANT}}}{P_{\mathsf{ANT}}}. \tag{2.23}$$

Comparing the energy efficiencies for the two scenarios provides a metric to analyze the tradeoff between the lower DMA power consumption and larger achievable beamforming gains for the phased array. We perform simulations to determine this tradeoff in Section 2.6.

2.5.3 DMA hierarchical codebook

Lastly, we develop methods to enable codebook-based beamforming with the designed DMA and DMA analog precoding architecture. Codebook-based beamforming involves creating a discrete list of possible beam patterns. In a wireless scenario, each beam pattern in the codebook is then tested to find the beam pattern that maximizes the receive SNR. A typical codebook design is the DFT codebook, which provides sufficient angular coverage and beamforming gain for a uniform linear array. Our goal is to apply current methods of designing codebooks to the DMA

Table 2.2. Power consumption and component loss in the transmitter architecture model.

Component	Notation	Value
Power amplifier efficiency	η_{PA}	27%
Power amplifier	P_{PA}	$P_{\mathsf{PA}} = \frac{P_{\mathsf{T}}}{\eta_{\mathsf{PA}}}$
Phase shifter (active ; passive)	P_{PS}	21.6 ; 0 mW
DAC	P_{DAC}	75.8 mW
Local oscillator	P_{LO}	22.5 mW
RF chain	P_{RF}	31.6 mW
Varactor diode	P_{VAR}	0 mW
Phase shifter (active ; passive)	L_{PS}	-2.3 ; 8.8 dB
Two-way power divider	$\bar{L}_{\mathsf{D}}$	0.6 dB

analog precoding architecture with the additional constraint of the DMA weights. We design a codebook for the DMA by mapping the weights of a desired beamformer $\mathbf{f}_{\mathsf{PS}}$ onto the DMA weights to create $\mathbf{f}_{\mathsf{DMA}}$. We will implement Euclidean and Lorentzian-constrained modulation for the DMA weights and the proposed phase rotation optimization to compare mapping techniques. We choose to integrate a binary hierarchical DFT codebook with the DMA to leverage the unique zero-weight in the Lorentzian-constrained weights. The configuration of the codebooks with weight mapping techniques is completed offline, and the same codebooks are used in Section 2.6. We will use the codebook beam pattern electromagnetic simulations to analyze the spectral and energy efficiency of DMA vs. phased array systems.

A hierarchical codebook contains multiple layers of codewords that gradually generate narrower beams. Therefore, hierarchical codebooks can lead to a quicker search of the best codeword in the codebook compared to exhaustive search methods [43]. Wider beams are generally created by turning off certain antenna elements, which involves additional switches and control mechanisms from a system design perspective. We analyze DMAs with hierarchical codebooks here as the Lorentzian-constrained weights contain a zero-weight, so no additional switches are required to turn off antennas. Because of this, a hierarchical codebook can leverage the Lorentzian-constrained weights to generate the desired wide beams. As the first layer consists of one single beam pattern, we will analyze the mapping techniques and optimizations for all

layers of the hierarchical codebook beyond the first layer.

We generate the binary hierarchical codebook based on the DEACT approach developed in [43]. We first define the array factor for L elements, wavenumber k, spacing d_{x}, and desired steering angle Ω as

$$\mathbf{a}(L,\Omega) = \frac{1}{\sqrt{L}}\left[e^{\mathrm{j}kd_{\mathsf{x}}0\Omega},\ldots,e^{\mathrm{j}kd_{\mathsf{x}}(L-1)\Omega}\right]^T. \tag{2.24}$$

Next, we define a hierarchical codebook layer r to consist of $2^{(r-1)}$ DFT codewords that adequately span angular space through the resulting beamwidths. The number of DFT beams scales with the hierarchical codebook layer, thus lower layers have fewer beams with wider beamwidths, and higher layers have many beams with narrower beamwidths. For the rth hierarchical codebook layer and cth codeword, the desired antenna weights are given by

$$\mathbf{f}_{\mathsf{HCB}}(r,c) = \left[\mathbf{a}\left(2^r,-1+\frac{2c-1}{2^r}\right)^T,\mathbf{0}^T_{(L-2^r)-1}\right]^T. \tag{2.25}$$

For our DMA scenario of $L=8$, there will be $R=4$ hierarchical codebook layers, with the final layer having $C=L=8$ codewords.

As the DEACT approach is designed for uniform linear arrays in $\mathbf{f}_{\mathsf{HCB}}(r,c)\in\mathbb{C}^{L\times 1}$, we assume that the elevation angle is zero for the planar array and use the same weights $\mathbf{f}_{\mathsf{HCB}}(r,c)$ for the L DMA elements in all D waveguides. We apply D copies of $\mathbf{f}_{\mathsf{HCB}}(r,c)$ to form $\mathbf{f}_{\mathsf{PS}}$ for the desired weights as $\mathbf{f}_{\mathsf{PS}}(r,c) = \mathsf{vec}\left([\mathbf{f}_{\mathsf{HCB}}(r,c),\ldots,\mathbf{f}_{\mathsf{HCB}}(r,c)]\right)$. Applying $\mathbf{f}_{\mathsf{HCB}}(r,c)$ to all waveguides of the DMA creates larger beamforming gains in the desired direction of the DEACT beams through the DMA. We simulate beams along the azimuth direction. The DMA could also be used for 3D beamforming by configuring the weights jointly for the desired azimuth and elevation angles through the DMA mapping methods. We focus solely on beamforming in the azimuth direction here to simplify the codebook design process, and leave the extension of elevation beamforming for future work. We assume the channel to have small elevation variation such that the loss in our approach is minimal. The entries in $\mathbf{f}_{\mathsf{PS}}$ are the desired weights $w_{d,\ell}$,

which can be mapped through the Euclidean and Lorentzian-constrained modulation techniques to find $q_{d,\ell}$. As $q_{d,\ell}$ are the resulting entries to $\mathbf{f}_{\mathsf{DMA}}$, we define the final Lorentzian-constrained and Euclidean modulated beamformers as $\mathbf{f}_{\mathsf{DMA}}^{\mathsf{LC}} = -\frac{\mathrm{j}-e^{\mathrm{j}\angle(\mathbf{f}_{\mathsf{PS}}\odot\mathbf{m}^C)}}{2}$, $\mathbf{f}_{\mathsf{DMA}}^{\mathsf{EM}} = -\frac{\mathrm{j}+e^{\mathrm{j}(\angle(2(\mathbf{f}_{\mathsf{PS}}\odot\mathbf{m}^C)+\mathrm{j})-\pi)}}{2}$. In the following section, we analyze the different mapping techniques and their effects on coverage, beamforming gain, and steering accuracy for the different codebook layers.

2.6 Results

We now analyze the hierarchical codebook design and mapping techniques with the realistic DMA. We simulate the Euclidean, Lorentzian-constrained and brute-force phase rotation optimization modulation techniques with the designed DMA in the electromagnetic simulation software HFSS to extract the resulting beam patterns. As typical directional base station antennas are designed to cover an angular region of around 120° in the azimuth direction [68], we analyze the DMA beam patterns primarily for their performance in the azimuth angle region $\phi \in [-60^\circ, 60^\circ]$. We assume the DMA is oriented along the x-z plane such that the simulated beam patterns span the azimuth angular region. We also create a realistic phased array for direct comparison with the DMA through a simulated patch antenna array. We first design a patch antenna at the desired resonant frequency of 15 GHz in HFSS. We then create a 4×5 array with $\frac{\lambda}{2}$ spacing using this element as the realistic phased array. Since the DMA allows for element spacing smaller than half of a wavelength, the 4×5 phased array maintains the same total aperture area as the 8×5 DMA. For the fourth hierarchical codebook layer, we simulate the desired beamforming angles with the realistic phased array to extract the beam patterns in the same way as the DMA. As the realistic phased array has a directional patch antenna element and the same aperture area as the DMA, this offers a fair comparison for coverage, spectral, and energy efficiency.

We briefly discuss the notation used in the following section. We have two different mapping techniques, Euclidean and Lorentzian-constrained modulation, and the additional

mapping optimization with a phase rotation. We denote EM as Euclidean modulation and LC as Lorentzian-constrained modulation to represent the mapping technique used. We then denote NR to represent the case with no phase rotation and BF as the brute-force search optimization method for the phase rotation. As the brute-force method involves a computationally intensive search with electromagnetic simulation results, we only implement this optimization with Euclidean modulation. We further denote PS as the realistic patch antenna array with phase shifters, where A represents active phase shifters and P represents passive phase shifters. We also use HCB to indicate the hierarchical codebook. This notation is summarized in Table 2.3.

Table 2.3. Notation used to represent simulation results.

HCB	Hierarchical codebook
EM: NR	Euclidean mod.: No phase rotation
EM: BF	Euclidean mod.: Brute-force search
LC: NR	Lorentzian-constrained mod.: No phase rotation
PS: P	Passive phased array with patch antenna elements
PS: A	Active phased array with patch antenna elements

2.6.1 Impact of phase rotation optimization

We first analyze the effect of the proposed phase rotation on the codebook through electromagnetic simulation results. The phase rotation optimization reconfigures the DMA weights to alter the beamforming gain depending on the amplitude and phase of the Lorentzian-constrained weights. Since the amplitude relates to the radiated power for an element, the optimized phase rotation configures the DMA weights to maximize the power output of the DMA. We will primarily determine the effectiveness of the phase rotation optimization via the antenna efficiency and realized gain. As DMAs are a leaky-wave antenna, there is the possibility that some of the input power is not radiated out through the elements, but rather absorbed and wasted at the end of the waveguide. Normally, a DMA or leaky-wave antenna is designed such that a negligible amount of power is wasted at the end of the waveguide. In our case, however, we use the DEACT approach and have a layer in the hierarchical codebook where only two of

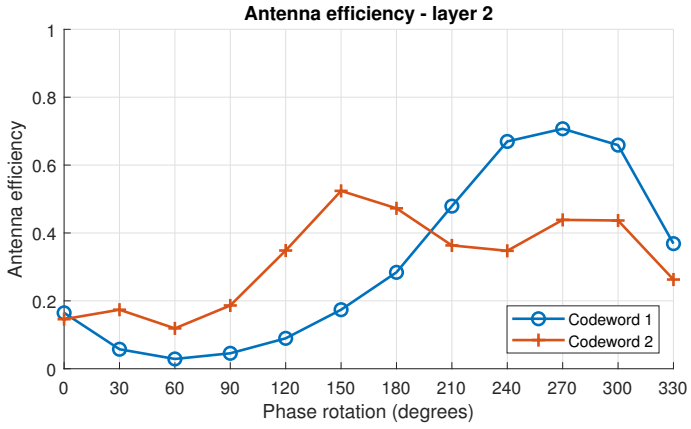
the eight elements are desired to radiate. Therefore, the phase rotation optimization can help to maximize output power for layers 2 and 3 of the hierarchical codebook, while the fourth layer may not benefit significantly from the optimization.

We now define the simulated antenna efficiency results for the DMA and hierarchical codebook beam patterns. For a total radiated power P_{RAD}, the antenna efficiency is [69]

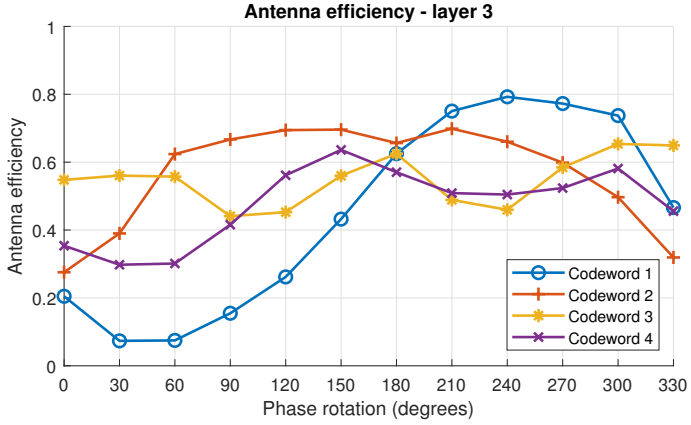
$$\eta_{\mathsf{EFF}} = \frac{P_{\mathsf{RAD}}}{P_{\mathsf{IN}}}. \tag{2.26}$$

The input power P_{IN} is set to 1 W for all electromagnetic simulations. Antenna efficiency accounts for both the radiation efficiency of the DMA, as well as losses due to reflections and power transmitted through towards the other end of the waveguide. Therefore, we use antenna efficiency to analyze the radiated power of the DMA as it incorporates all possible forms of loss. For each beam pattern in every hierarchical codebook layer, the antenna efficiency is calculated as a function of the discrete phases ζ in the brute-force phase rotation optimization, where $Z = 12$.

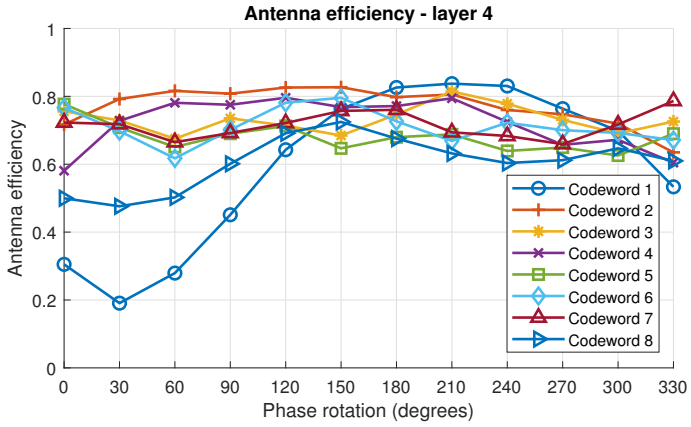
Next, we discuss the antenna efficiency results shown in Fig. 2.5 for all three layers. Focusing on layer 2 in Fig. 2.5, we see that the phase rotation for codeword 1 leads to an antenna efficiency range from 0.05 to 0.7, while codeword 2 has an antenna efficiency range from 0.12 to 0.53. This is a significant range, and could drastically increase the beamforming gain of the DMA for this layer, which will be further analyzed in the next section. We see a similar trend in layer 3, where the output antenna efficiency of the DMA depends heavily on the set of weights chosen from the phase rotation. However, the antenna efficiency for layer 4 generally has a flatter dependency on the phase rotation. Since layer 4 uses all DMA elements, most of the power will be radiated out regardless of the configuration of the weights due to the phase rotation, so the phase rotation has less impact in this situation. Therefore, we find that the optimized mapping technique due to the proposed phase rotation increases the output power of the DMA when certain DMA elements are tuned to a zero-weight. We will further investigate the phase rotation optimization through beam pattern and coverage results.



(a)



(b)



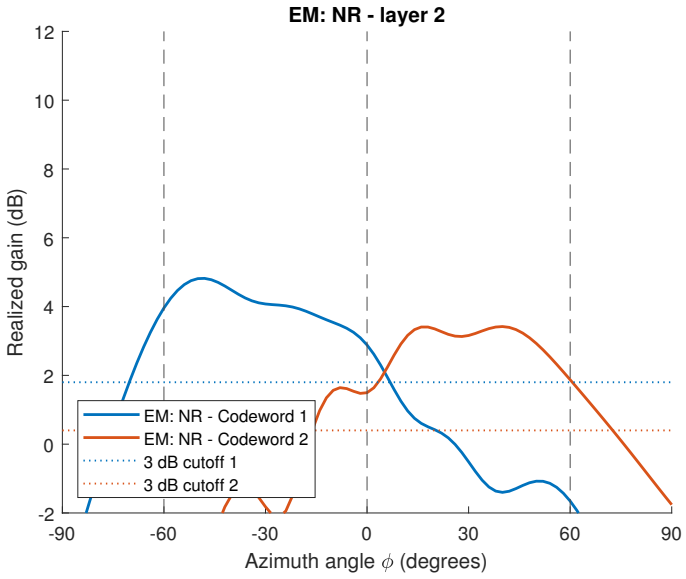
(c)

Figure 2.5. Antenna efficiency simulation results for (a) layer 2, (b) layer 3, and (c) layer 4. We find in layers 2 and 3 that the phase rotation optimization can make a significant difference in the overall antenna efficiency by configuring the weights to maximize the output power of the DMA.

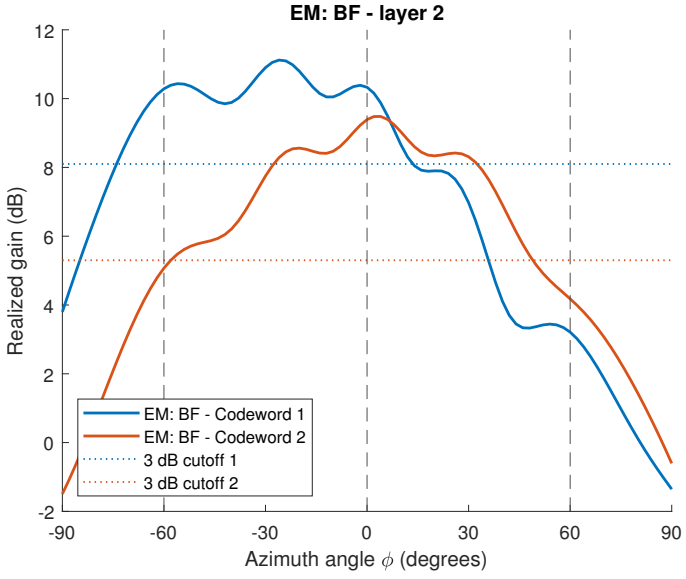
2.6.2 DMA with wide beam patterns

We now demonstrate how the proposed phase rotation can be leveraged to provide wide beamwidths for the hierarchical codebook. We determine this through the half-power beamwidth of the DMA beams. For layer 2 of the hierarchical codebook, Fig. 2.6 displays the HFSS simulated results for the two codeword beam patterns using Euclidean modulation with and without the phase rotation optimization. We choose here to analyze realized gain over gain as realized gain will account for all losses in the DMA, which we will use to determine the impact of the phase rotation optimization. We expect the two beams here to adequately span the angular region from $\phi \in [-60^\circ, 60^\circ]$, and have beamwidths that intersect near the $\phi = 0^\circ$ angle. We also plot the approximate 3 dB beamwidth cutoff for each pattern. Fig. 2.6 shows that normal Euclidean modulation provides beamwidths that remain above the 3 dB cutoff within the desired angular region, while Euclidean modulation with the phase rotation optimization does not meet this criteria for the second codeword. We also see that the phase rotation optimization provides beam patterns with much higher realized gain. For the phase rotation optimization, the codewords have a 3 dB cutoff at around 8 dB and 5.5 dB, while normal Euclidean modulation has 3 dB cutoff values at around 1.9 dB and 0.6 dB. The phase rotation optimization configures the DMA weights to significantly increase the realized gain for the beam patterns. As desired, both beam patterns approximately intersect around the $\phi = 0^\circ$ value. The proposed method is able to achieve wide beam patterns with the DMA through the zero-weight, which has not been discussed in prior work.

Although the beam patterns from the simulated results provide adequately wide beams for the hierarchical codebook, there is still some distortion in the beam pattern for each codeword. This distortion is mostly due to the weight gap near the zero-weight for the simulated weights in Fig. 2.4. When implementing the codebook layers, we chose the closest weight to zero since the zero-weight is unavailable. This led to small amounts of radiation from the "off" elements that distort the DMA beam. Fortunately, for our DMA design, the weight gap did not significantly



(a)



(b)

Figure 2.6. Simulated beam patterns for the second hierarchical codebook layer using (a) Euclidean modulation and (b) Euclidean modulation with optimized phase rotation. The vertical, dashed lines at $\phi \in [-60°, 0°, 60°]$ represent the desired angular range for each beam pattern. We see that the phase rotation optimization leads to beam patterns with larger realized gain.

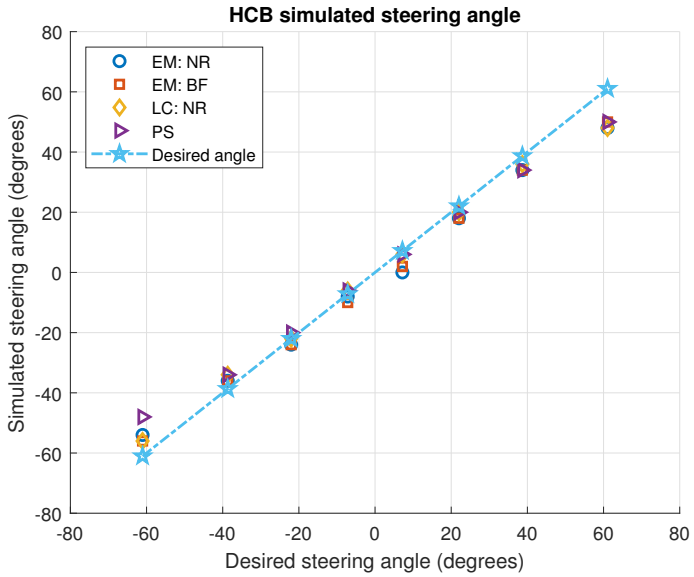
degrade the performance of the second hierarchical codebook layer. This weight-gap, however, is not included in typical DMA models, so we highlight its ability to distort wider beamwidths through Fig. 2.6.

2.6.3 DMA steering accuracy

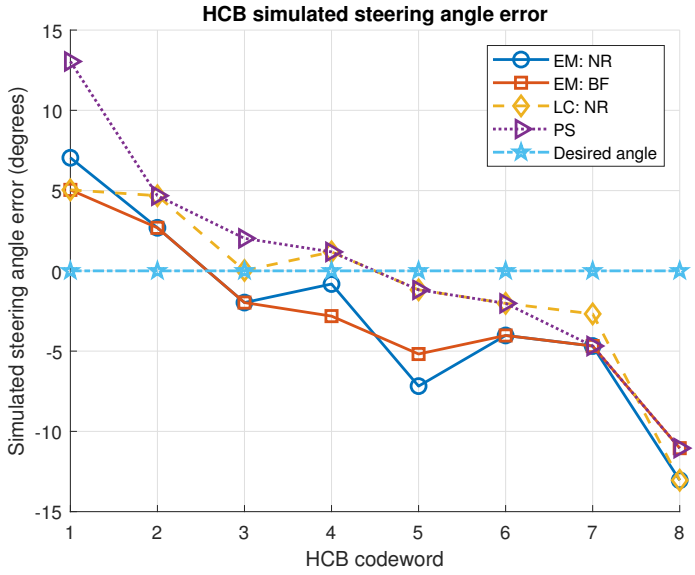
We determine the steering accuracy of the DMA by looking at the fourth layer of the hierarchical codebook and the eight beams generated. Fig. 2.7 displays the desired versus simulated steering angle for the various mappings and the resulting beamsteering error. Overall, we find that the DMA performs well with steering the beam in the correct direction despite the Lorentzian-constrained weights. Moreover, the DMA provides a similar steering accuracy to the patch antenna phased array. Therefore, the Lorentzian-constrained weights do not cause steering accuracy to diminish compared to typical antenna arrays. We note that both the DMA and patch elements have directional beam patterns, which naturally diminishes the beamsteering accuracy towards the end-fire angles. As expected from [55], Lorentzian-constrained modulation enables the highest steering accuracy as it provides a constant phase difference across the DMA elements.

2.6.4 DMA coverage

Next, we analyze the coverage provided by the DMA hierarchical codebook for the different mapping techniques. To determine the effectiveness of the codebook beam patterns in spanning the desired angular range of $\phi \in [-60°, 60°]$, we use a user coverage percentile curve as $1 -$ CDF of the codebook gain CDF. The curve indicates the codebook coverage via the percentile of users in the desired angular range that could observe a certain realized gain. We assume that user locations lie within the angular range $\phi \in [-60°, 60°]$. Fig. 2.8 displays the coverage results. In this figure, the curve furthest to the right generally provides the best coverage as a codebook and enables on average the highest beam pattern realized gain. For the three DMA mapping techniques, we find that the brute-force method provides the best coverage for all three hierarchical codebook layers, as it enables greater beamforming gain to cover the

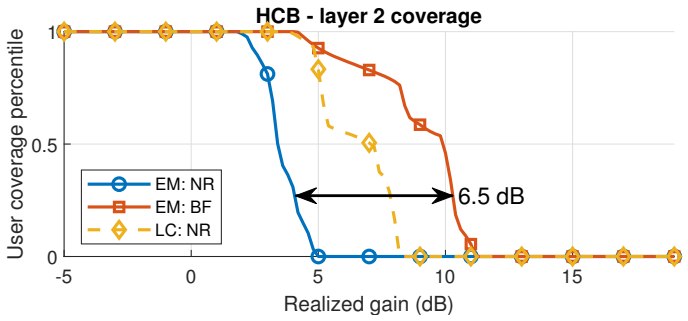


(a)

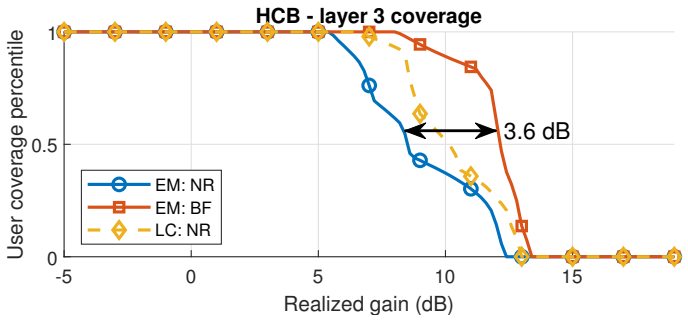


(b)

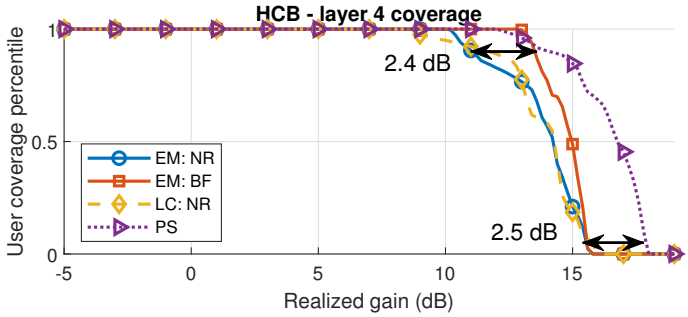
Figure 2.7. (a) Desired versus simulated steering angle for the fourth hierarchical codebook layer and (b) steering angle error for each codeword. All mapping methods enable accurate beamsteering compared to the phased array.



(a)



(b)



(c)

Figure 2.8. Coverage analysis of simulated beam patterns for the hierarchical codebook layers. We find that the brute-force search provides the best coverage of the mapping techniques for the DMA.

desired angular space. As expected, the impact of the phase rotation optimization for coverage is especially effective in layers 2 and 3, where not all DMA elements are tuned to radiate and power output maximization helps to increase the realized gain of the beam patterns. These coverage plots summarize the advantage of using the phase rotation optimization method to maximize single-beam beamforming gain through the DMA. Though computationally intensive, the brute-force search simulations can be performed offline prior to the deployment of a DMA, and provides a faster method than checking all possible weight combinations to find the best DMA beam pattern.

We now analyze the fourth hierarchical codebook layer coverage with the phased array implementation. As expected, we find that the phased array ultimately provides higher beamforming gain of around 2.5 dB in many of the beam patterns compared to the DMA. This is due to the highly-efficient patch antenna design, where DMAs exhibit loss from the resonant response of each element. Although the phased array may generally provide better coverage from increased beamforming gain, this comes at the cost of transmit power loss and increased power consumption. We further analyze the effects of power consumption and overall performance of the phased array and DMA through spectral and energy efficiency results.

2.6.5 Spectral efficiency

We analyze spectral and energy efficiency for the DMA and realistic phased array through the channel simulation software QuaDRiGa [70]. QuaDRiGa is a sophisticated simulation tool that allows for realistic channel modeling with a variety of settings and parameters. We choose to use this tool as the channel generation model is based on real-world channel measurements and is a tool commonly used by many researchers due to its accuracy and reproducibility. We are also able to easily implement the simulated beam patterns from the designed DMA and phased array into QuaDRiGa to examine the codebook design. We use a 3GPP urban macrocell environment as the simulation channel generation setting. We set a radial distance of 500 meters for each user from the base station DMA, and assume the user locations lie within the angular

range $\phi \in [-60°, 60°]$. Additionally, we take the number of OFDM subcarriers as $K = 64$ for a narrow channel bandwidth of $B = 20$ MHz and assume the simulated gain patterns do not change significantly with frequency over the small bandwidth.

For the simulations, we assume a limited feedback beamforming scheme where each beam pattern in the codebook is tested for the channel and the beam pattern with the highest channel gain is selected. The final output of the simulation is a post-beamforming channel value. We gather this data for the fourth hierarchical codebook layer for all simulated DMA codebooks and the realistic phased array codebook. We define the system SNR for a transmit power P_{T} and thermal noise power N_0 as $\rho = \frac{P_{\mathsf{T}}}{BN_0}$. It is important to note that the transmit power will be different for the DMA, active phased array, and passive phased array due to the varying component losses between these three cases. Therefore, each scenario will have different SNR values for calculating spectral efficiency from the simulated channel measurements using (2.5). We compare the scenarios fairly by plotting the resulting codebook spectral efficiency values against the system input power P_{IN}.

Using the resulting QuaDRiGa channel simulations, the input-output transmit power relation (2.21), and the channel spectral efficiency equation (2.5), we show the spectral efficiency values against the input power in Fig. 2.9a. Since the brute-force method provided the best coverage, we only plot the spectral efficiency of the brute-force method for clarity. First, we see that the best-performing codebook is the realistic phased array with active phase shifters, resulting in a 2 dB input power difference with the brute-force DMA method. This is anticipated as the active phase shifters give additional gain to the transmit power signal (2.3 dB), and the realistic phased array beam patterns generally provide greater beamforming gain than the DMA. Naturally, this case also consumes the most power, which we will analyze in the next section through energy efficiency. The worst-performing case is the realistic phased array with high-resolution passive phase shifters, allowing for a 9 dB input power difference with the brute-force DMA method. This is due to the significant component loss (8.8 dB) from the phase shifters, which attenuates the input power signal and gives lower SNR values. We can conclude from these results that

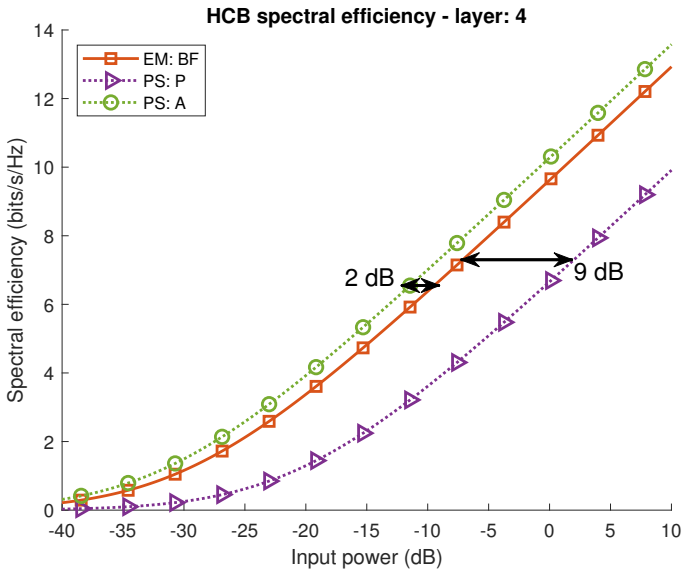
the designed DMA enables higher spectral efficiency values than the traditional phased array equipped with high-resolution passive phase shifters, but falls short from the active phase shifter case.

2.6.6 Energy efficiency

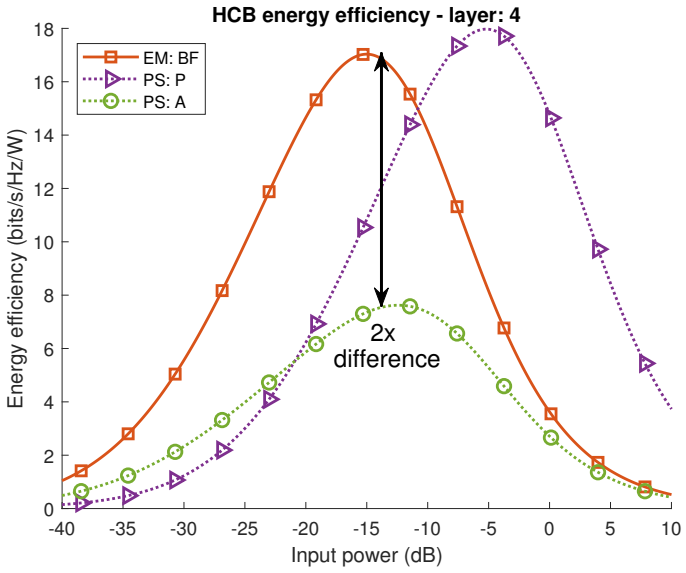
Lastly, we analyze the energy efficiency of the DMA and realistic phased array codebooks using (2.22) and (2.23). Fig. 2.9b shows the energy efficiency results from the spectral efficiency and power consumption calculations. While the realistic phased array with active phase shifters yielded the highest spectral efficiency, we see here that the increased power consumption for this case causes the lowest energy efficiency values across the input power. Therefore, the significant power consumption savings due to the reconfigurable component and fewer power dividers causes the DMA to achieve around twice the energy efficiency of the active phased array at the peak energy efficiency value. While the passive phased array curve actually provides better energy efficiency than the DMA at higher input power values, this is mostly due to component loss. As the passive phase shifters attenuate the input power by 8.8 dB, the power consumption due to power amplifiers is significantly reduced for this case, leading to an overall lower power consumption than the DMA. The passive phased array case, however, still provides lower spectral efficiency than the DMA by around 9 dB in terms of input power. Thus, its energy efficiency does not make up for this significant gap in spectral efficiency performance. The spectral and energy efficiency results in Fig. 2.9a and 2.9b show the capabilities of the DMA to form energy-efficient arrays that maintain or surpass the performance of typical phased arrays.

2.7 Conclusions

In this chapter, we investigated the use of DMAs with a hierarchical codebook and proposed a novel technique for enhancing the beamforming gain compared to current methods. Through the implementation of simulated DMA beam patterns and channel environments, we found that the proposed mapping technique of a brute-force phase rotation search provides better



(a)



(b)

Figure 2.9. Simulated results with the DMA and phased array for (a) spectral efficiency and (b) energy efficiency. We find that the DMA outperforms a traditional passive phased array due to the significant transmit power attenuation for the high-resolution phase shifter. While the active phased array provides the highest spectral efficiency, its large power consumption makes it the least energy-efficient option.

coverage and spectral efficiency than the unoptimized Euclidean and Lorentzian-constrained modulation. Moreover, in terms of spectral efficiency, we found that the DMA significantly outperforms a traditional phased array with passive phase shifters due to high component loss. While providing lower spectral efficiency than an active phased array, the DMA results in greater energy efficiency due to the increased power consumption from active phase shifters. Therefore, DMAs are shown as a suitable replacement for phased arrays in situations where power consumption should be minimal. In future work, we plan to develop novel precoding techniques further optimized around realistic DMA effects. This includes aspects like element perturbation of the waveguide, DMA weight tuning constraints, and refining the DMA geometry. Furthermore, we aim to revisit many MIMO applications, such as channel estimation or localization, with the DMA weight constraint to analyze potential benefits and tradeoffs for using DMAs in these scenarios.

Appendix

2.7.1 Proof of Lemma 1

For the Euclidean modulation equation described in Section 2.4 as $q^{\mathsf{EM}} = \underset{q\in\mathcal{Q}}{\operatorname{argmin}} |q-\tilde{w}|^2$, we substitute and solve for the DMA weight angle ψ as

$$\psi^{\mathsf{EM}} = \underset{\psi\in[0,2\pi)}{\operatorname{argmin}} | - \frac{\mathsf{j}+e^{\mathsf{j}\psi}}{2} - \tilde{w}|^2. \tag{2.27}$$

We further define $\bar{w} = 2\tilde{w} + \mathsf{j}$, so that ψ^{EM} becomes

$$\begin{aligned} \psi^{\mathsf{EM}} &= \underset{\psi\in[0,2\pi)}{\operatorname{argmin}} |e^{\mathsf{j}\psi} - \bar{w}|^2 \\ &= \underset{\psi\in[0,2\pi)}{\operatorname{argmin}} |e^{\mathsf{j}\psi}|^2 + |\bar{w}|^2 - 2\,\mathrm{Re}\left\{e^{-\mathsf{j}\psi}\bar{w}\right\}. \end{aligned} \tag{2.28}$$

Since $|e^{\mathsf{j}\psi}|^2 = 1$ and $|\bar{w}|^2$ is not a function of the unknown, these terms can be ignored to simplify the optimization as

$$\psi^{\mathsf{EM}} = \underset{\psi\in[0,2\pi)}{\operatorname{argmin}} \operatorname{Re}\left\{e^{-\mathsf{j}\psi}\bar{w}\right\}. \tag{2.29}$$

Then, for $\bar{w} = |\bar{w}|e^{\mathsf{j}\angle\bar{w}}$, we have $\operatorname{Re}\left\{e^{-\mathsf{j}\psi}\bar{w}\right\} = |\bar{w}| \operatorname{Re}\left\{e^{\mathsf{j}(\angle\bar{w}-\psi)}\right\} = |\bar{w}| \cos(\angle\bar{w} - \psi)$. The maximum value of 1 for $|\cos(\angle\bar{w} - \psi)|$ is achieved for the argument $(\angle\bar{w} - \psi) = \pi + 2\pi k, k \in \mathbb{Z}$. Therefore, we set $\psi = \angle\bar{w} - \pi$ to find the Euclidean modulation weight. From the substitutions for ψ and $\bar{w}$, the final DMA weight is then $q^{\mathsf{EM}} = -\frac{\mathsf{j}+e^{\mathsf{j}(\angle(2\bar{w}+\mathsf{j})-\pi)}}{2}$.

Publication Acknowledgment

Chapter 2, in full, is a reprint of the material as it appears in J. Carlson, M. R. Castellanos, and R. W. Heath, "Hierarchical Codebook Design With Dynamic Metasurface Antennas for Energy-Efficient Arrays," *IEEE Transactions on Wireless Communications*, vol. 23, no. 10, pp. 14790–14804, 2024. The dissertation author was the primary investigator and author of this paper.

Chapter 3

Wideband dynamic metasurface antenna performance with practical design characteristics

3.1 Overview

In this chapter, we explore the wideband characteristics of dynamic metasurface antennas. In addition to the Lorentzian weights, we impose three additional constraints to the DMA model: frequency-selectivity from the per-element resonances, a limited resonant frequency tuning range due to the varactor diode limitations, and the attenuation of the electromagnetic fields within the waveguide as power is radiated out for each slot. With these constraints, we derive a closed-form approximation for the beamforming gain of a DMA as a function of the bandwidth. We also propose a successive beamforming algorithm aimed at miproving the DMA performance across large bandwidths, with the goal of making DMAs more feasible for wideband systems.

3.2 Introduction

Dynamic metasurface antennas (DMAs) are a type of tunable leaky-wave antenna that gradually radiates power out through reconfigurable slots in a waveguide [34]. DMAs differ from reflective or transmissive metasurfaces in that they operate as active antennas with a dedicated radio frequency (RF) feed, and can be integrated into a wireless transmitter or receiver

architecture as an antenna array. Low-power, low-cost tunable components are integrated into the DMA elements to control their resonant frequency and enable beamforming. Through the reconfigurable components, DMAs provide a potential solution to minimize both power consumption and hardware costs in multiple-input multiple-output (MIMO) systems when compared with phase shifter or digital beamforming methods [29]. DMAs also have favorable wideband characteristics over static antennas due to the ability to tune the resonant frequency of each DMA element. Despite this, prior work has focused largely on narrowband communications for DMAs. In our work, we expand upon the current narrowband DMA models to evaluate the beamforming gain of DMAs with large signal bandwidths.

3.2.1 Prior work

DMAs have been studied extensively in the past five years due to their potential power consumption and cost benefits over digital and phased arrays. The concept of metasurface antennas stems from using the electrically-small resonators in metasurface designs, such as split-ring-resonators [71], as active antennas [72, 73]. The extension to dynamic metasurface antennas involves the integration of reconfigurable components into the metasurface antenna design to dynamically tune the antenna characteristics [34, 1, 35]. DMA designs have been proposed in literature using both varactor diodes [1] and p-i-n diodes [36] to actively reconfigure the metasurface antenna with continuous or binary tuning capabilities. Both metasurface designs in [1] and [36] were fabricated and experimentally measured to obtain steered beam patterns using the reconfigurable components. In essence, the experimental work shows that DMAs provide a novel and practical beamsteering architecture with reduced power consumption compared to digital and phased arrays, making them a potentially interesting technology for cellular systems.

There are several papers that have incorporated DMAs into more elaborate MIMO configurations. Simple beamforming strategies have been developed to map desired antenna weights to the Lorentzian-constrained weights [34, 35] and binary weights [74, 36, 75, 76] to mimic a line-of-sight (LOS) beam pattern. More complex algorithms to configure the DMA

Lorentzian weights have been developed to maximize spectral efficiency [39, 77, 78], minimize bit-error rate in MIMO-orthogonal frequency division multiplexing (OFDM) systems [40], and maximize massive MIMO energy efficiency [41]. Extensions of the work in [39, 77, 78, 40, 41] consider a hybrid precoding architecture with a DMA-based analog precoder and a digital precoder with limited RF chains [79, 80, 81, 58]. Despite the Lorentzian weight constraint, DMA-based systems have been shown to provide spectral efficiency that approaches what can be achieved with typical phased arrays.

A common limitation of the work in [39, 77, 41, 79, 80, 81, 58] is that the DMA element is modeled solely by the Lorentzian-constrained antenna weights, which does not account for all of the design features of DMAs that make them different from static antennas. Key aspects of the DMA model that are neglected in [39, 77, 41, 79, 80, 81, 58] include the frequency-selectivity in the DMA element resonance, minimal impact of the waveguide attenuation as power is leaked out through the DMA elements, and the range of tunability for the DMA element resonant frequency. All three of these neglected assumptions will affect DMA beamforming, but the extent is unclear in current literature. Moreover, the work in [39, 77, 41, 79, 80, 81, 58] largely assumes a narrowband system model, where the fractional bandwidth is small enough such that frequency-selective DMA effects are negligible. While work in [78] and [40] includes the frequency-selective DMA resonance in the DMA model, the waveguide attenuation and resonant frequency tunability are not considered and could significantly impact the resulting spectral efficiency. Since the DMA element resonance, waveguide attenuation, and resonant frequency tunability are all frequency-selective, increasing the signal bandwidth to consider a wideband wireless communication system has not been explored with these practical DMA design characteristics.

Design work on DMAs has provided a more complete characterization of their behavior. Foundational modeling of DMAs was done in [42, 82, 83] to relate DMA elements to magnetic dipoles and show the frequency-selectivity resonant response of DMAs. The work in [42, 82, 83], however, does not explore the frequency-selective characteristics of DMAs in the context of

communications and beamforming. Additional DMA models in [84, 34, 1, 56] were developed to account for waveguide attenuation and impedance in the context of beamforming, but did not provide a thorough analysis for how to design the DMA for a specific waveguide attenuation or how different attenuation values impact the resulting DMA beamforming. Moreover, all of the studies in [42, 82, 83, 34, 1, 56] do not discuss the impact of the DMA resonant frequency tuning abilities on DMA beamforming. In a conference version of this work, we include the resonant frequency tuning, waveguide attenuation and frequency-selectivity in the DMA model, but do not analyze how these parameters impact the DMA beamforming gain for large bandwidths [85]. In this chapter, we will close this gap and analyze the affects of the DMA element resonance, waveguide attenuation, and resonant frequency tunability on the DMA beamforming gain for large signal bandwidths, where the DMA frequency-selectivity cannot be neglected.

To highlight the challenges addressed in this chapter, it is important to understand the impact of DMA element frequency-selectivity, waveguide attenuation, and resonant frequency tunability on the DMA wideband beamforming gain. For example, the frequency-selectivity of the DMA element resonant response causes the amplitude and phase of the effective DMA beamforming weights to vary drastically across frequency, and the waveguide attenuation applies a frequency-selective amplitude taper across all the DMA beamforming weights. The resonant frequency tunability also places limits on the possible DMA beamforming weights, which adds to the difficulty in obtaining a tractable analysis of the DMA wideband beamforming gain. Overall, the general relationship for DMA wideband beamforming gain as a function of frequency is not clear, and configuring the DMA beamforming weights to improve wideband beamforming gain with these practical design characteristics remains an open challenge. We address these challenges in this chapter by deriving a DMA wideband beamforming gain approximation based on the impact of the frequency-selective DMA resonance, waveguide attenuation, and resonant frequency tunability, and we propose a successive beamforming algorithm to improve the DMA wideband spectral efficiency under the practical design characteristics.

3.2.2 Contributions

We analyze the impact of DMA characteristics, such as resonant frequency tunability and waveguide attenuation, on the beamforming gain and spectral efficiency in a multiple-input single-output (MISO) DMA-analog wireless communication system with large signal bandwidths. The key contributions in this chapter are summarized as follows. We develop a wideband DMA signal model that includes the waveguide attenuation, resonant frequency tunability, and DMA resonance frequency-selectivity. These three DMA design characteristics have a significant impact on the resulting DMA beamforming gain as the signal bandwidth increases, yet there has been no comprehensive analysis in prior work that integrates these DMA characteristics into a signal model. Next, we derive an approximation of the beamforming gain for a wideband MISO DMA system under the influence of the waveguide attenuation, limited resonant frequency tunability, and frequency-selective elements. The approximation provides a closed-form expression for the resulting beamforming gain of the DMA as a function of the signal bandwidth and DMA design parameters, such as the coupling and damping factors, as well as the DMA array spacing. Therefore, the design parameters for any physical DMA can be applied to the approximation to obtain an accurate estimate on the achievable beamforming gain and spectral efficiency in a DMA-based wireless system.

Using the derived approximation, we gain valuable insights into the best DMA design characteristics to maximize the MISO spectral efficiency for small and large signal bandwidths. We show that the limited resonant frequency tunability decreases spectral efficiency by reducing the available beamforming weights, meaning the range of resonant frequency tunability is a crucial DMA design characteristic for DMA-based wireless systems. We also demonstrate the need for small antenna element spacing to minimize the impact of high frequency-selectivity due to the wireless and waveguide channels, as well as the DMA resonance frequency-selectivity. Moreover, in simulation results we show that large damping factors generally lead to higher data rates since there is less frequency-selectivity in the DMA element response. Finally, we propose

a successive beamforming algorithm to configure the DMA elements. The proposed successive beamforming algorithm accounts for both the frequency-selective DMA design characteristics and the configurations of other DMA elements to improve the wideband spectral efficiency. We find that the proposed algorithm provides an increase in spectral efficiency and data rates when compared with a baseline DMA beamforming approach, especially as the signal bandwidth becomes large. We also demonstrate that the proposed successive beamforming algorithm outperforms the baseline beamforming algorithm and hybrid beamforming architectures when extended to a multipath channel environment, which shows that the proposed algorithm functions well in complex channel scenarios beyond the initial LOS case.

Organization: In Section 3.3, we outline the wideband MISO-OFDM signal model. In Section 3.4, we define the frequency-selective DMA model and waveguide propagation model. We also introduce a novel DMA parameter called the tuning bandwidth to account for the ability to tune the DMA resonant frequency. In Section 3.5, we derive a beamforming gain approximation to analyze spectral efficiency. The beamforming gain approximation includes the effects of the DMA element frequency-selectivity, tuning bandwidth, and waveguide attenuation unlike prior work in [39, 77, 41, 79, 80, 81, 58]. Next, in Section 3.6 we define a baseline DMA algorithm for configuring the antenna weights based on [34] and propose a successive algorithm to increase the DMA wideband spectral efficiency. Unlike [34, 1], the proposed beamforming algorithm is frequency-selective and maximizes the spectral efficiency across a multi-carrier system, rather than simply at a center frequency. In Section 3.7, we then show simulation results to compare the proposed successive algorithm, baseline DMA algorithm and beamforming gain approximation. The simulation results extend the DMA modeling work developed in [42, 82, 83] to a wireless setting, where we convey how different DMA design parameters can be optimized to improve spectral efficiency. Lastly, in Section 3.8 we provide a summary of the chapter and future research directions.

Notation: We denote a bold, capital letter $\mathbf{A}$ as a matrix, a bold, lowercase letter $\mathbf{a}$ as a vector, and a script letter $\mathcal{A}$ as a set. Let $\mathbf{A}^*$ represent the matrix conjugate transpose, $\mathbf{A}^{\mathsf{c}}$

represent the matrix conjugate, and $\mathbf{A}^{\mathsf{T}}$ represent the matrix transpose. For a complex number a, we use $\mathrm{Re}(a)$ and $\mathrm{Im}(a)$ to indicate its real and imaginary part, $|a|$ as its magnitude, and $\angle a$ as its phase. We define the operator $\odot$ as the Hadamard product. We denote $||\mathbf{a}||_{\mathsf{F}}$ as the Frobenius norm of vector $\mathbf{a}$. We use $O(\cdot)$ to denote the big O notation.

3.3 System model

We first establish a frequency-selective MISO-OFDM signal model for a DMA-based wireless system. We also define the key metrics for evaluating the DMA performance as the wideband beamforming gain and spectral efficiency.

3.3.1 MISO-OFDM signal model

The system consists of a uniform linear array (ULA) DMA transmitter with N_{slot} elements communicating with a single-antenna user through a wideband MISO-OFDM channel. Fig. 3.1 shows the DMA ULA architecture with N_{slot} radiating elements atop a waveguide. Our goal is to analyze the effects of the frequency-selective DMA elements on the overall MISO-OFDM data rates and spectral efficiency. We consider a DMA model with continuous tunable components, such as varactors, that are configured to beamform by adjusting the components to create a resonant response in the DMA element.

We now define the MISO-OFDM signal model. The DMA transmitter communicates with the user over K subcarriers by precoding the kth subcarrier transmit symbol $s[k]$, which has zero-mean unit-variance. Let $\mathbf{f}_{\mathsf{dma}}[k] \in \mathbb{C}^{N_{\mathsf{slot}} \times 1}$ be the DMA transmit beamforming vector for the kth subcarrier and $\mathbf{h}_{\mathsf{att}}[k] \in \mathbb{R}^{N_{\mathsf{slot}} \times 1}$ be an amplitude taper on the DMA beamforming weights based on the leakage of radiated power. This is discussed in further detail in Section 3.4.1. The transmit power input to the DMA is P_{in} for all subcarriers, such that for a total system input power $P_{\mathsf{in,tot}}$, the per-subcarrier input power is $P_{\mathsf{in}} = \frac{P_{\mathsf{in,tot}}}{K}$. Let G_{dma} be a DMA loss term that accounts for the DMA efficiency, and let M_k be a normalization term that satisfies a power

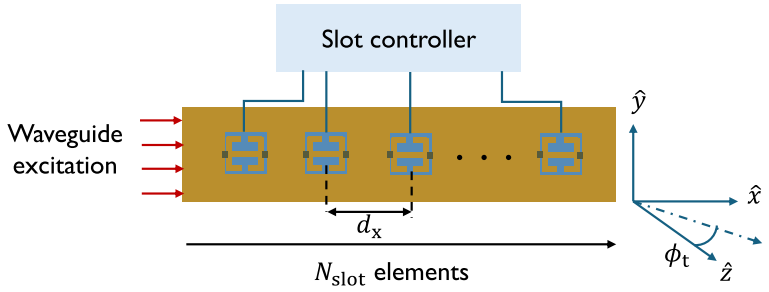


Figure 3.1. Architecture of a DMA as a leaky-wave uniform linear array of antenna elements. Varactor diodes are integrated into each antenna element to enable low-power beamforming with the use of an external controller.

constraint on the DMA beamformer. The transmit signal vector is denoted as

$$\mathbf{x}[k] = \sqrt{P_{\text{in}} G_{\text{dma}} M_k}(\mathbf{f}_{\text{dma}}[k] \odot \mathbf{h}_{\text{att}}[k])s[k]. \tag{3.1}$$

We assume Gaussian-distributed noise $n[k] \sim \mathcal{N}_{\mathbb{C}}(0, \sigma_{\text{N}}^2)$.

Next, we define the received signal model for the DMA. Let $\mathbf{h}[k] \in \mathbb{C}^{N_{\text{slot}} \times 1}$ be the small-scale fading channel between the DMA and user receive antenna. Let $G_{\text{P},k}$ be the term which captures the frequency dependent large-scale fading path loss, which is further defined in Section 3.3.2. The MISO-OFDM single-stream received signal for a single time slot is

$$y[k] = \sqrt{G_{\text{P},k}}\mathbf{h}^{\text{T}}[k]\mathbf{x}[k] + n[k]. \tag{3.2}$$

The characteristics of the DMA element are incorporated into the beamformer $\mathbf{f}_{\text{dma}}[k]$, while properties of the waveguide are integrated into the channel $\mathbf{h}[k]$ and the leakage vector $\mathbf{h}_{\text{att}}[k]$.

3.3.2 Wideband beamforming gain and spectral efficiency

We now describe the signal-to-noise ratio (SNR) model that incorporates the signal bandwidth of the DMA wideband system, and the performance metrics as the wideband beamforming gain and spectral efficiency. The large-scale fading path loss is assumed to be

free space path loss and expressed as $G_{\mathsf{P},k} = \left(\frac{c}{f_k 4\pi r}\right)^2$ for a distance r from the DMA. Let $\sigma^2_{\mathsf{N}} = k_{\mathsf{B}} T_{\mathsf{temp}} B/K$ be the noise power for the Boltzmann constant k_{B}, temperature T_{temp}, and subcarrier bandwidth B/K. Then, we define the per-subcarrier SNR with the DMA as

$$\rho_k = G_{\mathsf{P},k} G_{\mathsf{dma}} \frac{P_{\mathsf{in}}}{\sigma^2_{\mathsf{N}}}. \tag{3.3}$$

We see that the SNR in (3.3) depends on the subcarrier bandwidth B/K within the noise power term σ^2_{N}, which we will examine in Section 3.7.3.

Next we describe the key performance metrics to evaluate the DMA beamformer. We define the sum beamforming gain for the system across all subcarriers as

$$G_{\mathsf{sum}} = \sum_{k=1}^{K} M_k |\mathbf{h}^{\mathsf{T}}[k] \left(\mathbf{f}_{\mathsf{dma}}[k] \odot \mathbf{h}_{\mathsf{att}}[k]\right)|^2 \tag{3.4}$$

and the spectral efficiency as

$$C\Big(\{\rho_k, \mathbf{h}[k]\}_{k=1}^{K}\Big) = \frac{1}{K} \sum_{k=1}^{K} \log_2 \left(1 + \rho_k M_k |\mathbf{h}^{\mathsf{T}}[k] \left(\mathbf{f}_{\mathsf{dma}}[k] \odot \mathbf{h}_{\mathsf{att}}[k]\right)|^2\right). \tag{3.5}$$

The resulting sum beamforming gain and spectral efficiency depend on a multitude of DMA design parameters: the resonant frequency tuning bandwidth, waveguide power leakage, element frequency-selectivity, and system parameters like the signal bandwidth. We will derive an expression to approximate the DMA sum beamforming gain, and extend the approximation to investigate how spectral efficiency changes as a function of the DMA design parameters.

3.4 DMA channel and beamformer model

We now define the LOS DMA channel model that incorporates the DMA waveguide propagation effects and the wireless channel. We also model the DMA beamformer by the reconfigurable magnetic dipole response of each element, and derive a frequency-selective

Lorentzian-constraint to extend the prior DMA weight model in [34] to a wideband setting.

3.4.1 Channel and waveguide model

The channel between the transmitter and the receiver includes the effects of over-the-air propagation and the DMA waveguide. We assume a LOS channel model to simplify the wideband system analysis. Let f be the signal frequency, let f_k be the kth subcarrier passband frequency, let c indicate the speed of light in a vacuum, let d_{x} be the inter-element spacing, and let ϕ_{t} be the LOS direction of the user from broadside, as shown in Fig. 3.1. We assume the DMA is oriented in the xy plane and the DMA elements are spaced along the x direction. The transmit array response vector is

$$\mathbf{a}[\phi_{\mathsf{t}}, k] = \left[e^{\mathsf{j}0\left(\frac{2\pi f_k}{c}\right)d_{\mathsf{x}}\sin\phi_{\mathsf{t}}}, \ldots, e^{\mathsf{j}(N_{\mathsf{slot}}-1)\left(\frac{2\pi f_k}{c}\right)d_{\mathsf{x}}\sin\phi_{\mathsf{t}}}\right]^{\mathsf{T}}. \tag{3.6}$$

In addition to the transmit array vector, the DMA waveguide also produces attenuation and phase shift effects on the DMA elements due to the propagation of the transmit signal through the waveguide.

Since DMAs act as reconfigurable leaky-wave antennas, the feed for the individual DMA elements is the waveguide. The electromagnetic fields attenuate along the waveguide as power is radiated out through the elements. There is an inherent phase advance that is introduced for each DMA element from the propagation of the electromagnetic fields. We denote the waveguide phase constant as $\beta_{\mathsf{g}}(f)$. Similar to [34], we ignore the resistive loss and only model the waveguide attenuation due to radiated power leakage which is denoted as $\bar{\alpha}_{\mathsf{g}}(f)$. The subscript g represents the waveguide. Assuming zero phase angle at the first element, we define the DMA waveguide channel that incorporates the phase advance as [34]

$$\mathbf{h}_{\mathsf{dma}}[k] = \left[e^{-\mathsf{j}(0)d_{\mathsf{x}}\beta_{\mathsf{g}}(f_k)}, \ldots, e^{-\mathsf{j}(N_{\mathsf{slot}}-1)d_{\mathsf{x}}\beta_{\mathsf{g}}(f_k)}\right]^{\mathsf{T}}, \tag{3.7}$$

The total wireless channel is obtained by combining the array vector $\mathbf{a}[\phi_{\mathsf{t}}, k]$ with the effects of the DMA waveguide channel $\mathbf{h}_{\mathsf{dma}}[k]$ as

$$\mathbf{h}[k] = \mathbf{a}[\phi_{\mathsf{t}}, k] \odot \mathbf{h}_{\mathsf{dma}}[k]. \tag{3.8}$$

The expression in (3.8) describes the total array response vector including both wireless and waveguide channel propagation.

Additionally, we define a waveguide attenuation vector that describes the leakage of radiated power along the length of the waveguide. As the specific configuration of DMA elements impacts the leakage of radiated power, we define a leakage constant $\bar{\alpha}_{\mathsf{g}}(f)$ that approximates the attenuation of the waveguide fields as power is radiated out through the DMA elements. We provide further justification of using an approximate leakage constant in Section 3.7. We define the leakage vector as

$$\mathbf{h}_{\mathsf{att}}[k] = \left[e^{-(0)d_{\mathsf{x}}\bar{\alpha}_{\mathsf{g}}(f_k)}, \ldots, e^{-(N_{\mathsf{slot}}-1)d_{\mathsf{x}}\bar{\alpha}_{\mathsf{g}}(f_k)}\right]^{\mathsf{T}}. \tag{3.9}$$

We provide separate expressions for the waveguide effects of phase propagation and leakage because of their impact on the DMA beamformer. The DMA phase propagation channel in (3.7) contributes a phase advance to the wireless channel that must be accounted for and counteracted by the DMA beamformer to steer a beam in a desired direction. The DMA leakage vector in (3.9), however, applies an effective amplitude taper on the resulting DMA beamforming weights $\mathbf{f}_{\mathsf{dma}}[k]$. For now, we focus on configuring the DMA beamforming weights prior to incorporating the amplitude taper from the leakage vector in (3.9) for simplicity. Later on, we propose a novel method to configure the DMA beamforming weights in Section 3.6.2 which accounts for the amplitude taper.

3.4.2 Frequency-selective DMA beamforming model

We establish a model for the tunable responses of the DMA elements and incorporate additional physical DMA effects into the DMA beamforming model. The polarizable dipole framework from [34] is used to model the DMA beamforming similar to prior work[86, 87]. The radiation properties of each DMA slot resembles that of magnetic dipoles as was experimentally verified in [88]. The radiated field is governed by the magnetic polarizability of each dipole[34]. Following the notation from [34], let F_{coupl} be the coupling factor, Γ be the damping factor, and $f_{\mathsf{r},n}$ be the tunable element resonant frequency of the nth slot. The DMA magnetic polarizability as a function of the subcarrier frequency and the nth element resonant frequency is [34]

$$\alpha_{\mathsf{M}}(f_k, f_{\mathsf{r},n}) = \frac{2\pi f_k^2 F_{\mathsf{coupl}}}{2\pi f_{\mathsf{r},n}^2 - 2\pi f_k^2 + \mathrm{j}\Gamma f_k}. \tag{3.10}$$

Since (3.10) depends on both $f_{\mathsf{r},n}$ and f_k, the frequency-selective resonant response is dependent on the resonant frequency and the signal bandwidth B that contains the subcarrier frequencies f_k.

Next, we define a tuning bandwidth term to model the physical limitations and tuning capabilities of the reconfigurable varactors. For a minimum resonant frequency $f_{\mathsf{r,min}}$ and maximum resonant frequency $f_{\mathsf{r,max}}$, the resonant frequency tuning range is $R_{\mathsf{tune}} \in [f_{\mathsf{r,min}}, f_{\mathsf{r,max}}]$. We define the tuning bandwidth as

$$B_{\mathsf{tune}} = f_{\mathsf{r,max}} - f_{\mathsf{r,min}} \tag{3.11}$$

which represents the bandwidth of possible resonant frequency tuning values f_{r} around the center operating frequency f_{t}.

The tuning bandwidth B_{tune} has a large impact on the resulting spectral efficiency as it limits the flexibility of the DMA elements to create different antenna weights. Several design parameters affect the tuning bandwidth: DMA element geometry and varactor diode parameters. We discuss this further in Section 3.5. In this chapter, we assume the tuning bandwidth can

be adjusted based on a DMA design, such as through altering the DMA geometry or selecting different varactor diodes [36]. We will analyze the importance of large and small tuning bandwidths on the DMA wideband performance.

The tunable element responses allow the DMA to achieve beamforming based on the tuning configuration. The magnetic polarizability then becomes the effective antenna weight. We define the quality factor as $Q_k = \frac{2\pi f_k}{\Gamma}$ and the normalized magnetic polarizability response as

$$\bar{\alpha}_{\mathsf{M}}(f_k, f_{\mathsf{r},n}) = \frac{1}{Q_k F}\alpha_{\mathsf{M}}(f_k, f_{\mathsf{r},n}). \tag{3.12}$$

The factor $Q_k F$ ensures that the highest magnitude beamforming weight possible is one, which maintains consistency with the Lorentzian model for the DMA weights. We can then leverage the beamforming methods for DMAs using the Lorentzian model to map unit-amplitude weights onto a frequency-selective Lorentzian-constraint. The transmit beamforming vector for the DMA based on the varactor tunings per element is

$$\mathbf{f}_{\mathsf{dma}}[k] = [\bar{\alpha}_{\mathsf{M}}(f_k, f_{\mathsf{r},0}), \ldots, \bar{\alpha}_{\mathsf{M}}(f_k, f_{\mathsf{r},N_{\mathsf{slot}}-1})]^{\mathsf{T}}. \tag{3.13}$$

We use the normalization term M_k to satisfy a radiated power constraint on the DMA beamformer, as discussed in Section 3.7.

3.4.3 Frequency-selective Lorentzian constraint

Next, we define the frequency-selective Lorentzian constraint to describe the DMA beamforming weights $\bar{\alpha}_{\mathsf{M}}$. Presenting the frequency-selective magnetic polarizability term from (3.10) in terms of a frequency-selective Lorentzian constraint allows for a simplified analysis of the DMA beamformer and its wideband beamforming gain performance. For a phase angle ζ

representing the reconfigurability of the DMA element, the Lorentzian constraint is [34]

$$\mathcal{Q} = \left\{ -\frac{\mathsf{j} - e^{\mathsf{j}\zeta}}{2} : \zeta \in [0, 2\pi] \right\}. \tag{3.14}$$

Fig. 3.2 shows a plot of the Lorentzian weight distribution in (3.14) compared with a unit-amplitude weight distribution as $\mathcal{Q} = \left\{ e^{\mathsf{j}\zeta} : \zeta \in [0, 2\pi] \right\}$. It is important to note that the Lorentzian weight distribution restricts the available phase range for beamforming to $[-\pi, 0]$, whereas the unit-amplitude weight distribution allows for the full $[0, 2\pi]$ phase range.

Based on the Lorentzian constraint in (3.14), to derive the frequency-selective magnetic polarizability term, let

$$\Psi(f, f_{\mathsf{r},n}) = \arctan\left(\frac{2\pi(f_{\mathsf{r},n}^2 - f^2)}{\Gamma f} \right) \tag{3.15}$$

represent an auxiliary angle, where the phase of the magnetic polarizability is $\Psi(f, f_{\mathsf{r},n}) - \frac{\pi}{2}$. Then, we can express the magnetic polarizability in (3.12) using the Lorentzian form in (3.14) as

$$\bar{\alpha}_{\mathsf{M}}(f, f_{\mathsf{r},n}) = \cos(\Psi(f, f_{\mathsf{r},n})) e^{\mathsf{j}(\Psi(f, f_{\mathsf{r},n}) - \frac{\pi}{2})}. \tag{3.16}$$

We relate (3.16) to the Lorentzian constraint in (3.14) as follows.

Lemma 2. *The magnetic polarizability term* α_{M} *in* (3.12) *is related to the Lorentzian constraint in* (3.14) *by*

$$\bar{\alpha}_{\mathsf{M}}(f, f_{\mathsf{r},n}) = -\frac{\mathsf{j}\left(1 + e^{\mathsf{j}2\Psi(f, f_{\mathsf{r},n})}\right)}{2}. \tag{3.17}$$

Proof. Check Appendix 3.8.1 for the proof. □

The magnetic polarizability expression in (3.17) provides a useful reformulation of the original magnetic polarizability expression in (3.10) to match the Lorentzian constraint in (3.14). While (3.17) does not provide a solution for optimizing the resonant frequencies, the Lorentzian form of the frequency-selective magnetic polarizability in (3.17) helps to simplify the analysis for developing a wideband beamforming gain approximation.

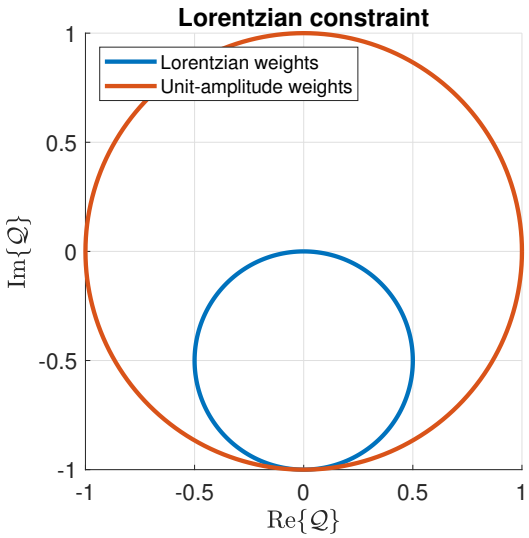


Figure 3.2. Lorentzian-constrained weight distribution for the DMA elements compared with unit-amplitude weights. We find that the Lorentzian-constrained weights allow for a total phase range of $[-\pi, 0]$.

Next, we use the magnetic polarizability in (3.17) to derive an approximation on the beamforming gain of the wideband DMA system. The DMA beamformer takes the form of (3.17) as

$$\mathbf{f}_{\mathsf{dma}}[k] = \left[-\frac{\mathrm{j}\left(1+e^{\mathrm{j}2\Psi(f_k,f_{\mathsf{r},0})}\right)}{2}, \ldots, -\frac{\mathrm{j}\left(1+e^{\mathrm{j}2\Psi(f_k,f_{\mathsf{r},N_{\mathsf{slot}}-1})}\right)}{2}\right]^{\mathsf{T}}. \tag{3.18}$$

We derive an approximation for the beamforming gain based on the formulation of the DMA beamformer in (3.18) to simplify the beamforming gain analysis as follows. We also denote $\boldsymbol{\Psi}(f_k) = [\Psi(f_k, f_{\mathsf{r},0}), \ldots, \Psi(f_k, f_{\mathsf{r},N_{\mathsf{slot}}-1})]^{\mathsf{T}}$ as the vector of frequency-selective DMA angles to simplify the notation.

Lemma 3. *For large N_{slot} and either $\phi_{\mathsf{t}} \neq \phi_{\mathsf{g}}$ or $\beta_{\mathsf{g}} > \frac{2\pi f}{c}$, the DMA beamforming gain is approximately*

$$|\mathbf{h}^{\mathsf{T}}[k]\mathbf{f}_{\mathsf{dma}}[k]|^2 \approx \left|\frac{1}{2}\mathbf{h}^{\mathsf{T}}[k]e^{\mathrm{j}2\boldsymbol{\Psi}(f_k)}\right|^2. \tag{3.19}$$

Proof. Check Appendix 3.8.2 for the proof. □

In Section 3.5, we develop methods to account for the impact of frequency-selective, tuning

bandwidth and waveguide attenuation on the DMA beamforming gain based on (3.19).

3.4.4 Approximation of the polarizability angle and center-frequency DMA beamforming

We now provide an approximation for the magnetic polarizability function to further simplify the analysis of the DMA beamforming gain. The following lemma gives an approximation for the polarizability phase using a first-order Taylor series expansion.

Lemma 4. *A linear approximation for the angle* Ψ *is*

$$\Psi(f, f_{\mathsf{r},n}) = -\frac{4\pi}{\Gamma}(f - f_{\mathsf{r},n}) + O(f^2). \tag{3.20}$$

Proof. Check Appendix 3.8.3 for the proof. □

In Section 3.5, we use (3.20) to determine the impact of frequency-selectivity, tuning bandwidth, and waveguide attenuation on the wideband MISO beamforming gain.

We now define a simple DMA beamforming method for configuring the DMA weights based on the Lorentzian mapping technique defined in [34] that configures the DMA elements at the center frequency of the bandwidth. Since the beamformer does not attempt to incorporate the frequency-selective channel or DMA effects, we consider this beamformer as a performance baseline. We first define the phase of the frequency-selective effective wireless channel. Based on the effective channel model in (3.8), we define the phase of the nth effective channel element $h_n = e^{\mathsf{j}\varphi_{n,k}}$ for a substrate permittivity ϵ_{r} and waveguide cutoff frequency $f_{\mathsf{c},10}$ as

$$\varphi_{n,k} = d_{\mathsf{x}}(n-1)\left(\frac{2\pi f_k}{c}\sin\phi_{\mathsf{t}} + \frac{2\pi\epsilon_{\mathsf{r}}}{c}\sqrt{f_k^2 - f_{\mathsf{c},10}^2}\right) \tag{3.21}$$

The phase term in (3.21) includes both the wireless and waveguide propagation, where the propagation phase constant β_{g} has been decomposed [69]. We will account for the effects of waveguide attenuation in Section 3.5.3.

Next, we use (3.20) to match the magnetic polarizability angle to the angle of the effective channel at the center frequency. We consider only the $e^{\mathrm{j}2\Psi}$ term in (3.17) as it accounts for the reconfigurability of the DMA elements for beamforming. Substituting (3.20) into (3.17) as the approximate Lorentzian beamformer, we find that a tuning bandwidth of $B_{\mathsf{tune}} = \frac{\Gamma}{4}$ results in a phase tunability over the range $[-\pi, 0]$ at the center frequency. We assume this tuning bandwidth to define the DMA beamformer at the center frequency $f_{\frac{K}{2}}$, and aim to counteract the channel phase $\varphi_{n,k}$ with

$$f_{\mathsf{r},n} = -\frac{\Gamma}{8\pi}\varphi_{n,\frac{K}{2}} + f_{\frac{K}{2}}. \tag{3.22}$$

Setting the resonant frequencies of the DMA elements according to (3.22) will guarantee that the phase of the effective wireless channel aligns with the DMA beamformer at the center frequency of the signal bandwidth. In the next section, we will use the center frequency DMA beamforming method based on (3.22) to derive an approximation for the wideband DMA beamforming gain.

3.5 Beamforming gain approximation for a DMA-based wideband communication system

In this section, we derive an approximation for the beamforming gain of a wideband DMA system with a LOS wireless channel. We investigate the impact of the DMA frequency selectivity, tuning bandwidth and waveguide power leakage on the resulting data rates as a function of the signal bandwidth B and use the approximation to give valuable insights into the wideband performance of DMAs. We develop the approximation by deriving separate expressions for the DMA frequency selectivity, tuning bandwidth and waveguide power leakage, and combining these terms heuristically to create the full approximation for the DMA beamforming gain. We assume an LOS wireless channel to allow for the tractable analysis of the DMA wideband beamforming gain, where a multipath channel environment would significantly complicate the development of a closed-form expression. Therefore, we focus on the LOS case now, and include simulation results in Section 3.7.5 to demonstrate the effectiveness of DMAs in a wideband

system with multipath propagation.

Due to the non-convex frequency-selective Lorentzian constraint, it is very difficult to derive a closed-form solution for optimizing the design variables. Moreover, optimizing the design variables for a specific set of resonant frequencies is not practical, since the resonant frequencies need to be changed to enable beamforming while the design variables are a part of the physical DMA design that cannot be changed once the DMA is fabricated. Therefore, we focus on deriving an approximation for the beamforming gain of a wideband DMA system and extract important insights from the beamforming gain expression to propose broad design guidelines for the DMA elements.

To define the DMA beamforming gain approximation, let $F_{\mathsf{freq}}(f_k)$ be a term accounting for the frequency-selectivity of the beamforming gain. In addition to the term $F_{\mathsf{freq}}(f_k)$, to account for the losses due to practical issues like waveguide attenuation and limited tunability of the DMA, we define two penalty terms. We denote a DMA angular weight fill as $\xi \in [0, \pi)$ which is defined in Section 3.5.2 as the range of available phase values for the DMA weights. For a radiated power P_{rad}, we also denote a fractional radiated power term as $\Lambda = \frac{P_{\mathsf{rad}}}{P_{\mathsf{in}}}$, which is discussed further in Section 3.7.1. Let $W_{\mathsf{fill}}(\xi) \in [0, 1]$ be the penalty term which accounts for the impact of the limited tuning bandwidth. Let $A_{\mathsf{leak}}(\Lambda) \in [0, 1]$ be the term which accounts for the impact of waveguide attenuation on beamforming gain. With these terms, we propose a heuristic approximation for the wideband DMA beamforming gain as

$$|\mathbf{h}^{\mathsf{T}}[k]\left(\mathbf{f}_{\mathsf{dma}}[k] \odot \mathbf{h}_{\mathsf{att}}[k]\right)|^2 \approx F_{\mathsf{freq}}(f_k) W_{\mathsf{fill}}(\xi) A_{\mathsf{leak}}(\Lambda). \tag{3.23}$$

Our goal is to use the approximation to extract important insights into the performance of a wideband DMA system. By separating the beamforming gain terms, we can determine how each term is affected by the DMA design parameters like the damping factor, steering angle, or propagation constant. We describe the methodology and derive expressions for each of these terms in the following sections.

3.5.1 Impact of frequency selectivity

We now derive an expression to characterize the beamforming gain of the DMA across the entire bandwidth. Using (3.22), the MISO beamforming gain with the center-frequency beamformer (without waveguide attenuation) is

$$F_{\mathsf{freq}}(f_k) = |\mathbf{h}^{\mathsf{T}}[k]\mathbf{f}_{\mathsf{dma}}[k]|^2 = \left| \frac{1}{2\sqrt{N_{\mathsf{slot}}}} \sum_{n=1}^{N_{\mathsf{slot}}} \exp\left(\mathrm{j}\varphi_{n,k} - \mathrm{j}\varphi_{n,\frac{K}{2}}\right) \right|^2 . \tag{3.24}$$

The DMA at the center frequency $f_{\frac{K}{2}}$ achieves the maximum beamforming gain, but there is a phase mismatch at other frequencies in the bandwidth that will degrade the overall beamforming gain. This effect is well-studied in the context of phased arrays and is known as beam-squint [89]. DMAs, however, suffer greater losses in wideband settings compared to phased arrays because of the combination of wireless and waveguide channel frequency-selectivity. We quantify the frequency-selective beamforming gain loss from beam-squint at each subcarrier frequency as follows.

Let $\Delta_k = f_k - f_{\frac{K}{2}}$ be the difference between a subcarrier frequency and the center frequency of the bandwidth. The phase difference between the subcarrier frequency f_k and center frequency $f_{\frac{K}{2}}$ of the nth element due to the effective channel is then

$$\chi_{\mathsf{o}}[k] = -d_{\mathsf{x}}\left(\frac{2\pi\Delta_k}{c} \sin\phi_{\mathsf{t}} + \frac{2\pi\epsilon_{\mathsf{r}}}{c} \left(\sqrt{(f_{\frac{K}{2}} + \Delta_k)^2 - f_{\mathsf{c},10}^2} - \sqrt{f_{\frac{K}{2}}^2 - f_{\mathsf{c},10}^2} \right) \right). \tag{3.25}$$

The expression in (3.25) encapsulates the beam-squint effect of the wireless channel and DMA waveguide propagation since (3.25) describes the phase difference for the DMA beamforming weights between a specific subcarrier frequency and the center frequency of operation. We can then define the frequency-selective beamforming gain per subcarrier frequency including the approximate linear phase profile of the magnetic polarizability in the following lemma.

Lemma 5. *The frequency-selective beamforming gain at each subcarrier frequency is*

$$F_{\mathsf{freq}}(f_k) = \left| \frac{1}{2} \frac{1}{\sqrt{N_{\mathsf{slot}}}} \frac{\sin\left(\frac{N_{\mathsf{slot}}}{2}\chi_{\mathsf{o}}[k]\right)}{\sin\left(\frac{1}{2}\chi_{\mathsf{o}}[k]\right)} \right|^2 . \tag{3.26}$$

Proof. Check Appendix 3.8.4 for the proof. □

It is important to note that since the DMA elements are assumed to have a linear phase profile from the polarizability approximation, the frequency-selectivity of the DMA elements has no impact on the overall frequency-selective beamforming gain. Under this assumption, the beam-squint of the wireless channel and DMA waveguide are the primary frequency-selective effects that degrade wideband performance for a DMA. This is valid for subcarrier frequencies near the resonant frequency tuning of the DMA elements and generally becomes less accurate as the signal bandwidth increases.

3.5.2 Impact of tuning bandwidth

We now discuss the impact of the tuning bandwidth B_{tune} on the overall DMA performance. DMA weights do not achieve the full $[0, -\pi]$ phase range possible with the Lorentzian-constrained weight formulation in (3.14) unless there is an infinite tuning bandwidth, which is not practically possible. The feasible weights are a function of both the varactor capacitance due to tuning bandwidth constraints and the damping factor. We use the term *weight fill* to describe the ratio of Lorentzian-constrained weights available compared to the full set in (3.14). In the previous section, we made the assumption that the DMA elements had access to the full Lorentzian-constrained weights at the center frequency. Since the weight fill depends on the damping factor and tuning bandwidth, we develop an expression to account for the additional weight constraint of the weight fill on the final beamforming gain.

To derive a weight fill expression that describes how a weight fill impacts the DMA beamforming gain, we first introduce the weight fill ratio. The weight fill ratio $W_{\mathsf{ratio}}(\Gamma, B_{\mathsf{tune}})$ is described by the difference in phase of the lowest and highest resonant frequencies within the

tuning bandwidth as

$$W_{\mathsf{ratio}}(\Gamma, B_{\mathsf{tune}}) = \frac{|\angle\bar{\alpha}_{\mathsf{M}}(f_{\mathsf{t}}, f_{\mathsf{r,max}}) - \angle\bar{\alpha}_{\mathsf{M}}(f_{\mathsf{t}}, f_{\mathsf{r,min}})|}{\pi}, \tag{3.27}$$

where it is normalized by π to ensure the weight fill ratio remains between $[0, 1]$. We also define $\xi = \pi W_{\mathsf{ratio}}(\Gamma, B_{\mathsf{tune}})$ to represent the angular weight fill of the DMA, with a range from $[0, \pi]$. Next, we use the weight fill ratio to derive an approximation for the normalized beamforming gain from an incomplete Lorentzian-constrained curve as follows.

Lemma 6. *For a given weight fill ratio, the normalized beamforming gain is approximately*

$$W_{\mathsf{fill}}(\xi) = \left| \frac{1}{2\pi} \left(2\sin(\xi) + 2\xi\right) \right|^2. \tag{3.28}$$

Proof. Check Appendix 3.8.5 for the proof. □

Based on the weight fill expression in (3.28), we find that small weight fill values lead to a large amount of beamforming gain loss since there is a minimal phase range to use for beamforming. Then, as the weight fill increases, the normalized beamforming gain approaches 1 as the phase range of the DMA beamformer approaches the full $[0, \pi]$ range. Therefore, a sufficient weight fill ratio, achieved through the DMA design, is necessary to ensure that the DMA can steer a beam pattern in a desired direction with minimal loss.

3.5.3 Impact of waveguide attenuation

Lastly, we derive an expression to account for the impact of DMA waveguide attenuation due to power leakage on the MISO beamforming gain. As power is gradually radiated out through the DMA elements, the waveguide attenuation will alter the amplitude of each subsequent DMA element weight as an effective amplitude taper. This can potentially lead to additional losses. Let P_{rad} be the radiated power from the DMA across the center subcarrier bandwidth and $\Lambda = \frac{P_{\mathsf{rad}}}{P_{\mathsf{in}}}$ be the fractional radiated power. We derive a factor $A_{\mathsf{leak}}(\Lambda) \in [0, 1]$ that describes the beamforming

gain loss due to waveguide attenuation.

To define the penalty $A_{\mathsf{leak}}(\Lambda)$ independent of the DMA beamforming capability, we assume a frequency-selective matched-filter precoding $\mathbf{f}_{\mathsf{mf}}[k]$ such that $h_n[k]f_{\mathsf{mf},n}[k] = 1 \forall k, n$. We make this assumption because we have separately accounted for the non-ideal effects of the frequency-selectivity, weight amplitude distribution, and tuning bandwidth in the previous sections. Therefore, with this assumption of ideal matched filtering and isolating the waveguide power leakage vector $\mathbf{h}_{\mathsf{att}}[k]$, we define the penalty $A_{\mathsf{leak}}(\Lambda)$ as

$$A_{\mathsf{leak}}(\Lambda) = \frac{|\mathbf{h}^{\mathsf{T}}[k](\mathbf{f}_{\mathsf{mf}}[k] \odot \mathbf{h}_{\mathsf{att}}[k])|^2}{\|\mathbf{h}^{\mathsf{T}}[k]\|^2 \|(\mathbf{f}_{\mathsf{mf}}[k] \odot \mathbf{h}_{\mathsf{att}}[k])\|^2} = \frac{1}{N_{\mathsf{slot}}} \frac{|\mathbf{1}^{\mathsf{T}}\mathbf{h}_{\mathsf{att}}[k]|^2}{\|\mathbf{h}_{\mathsf{att}}[k]\|^2}. \tag{3.29}$$

By above definition and from Cauchy-Schwarz inequality, we see that the maximum value of the penalty term is one. The final expression in (3.29) now depends only on the frequency-selective waveguide attenuation, and takes the form of a geometric series. Therefore, we simplify the attenuation penalty term $A_{\mathsf{leak}}(\Lambda)$ in the following lemma.

Lemma 7. *Assuming ideal matched filtering and large N_{slot}, the DMA waveguide attenuation affects the ideal DMA beamforming gain by a penalty factor $S(\Lambda)$ approximated as*

$$A_{\mathsf{leak}}(\Lambda) \approx \frac{4}{\ln(1-\Lambda)} \tanh\left(\frac{\ln(1-\Lambda)}{4}\right). \tag{3.30}$$

Proof. Check Appendix 3.8.6 for the proof. □

The derived expression in (3.30) gives the important insight that the DMA waveguide attenuation reduces the beamforming gain compared to a normal antenna array, depending on the total radiated power P_{rad} and leakage constant $\bar{\alpha}_{\mathsf{g}}$. We also justify the assumption for large N_{slot} by noting that many DMA elements are required to provide a slow leakage of power and narrow beam patterns, meaning N_{slot} must be large.

3.6 DMA successive beamforming algorithm

We now describe two beamforming methods used to evaluate the wideband spectral efficiency of a DMA-based system. First, we define the DMA center-frequency beamforming algorithm as a baseline beamforming method to compare and validate the DMA beamforming gain approximation in (3.23). Next, we define a novel, successive beamforming algorithm to improve upon the center-frequency beamforming method for larger signal bandwidths.

3.6.1 DMA center-frequency beamforming algorithm

The center-frequency beamforming algorithm selects the DMA resonant frequency tuning that best matches the channel phase at the center frequency. For the center frequency subcarrier $f_{\frac{K}{2}}$, the resonant frequency values for the center frequency beamformer are given by

$$f_{\mathsf{r},n}^{\mathsf{cf}} = \underset{f_{\mathsf{r},n}\in[f_{\mathsf{r},\mathsf{min}},f_{\mathsf{r},\mathsf{max}}]}{\operatorname{argmin}} \left| -\frac{\mathsf{j} - e^{\mathsf{j}\angle h^{\mathsf{c}}_{n,\frac{K}{2}}}}{2} - \bar{\alpha}_{\mathsf{M}}(f_{\frac{K}{2}}, f_{\mathsf{r},n}) \right|. \tag{3.31}$$

Since the DMA approximation in (3.23) was derived based on a center frequency beamforming assumption, we will use the center frequency beamforming method in (3.31) to evaluate the validity of the DMA approximation.

3.6.2 DMA successive beamforming algorithm

We now develop a successive algorithm to configure the DMA elements and improve the DMA wideband spectral efficiency compared to the center-frequency beamformer. While the DMA approximation in (3.23) will help to give insights into wideband DMA element design, it does not provide insight into how the DMA element weights should be configured to improve the wideband spectral efficiency performance. The objective of the successive beamformer is to increase spectral efficiency by configuring each DMA element sequentially such that spectral efficiency is maximized for every subsequent element. This differs from the center-frequency

algorithm which selects the DMA configuration solely based on the phase total channel.

To define the beamforming algorithm, let $f_{\mathsf{r},n}^{\mathsf{S}}$ be the resonant frequency selected for the nth element of the successive beamformer, and let $U(f_k, f_{\mathsf{r},n}) = \bar{\alpha}_{\mathsf{M}}(f_k, f_{\mathsf{r},n}) h_{\mathsf{att},n}[k] h_n[k]$ represent the per-element beamforming gain for the DMA with the wireless and waveguide channel. We define the selection process for the nth DMA element through the successive beamforming algorithm as

$$f_{\mathsf{r},n}^{\mathsf{S}} = \underset{f_{\mathsf{r},n} \in [f_{\mathsf{r,min}}, f_{\mathsf{r,max}}]}{\operatorname{argmax}} \frac{1}{K} \sum_{k=1}^{K} \log_2 \left(1 + \rho_k \left| U(f_k, f_{\mathsf{r},n}) + \sum_{m=0}^{n-1} U(f_k, f_{\mathsf{r},m}^{\mathsf{S}}) \right|^2 \right). \tag{3.32}$$

The successive algorithm in (3.32) first selects the resonant frequency that maximizes the wideband spectral efficiency for the DMA element closest to the waveguide feed. Then, with the chosen, fixed resonant frequency value of the first element, the successive algorithm then selects the resonant frequency for the second DMA element that maximizes the total spectral efficiency. We repeat this process until all resonant frequency values are selected to create the DMA successive beamforming vector.

The DMA successive algorithm has two primary advantages over the center-frequency beamforming algorithm. First, the successive algorithm maximizes the spectral efficiency over all frequencies in the bandwidth, rather than focusing solely on the center frequency. Second, the resonant frequency selection process takes into account the previously-selected resonant frequencies to improve spectral efficiency, while the center-frequency algorithm simply attempts to match the DMA weight to the phase of the channel. We compare these two approaches in Section 3.7.

We now compare the complexity of the proposed successive beamforming algorithm with the center-frequency beamforming algorithm. For both the center-frequency beamforming algorithm in (3.31) and the successive beamforming algorithm in (3.32), resonant frequency values are calculated from a continuous set $f_{\mathsf{r}} \in [f_{\mathsf{r,min}}, f_{\mathsf{r,max}}]$. When implementing these algorithms computationally to calculate the resonant frequencies, however, the possible continuous

Table 3.1. Summary of DMA model parameters incorporated into the beamforming algorithm design

Parameter	[74, 75, 39, 77, 41, 79, 80, 81, 58]	[34, 1]	[40, 78]	This work
Narrowband	✓	✓	✓	✓
Wideband				✓
Frequency-selective			✓	✓
Tuning bandwidth		✓		✓
Waveguide power leakage		✓		✓

resonant frequency values must be transformed into a discrete set with resolution R_{res}, such that $f_{\mathsf{r}} \in \{f_{\mathsf{r,min}}, f_{\mathsf{r,min}}+1\frac{f_{\mathsf{r,max}}-f_{\mathsf{r,min}}}{R_{\mathsf{res}}-1}, f_{\mathsf{r,min}}+2\frac{f_{\mathsf{r,max}}-f_{\mathsf{r,min}}}{R_{\mathsf{res}}-1}, \ldots, f_{\mathsf{r,min}}+(R_{\mathsf{res}}-2)\frac{f_{\mathsf{r,max}}-f_{\mathsf{r,min}}}{R_{\mathsf{res}}-1}, f_{\mathsf{r,max}}\}$. To calculate the resonant frequency for each nth element with N_{slot} total elements, the minimization for (3.31) and maximization for (3.32) then occurs over the discrete resonant frequency set with R_{res} values. Therefore, the complexity of both the center-frequency beamforming algorithm and the successive beamforming algorithm scale as $O(N_{\mathsf{slot}}R_{\mathsf{res}})$ when performing the computations. This means that the proposed algorithm does not impose a greater complexity scaling than the baseline center-frequency beamforming algorithm.

Lastly, we compare the proposed algorithm with prior work in Table 3.1 based on the various DMA modeling parameters that are incorporated into the algorithm. We find that our proposed successive beamforming algorithm is the only work that accounts for the frequency-selectivity of the DMA elements, tuning bandwidth, and waveguide power leakage all together, where [34, 1] and [40, 78] account for different combinations of these three parameters. Moreover, we have designed the successive beamforming algorithm to improve the spectral efficiency in wideband scenarios, which differs significantly from all prior work that has primarily focused on narrowband scenarios. We evaluate the performance of the proposed successive beamforming algorithm for large bandwidths in the next section.

3.7 Data rate and spectral efficiency results

We now examine the data rate and spectral efficiency results for the center-frequency DMA beamformer, the approximate model, and the DMA successive beamformer. For specific DMA design parameters, each value in the approximate model is calculated to approximate the total DMA beamforming gain for spectral efficiency and data rate results, while the center-frequency DMA beamformer and successive beamformer configures the DMA elements based on (3.31) and (3.32), respectively.

3.7.1 Simulation setup and design considerations

In all cases, the spectral efficiency $C(\{\rho_k, \mathbf{h}[k]\}_{k=1}^K)$ is calculated using (3.5) with the configured DMA elements. The channel in every case is an LOS channel at a particular target direction ϕ_{t}. Data rates D are then calculated for the signal bandwidth B as

$$D = BC(\{\rho_k, \mathbf{h}[k]\}_{k=1}^K). \tag{3.33}$$

Design parameters for the DMA, such as tuning bandwidth, damping factor, and number of elements, will be varied and analyzed for their impact on the resulting spectral efficiency and data rates.

Next, we discuss the frequency-selective DMA and waveguide design parameters for simulations. As discussed in Lemma 6, leaky-wave antennas are typically designed such that a predetermined fraction Λ of the input power is radiated. The desired leakage constant $\bar{\alpha}_{\mathsf{g}}$ at the center frequency for a typical leaky-wave antenna is [90]

$$\bar{\alpha}_{\mathsf{g}}(f_{\mathsf{t}}) = -\frac{\ln(1-\Lambda)}{2d_{\mathsf{x}}(N_{\mathsf{slot}}-1)}. \tag{3.34}$$

As an example, designing the DMA leakage constant $\bar{\alpha}_{\mathsf{g}}$ for $\Lambda = 0.9$ in (3.34) ensures that 90% of the input power is radiated. Calculating the attenuation due to the radiated power of DMA

elements, however, is a more difficult task since each DMA element has its own unique element configuration and radiated power. We follow a procedure outlined in [34] to determine the DMA waveguide leakage as a function of frequency based on an averaged value of the different element configurations.

The attenuation model in [34] implements ideal waveguide assumptions such that there is no power loss due to waveguide imperfections, and only power radiated through the DMA elements contributes to the electromagnetic field decay. A more complete model for the attenuation of the waveguide fields involves calculating the radiated electromagnetic fields from each DMA element and subtracting the radiated power from the waveguide fields. This method depends on the specific configuration of DMA element weights and complicates the analysis of the impact of waveguide field attenuation on the wideband performance significantly. Therefore, we use the averaged attenuation to simplify the wideband analysis and allow for the derivation of the leakage term A_{leak}. Moreover, we assume that we can alter the DMA coupling factor F_{coupl} to achieve the desired attenuation constant $\bar{\alpha}_{\mathsf{g}}$ for the DMA.

The normalization of the DMA beamformer is based on the radiated power per subcarrier bandwidth. For a typical fully-digital MISO system, a beamformer $\mathbf{f}[k]$ is subject to a power constraint for a normalization constant M such that $\sum_{k=1}^{K} ||\sqrt{M}\mathbf{f}[k]||^2 = KP_{\mathsf{in}}$. With this normalization comes the assumption that 100% of the input power is radiated out through the antenna array. The radiated power for the DMA, however, is given by [90]

$$P_{\mathsf{rad}}(f_k) = P_{\mathsf{in}}\left(1 - e^{-2\bar{\alpha}_{\mathsf{g}}(f_k)d_{\mathsf{x}}(N_{\mathsf{slot}}-1)}\right) \tag{3.35}$$

and describes the DMA radiated power across each subcarrier bandwidth, which does not guarantee that 100% of the input power is radiated. We reformulate the power constraint for all subcarriers based on (3.35) and configure the power normalization constant M_k for $\mathbf{f}_{\mathsf{dma}}[k]$ such that

$$||\sqrt{M_k}\mathbf{f}_{\mathsf{dma}}[k] \odot \mathbf{h}_{\mathsf{att}}[k]||^2 = P_{\mathsf{in}}\left(1 - e^{-2\bar{\alpha}_{\mathsf{g}}(f_k)d_{\mathsf{x}}(N_{\mathsf{slot}}-1)}\right),\ \forall k \tag{3.36}$$

The power constraint in (3.36) ensures that the frequency-selectivity of the radiated power in (3.35) for a specific DMA design is physically consistent with the DMA beamforming weights in $\mathbf{f}_{\mathsf{dma}}$ through the normalization constant M_k.

Since we have an averaged attenuation model, the normalization procedure comes with the assumption that regardless of the DMA element configuration, a certain radiated power value is met. Because of the waveguide phase advance, the DMA element configuration to steer a beam pattern will have a somewhat uniform distribution of the antenna weights around the Lorentzian-constraint, as discussed in Lemma 5. All DMA element configurations will have a very similar radiated power, allowing us to justify the radiated power assumption.

3.7.2 Validation for the DMA beamforming gain approximation

Next, we validate the accuracy of the DMA beamforming gain approximation expression in (3.23). Unless otherwise specified, we consider a DMA design that operates at $f_{\mathsf{t}} = 15$ GHz, has $N_{\mathsf{slot}} = 32$ elements with an element spacing of $d_{\mathsf{x}} = \lambda/4$, and has a quality factor of $Q = 100$. We will isolate the three approximation terms $F_{\mathsf{freq}}, W_{\mathsf{fill}}, A_{\mathsf{leak}}$ and compare the beamforming gain with the center-frequency beamformer to determine validity of each term separately.

To validate the approximation in (3.23), we denote the per-subcarrier beamforming gain for the center-frequency beamformer as $G_{\mathsf{cf}}[k] = |\mathbf{h}^{\mathsf{T}}[k]\,(\mathbf{f}_{\mathsf{dma}}[k] \odot \mathbf{h}_{\mathsf{att}}[k])\,|^2$ and for the approximation as $G_{\mathsf{approx}}[k] = F_{\mathsf{freq}}(f_k)W_{\mathsf{fill}}(\xi)A_{\mathsf{leak}}(\Lambda)$. We then define the sum beamforming gain for the center-frequency beamformer as

$$G_{\mathsf{cf,sum}} = \sum_{k=1}^{K} M_k |\mathbf{h}^{\mathsf{T}}[k]\,(\mathbf{f}_{\mathsf{dma}}[k] \odot \mathbf{h}_{\mathsf{att}}[k])\,|^2 \tag{3.37}$$

and for the approximation as

$$G_{\mathsf{approx,sum}} = \sum_{k=1}^{K} M_k F_{\mathsf{freq}}(f_k)W_{\mathsf{fill}}(\xi)A_{\mathsf{leak}}(\Lambda). \tag{3.38}$$

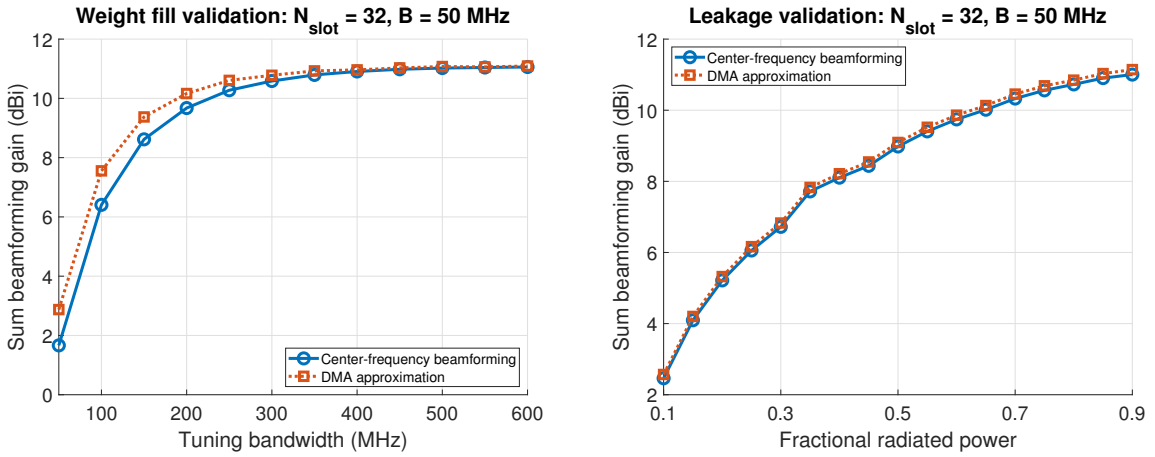


Figure 3.3. We plot the validation for the (a) weight fill term, (b) leakage term, and (c) frequency-selectivity term using the DMA approximation against the center-frequency beamformer. We find that the weight fill and leakage terms provide an accurate model to approximate the wideband DMA performance, while the frequency-selectivity term is accurate at small signal bandwidths and becomes less accurate as the signal bandwidth increases.

We validate the DMA approximation using the per-subcarrier and sum beamforming gain as follows.

First, we compare $G_{\mathsf{cf,sum}}$ and $G_{\mathsf{approx,sum}}$ for a small bandwidth to isolate the weight fill term W_{fill}. For a small bandwidth and fixed radiated power, the frequency-selective term and and leakage term will not have a significant impact on the resulting sum beamforming gain, while the weight fill term W_{fill} changes significantly as a function of the tuning bandwidth B_{tune}. We show the sum beamforming gain for the center-frequency beamforming and approximation in Fig. 3.3(a). As the tuning bandwidth increases, we find that the approximation closely matches the sum beamforming gain of the center-frequency beamformer, meaning that the weight fill term provides an accurate analysis of how the DMA beamforming gain changes as a function of the tuning bandwidth. As expected, we also find that as the tuning bandwidth grows, the sum beamforming gain increases due to the additional available beamforming weights.

Next, for a small signal bandwidth and large tuning bandwidth, we show the validation for the leakage term A_{leak} through the sum beamforming gain as a function of the fractional radiated power Λ in Fig. 3.3(b). Here, we see that the approximation very closely matches the center-frequency beamformer and that the sum beamforming gain increases as we increase the power radiated from the DMA.

Lastly, for a large tuning bandwidth and fixed radiated power, Fig. 3.3(c) shows the per subcarrier beamforming gain as a function of the subcarrier frequency. Using a very large tuning bandwidth, we isolate the frequency-selective term $F_{\mathsf{freq}}(f_k)$ to compare with the center-frequency beamformer. In Fig. 3.3(c) at frequencies near the center frequency $f_{\mathsf{t}} = 15$ GHz, the per subcarrier beamforming gain matches very closely to the center-frequency beamforming method and becomes less accurate at subcarrier frequencies further from the center frequency. This is due to the linear approximation for the DMA frequency-selectivity in (3.20), which becomes less accurate as the subcarrier frequency deviates further from the center frequency. Overall, the leakage term A_{leak} and the weight fill term W_{fill} provide an accurate model for the DMA beamforming gain as the tuning bandwidth and fractional radiated power vary, while

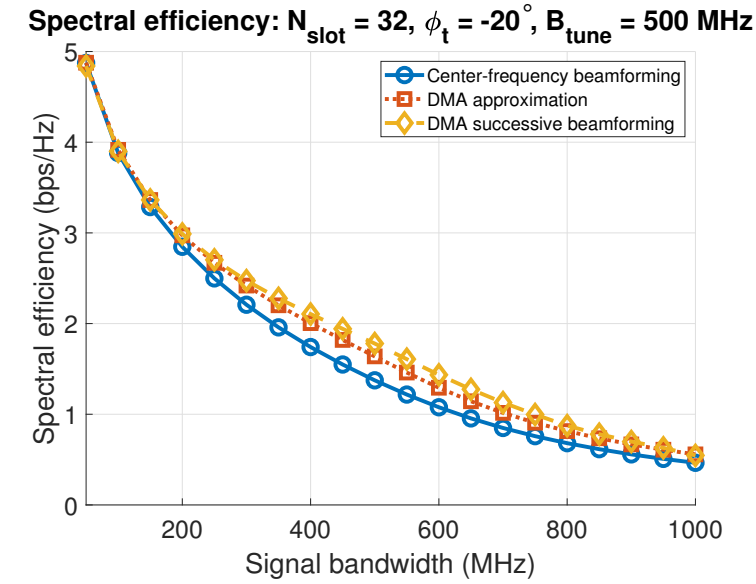
the frequency-selectivity term F_{freq} is accurate at smaller signal bandwidths and becomes less accurate at larger signal bandwidths.

3.7.3 Simulation results for the approximation and successive DMA beamformer

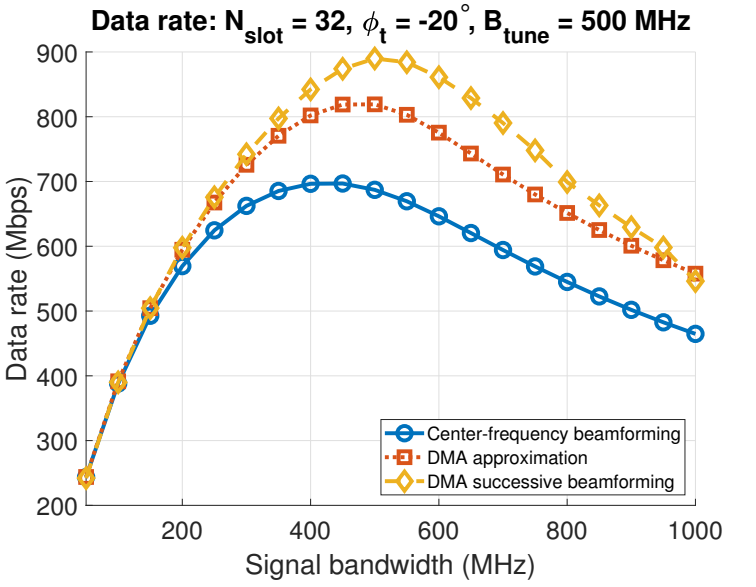
We now investigate the performance of the DMA successive algorithm compared to the baseline center-frequency beamforming performance. Fig. 3.4(a) shows the DMA wideband spectral efficiency as a function of signal bandwidth for a large tuning bandwidth. As expected, we find that the spectral efficiency decreases with signal bandwidth due to the increased noise power and higher DMA frequency selectivity. Given the large tuning bandwidth, the DMA successive algorithm is able to increase the spectral efficiency compared to the baseline center-frequency beamformer since the successive algorithm better configures the DMA elements across a wide signal bandwidth.

Fig. 3.4(b) also shows the data rates for the DMA wideband scenario. We see that as the signal bandwidth increases, the data rate continues to increase until the DMA elements exhibit very large frequency-selectivity. From the attenuation analysis, we see that the tuning bandwidth provides an approximate limit for the maximum data rate, since the DMA cannot support frequencies beyond the tuning bandwidth. The approximation holds for smaller signal bandwidths, but begins to breakdown at larger signal bandwidths due to the magnetic polarizability approximation in (3.20). We use the insights in the approximation to understand how the frequency-selectivity, tuning bandwidth, and attenuation impact the DMA wideband performance in Section 3.7.4. Lastly, Fig. 3.5 shows the spectral efficiency as a function of the steering angle. We find that the spectral efficiency does not change significantly as the steering angle varies, meaning the we can extend the insights gained from Fig. 3.4 at the angle $\phi_{\mathsf{t}} = -20^{\circ}$ to all steering angles.

We now discuss the main benefit of the DMA successive algorithm to enhance the achievable data rates of the DMA wideband system. Fig. 3.6 shows the maximum data rate



(a)



(b)

Figure 3.4. We plot spectral efficiency in (a) and data rate in (b) as a function of the signal bandwidth. We find that spectral efficiency decreases with signal bandwidth due to the noise power term and increased frequency-selectivity of the DMA elements. We also see that the successive algorithm provides better data rates and spectral efficiency than the center-frequency beamformer.

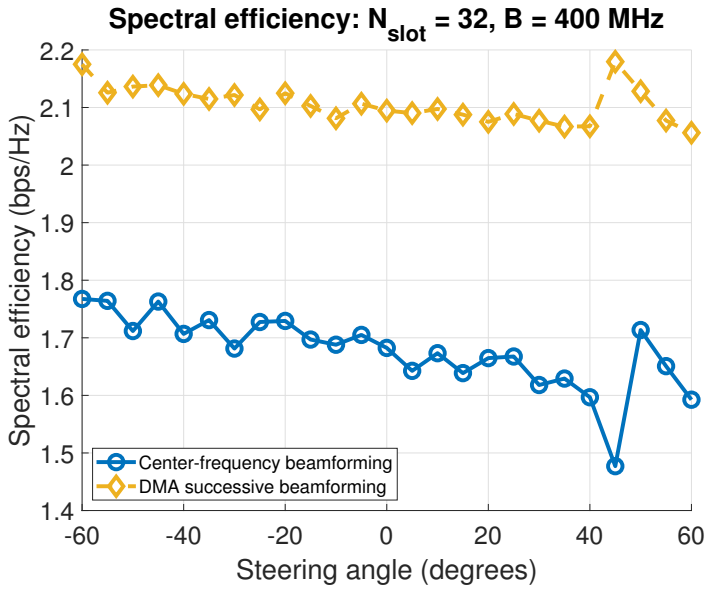


Figure 3.5. Spectral efficiency as a function of the steering angle ϕ_t. As the steering angle varies, the spectral efficiency does not change significantly for both the center-frequency beamformer and the successive beamformer.

achievable for a given tuning bandwidth as $D_{\text{max}} = \max_{B} D(B, B_{\text{tune}})$. For both the DMA center-frequency beamformer and the successive algorithm, we find that there is ultimately a data rate plateau as we increase the DMA tuning bandwidth. This is due to the high frequency-selectivity of the DMA system, where increasing the tuning bandwidth no longer yields greater wideband beamforming capabilities. We find that the successive algorithm, however, can significantly extend the maximum achievable data rate at higher signal bandwidths by configuring the frequency-selective DMA elements for the wideband signal. Therefore, the proposed successive algorithm can perform significantly better than the baseline algorithm for a large signal bandwidth and tuning bandwidth.

3.7.4 Impact of DMA element spacing and damping factor

We now look at the impact of the DMA element spacing and the damping factor on the resulting DMA wideband spectral efficiency. Fig. 3.7 shows spectral efficiency results for the center-frequency beamformer as a function of the DMA element spacing. From the

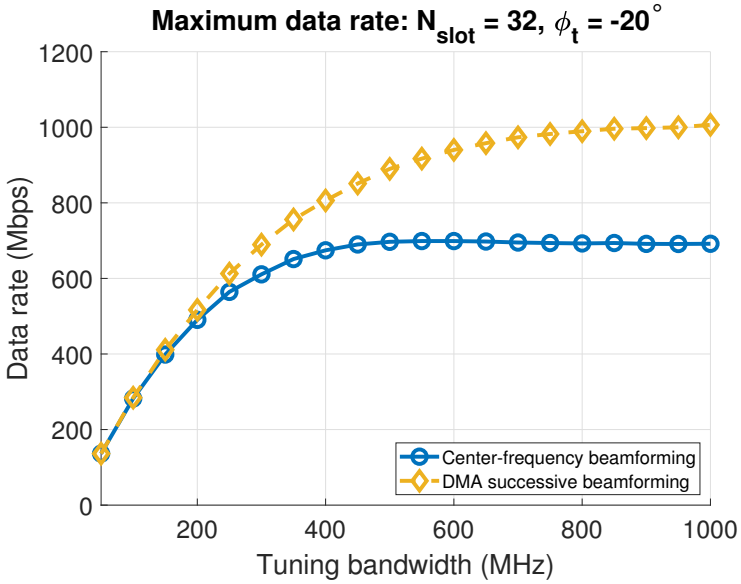


Figure 3.6. Maximum data rate results comparing the center-frequency beamforming and DMA successive algorithm. The DMA successive algorithm allows for larger data rates and signal bandwidths as it can better configure the DMA elements for a wideband frequency-selective scenario.

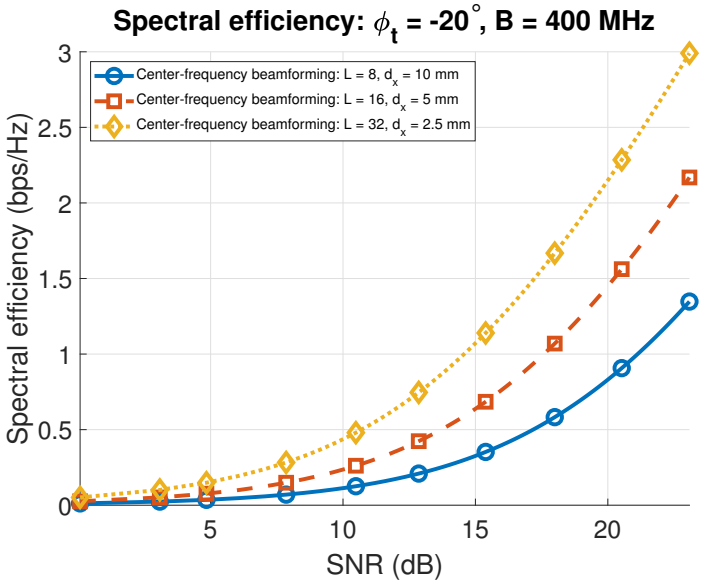


Figure 3.7. DMA element spacing analysis for spectral efficiency. As the approximation predicts, smaller DMA element spacing leads to lower frequency-selectivity and higher spectral efficiency. As DMAs are impacted more by the beam-squint effect than phased arrays, it is important to minimize DMA element spacing to mitigate beam-squint.

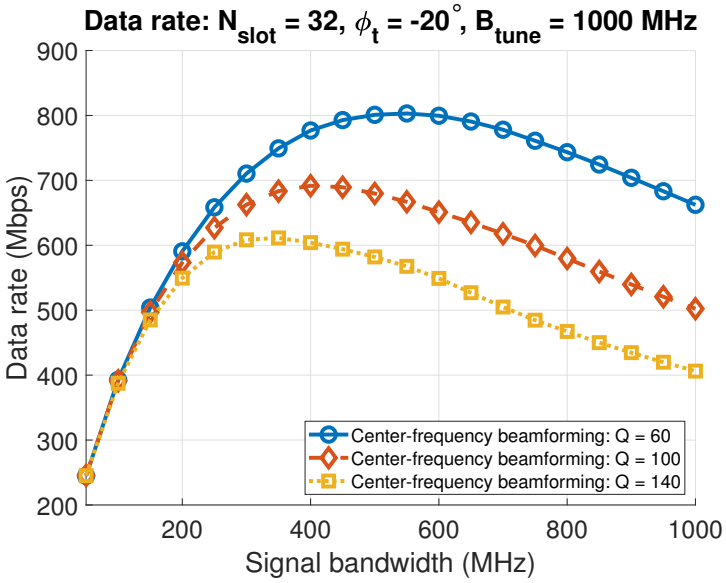


Figure 3.8. Data rates for the center-frequency beamformer and different damping factors. We show that larger damping factors lead to improved data rates due to the lower impact of frequency-selectivity.

frequency-selectivity term in (3.26), we expect the frequency-selectivity to increase as the DMA element spacing increases. Lower element spacing will be less frequency-selective and result in improved spectral efficiency. Fig. 3.7 verifies this relationship, where spectral efficiency increases as d_{x} decreases, while maintaining the same overall DMA length. This also leads to key insight on how the DMA frequency-selectivity compares to a phased array. The addition of the waveguide channel greatly increases the frequency-selectivity. Therefore, small dense element spacing is crucial for a DMA wideband system to minimize the impact of the frequency-selective waveguide and wireless channel.

Next, we examine the effects of the damping factor on the DMA performance. Fig. 3.8 shows the data rate results for a high, medium and low damping factor. We define the damping factor in terms of the Q-factor at the center frequency as $\Gamma = \frac{2\pi f_{\text{t}}}{Q}$. Larger damping factors leads to lower amounts of frequency-selectivity in the magnetic polarizability resonance curve but also a lower weight fill ratio. We show in Fig. 3.8 that a large damping factor leads to the highest data rates for a large tuning bandwidth due to lower frequency-selectivity.

3.7.5 Impact of multipath on DMA beamforming performance

Lastly, we determine the effectiveness of the proposed successive beamforming algorithm in a multipath environment and make comparisons to hybrid and analog beamforming architectures. Thus far, we have primarily considered an LOS scenario to derive the wideband beamforming gain approximation and extract important design insights for a wideband DMA system. Since practical channel environments often involve multiple propagation paths, we include multipath channel simulation results to ensure that our proposed algorithm remains effective in various channel environments. A more in-depth analysis on the impact of multipath environments for DMA wideband beamforming can be found in our related work [85]. Here, we extend the work in [85] to focus on the comparison of DMAs with typical hybrid beamforming architectures that employ passive phase shifters.

Next, we discuss the simulation parameters and setup. The multipath channel model is outlined in [85], which includes L_{path} channel paths and frequency-selective filtering effects. We do not repeat the multipath channel model here for brevity. We also consider a uniform planar array (UPA) architecture at the transmitter instead of a ULA, where antenna elements are also placed in the y direction with spacing d_{y} to form subarrays. For the hybrid beamforming architecture and analog-only architecture, let there be N_{ele} antenna elements per subarray with spacing $d_{\mathsf{x}} = \lambda/2$ in the x direction, and N_{rf} subarrays with spacing $d_{\mathsf{y}} = \lambda/2$ in the y direction. Although a spacing of $d_{\mathsf{x}} = \lambda/2$ is common in phased arrays due to antenna sizes, mutual coupling, and grating lobe mitigation, DMA elements are typically much smaller than traditional antenna elements and can allow for tight element spacing. This is due to a combination of the metasurface-inspired geometry as well as the slotted-waveguide implementation of DMAs. Because DMA elements can be placed more densely than typical antenna elements, let there be $2N_{\mathsf{ele}}$ antenna elements per subarray with spacing $d_{\mathsf{x}} = \lambda/4$ in the x direction, and N_{rf} subarrays with spacing $d_{\mathsf{y}} = \lambda/2$ in the y direction. While the DMA will contain twice the number of antenna elements, the aperture area of both the DMA and hybrid architecture will be the same to

maintain consistency between the two architectures. We calculate the beamforming vectors for both a partially-connected and fully-connected hybrid architecture based on [23, 91]. For the hybrid architectures, the number of subarrays N_{rf} dictates the number of RF chains. Lastly, it is crucial to account for the loss due to RF components when comparing DMAs with a hybrid architecture. We use the component loss and SNR model outlined in [11] to determine the loss due to the passive phase shifters and power dividers for the DMA, analog-only, and hybrid architectures. We assume the loss due to the passive phase shifters is 8.8 dB [11].

For the multipath channel environment with $N_{\mathsf{ele}} = 6$ elements, $N_{\mathsf{rf}} = 4$ RF chains, and $L_{\mathsf{path}} = 4$ channel paths, Fig. 3.9 shows the resulting spectral efficiency for the DMA and hybrid architectures through a Monte Carlo simulation. We vary the total transmit power P_{t}, which modifies the input power P_{in} based on the component loss L_{loss} as $P_{\mathsf{in}} = L_{\mathsf{loss}} P_{\mathsf{t}}$. This is further discussed in [86]. Because the multipath environment introduces more frequency-selectivity into the wireless channel, we find here that the proposed DMA successive beamforming algorithm significantly outperforms the DMA center-frequency beamforming algorithm. This shows that our proposed algorithm remains very effective for channel environments beyond the LOS scenario. Moreover, we find that the DMA outperforms both the hybrid architectures and the analog-only architecture in terms of spectral efficiency. This is primarily due to the component loss in the passive phase shifters, which is set to 8.8 dB [86] and contributes to a significant loss in the SNR compared with DMAs that employ no phase shifters. Overall, the proposed successive beamforming algorithm provides a large performance improvement in wideband wireless systems compared to the baseline DMA beamforming method and hybrid architectures that use passive, lossy phase shifters.

Fig. 3.10 shows simulation results for the average spectral efficiency as a function of the number of channel paths in the multipath environment. We assume the same array architectures for both the DMA and hybrid cases as in Fig. 3.9, where $N_{\mathsf{ele}} = 6$ elements and $N_{\mathsf{rf}} = 4$ RF chains. We find that the proposed successive beamforming algorithm outperforms both the center-frequency algorithm and hybrid beamforming architectures in terms of spectral efficiency

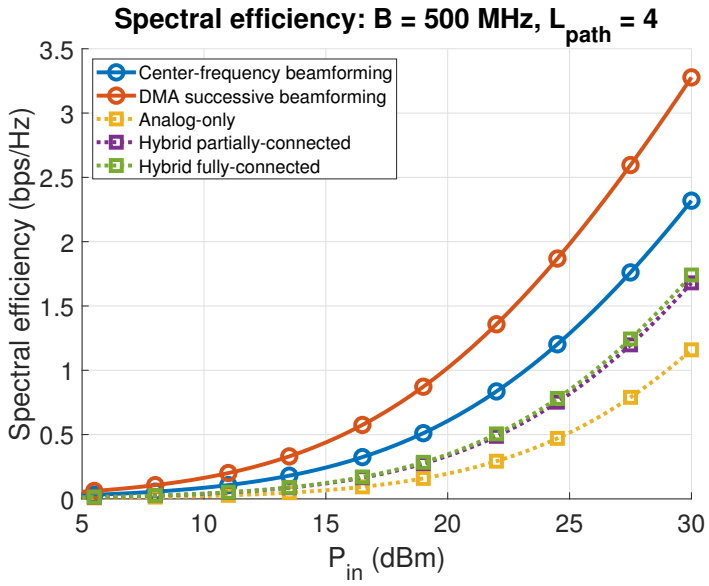


Figure 3.9. Spectral efficiency results for a multipath channel environment with $N_{\text{ele}} = 6$ elements per subarray and $N_{\text{rf}} = 4$ subarrays. We find that the proposed DMA successive beamforming algorithm outperforms both the baseline DMA center-frequency beamforming method and the hybrid architectures. This is due to the flexible algorithm design that adapts to the DMA and channel frequency-selectivity, dense DMA element spacing, and high component loss from passive phase shifters for the hybrid architecture.

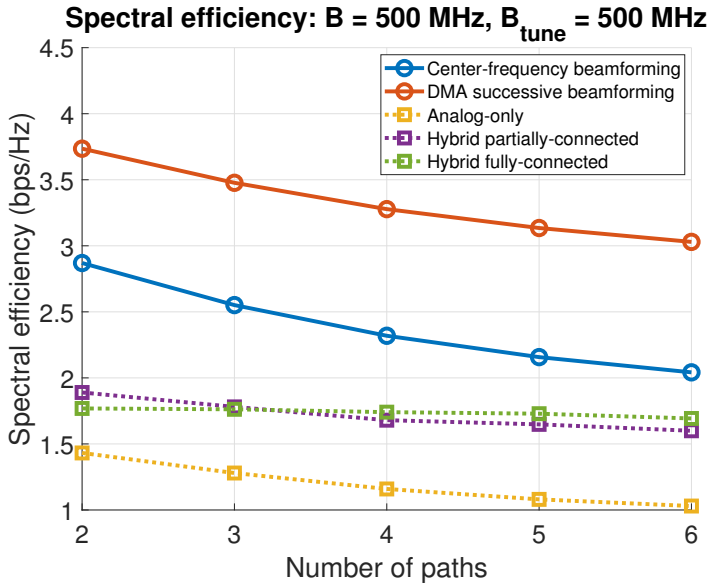


Figure 3.10. Average spectral efficiency for a multipath channel environment as a function of the number of channel paths. We find that the proposed DMA successive beamforming algorithm provides the best performance across every number of channel paths.

across every number of channel paths. Notably, as the number of channel paths increases, the gap between the DMA successive beamforming algorithm and the center-frequency beamforming algorithm also grows wider. This shows how the successive beamforming algorithm adapts better to a more complicated channel environment with multipath and additional frequency-selectivity. Similar to the results in Fig. 3.9, the large performance difference between the DMA successive beamforming algorithm and the hybrid architecture lies mostly in the component loss for the integrated phase shifters and power dividers. Since the partially-connected architecture contains fewer power dividers than the fully-connected case, this is also why the partially-connected architecture outperforms the fully-connected architecture for the scenario with two paths. In summary, both Figs. 3.9 and 3.10 demonstrate the resilience of the proposed beamforming algorithm to complicated channel environments, showing that DMAs provide a promising alternative to hybrid arrays for wideband wireless communications.

3.8 Conclusions and future work

In this chapter, we analyzed how DMA design characteristics impact DMA beamforming gain for large signal bandwidths. With the exception of very small signal bandwidths, we found that the frequency-selective DMA resonance, wireless channel, and waveguide channel effects cannot be neglected since the per-subcarrier beamforming gain degrades quickly outside the center frequency. We also showed that reducing the DMA element spacing can help decrease the amount of frequency-selectivity and improve the beamforming gain. Moreover, we illustrated how the tuning bandwidth plays a crucial role in maximizing the DMA performance by allowing for the entire set of Lorentzian-constrained weights to be available for beamforming. Lastly, we proposed a successive DMA beamforming algorithm that significantly improved the wideband DMA data rates by configuring the DMA elements to consider their frequency-selective response and the previously-configured DMA elements. We also demonstrated the effectiveness of the proposed algorithm in a multipath setting to show how the proposed algorithm can continue to improve spectral efficiency in complicated channel environments. A major limitation of our work is the that the DMA beamforming gain approximation was derived solely for a LOS channel. In future work, we plan to generalize the DMA approximation approach to non-LOS channels, which is non-trivial due to the additional frequency-selectivity and fading from a multi-path environment. We also plan to extend the successive beamforming algorithm to consider more complex optimization algorithms, which is challenging due to the non-convex nature of optimizing spectral efficiency under the Lorentzian-constrained weights.

Appendix

3.8.1 Proof of Lemma 2

We derive here the frequency-selective Lorentzian constraint. We begin with the formulation of the magnetic polarizability in (3.16). We omit the dependence of the magnetic polarizability $\bar{\alpha}_{\mathsf{M}}$ and Ψ on the subcarrier frequency and resonant frequency for brevity. We then

apply the identity $\cos(\Psi) = 1 - 2\sin^2(\frac{\Psi}{2})$ to rewrite (3.16) as

$$\bar{\alpha}_{\mathsf{M}} = \left(1 - 2\sin^2\left(\frac{\Psi}{2}\right)\right) e^{\mathsf{j}(\Psi - \frac{\pi}{2})}. \tag{3.39}$$

We then use the identity $\sin^2(\frac{\Psi}{2}) = \left(\frac{e^{\mathsf{j}\frac{\Psi}{2}} - e^{-\mathsf{j}\frac{\Psi}{2}}}{2\mathsf{j}}\right)^2$ to obtain

$$\bar{\alpha}_{\mathsf{M}} = -\frac{\mathsf{j}\left(1 + e^{\mathsf{j}2\Psi}\right)}{2}. \tag{3.40}$$

3.8.2 Proof of Lemma 3

We now define an approximation for the beamforming gain of a DMA. We omit the frequency-selectivity of the channel and DMA beamformer for brevity in this derivation. To derive the beamforming gain $|\mathbf{h}^{\mathsf{T}}\mathbf{f}_{\mathsf{dma}}|^2$, we find that we can split up the beamforming gain into two terms as

$$|\mathbf{h}^{\mathsf{T}}\mathbf{f}_{\mathsf{dma}}|^2 = \left|-\frac{\mathsf{j}}{2}\mathbf{h}^{\mathsf{T}}\mathbf{1} - \frac{\mathsf{j}}{2}\mathbf{h}^{\mathsf{T}}e^{\mathsf{j}2\mathbf{\Psi}}\right|^2. \tag{3.41}$$

For a wavenumber k_0, we define the propagation angle $\phi_{\mathsf{g}} = \arcsin\left(\frac{\beta_{\mathsf{g}}}{k_0}\right)$ as the propagation lobe created by the effective channel $-\frac{\mathsf{j}}{2}\mathbf{h}^{\mathsf{T}}\mathbf{1}$, and the main lobe as $-\frac{\mathsf{j}}{2}\mathbf{h}^{\mathsf{T}}e^{\mathsf{j}2\mathbf{\Psi}}$. We assume single-beam beamsteering to steer a main lobe in a desired direction ϕ_{t} for an LOS channel. We model the effective channel for the phase φ_{o} as $\mathbf{h} = [e^{\mathsf{j}0\varphi_{\mathsf{o}}}, e^{\mathsf{j}1\varphi_{\mathsf{o}}}, \ldots, e^{\mathsf{j}(N_{\mathsf{slot}}-1)\varphi_{\mathsf{o}}}]^T$. The effective channel phase is given by wireless channel and DMA channel phases as

$$\varphi_{\mathsf{o}} = d_{\mathsf{x}}\left(\frac{2\pi f_{\mathsf{t}}}{c}\sin\phi_{\mathsf{t}} + \beta_{\mathsf{g}}\right). \tag{3.42}$$

The normalized propagation lobe term $G_{\mathsf{p}}(\phi_{\mathsf{t}}) = -\frac{\mathsf{j}}{2}\mathbf{h}^{\mathsf{T}}\mathbf{1}$ can then be written as

$$G_{\mathsf{p}}(\phi_{\mathsf{t}}) = \frac{1}{N_{\mathsf{slot}}} \sum_{n=1}^{N_{\mathsf{slot}}} e^{\mathsf{j}(n-1)\varphi_{\mathsf{o}}}$$
$$= e^{\mathsf{j}\frac{(N_{\mathsf{slot}}-1)\varphi_{\mathsf{o}}}{2}} \frac{1}{N_{\mathsf{slot}}} \frac{\sin\frac{N_{\mathsf{slot}}}{2}\varphi_{\mathsf{o}}}{\sin\frac{1}{2}\varphi_{\mathsf{o}}}. \quad (3.43)$$

In the limit of a large number of elements as $N_{\mathsf{slot}} \to \infty$, the magnitude of the propagation lobe term forms an infinitely thin sinc function and can be approximated as [92]

$$\lim_{N_{\mathsf{slot}}\to\infty} |G_{\mathsf{p}}(\phi_{\mathsf{t}})| \approx \begin{cases} 1, & \text{if } \phi_{\mathsf{t}} = \phi_{\mathsf{g}}, \\ 0, & \text{if } \phi_{\mathsf{t}} \neq \phi_{\mathsf{g}}. \end{cases} \quad (3.44)$$

Therefore, we find that for a sufficiently large N_{slot} and $\phi_{\mathsf{t}} \neq \phi_{\mathsf{g}}$, the propagation lobe term $G_{\mathsf{p}}(\phi_{\mathsf{t}}) \approx 0$ and

$$\left|\mathbf{h}^{\mathsf{T}}\mathbf{f}_{\mathsf{dma}}\right|^2 \approx \left|\frac{1}{2}\mathbf{h}^{\mathsf{T}}e^{\mathsf{j}2\mathbf{\Psi}}\right|^2. \quad (3.45)$$

We can also avoid the propagation lobe altogether with the condition $\beta_{\mathsf{g}} > k_0$ to ensure that the beamforming gain due to the propagation lobe is very small, since $\phi_{\mathsf{g}} = \arcsin\left(\frac{\beta_{\mathsf{g}}}{k_0}\right) \in \mathbb{C}$. For now, we assume that $\beta_{\mathsf{g}} > k_0$ and N_{slot} is sufficiently large such that (3.45) holds.

3.8.3 Proof of Lemma 4

We derive an approximation for the angle Ψ. We apply a Taylor series expansion to the polarizability function in (3.10) around $f = f_{\mathsf{r},n}$. Let $\Psi(f) = \arctan\left(\frac{2\pi(f_{r,n}^2 - f^2)}{\Gamma f}\right)$. We obtain

$$\Psi(f) = \Psi(f_{\mathsf{r},n}) + \Psi'(f_{\mathsf{r},n})(f - f_{\mathsf{r},n}) + O(f^2). \quad (3.46)$$

It can be verified that $\Psi(f_{\mathsf{r},n}) = \arctan(0) = 0$ and $\Psi'(f_{\mathsf{r},n}) = -\frac{4\pi}{\Gamma}$.

3.8.4 Proof of Lemma 5

We determine an approximation for the impact of frequency selectivity on the DMA beamforming gain. Based on the channel phase in (3.25) and the linear DMA weight approximation in (3.20), we can decompose the frequency-selective DMA beamforming gain as

$$F_{\mathsf{freq}}(f_k) = \left| \frac{1}{2} \frac{1}{\sqrt{N_{\mathsf{slot}}}} \sum_{n=1}^{N_{\mathsf{slot}}} e^{\mathsf{j}\frac{8\pi\Delta_k}{\Gamma}} e^{\mathsf{j}(n-1)\chi_{\mathsf{o}}[k]} \right|^2, \tag{3.47}$$

which simplifies to

$$F_{\mathsf{freq}}(f_k) = \left| \frac{1}{2} \frac{1}{\sqrt{N_{\mathsf{slot}}}} \frac{\sin\left(\frac{N_{\mathsf{slot}}}{2}\chi_{\mathsf{o}}[k]\right)}{\sin\left(\frac{1}{2}\chi_{\mathsf{o}}[k]\right)} \right|^2. \tag{3.48}$$

3.8.5 Proof of Lemma 6

We determine the impact of the tuning bandwidth and available DMA weights on the DMA beamforming gain. For a given weight fill ratio, we assume the center-frequency DMA beamformer and assume any channel phase outside the Lorentzian-constrained weight range maps to the outermost DMA weight, as this minimizes the phase error between the two weights. We assume there to be no waveguide attenuation.

First, we define the phase term of the feasible DMA weights with a certain weight fill ratio as

$$\mathcal{W} = \left\{ e^{-\mathsf{j}\frac{\pi}{2}} e^{\mathsf{j}\delta} \ : \delta \in [-\xi, \xi] \right\}. \tag{3.49}$$

Next, we assume that the channel weights are uniformly sampled on the complex unit circle such that $|h_n| = 1, \angle h_n \in U(0, 2\pi]$. We justify this assumption based on the channel weight formulation. The channel weights sample the complex unit circle based on the array steering vector in (3.6) and the DMA waveguide channel in (3.7). The phase advance for the channel φ_{o} in (3.42) is nonzero for $\phi_{\mathsf{t}} \neq \phi_{\mathsf{g}}$, meaning there will always be a phase advance between DMA elements as $\varphi_{\mathsf{o}} \neq 0$. As the number of elements N_{slot} increases, the number of samples increases and begins to approach a uniform sampling of the complex unit circle. Then, the proportion of

channel weights h_n within the feasible DMA weights $\mathcal{W}$ is approximately equal to the normalized arc length of $\mathcal{W}$ as $\frac{\xi}{\pi}$.

Given this uniform sampling assumption, we define the beamforming gain for the DMA beamformer in three different regions of interest. Since losses due to the amplitude distribution of the DMA weights is incorporated in (3.26), we assume a unit-amplitude DMA beamformer given by $w_n \in \mathcal{W}$ to isolate the effects of the phase mismatch between the DMA beamformer and channel.

- $h_n \in \mathcal{W}$: Here, the effective channel phase lies within the DMA feasible weights, allowing $h_n w_n = 1$.

- $h_n \notin \mathcal{W}$ and $\mathsf{Re}\{h_n\} \geq 0$: The effective channel phase lies outside the DMA feasible weights leading to a phase mismatch. The effective channel phase will configure the DMA element to map to the outermost weight in the righthand side of the complex plane. The beamforming gain is then $h_n w_n = h_n e^{-\mathsf{j}\frac{\pi}{2}} e^{\mathsf{j}\xi}$.

- $h_n \notin \mathcal{W}$ and $\mathsf{Re}\{h_n\} < 0$: The effective channel phase lies outside the DMA feasible weights and in the lefthand side of the complex plane. Similar to the prior region, the beamforming gain is then $h_n w_n = h_n e^{-\mathsf{j}\frac{\pi}{2}} e^{-\mathsf{j}\xi}$.

We take the average value of the beamforming gain normalized by the number of elements N_{slot} for these three regions as the beamforming gain term due to an incomplete weight fill, defined by

$$W_{\mathsf{fill}}(\xi) = \left| \frac{1}{2\pi} \left\{ \int_{-\frac{\pi}{2}-\xi}^{-\frac{\pi}{2}+\xi} 1 dz + \int_{-\frac{\pi}{2}+\xi}^{\frac{\pi}{2}} e^{-\mathsf{j}\frac{\pi}{2}} e^{\mathsf{j}\xi} e^{-\mathsf{j}z} dz + \int_{-\frac{3\pi}{2}}^{-\frac{\pi}{2}-\xi} e^{-\mathsf{j}\frac{\pi}{2}} e^{-\mathsf{j}\xi} e^{-\mathsf{j}z} dz \right\} \right|^2 = \left| \frac{1}{2\pi} \left(2\sin(\xi) + 2\xi \right) \right|^2 . \quad (3.50)$$

3.8.6 Proof of Lemma 7

We derive an expression for the impact of the waveguide field attenuation on the resulting DMA beamforming gain. The penalty term $A_{\mathsf{leak}}(\Lambda)$ from (3.29) is simplified as

$$A_{\mathsf{leak}}(\Lambda) = \frac{\left|\sum_{n=1}^{N_{\mathsf{slot}}} e^{-\bar{\alpha}_{\mathrm{g}}[k]d_{\mathrm{x}}(n-1)}\right|^2}{N_{\mathsf{slot}} \sum_{n=1}^{N_{\mathsf{slot}}} \left|e^{-\bar{\alpha}_{\mathrm{g}}[k]d_{\mathrm{x}}(n-1)}\right|^2}. \tag{3.51}$$

We find that both the numerator and denominator have the form of a geometric series that is simplified as

$$A_{\mathsf{leak}}(\Lambda) = \frac{\left|\frac{1-e^{-\bar{\alpha}_{\mathrm{g}}d_{\mathrm{x}}(N_{\mathsf{slot}}-1)}}{1-e^{-\bar{\alpha}_{\mathrm{g}}d_{\mathrm{x}}}}\right|^2}{N_{\mathsf{slot}}\frac{1-e^{-2\bar{\alpha}_{\mathrm{g}}d_{\mathrm{x}}(N_{\mathsf{slot}}-1)}}{1-e^{-2\bar{\alpha}_{\mathrm{g}}d_{\mathrm{x}}}}} = \frac{\tanh\left(\frac{-\bar{\alpha}_{\mathrm{g}}(N_{\mathsf{slot}}-1)d_{\mathrm{x}}}{2}\right)}{N_{\mathsf{slot}}\tanh(\frac{-\bar{\alpha}_{\mathrm{g}}d_{\mathrm{x}}}{2})}. \tag{3.52}$$

Lastly, we have defined the waveguide attenuation constant $\bar{\alpha}_{\mathrm{g}}$ to ensure that a specified fraction of radiated power Λ is met as $e^{-2\bar{\alpha}_{\mathrm{g}}(N_{\mathsf{slot}}-1)d_{\mathrm{x}}} = 1-\Lambda$. We can then solve for $\bar{\alpha}_{\mathrm{g}}$ as $\bar{\alpha}_{\mathrm{g}} = -\frac{\ln(1-\Lambda)}{2(N_{\mathsf{slot}}-1)d_{\mathrm{x}}}$. Plugging this back into (3.52) gives

$$A_{\mathsf{leak}}(\Lambda) = \frac{\tanh\left(\frac{\ln(1-\Lambda)}{4}\right)}{N_{\mathsf{slot}}\tanh\left(\frac{\ln(1-\Lambda)}{4(N_{\mathsf{slot}}-1)}\right)}. \tag{3.53}$$

As N_{slot} grows larger, we make the approximation that $\tanh(x) = x + O(x^2),\ x << 1$ and $\frac{N_{\mathsf{slot}}-1}{N_{\mathsf{slot}}} \approx 1$ to obtain the final expression

$$A_{\mathsf{leak}}(\Lambda) \approx \frac{4}{\ln(1-\Lambda)}\tanh\left(\frac{\ln(1-\Lambda)}{4}\right). \tag{3.54}$$

Publication Acknowledgment

Chapter 3, in full, is a reprint of the material as it appears in J. M. Carlson, N. V. Deshpande, M. R. Castellanos, and R. W. Heath, "Wideband Dynamic Metasurface Antenna Performance With Practical Design Characteristics," *IEEE Transactions on Wireless Communications*, vol. 25,

pp. 4674–4690, 2026. The dissertation author was the primary investigator and author of this paper.

Chapter 4

Advanced array processing for nullsteering and DOA estimation with dynamic metasurface antennas

4.1 Overview

In this chapter, we extend the previous work on beamforming to include placing nulls within the beam pattern and the localization of sources through DOA estimation with DMAs. Since pattern nulls are very sensitive to inaccuracies in the antenna weight model, we build up a machine learning model to predict the beam pattern of a DMA based on a set of varactor capacitances. This allows for the accurate placement of deep nulls, despite both external mutual coupling between elements and internal coupling of DMA elements through the waveguide. Using pattern nulls, we also propose a methodology for DOA estimation by leveraging a pre-defined set of null scans that detects dips in the received power.

4.2 Introduction

Reconfigurable antennas allow wireless communication systems to adapt the antenna electromagnetic properties in real time to dynamic propagation environments. Among the various reconfigurable antenna technologies, dynamic metasurface antennas (DMAs) are a type of slotted-waveguide antenna that provides electronically steerable beamforming through arrays

of sub-wavelength resonant elements [34]. Each DMA element is equipped with low-power tunable components, such as a varactor or p-i-n diodes, that control the element resonant frequency and adjust both the radiated amplitude and phase [1, 93]. Low-power digital-to-analog converters (DACs) set bias voltages on passive varactors to configure the beamforming weights. This approach provides cost-effective and energy-efficient beamforming compared to conventional phased arrays that rely on phase shifters or fully-digital architectures [34, 86]. These advantages make DMAs well-suited for energy-constrained systems such as mobile ad hoc networks (MANETs), where both interference management and low power consumption are critical.

While DMAs offer hardware and power consumption advantages, using them for advanced array processing presents several challenges. In wireless networks with multiple users and potential jammers, the receiver may form directive beams toward desired users while simultaneously placing deep nulls in the directions of interferers. Conventional adaptive beamforming methods can achieve this through both amplitude and phase control of the antenna weights, placing up to $N - 1$ nulls with N elements [94]. For phased arrays with unit-amplitude weight constraints, the nullsteering problem becomes more complicated and typically requires iterative algorithms [45, 95, 96]. DMAs impose an even more restrictive weight constraint because each resonant element has a coupled amplitude-phase response. Internal waveguide scattering further limits the achievable beam patterns and introduces mutual coupling that can degrade nulls if not properly accounted for. In addition, direction-of-arrival (DOA) estimation is essential for locating both target and interfering users, yet classical DOA algorithms such as multiple signal classification (MUSIC) are inapplicable to DMAs due to the single-port architecture. New solutions are therefore required to enable a complete DMA-based wireless system capable of high-performance adaptive beam pattern shaping and robust DOA estimation.

4.2.1 Prior work

DMA elements consist of electrically small, complementary-electric LC resonators etched into a waveguide or planar aperture. Foundational work modeled each element as a magnetic dipole characterized by a Lorentzian-constrained polarizability, which describes its frequency-selective resonant response [34, 42]. Early beamforming strategies mapped desired array weights onto the Lorentzian-constrained DMA weights through projection techniques [34]. Experimental validation of varactor-based DMAs demonstrated accurate electronic beam steering with continuous tuning [1, 35], while p-i-n diode-based designs enabled beamsteering through binary reconfigurability for a simpler control architecture [97, 29, 36, 98]. Beyond communications, DMAs have been applied to computational microwave imaging, including synthetic aperture radar [38], 2D aperture imaging [99], and near-field 3D reconstruction [100]. More sophisticated signal processing algorithms have since been developed to configure DMA weights for spectral efficiency maximization [39, 58], energy efficiency maximization in massive MIMO systems [41], and hybrid precoding with limited RF chains, as in our prior work [91, 101]. Despite the Lorentzian weight constraint, these studies have demonstrated that DMA-based systems can approach the spectral efficiency of conventional phased arrays.

A common limitation of the work in [39, 58, 41] is that the DMA is modeled solely by the Lorentzian-constrained antenna weights, neglecting internal waveguide scattering and its impact on the effective beam pattern. In our prior work [84], we extended the DMA model to account for forward and backward scattering within the waveguide through transfer matrix formulations. While this scattering-aware analytical model improves the prediction of the main lobe, it still does not fully capture the mutual coupling between DMA elements. This coupling is configuration-dependent and changes with every new set of varactor states, making the analytical model particularly unreliable for predicting the fine structure of the beam pattern, including null locations and depths. This limitation is especially problematic for nullsteering, where even small modeling errors can degrade the null depth by tens of decibels. Prior work [39, 58, 41] also relies

solely on analytical models for evaluation without validation through electromagnetic simulations or experimental measurements. Related work on multi-user MIMO interference management with DMAs [77, 102] similarly lacks electromagnetic simulation or experimental verification. Our prior conference paper [103] demonstrated DMA nullsteering verified through full-wave electromagnetic simulations, showing that a 16-element DMA can achieve 20–52 dB peak-to-null ratios. Concurrent work in [104] has since demonstrated an end-to-end DMA wireless system prototype with up to 43 dB beam-to-jammer discrimination, further validating the feasibility of DMA-based interference mitigation. This chapter extends [103] by introducing machine learning to bridge the gap between the analytical model and true electromagnetic behavior.

Machine learning (ML) has been increasingly applied to antenna design and array signal processing. Neural networks have been used to predict radiation patterns [105, 106] and synthesize beam coefficients that account for mutual coupling [107, 108]. For reconfigurable antenna systems, ML has been employed to predict performance from geometric and switching parameters, including portable devices [109], compact frequency-reconfigurable designs [110], and wearable 5G antennas [111]. Prior ML work on reconfigurable antennas [105, 107, 108, 106, 109, 110, 111], however, has not addressed DMA-specific constraints such as Lorentzian weights and configuration-dependent coupling. Existing ML approaches for phased arrays predict weights or patterns from independent per-element controls, whereas DMA elements are coupled through the shared waveguide, requiring models that capture configuration-dependent inter-element interactions. The Lorentzian weight constraint and configuration-dependent coupling create a nonlinear mapping from varactor states to beam patterns that analytical models approximate poorly but neural networks can learn from simulation data. In this chapter, we train an ensemble of multilayer perceptron (MLP) models on full-wave simulation data to predict beam patterns from DMA element configurations. The ML-based predictions account for the full electromagnetic behavior of the DMA, including mutual coupling, and allow accurate null placement that the analytical model alone cannot achieve.

Accurate beam pattern prediction also enables DOA estimation with the DMA. Direction-

of-arrival estimation is a well-studied problem in array signal processing. Classical algorithms such as MUSIC provide high-resolution estimates for fully-digital arrays with independent access to each element's received signal [94, 46]. For single-port or reduced-RF-chain architectures, however, the full array covariance matrix is not directly accessible, necessitating alternative approaches. Reactance-domain MUSIC was developed for electronically steerable parasitic array radiator (ESPAR) antennas, which cycle through multiple reactive load configurations to construct a virtual covariance matrix from sequential single-port measurements [112, 113]. Similar approaches have been adapted for composite right/left-handed (CRLH) leaky-wave antennas, where voltage tuning of metamaterial unit cells provides the pattern diversity needed for DOA estimation [114]. For DMAs specifically, recent work has adapted beam-space MUSIC by cycling through multiple DMA configurations to construct a virtual array [115, 116]. These approaches, however, require signal stationarity across all DMA reconfigurations, covariance matrix estimation from repeated measurement cycles, and known pilot signals from cooperative sources. These requirements limit their applicability to controlled communication scenarios and preclude their use for detecting uncooperative interferers or jammers. In this chapter, we propose a null-scanning DOA estimation method that identifies source directions from power dips caused by sequentially steering nulls across the angular domain. The proposed approach eliminates the need for signal stationarity, covariance estimation, and pilot information.

4.2.2 Contributions

In this chapter, we develop a machine learning-based framework for advanced array processing with DMAs that simultaneously steers beams and places deep nulls. All training data and validation results in this chapter come from full-wave electromagnetic simulations in Ansys HFSS, which captures mutual coupling and waveguide scattering that prior DMA signal processing studies omit. The key contributions are summarized as follows.

- We extend the analytical DMA weight model from [34, 42] to include transfer matrix-based waveguide scattering and connect it to the Lorentzian weight constraint, providing a unified

model for DMA beam pattern computation. We show that while this analytical model accurately predicts the main lobe, it often fails to capture null locations and depths due to unmodeled mutual coupling, motivating the need for machine learning.

- We propose an ML-based beam pattern prediction approach using an ensemble of MLP models trained on full-wave simulation data. The ML model takes the analytical model predictions as a physically informed input and learns residual coupling corrections that allow accurate null prediction beyond what the analytical model alone can achieve.

- We introduce a null-scanning DOA estimation algorithm for DMAs that estimates the directions of arrival of multiple sources from sequential received power measurements through a single RF chain, without requiring a covariance matrix. To the best of our knowledge, no prior DMA-based DOA method combines power-only measurements, covariance-free operation, and independence from pilot signals.

- Through full-wave electromagnetic simulations in HFSS, we show that a 10-element DMA can simultaneously steer a beam and place up to three nulls with depths near -20 dBi and sub-degree angular accuracy. For DOA estimation, the null-scanning method detects up to four sources at moderate SNR with detection probability approaching that of conventional MUSIC applied to a 10-element fully digital array.

Our results demonstrate that a 10-element DMA can reliably locate sources and steer simultaneous beams and nulls with performance approaching that of conventional arrays, while using a single RF chain. The remainder of this chapter is organized as follows. Section 4.3 presents the DMA weight model with transfer matrix-based scattering. Section 4.4 describes the ML beam pattern prediction approach. Section 4.5 introduces the null-scanning DOA estimation algorithm. Section 4.6 evaluates the adaptive nullsteering performance. Section 4.7 concludes the chapter.

4.3 DMA model and beamforming

This section presents the beamforming model for DMAs by defining the effective antenna weight for each element. As illustrated in Fig. 4.1, the proposed framework operates in two stages. The DOA estimation stage determines source locations by scanning nulls across the angular domain. The adaptive nullsteering stage then configures the DMA to steer a beam toward the target user while placing nulls at the estimated interferer directions. Both stages require an accurate relationship between the varactor capacitances and the resulting beam pattern, motivating the rigorous weight model developed in this section.

Given a DMA with N elements connected to a single RF chain, we address three interconnected problems. First, for a given set of varactor capacitances $\mathbf{c}_{\mathsf{var}} = [c_{\mathsf{var},0}, \ldots, c_{\mathsf{var},N-1}]^T$, we seek to accurately predict the resulting beam pattern $D(\theta, \mathbf{c}_{\mathsf{var}})$, which depends on the element radiation, internal waveguide scattering, and configuration-dependent mutual coupling. Second, K unknown sources at angles $\theta_0, \ldots, \theta_{K-1}$ transmit with unknown powers $P_0, \ldots, P_{K-1}$. The goal is to estimate their directions of arrival from sequential received power measurements through the single RF chain, without access to the full array covariance matrix or prior knowledge of K. Third, given a desired beam direction $\theta_{k^\star}$ for target user $k^\star$ and $K-1$ interferer directions θ_k for $k \neq k^\star$, the goal is to find a varactor configuration $\mathbf{c}^\star_{\mathsf{var}}$ that maximizes the gain $D(\theta_{k^\star}, \mathbf{c}^\star_{\mathsf{var}})$ while minimizing $D(\theta_k, \mathbf{c}^\star_{\mathsf{var}})$ for $k \neq k^\star$. This optimization is subject to the Lorentzian weight constraint and waveguide scattering effects. We consider the beam patterns at a single frequency in the far-field.

4.3.1 DMA weights

We first present the analytical model for the radiation and effective beamforming weights of DMA elements. Since we aim to accurately predict beam patterns and design beam patterns for DOA estimation and nullsteering, understanding the analytical weight model is crucial for establishing the relationship between the varactor capacitances and the resulting beam pattern.

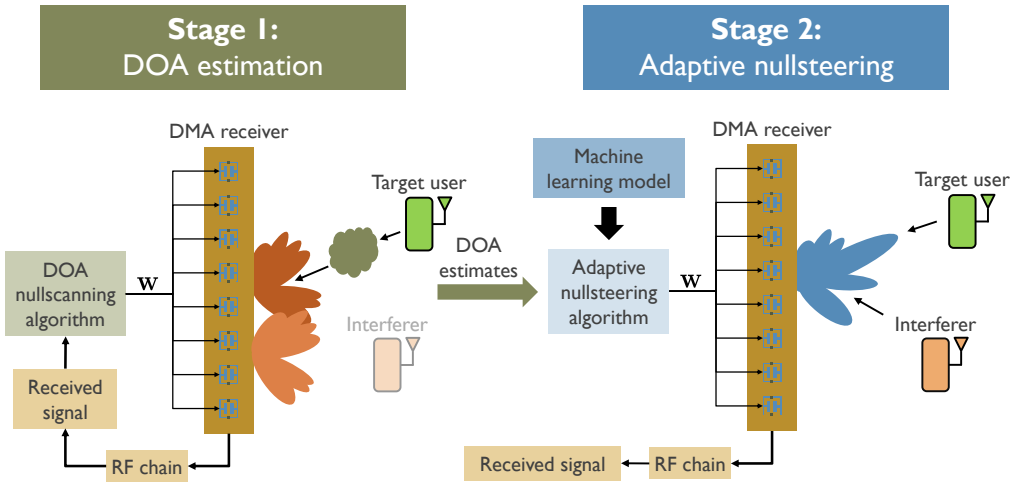


Figure 4.1. Overview of the DMA-based communication system for DOA estimation and adaptive nullsteering. The DMA receiver determines the location of various sources, and steers a beam toward the target user while placing nulls at the directions of interferers. The weight vector $\mathbf{w}$ is generated to configure the DMA elements connected to a single RF chain.

From a physics perspective, each DMA element can be modeled as a magnetic or electric dipole characterized by a frequency-dependent polarizability [34]. The polarizability depends on the coupling factor F_{coupl}, the damping factor Γ, and the resonant frequency $\mathrm{f}_{\mathrm{r},n}$ for the nth element, which is tunable through the integrated reconfigurable component. Assuming varactor diodes as the reconfigurable components for continuous tunability, the polarizability for a DMA dipole radiator is given as a function of the frequency f by [34],

$$\alpha(\mathrm{f}, \mathrm{f}_{\mathrm{r},n}) = \frac{(2\pi \mathrm{f})^2 F_{\text{coupl}}}{(2\pi \mathrm{f}_{\mathrm{r},n})^2 - (2\pi \mathrm{f})^2 + \mathrm{j}\Gamma(2\pi \mathrm{f})}. \tag{4.1}$$

The polarizability determines the amplitude and phase of radiation from each DMA element, serving as the physical mechanism through which beamforming weights are controlled. As the resonant frequency changes, the magnitude and phase of α in (4.1) change accordingly. Tuning the resonant frequency therefore alters the radiation from the nth DMA element, which allows for beamforming across the array.

The polarizability in (4.1) depends on the resonant frequency $\mathrm{f}_{\mathrm{r},n}$, which is determined by

the varactor capacitance $c_{\mathsf{var},n}$ through a geometry-dependent mapping $\mathrm{f}_{\mathsf{r},n} = \mathrm{f}_{\mathsf{r}}(c_{\mathsf{var},n})$. Since the operating frequency f_{t} is fixed, the polarizability for the nth element is ultimately a function of its varactor capacitance as $\alpha_n = \alpha(\mathrm{f}_{\mathsf{t}}, \mathrm{f}_{\mathsf{r}}(c_{\mathsf{var},n}))$. For brevity, we use the subscript n throughout to denote quantities evaluated at the nth element's varactor state. Moreover, the polarizability α can refer to both the electric α_{e} or magnetic α_{m} polarizability of a DMA element, depending on which dominates the radiation. We discuss this topic further in this section.

While (4.1) provides a useful model for DMA element radiation, it is incomplete for describing the full effective antenna weights. As a slotted-waveguide antenna, each DMA element scatters a portion of the incident waveguide fields both forward and backward within the waveguide, in addition to radiating into free space. These scattered fields reach adjacent elements and modify their effective antenna weights, introducing inter-element dependencies that (4.1) does not account for. Furthermore, the values of F_{coupl} and Γ cannot be extracted analytically for a given DMA element geometry and must be obtained through full-wave simulations. To capture these effects, we extend the weight model with scattering parameters extracted from full-wave simulations.

We decompose the DMA effective antenna weight into two components: a reconfigurability term and a scattering term. The reconfigurability term captures the radiated amplitude and phase that depends purely on the varactor diode state of the nth element, while the scattering term captures the forward and backward scattering from all elements based on their respective varactor states. To compute the reconfigurability term, we extract the backward scattering S_{11} and forward scattering S_{12} parameters from full-wave simulations of a DMA element at each desired varactor capacitance. For a waveguide with height b, width a, propagation constant β_{g}, and free-space propagation constant k_0, the magnetic and electric polarizabilities are then given by [42]

$$\alpha_{\mathsf{m},n} = \frac{\mathrm{j}ab}{2\beta_{\mathrm{g}}} \left(S_{11,n} + S_{12,n} - 1\right), \tag{4.2}$$

$$\alpha_{\mathsf{e},n} = \frac{\mathrm{j}ab\beta_{\mathrm{g}}}{2k_0^2} \left(-S_{11,n} + S_{12,n} - 1\right). \tag{4.3}$$

Eqs. (4.2) and (4.3) define the reconfigurability term for the nth DMA element, capturing how the radiated amplitude and phase change as a function of the varactor capacitance $c_{\mathsf{var},n}$. Here, $S_{11,n}$ and $S_{12,n}$ are the backward and forward scattering parameters of the nth DMA element, which describe the fraction of the guided wave reflected and transmitted at each element for a given varactor capacitance. Both expressions require these scattering parameters to be extracted from full-wave simulations for each capacitance value, since they cannot be obtained analytically for a given element geometry. The choice between the magnetic polarizability in (4.2) and the electric polarizability in (4.3) depends on the orientation of the DMA element relative to the waveguide fields. For the remainder of this section, we use a general polarizability α to represent either case.

Next, we define the scattering term through transfer matrices that capture the cascaded scattering across all elements. Unlike conventional arrays where mutual coupling is modeled through an impedance or coupling matrix, DMA elements share a single waveguide, creating cascaded scattering interactions that the transfer matrix formulation captures through a recursive structure. The forward and backward scattering from one element causes adjacent elements to re-radiate, producing a recursive chain of interactions along the waveguide. Let x_n denote the position of the nth element along the array, let $\mathbf{P}_n = \mathrm{diag}(e^{-\mathrm{j}\beta_{\mathsf{g}}(x_{n+1}-x_n)},\, e^{+\mathrm{j}\beta_{\mathsf{g}}(x_{n+1}-x_n)})$ denote a propagation matrix, and let

$$\mathbf{S}_n = \frac{1}{S_{12,n}} \begin{bmatrix} S_{12,n}^2 - S_{11,n}^2 & S_{11,n} \\ -S_{11,n} & 1 \end{bmatrix} \tag{4.4}$$

be a scattering parameter matrix. The transfer matrix for each DMA element is then $\mathbf{T}_n = \mathbf{P}_n\mathbf{S}_n$ [117]. To obtain the forward F_n and backward B_n scattering coefficients, we apply a recursive formulation. We first compute the total transfer matrix as $\mathbf{T}_{\mathsf{total}} = \mathbf{T}_{N-1}\mathbf{T}_{N-2}\cdots\mathbf{T}_0$, and then

use the boundary conditions $F_0 = 1$ and $B_{N-1} = 0$ to solve for B_0 via

$$\begin{bmatrix} F_{N-1} \\ B_{N-1} \end{bmatrix} = \mathbf{T}_{\mathsf{total}} \begin{bmatrix} F_0 \\ B_0 \end{bmatrix}. \tag{4.5}$$

Given B_0 and F_0, we recursively solve for all F_n and B_n values through

$$\begin{bmatrix} F_{n+1} \\ B_{n+1} \end{bmatrix} = \mathbf{T}_n \begin{bmatrix} F_n \\ B_n \end{bmatrix}, \tag{4.6}$$

which fully describes the internal waveguide scattering and its impact on the effective antenna weights. Additional details on the transfer matrix formulation can be found in [117].

Combining the reconfigurability and scattering terms, the final effective weight for the nth DMA element is

$$w_n = \alpha_n \left(F_n + B_n e^{\mathrm{j}2\beta_{\mathrm{g}} x_n} \right). \tag{4.7}$$

The term $e^{\mathrm{j}2\beta_{\mathrm{g}} x_n}$ accounts for the phase correction associated with backward-propagating waves. We define the weight vector as $\mathbf{w} = [w_0, w_1, \ldots, w_{N-1}]^{\mathrm{T}}$. The weight in (4.7) reveals a key distinction from conventional phased arrays. Each element's effective weight w_n depends not only on its own varactor state through α_n, but also on the varactor states of all other elements through the scattering coefficients F_n and B_n. This inter-element coupling means that the DMA weights cannot be tuned independently, and changing a single varactor capacitance alters the effective weights across the entire array.

4.3.2 Beam pattern

With the effective weights defined, we now compute the directivity and realized gain for the DMA. For an operating wavelength λ, the array response at each element is

$$a_n(\theta) = e^{\mathrm{j}\frac{2\pi}{\lambda} x_n \sin\theta}. \tag{4.8}$$

The array factor, which combines the element weights with the array response and an element pattern $\Omega(\theta, \phi)$, is

$$M(\theta, \phi) = \Omega(\theta, \phi) \sum_{n=0}^{N-1} w_n a_n(\theta). \tag{4.9}$$

The directivity is then computed from the array factor as [69]

$$D(\theta, \phi) = \frac{|M(\theta, \phi)|^2}{\frac{1}{4\pi} \int_0^{\pi} \int_0^{2\pi} |M(\theta, \phi)|^2 \, \sin\theta \, d\theta \, d\phi}, \tag{4.10}$$

which characterizes the DMA beam pattern.

To obtain the realized gain, we incorporate the total efficiency of the DMA. The radiation efficiency η_{rad} accounts for dielectric and ohmic losses in the DMA element and is typically extracted from full-wave simulations. The matching efficiency η_{match} is computed from the final reflection and transmission coefficients of the entire DMA array, given by the transfer matrix outputs F_{N-1} and B_0 as $\eta_{\mathsf{match}} = 1 - |F_{N-1}|^2 - |B_0|^2$. The total efficiency is $\eta_{\mathsf{eff}} = \eta_{\mathsf{rad}}\eta_{\mathsf{match}}$, and the realized gain is

$$G(\theta, \phi) = \eta_{\mathsf{eff}} D(\theta, \phi). \tag{4.11}$$

The realized gain in (4.11) fully characterizes the DMA beam pattern while including any additional losses due to radiation or matching efficiency. Since the DMA is a linear array, we evaluate the beam pattern in the array plane and write $D(\theta) \equiv D(\theta, 0)$ for brevity in subsequent sections. Throughout this chapter, we refer to configuring the DMA to orient the main lobe of $D(\theta)$ toward a desired direction as beamsteering, and to configuring the DMA to place a pattern null at a desired direction as nullsteering. Both operations are performed by selecting the varactor capacitances that produce the corresponding beam pattern.

4.3.3 Relationship to the Lorentzian constraint

The polarizability model in (4.1) gives rise to a Lorentzian constraint on the set of achievable DMA weights, which is used in several signal processing papers to model the DMA

weights [41, 40, 39]. Here, we relate the scattering parameter model to this Lorentzian-constrained weight set to unify the two perspectives.

Let δ denote the phase offset between the maximum resonant frequency configuration and the operating frequency,

$$\delta = \angle\alpha(\mathrm{f_t}, f_{\mathsf{r,max}}) - \angle\alpha(\mathrm{f_t}, \mathrm{f_t}). \tag{4.12}$$

The term δ represents the physical limitations of the tuning range for an actual DMA element, where varactor diodes always have a limited capacitance range. Next, the Lorentzian constraint set can be derived from the polarizability as the resonant frequency is tuned while holding a constant operating frequency $\mathrm{f_t}$, and this is given as

$$\mathcal{Q} = \left\{ -\frac{\mathsf{j}}{2}\left(1 + e^{\mathsf{j}z}\right),\ z \in [-\pi + \delta, \pi - \delta] \right\}. \tag{4.13}$$

In (4.13), the term z represents an abstraction of the resonant frequency tunability of the DMA element, which changes the amplitude and phase of the radiated fields.

Next, the per-element forward and backward scattering can be determined from an analytical model, where A represents a scattering strength, as

$$S_{12} = \left\{ 1 - \frac{A}{2}\left(1 + e^{\mathsf{j}z}\right),\ A \in (0, 1], z \in [-\pi + \delta, \pi - \delta] \right\}, \tag{4.14}$$

$$S_{11} = \left\{ -\frac{A}{2}\left(1 + e^{\mathsf{j}z}\right),\ A \in (0, 1], z \in [-\pi + \delta, \pi - \delta] \right\}. \tag{4.15}$$

Using the scattering parameters in (4.14) and (4.15) to calculate the scattering coefficients with (4.6), we define the final, DMA element weights as

$$w_n = -\frac{\mathsf{j}}{2}\left(1 + e^{\mathsf{j}z_n}\right)\left(F_n + B_n e^{\mathsf{j}2\beta_{\mathrm{g}} x_n}\right). \tag{4.16}$$

Eq. (4.16) is an equivalent version of the DMA weights found in (4.7), but with abstractions

for the DMA tunability z and the scattering strength A, which are incorporated in the full-wave simulation results used to calculate (4.7). While we use (4.7) for this work, we include the Lorentzian-constrained form in (4.16) for consistency with other DMA-based work.

4.3.4 Mutual coupling in DMAs

Although the DMA weight model in (4.7) accounts for element radiation and internal waveguide scattering, it does not capture the external mutual coupling between DMA elements. For beamsteering, mutual coupling generally has a minimal impact on the main lobe, since small perturbations to the antenna weights do not significantly affect a high-gain beam. For nullsteering, however, mutual coupling is critical. A proper null requires the radiation from all array elements to cancel precisely at a particular angle, and even small deviations in the antenna weights can degrade the null depth by tens of decibels.

A standard approach to modeling mutual coupling is to introduce a coupling matrix into the array response vector and use the embedded element pattern $\Omega_{\mathsf{embed}}(\theta, \phi)$ in place of the isolated pattern [118]. The coupling matrix is typically derived from the mutual impedances between elements, which can be extracted through per-element port measurements [69]. For DMAs, however, this approach faces two fundamental obstacles. First, all elements share a single waveguide port, making it impossible to extract individual mutual impedances from scattering parameter measurements. Second, the mutual coupling is strongly configuration-dependent such that two adjacent elements with similar varactor states couple more strongly than elements with dissimilar states. This coupling is highly nonlinear and varies with every new set of varactor configurations, fundamentally different from conventional phased arrays where the element resonance characteristics are fixed.

This creates a fundamental challenge for DMA nullsteering, where accurate null placement requires modeling the mutual coupling, yet extracting a coupling matrix for DMA elements is impractical. This limitation motivates the use of machine learning to predict beam patterns directly from full-wave simulations. By training an ML model on many beam pattern samples

from a simulated DMA, the ML model can learn the coupling effects implicitly and obtain accurate beam pattern predictions for reliable nullsteering without explicit coupling matrix extraction. We describe this ML methodology in the following section.

4.4 Beam pattern prediction with machine learning

The ML model trains on ground-truth beam patterns from many electromagnetic simulations of a DMA array, learning the mutual coupling effects that the analytical model in (4.7) does not capture. Once trained, the model predicts beam patterns for arbitrary DMA configurations with sufficient accuracy for nullsteering and DOA estimation.

We design a DMA element and array in HFSS for ML training and DOA estimation. We target an operating frequency of $\mathrm{f_t} = 15$ GHz, similar to the design in [103]. We adopt a rotated element geometry that produces primarily an electric polarizability response, in contrast to the majority of prior work where DMA elements exhibit a magnetic dipole response. The rotated geometry yields a significantly narrower element beam pattern, which reduces mutual coupling between adjacent elements. We simulate the element across many varactor capacitance values to extract the scattering parameters and establish the relationship between varactor capacitance and DMA weight. Using these elements, we construct a 10×1 uniform linear array oriented along the x-direction with element spacing $d_{\mathrm{x}} = 0.525\lambda$, chosen to avoid internal waveguide resonances that degrade antenna efficiency [84].

To train the ML model, we generate a large dataset of ground-truth beam patterns by simulating many DMA configurations in the full-wave electromagnetic simulator HFSS. For each configuration, we use the weight model in (4.7) and a genetic algorithm to search for DMA weight configurations that place beams and nulls at various locations, then extract the resulting beam pattern $D_{\mathsf{em}}(\theta)$ from the HFSS simulation. We gather 6000 simulations in total for training.

With the training samples, we propose a residual MLP architecture that takes the analytical model predictions as an augmented input and learns to predict multiplicative corrections in

polar form to account for the unmodeled coupling effects. The MLP consists of three hidden layers with dimensions 256-512-256, using SiLU (Sigmoid Linear Unit) activation functions and residual skip connections. We train an ensemble of five independently initialized models to enable uncertainty quantification. For example, for a given DMA configuration, we compute the standard deviation of the predicted beam patterns across all ensemble members, which provides a measure of prediction confidence. Models that all ensemble members agree on are more likely to match the HFSS simulation, a property we exploit in the genetic algorithm for nullsteering optimization described in Section 4.6. Each model is trained for 400 epochs using the Adam optimizer.

For the ML model input, we provide the varactor diode capacitances $\mathbf{c}_{\mathsf{var}}$ and the analytical DMA weights $\mathbf{w}_{\mathsf{model}}$ from (4.7) as

$$\mathbf{q}_{\mathsf{input}} = \begin{bmatrix} \mathbf{c}_{\mathsf{var}} \\ \mathrm{Re}(\mathbf{w}_{\mathsf{model}}) \\ \mathrm{Im}(\mathbf{w}_{\mathsf{model}}) \end{bmatrix} \in \mathbb{R}^{3N}. \tag{4.17}$$

The ML model outputs a log-magnitude correction vector $\mathbf{r}_{\mathsf{ml}}$ and phase correction vector $\boldsymbol{\phi}_{\mathsf{ml}}$ relative to the analytical weights as

$$\mathbf{q}_{\mathsf{output}} = \begin{bmatrix} \log(\mathbf{r}_{\mathsf{ml}}) \\ \boldsymbol{\phi}_{\mathsf{ml}} \end{bmatrix} \in \mathbb{R}^{2N}, \tag{4.18}$$

These corrections produce the final ML-predicted weight

$$w_{\mathsf{ml},n} = |w_{\mathsf{model},n}| \cdot e^{\log r_{\mathsf{ml},n}} \cdot e^{\mathsf{j}(\angle w_{\mathsf{model},n} + \phi_{\mathsf{ml},n})}. \tag{4.19}$$

The training procedure computes the directivity $D_{\mathsf{ml}}^{\mathsf{dB}}$ from the ML-predicted weights $\mathbf{w}_{\mathsf{ml}}$ and compares it against the directivity $D_{\mathsf{em}}^{\mathsf{dB}}$ obtained from HFSS. Over N_s training samples, each

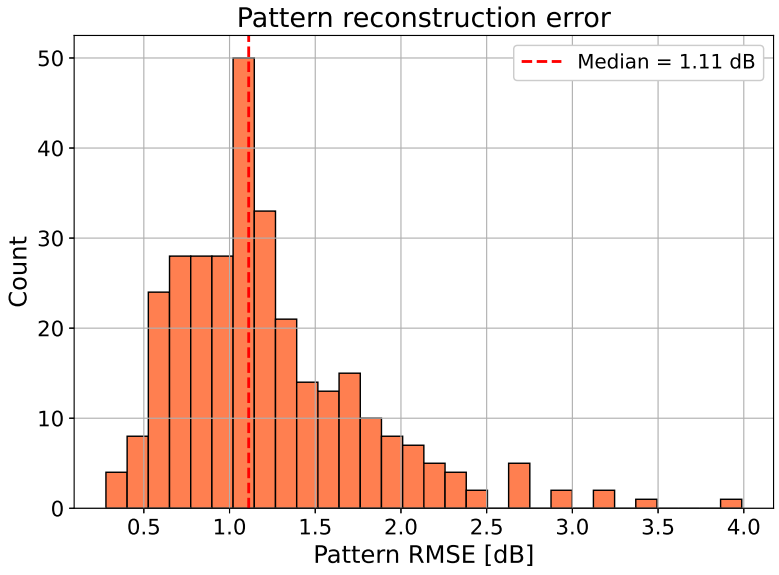
evaluated at N_p angular points, the training loss is defined as the mean squared error of the beam patterns and is given by

$$\mathcal{L} = \frac{1}{N_s} \sum_{s=0}^{N_s-1} \frac{1}{N_p} \sum_{p=0}^{N_p-1} \left(D^{\mathsf{dB}}_{\mathsf{ml},s}(\theta_p) - D^{\mathsf{dB}}_{\mathsf{em},s}(\theta_p) \right)^2 . \tag{4.20}$$

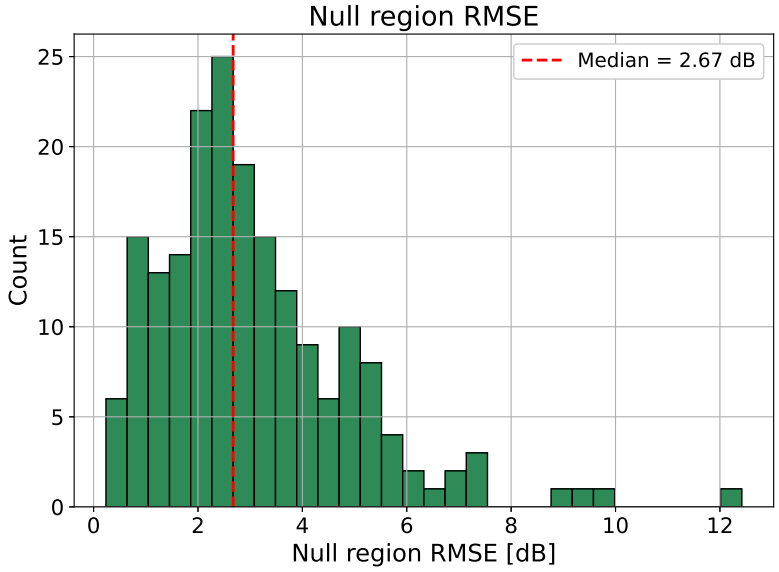
It is important to use a pattern-based loss function instead of a weight-based loss function, since accurate null prediction is the primary objective and training on weights alone does not guarantee accurate null prediction.

We now evaluate the trained ML model on a test set of 300 beam patterns that were not included in the training data. We also compare the ML model beam pattern predictions against the beam patterns from the analytical weight model. Figure 4.2(a) shows the pattern reconstruction error across all test samples using the ML model, while Fig. 4.2(b) shows the error specifically around pattern nulls, defined as any local minimum with gain below -15 dBi. We find that the ML model achieves a median root-mean-square error (RMSE) of 1.11 dB across the full pattern, compared to 4.85 dB for the analytical model. For the null regions specifically, the ML model achieves a median RMSE of 2.67 dB compared to 7.08 dB for the analytical model, confirming that the ML model captures the coupling-induced null behavior that the analytical model misses.

To illustrate the source of the ML model's improvement, we plot an example beam pattern and the corresponding weights in Fig. 4.3. We see in Fig. 4.3(a) that the ML-predicted pattern closely matches the HFSS ground truth, whereas the analytical model exhibits multiple sidelobe errors, including an incorrect null at -22° that does not appear in the HFSS simulation. This discrepancy is explained by examining the weights in Fig. 4.3(b), where the analytical model produces reasonable weights, but the absence of external coupling in the model leads to amplitude and phase errors relative to the ground-truth weights. The ML model learns these coupling effects and applies small corrections to the weight magnitudes and phases, yielding a beam pattern that closely reproduces the HFSS simulation. Figure 4.3(b) also highlights the



(a)

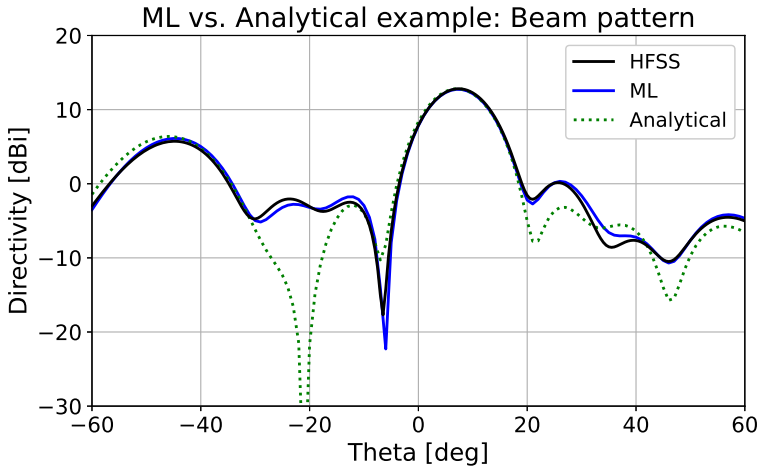


(b)

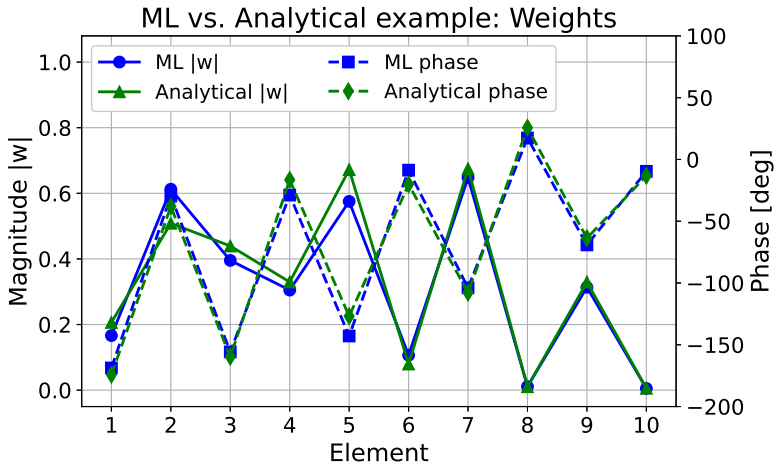
Figure 4.2. RMSE for (a) full pattern reconstruction and (b) null regions for 300 test beam patterns. The ML model achieves a median RMSE of 1.11 dB across the full pattern and 2.67 dB in null regions, compared to 4.85 dB and 7.08 dB for the analytical model.

importance of using the analytical model as a physically informed input to the ML model. With a solid basis for the weight amplitude and phase, the ML model can focus on learning the residual coupling corrections rather than predicting weights with no physical basis, substantially reducing

the amount of training data required.



(a)



(b)

Figure 4.3. Comparison of (a) beam patterns and (b) element weights for the HFSS simulation, ML prediction, and analytical model. The analytical model produces sidelobe errors and a spurious null near $-22°$ absent from the HFSS pattern. The ML model applies small corrections to the analytical weights, closely reproducing the HFSS ground truth.

Now that we have an accurate method to generate beam patterns that closely match electromagnetic simulations, we leverage the ML model for DOA estimation through null-scanning, and adaptive beam pattern optimization that places simultaneous beams and nulls at targeted locations.

4.5 DOA estimation with DMAs

We now use the ML model to address the problem of DOA estimation. Since all DMA elements share a single port, classical subspace methods such as MUSIC cannot be directly applied. In this section, we propose a DOA estimation algorithm that scans nulls across the angular domain to detect sources. The core idea is to generate DMA configurations that produce beam patterns with flat gain outside a sharp null at a specific angle. When a source is located at the null angle, the received power drops relative to the flat baseline, producing a measurable dip that indicates the presence of a source.

The DOA algorithm constructs the null-scanning beam patterns by steering nulls with the designed DMA across a uniform angular grid. Specifically, we define $C = 81$ configurations with directivity $D_c(\theta)$, each placing a null at a distinct angle within $\theta \in [-40^\circ, 40^\circ]$ at 1° intervals. We assume that all sources lie within this range. Using the ML model, we generate beam patterns with sharp, deep nulls centered at the desired angle while minimizing the pattern variation outside the null region to maintain a flat baseline. Pattern flatness is critical for producing unambiguous power dips and reducing false alarms. Figure 4.4 shows the resulting HFSS-simulated beam patterns, where the nulls scan uniformly across the angular range with deep nulls at the desired locations and relatively flat gain elsewhere.

We now define the received signal model for the DMA. The signal model consists of K sources at angles $\theta_0, \ldots, \theta_{K-1}$, each emitting a signal with power P_k. Let $s_k[\ell] \sim \mathcal{CN}(0,1)$ denote the unit-power signal from source k at sample ℓ, and let $v[\ell] \sim \mathcal{CN}(0,\sigma^2)$ denote the receiver noise with noise power σ^2. We represent the beam pattern for configuration c through the complex gain $h_c(\theta) = \sqrt{D_c(\theta)}e^{\mathrm{j}\phi_c(\theta)}$, where $\phi_c(\theta)$ is the phase of the electric fields obtained from HFSS. The received signal at the single RF output for configuration c is then

$$y_c[\ell] = \sum_{k=0}^{K-1} \sqrt{P_k} h_c(\theta_k) s_k[\ell] + v[\ell]. \tag{4.21}$$

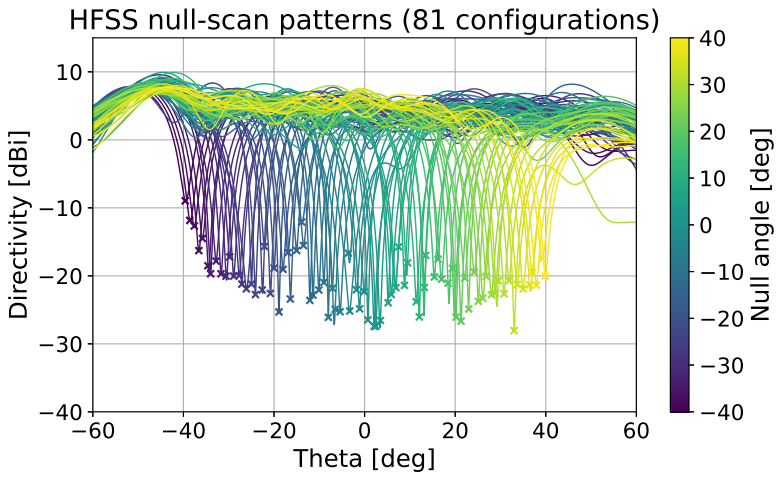


Figure 4.4. Null-scan beam patterns for the DMA-based DOA estimation algorithm with $C = 81$ configurations across $\theta \in [-40°, 40°]$ at $1°$ intervals. Each configuration places a deep null at a distinct angle while maintaining relatively flat gain elsewhere.

Since the DMA has a single RF output, the receiver measures the received power by averaging over L time samples per configuration as

$$\bar{P}_c = \frac{1}{L} \sum_{\ell=0}^{L-1} |y_c[\ell]|^2. \tag{4.22}$$

The algorithm subtracts the noise floor σ^2, estimated from the receiver noise figure and bandwidth, to form the noise-corrected received power $\tilde{P}_c = \max(\bar{P}_c - \sigma^2, 0)$ and define the measurement vector as

$$\tilde{\mathbf{P}} = [\tilde{P}_0, \ldots, \tilde{P}_{C-1}]^{\mathrm{T}}. \tag{4.23}$$

We use received power rather than complex voltage for DOA estimation because the single RF chain precludes forming a spatial covariance matrix across elements. While coherent voltage measurements would enable subspace-based methods such as MUSIC, this would require all DMA configurations to be measured within the coherence time of the source signals. This assumption may not hold for uncooperative interferers with unknown waveform characteristics, differentiating our approach from [115, 116]. The power-based approach requires only that the source powers and positions remain constant during the measurement period, making no

assumptions about source signal bandwidth, modulation, or symbol rate.

Next, using N_θ candidate angles for the DOA estimation, we create a beam pattern configuration matrix as

$$\mathbf{D} = \begin{bmatrix} |h_0(\theta_0)|^2 & |h_0(\theta_1)|^2 & \dots & |h_0(\theta_{N_\theta-1})|^2 \\ |h_1(\theta_0)|^2 & |h_1(\theta_1)|^2 & \dots & |h_1(\theta_{N_\theta-1})|^2 \\ \vdots & \vdots & \ddots & \vdots \\ |h_{C-1}(\theta_0)|^2 & |h_{C-1}(\theta_1)|^2 & \dots & |h_{C-1}(\theta_{N_\theta-1})|^2 \end{bmatrix}. \tag{4.24}$$

We then define the power vector $\mathbf{p} = [p_0, \dots, p_{N_\theta-1}]^{\mathrm{T}}$, where p_a is given by

$$p_a = \begin{cases} P_k & \text{if source } k \text{ is present at angle } \theta_a, \\ 0 & \text{otherwise,} \end{cases} \tag{4.25}$$

which represents a potential source at a certain location. We determine whether a source is at an angle by performing a non-negative least squares (NNLS) estimation [119] on the received power and source angles as

$$\hat{\mathbf{p}} = \underset{\mathbf{p}\geq 0}{\operatorname{argmin}} \left|\left| \tilde{\mathbf{P}} - \mathbf{D}\mathbf{p} \right|\right|_2^2. \tag{4.26}$$

The NNLS formulation simultaneously estimates the number, locations, and received powers of all sources. Source directions are extracted by detecting peaks in $\hat{\mathbf{p}}$ that exceed a threshold γ relative to the total estimated power. Specifically, the algorithm normalizes $\hat{\mathbf{p}}$ by its sum and detects local maxima above $\gamma = 0.1$. This total-power normalization renders the detection threshold independent of the number of sources, since each source contributes approximately $1/K$ of the total power regardless of K. Unlike subspace methods such as MUSIC, this approach requires no prior knowledge or estimation of the number of sources.

Next, we perform Monte Carlo simulations to characterize the detection probability and angular accuracy of the DOA estimation method as functions of K, L, and the input

signal-to-noise ratio (SNR) defined as SNR $= P_k/\sigma^2$. We use $N_{\mathsf{trial}} = 1000$ Monte Carlo trials for each parameter setting. In each trial, source angles θ_k are drawn uniformly from $[-40^\circ, 40^\circ]$ with a minimum separation of 3°, and all sources have equal power. We generate random source signals $s_k[\ell]$, noise realizations $v[\ell]$, compute the received power measurements across $C = 81$ null-scanning configurations, and solve the NNLS optimization over $N_\theta = 801$ candidate angles to obtain the estimated angles of arrival. We implement MUSIC with a conventional 10-element uniform linear array with half-wavelength spacing as a baseline for comparison.

Figure 4.5 shows the detection probability at low (-10 dB) and high (20 dB) SNR values as a function of the number of sources, with $L = 80$ time-averaging samples. Let $\hat{\theta}$ be the estimated DOA angle. We define a correct detection as an estimated DOA that falls within $|\hat{\theta} - \theta_k| \leq \epsilon$ of a true source, with $\epsilon = 2^\circ$. Let $R_{\mathsf{match},t}$ denote the number of correct detections and $R_{\mathsf{all},t}$ the total number of true sources in trial t. The detection probability over N_{trial} Monte Carlo trials is

$$P_{\mathsf{detect}} = \frac{\sum_{t=0}^{N_{\mathsf{trial}}-1} R_{\mathsf{match},t}}{\sum_{t=0}^{N_{\mathsf{trial}}-1} R_{\mathsf{all},t}}. \tag{4.27}$$

We see in Fig. 4.5 that the proposed DMA-based method achieves detection probability above 0.8 for up to three sources across all tested SNR values. At 20 dB SNR, the null-scanning method achieves detection probability within 0.05 of MUSIC for up to three sources. Power-based null scanning can therefore detect multiple sources with a single RF chain.

Next, we evaluate the angular accuracy of the null-scanning method against MUSIC in Fig. 4.6. Let $\hat{\theta}_{r,t}$ and $\theta_{r,t}$ denote the estimated and true angles of the rth correctly detected source in trial t. The root-mean-square error of the estimated DOA is

$$\text{RMSE} = \sqrt{\frac{1}{\sum_{t=0}^{N_{\mathsf{trial}}-1} R_{\mathsf{match},t}} \sum_{t=0}^{N_{\mathsf{trial}}-1} \sum_{r=0}^{R_{\mathsf{match},t}-1} (\hat{\theta}_{r,t} - \theta_{r,t})^2}. \tag{4.28}$$

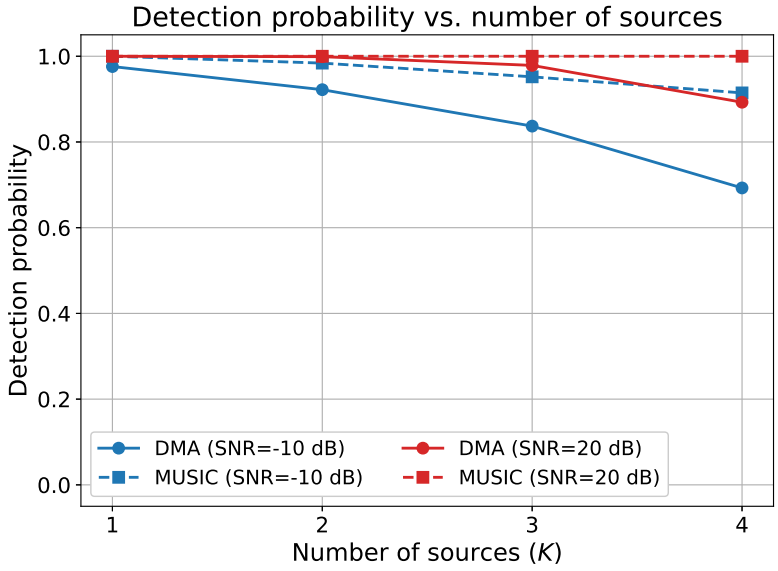


Figure 4.5. Detection probability versus number of sources for the DMA null-scanning method and MUSIC with $L = 80$ time-averaging samples. The null-scanning method approaches the detection probability of MUSIC at both low and high SNR.

which characterizes the angular accuracy of the estimated DOAs. We find that the RMSE increases with the number of sources for the null-scanning method. While the method continues to detect sources reliably, the NNLS algorithm produces less precise angular estimates as the number of sources grows. The RMSE for multiple sources also floors at moderate-to-high SNR because squaring the received voltage introduces cross-term interference between sources that persists even as thermal noise vanishes. This floor depends on the number of sources K and time-averaging samples L, not on SNR, and can be reduced by increasing L at the cost of longer measurement time. This represents a trade-off compared to subspace-based methods like MUSIC, which achieves near-perfect angular accuracy at moderate to high SNR values regardless of the number of sources.

We also characterize the angular resolution of the null-scanning method by measuring the fraction of two equal-power sources correctly resolved as a function of their angular separation, as shown in Fig. 4.7. At three separate SNR values, we find that the null-scanning algorithm consistently resolves sources separated by 3° or less, with resolution improving at higher SNR.

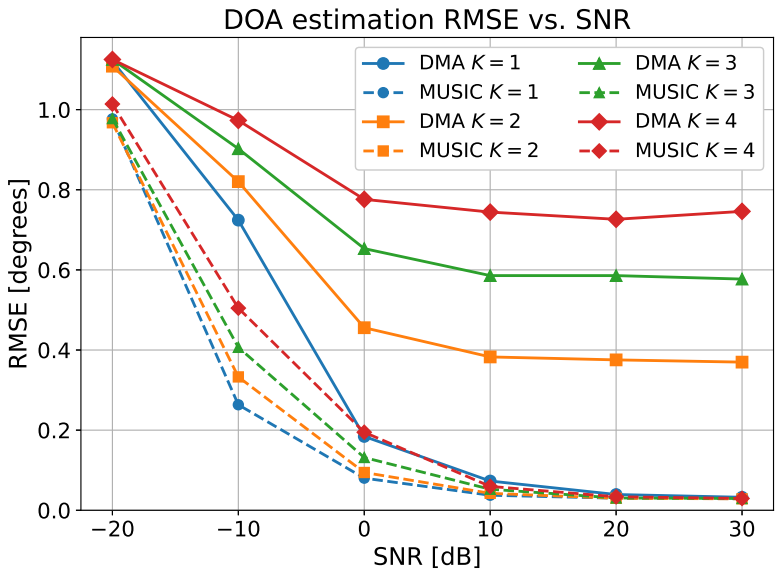


Figure 4.6. DOA estimation RMSE versus SNR for the DMA null-scanning method and MUSIC with $K = 1$ to 4 sources and $L = 80$ samples. The DMA achieves sub-degree RMSE above -10 dB SNR for all cases.

All three cases achieve a nearly perfect resolution rate for sources separated by $5°$, even at 0 dB SNR. This high resolution is a direct consequence of the null-scanning strategy, where the narrow nulls spaced at $1°$ intervals provide fine angular discrimination that a beam-scanning approach with broader main lobes would not achieve.

Figure 4.8 illustrates the effect of the number of time-averaging samples L on detection probability at a fixed SNR of 10 dB. We find that increasing L improves detection probability across all source counts, with the improvement being most pronounced for larger K. For a single source, near-perfect detection is achieved even at $L = 10$, while the four-source case improves from approximately 0.45 at $L = 10$ to over 0.95 at $L = 120$. This improvement occurs because time averaging suppresses the cross-term interference that arises from power-based detection of multiple simultaneous sources. Beyond $L \approx 100$, the detection probability saturates for all source counts, indicating sufficient cross-term suppression. The number of time samples can therefore be selected based on the expected number of sources to balance detection performance against measurement overhead.

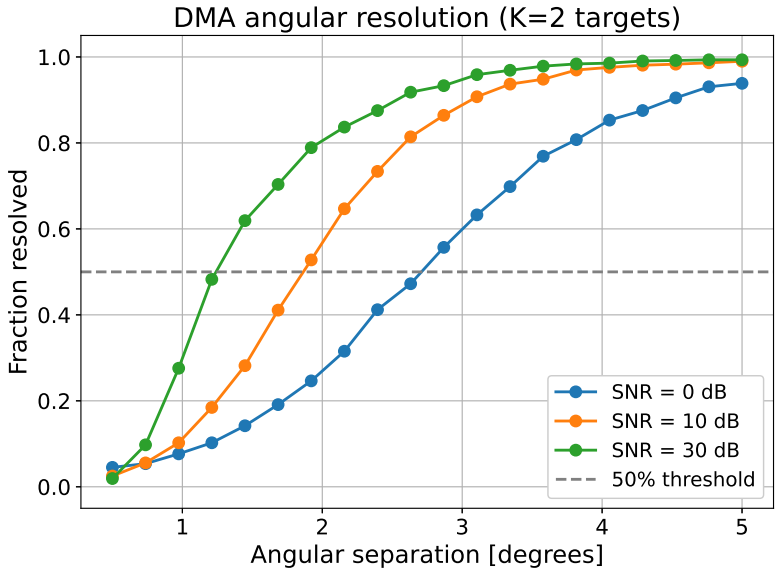


Figure 4.7. Angular resolution of the DMA null-scanning method for $K = 2$ equal-power sources. The 1° null spacing enables near-perfect resolution for sources separated by 3° or more, even at 0 dB SNR.

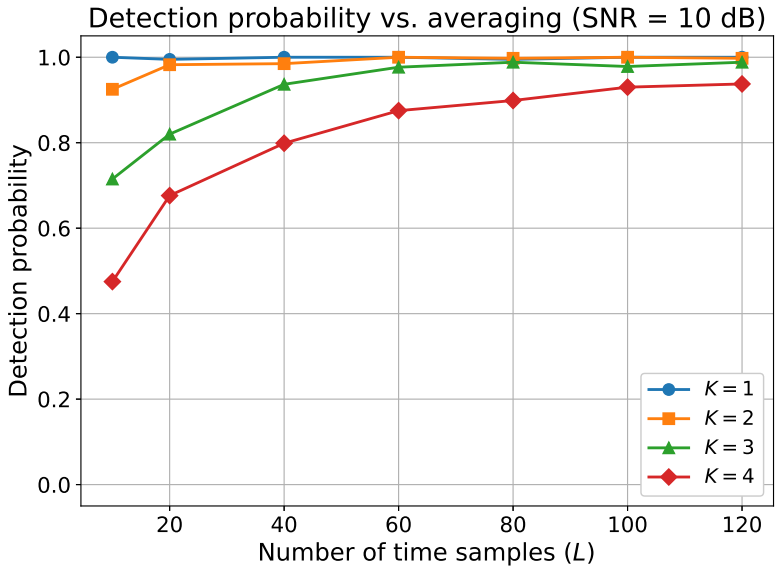


Figure 4.8. Detection probability versus number of time-averaging samples L for $K = 1$ to 4 sources at SNR $= 10$ dB. Increasing L suppresses cross-term noise, with diminishing returns beyond $L \approx 100$.

While Figs. 4.5, 4.6, 4.7, and 4.8 illustrate the effectiveness of the proposed null-scanning approach, the primary limitation of the null-scanning DOA estimation method is the measurement

time required. The DMA must cycle through all C configurations sequentially, collecting L samples per configuration. For a sample period t_{s} and varactor switching time t_{sw}, the resulting total measurement time is $T_{\text{DMA}} = C(Lt_{\mathsf{s}} + t_{\mathsf{sw}})$. In contrast, a conventional N-element array using MUSIC collects all elements simultaneously, requiring only $T_{\text{MUSIC}} = Lt_{\mathsf{s}}$. Additionally, the cross-term noise inherent to power-based detection means that the DMA requires more time samples per configuration as the number of sources increases, as shown in Fig. 4.8. Despite this measurement time overhead, the DMA offers significant advantages over the MUSIC method in terms of hardware, where a single RF chain replaces N parallel receive chains, each requiring a separate low-noise amplifier, mixer, and analog-to-digital converter.

With the source directions estimated, the DMA can then be reconfigured to steer a beam toward the target user while placing nulls at the estimated interferer locations. The quality of this nullsteering depends on how many simultaneous nulls the DMA can reliably produce and how accurately they can be placed. We evaluate this adaptive nullsteering capability in the following section.

4.6 Adaptive nullsteering with DMAs

We now evaluate the nullsteering capability of the 10-element DMA through full-wave electromagnetic simulations in HFSS. The goal is to determine how many simultaneous nulls the DMA can reliably place alongside a main beam, given the Lorentzian weight constraint, internal waveguide scattering, and external mutual coupling. For each scenario, the ML ensemble generates candidate varactor configurations, and the resulting beam patterns are simulated in HFSS to measure the achievable beam gain and null depths.

For each nullsteering scenario, the optimization algorithm configures the DMA by optimizing the varactor capacitances using a genetic algorithm with the ML ensemble as the fitness evaluator. The genetic algorithm enables an efficient search over the large space of possible DMA weight configurations. To ensure that the resulting beam patterns meet performance

requirements, we impose minimum thresholds on the beam gain and null depth. Since all ML models in the ensemble predict a beam pattern for a given $\mathbf{c}_{\mathsf{var}}$, we also leverage the ensemble to penalize configurations with high inter-model disagreement, favoring solutions where the ML prediction is likely to match the HFSS result. Let $k^\star$ denote the target source (beam direction), $D^{\mathsf{dB}}_{\mathsf{beam}}$ the minimum beam gain threshold, $D^{\mathsf{dB}}_{\mathsf{null}}$ the maximum null depth threshold, $\bar{\sigma}_{\mathsf{ens}}$ the standard deviation of the pattern across all ensemble models, and $\nu_{\mathsf{beam}}, \nu_{\mathsf{null}}, \nu_{\mathsf{unc}}$ the corresponding penalty weights. The cost function for the genetic algorithm is

$$J(\mathbf{c}_{\mathsf{var}}) = \frac{1}{D(\theta_{k^\star})} + \frac{1}{K-1}\sum_{k\neq k^\star}^{K-1} D(\theta_k) + \nu_{\mathsf{beam}}(\max\left(D^{\mathsf{dB}}_{\mathsf{beam}} - D^{\mathsf{dB}}(\theta_{k^\star}), 0\right))^2 + \nu_{\mathsf{null}}\sum_{k\neq k^\star}^{K-1}(\max\left(D^{\mathsf{dB}}(\theta_k) - D^{\mathsf{dB}}_{\mathsf{null}}, 0\right))^2 + \nu_{\mathsf{unc}}\bar{\sigma}_{\mathsf{ens}}. \quad (4.29)$$

The first two terms use linear-scale directivity to maximize the beam gain while minimizing the null gain. The penalty terms use dB-scale values to enforce minimum thresholds on both quantities. The ensemble uncertainty term $\nu_{\mathsf{unc}}\bar{\sigma}_{\mathsf{ens}}$ favors configurations where all ML models agree, increasing confidence that the HFSS-simulated pattern will match the prediction. We set $D^{\mathsf{dB}}_{\mathsf{beam}} = 8$ dBi and $D^{\mathsf{dB}}_{\mathsf{null}} = -20$ dBi as the beam gain and null depth targets, with penalty weights $\nu_{\mathsf{beam}} = 10$, $\nu_{\mathsf{null}} = 10$, and $\nu_{\mathsf{unc}} = 5$. The genetic algorithm uses a population of 200 individuals, runs for 500 generations, and uses crossover and mutation rates of 0.8 and 0.1, respectively. Additional details on genetic algorithms for beam pattern design can be found in [103, 45].

We now define the metrics used to evaluate the nullsteering results. Since the ML-predicted patterns do not perfectly match the HFSS simulations, the actual null location may differ slightly from the desired angle. We determine the null location θ_{null} from the HFSS pattern as the angle of minimum gain within a small search window around the desired null location,

parameterized by $\theta_{\mathsf{off}} = 2^\circ$, as

$$\theta_{\mathsf{null}} = \underset{\theta \in [\theta_k - \theta_{\mathsf{off}}, \theta_k + \theta_{\mathsf{off}}]}{\operatorname{argmin}} D(\theta). \tag{4.30}$$

We then define the nullsteering angle error by the difference between the expected and simulated null angles as

$$\theta_{\mathsf{error}} = \theta_k - \theta_{\mathsf{null}}, \tag{4.31}$$

and the null depth for the kth source as

$$D_{\mathsf{depth},k} = D(\theta_{\mathsf{null}}). \tag{4.32}$$

We generate 20 example nullsteering cases with the $10-$element DMA array, simulate the beam patterns in HFSS, and use the metrics in (4.30), (4.31), (4.32) to quantify the nullsteering capabilities of the DMA.

We begin with the three-null scenario ($K = 4$) as a detailed case study. Figure 4.9 shows an example beam pattern with a main beam steered to -20° and three simultaneous nulls. We see that the ML-predicted pattern and the HFSS simulation match closely, which confirms the accuracy of the ML ensemble for beam pattern prediction. Despite the Lorentzian constraint, internal waveguide scattering, and mutual coupling, the ML ensemble identifies a set of varactor capacitances $\mathbf{c}_{\mathsf{var}}$ that produces three simultaneous nulls alongside a well-formed main lobe. This result shows that a DMA with interconnected, coupling-dependent weights is capable of advanced beam pattern shaping for interference mitigation.

Next, we examine all 20 nullsteering cases for the three-null scenario, with the beam gain shown in Fig. 4.10(a) and the null depth shown in Fig. 4.10(b). The beam gain averages 7.9 dBi across all configurations, consistently meeting the target of $D^{\mathsf{dB}}_{\mathsf{beam}} = 8$ dBi despite the additional constraint of three simultaneous nulls. The null depth averages -18 dBi, close to the target of $D^{\mathsf{dB}}_{\mathsf{null}} = -20$ dBi, and remains stable across all angles in the scan range. Consistent null depth

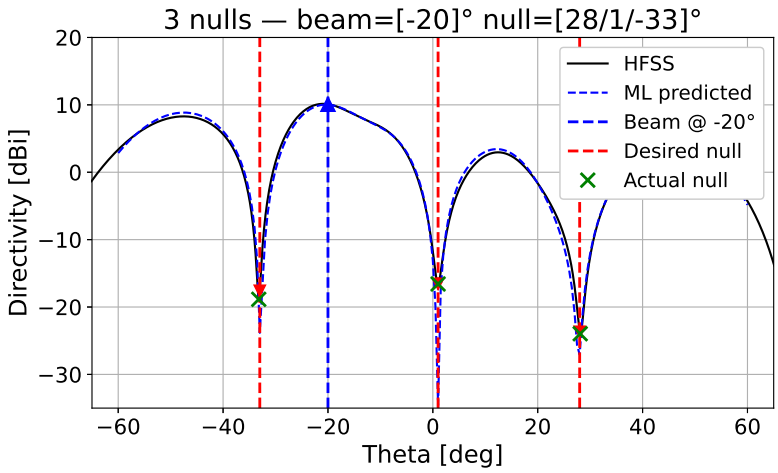
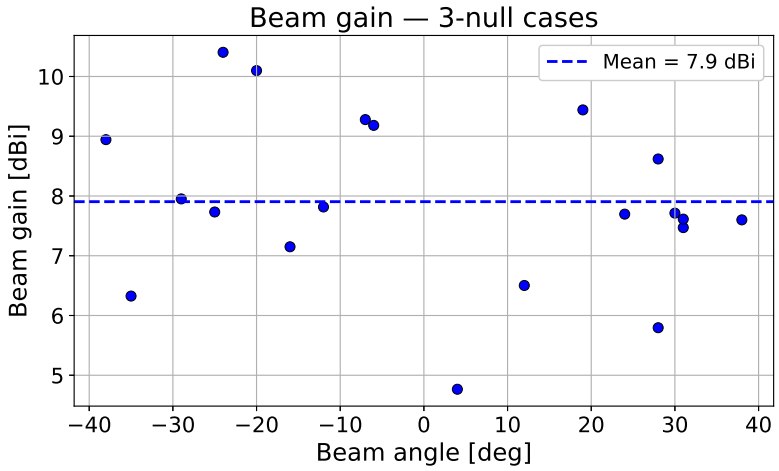


Figure 4.9. Example nullsteering beam pattern with a main beam at $-20°$ and three simultaneous nulls. The ML-predicted pattern closely matches the HFSS-simulated ground truth, with nulls accurately placed at the desired locations.

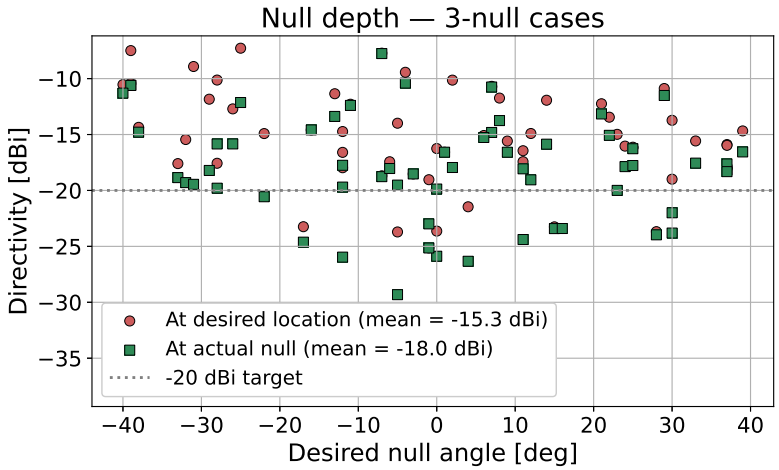
across scan angles allows the DMA to suppress interference at any direction within the $\pm 40°$ range.

Figure 4.11 shows the nullsteering accuracy for the three-null case. The scatter plot in Fig. 4.11(a) compares the desired and actual null locations with near-perfect agreement across all angles. Figure 4.11(b) confirms this through a histogram of the null location error, which shows that the angular error remains within $\pm 1°$ for the vast majority of cases. These results demonstrate that the DMA can simultaneously achieve the target null depth of -20 dBi and maintain accurate null placement with sub-degree precision.

We now evaluate how the number of simultaneous nulls affects the nullsteering performance across the 20 random scenarios per null count. Figure 4.12 shows the achievable beam gain as a function of the number of nulls. For each null count, the beam gain is plotted across all scenarios, scattered for visualization, along with the corresponding mean and standard deviation. With a single null, the mean beam gain is approximately 8.7 dBi, which decreases gradually to around 6.1 dBi with four nulls. This degradation is expected, as each additional null consumes degrees of freedom in the weight optimization. The variance also increases notably at four nulls, indicating that the DMA is approaching the practical limits of its ten-element architecture.



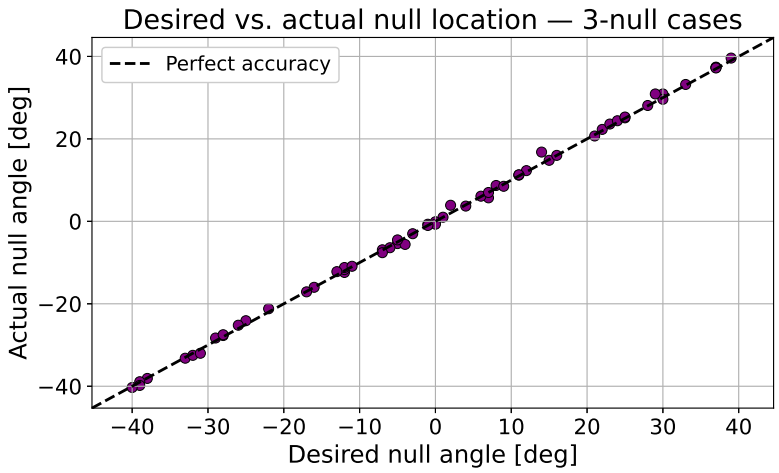
(a)



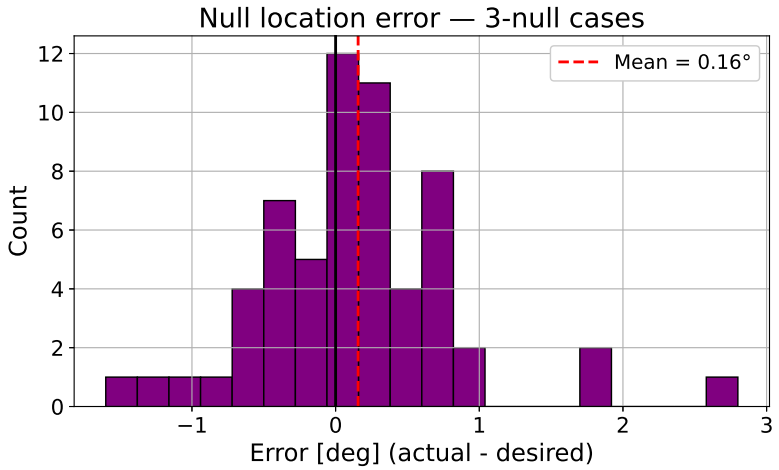
(b)

Figure 4.10. HFSS nullsteering results for the 3-null cases showing (a) beam gain and (b) null depth. The DMA consistently achieves close to the desired beam gain of $D^{\text{dB}}_{\text{beam}} = 8$ dBi and null depth of $D^{\text{dB}}_{\text{null}} = -20$ dBi across all tested beam patterns.

We also evaluate the null depth and null location accuracy as functions of the number of simultaneous nulls, as shown in Fig. 4.13. Figure 4.13(a) shows the achieved null depth at the actual null locations across all configurations. We find that the DMA maintains null depths close to the -20 dBi target for up to three simultaneous nulls, with relatively low variance across different beam patterns. With four nulls, however, the null depth becomes shallower on average and exhibits greater variance, indicating that the DMA is approaching the limits of its available degrees of freedom. Figure 4.13(b) shows the angular error between the desired and actual null



(a)



(b)

Figure 4.11. Nullsteering accuracy for the 3-null case showing (a) a scatter plot of the desired vs. actual null angle and (b) the null angle error. The null accuracy remains within $\pm 1^\circ$ of error for the majority of cases.

locations. For one to three nulls, the mean angular error remains within approximately 1°, which confirms accurate null placement. With four nulls, the error increases slightly due to the growing complexity of the coupling interactions, but the null locations still remain within a few degrees of the desired angles. These results suggest that a 10-element DMA can reliably steer up to three simultaneous nulls with both accurate depth and placement, while four nulls introduces noticeable degradation.

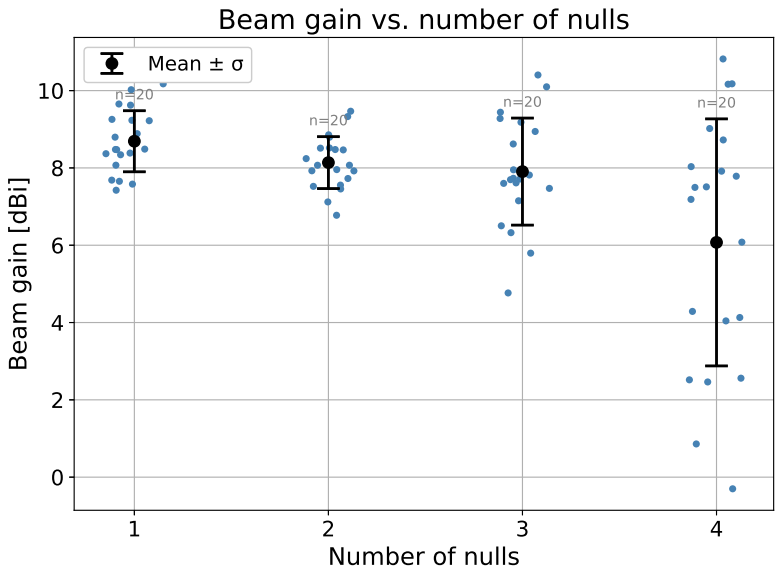
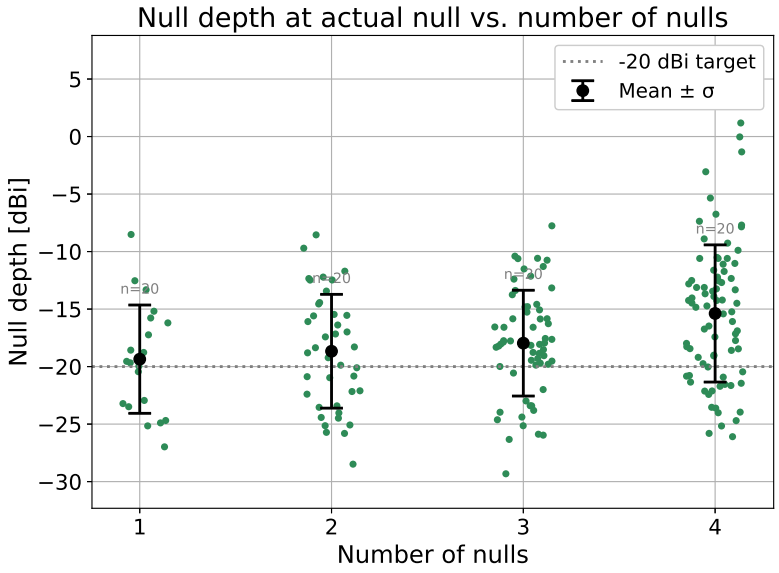


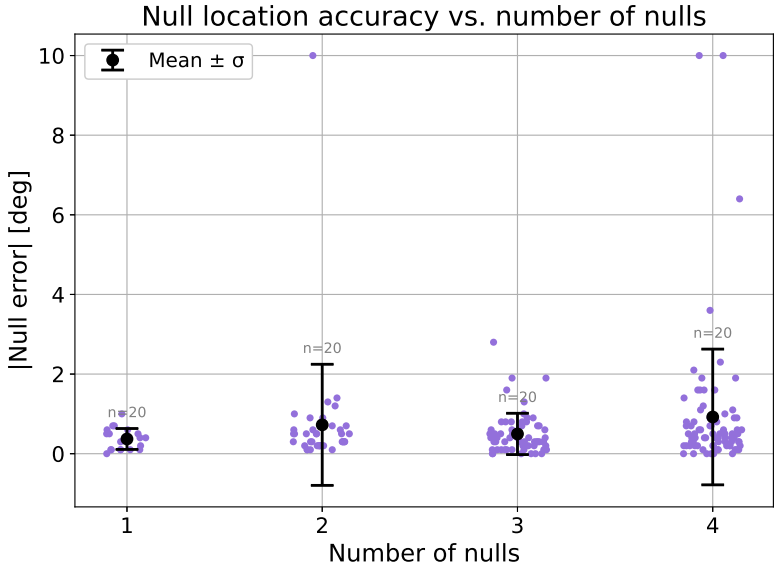
Figure 4.12. Beam gain as a function of the number of simultaneous nulls for the 20 random nullsteering scenarios. The beam gain decreases gradually as additional nulls consume degrees of freedom in the DMA weight optimization.

4.7 Conclusion

We have presented a machine learning-based framework for nullsteering and DOA estimation with dynamic metasurface antennas. By training an ensemble of MLP models on full-wave simulation data, we bridge the gap between the analytical DMA weight model and the true electromagnetic behavior, achieving a median pattern prediction RMSE of 1.11 dB and accurately capturing null locations that the analytical model alone cannot predict. Using the ML ensemble, we demonstrate that a 10-element DMA can simultaneously steer a beam and place up to three nulls with an average null depth near -20 dBi, beam gain close to 8 dBi, and angular null accuracy within $\pm 1^{\circ}$. With four simultaneous nulls, the performance degrades gradually as the DMA approaches the limits of its available degrees of freedom. The proposed null-scanning DOA estimation method identifies multiple source directions from sequential power measurements through a single RF chain, without requiring signal stationarity across configurations, covariance matrix estimation, or knowledge of the number of sources. Through comprehensive HFSS-validated Monte Carlo simulations, we demonstrate that the DMA achieves



(a)



(b)

Figure 4.13. Nullsteering performance as a function of the number of simultaneous nulls for the (a) achieved null depth at the actual null locations and (b) angular error between desired and actual null locations. The null depth and accuracy remain relatively constant for up to 3 nulls, while 4 nulls introduce greater uncertainty and shallower null depths.

high detection probability for up to four sources at moderate SNR, with angular estimation accuracy approaching that of conventional MUSIC. A 10-element DMA can therefore manage interference and localize sources in power-constrained wireless systems at a fraction of the

hardware cost of conventional arrays. A limitation of the proposed framework is that the learned model is tied to the array it was trained on. The network takes the capacitances and analytical weights of a 10-element DMA as its input, so the input dimension scales with the number of elements, and the coupling it learns is specific to one fixed geometry. Applying the framework to a different array size or element spacing would therefore require new full-wave training data and a retrained ensemble. Removing this restriction is an important direction for future work, and would likely require a predictor structured around the coupling between neighboring elements rather than the array as a whole, so that a single model could transfer across array sizes. We also plan to validate the framework experimentally with a fabricated DMA prototype and to extend it to two-dimensional arrays for joint azimuth and elevation estimation.

Publication Acknowledgment

Chapter 4, in full, has been submitted for publication of the material as it may appear in J. Carlson and R. W. Heath, “Advanced array processing for null steering and DOA estimation with dynamic metasurface antennas,” submitted to *IEEE Transactions on Wireless Communications*. The dissertation author was the primary investigator and author of this paper.

Chapter 5

A sub-6 GHz dynamic metasurface antenna design for improved gain and cross-polarization isolation

5.1 Overview

In this chapter, we focus on the actual DMA element design rather than the beamforming algorithms. We propose a rotated, elliptical element that improves upon the typical square element design in terms of radiation efficiency and cross-polarization isolation. Using a figure of merit called the tuning sensitivity, we compare multiple element geometries to uncover a key tradeoff between the tuning sensitivity and radiation efficiency, allowing us to select the element geometry with a favorable point in this tradeoff. We then fabricate the finalized DMA element to characterize its beamsteering capabilities using measurements from an anechoic chamber.

5.2 Introduction

Reconfigurable antennas move part of the signal processing from the digital baseband and RF front end into the radiating aperture. Various forms of reconfigurability have been demonstrated, including the radiation pattern [120, 121], operating frequency [122, 123], and polarization [124], each of which increases the number of degrees of freedom available to the wireless communication link. Electrical tuning mechanisms, such as p-i-n diodes or varactor

diodes, are typically employed to generate the reconfiguration in real-time while maintaining low costs and power consumption. Among these reconfigurable antenna architectures, dynamic metasurface antennas (DMAs) are a particularly attractive candidate for massive multiple-input multiple-output (MIMO) systems. By moving the beamforming functionality directly into the radiating aperture, DMAs avoid the per-element phase shifters and RF chains required in conventional digital and hybrid arrays, allowing them to scale to large array sizes with minimal additional power consumption [14]. Each radiating slot in a DMA, or meta-atom, behaves as an effective dipole whose magnitude and phase are governed by a Lorentzian-constrained polarizability [34, 93]. By integrating a varactor or p-i-n diode into each meta-atom, the resonant frequency can be electronically tuned to set the effective beamforming weight, allowing the array to gradually radiate the guided wave and steer or shape the radiated beam without per-element phase shifters [97].

The DMA architecture has been validated experimentally across a range of frequencies and tuning mechanisms. Foundational work demonstrated DMA-based computational imaging using square complementary electric-LC (cELC) meta-atoms. The first prototype used a 112-element one-dimensional aperture at K-band with p-i-n-diode tuning for synthetic-aperture radar [38]. A later prototype used a 96-element (8×12) two-dimensional aperture with varactor tuning for direct beamsteering at 10 GHz [1]. Subsequent prototypes have favored p-i-n diodes for binary-state tuning. A 16-element DMA at 12 GHz used two p-i-n diodes per element to demonstrate both narrow steerable beams and multibeam patterns through digital coding [125], and a 16-element one-dimensional array at 60 GHz extended this approach to the millimeter wave regime [98]. An alternative thread redesigned the meta-atom geometry itself for higher radiation efficiency and improved cross-polarization, validated only in full-wave simulation [126] and using p-i-n diode tuning in [36]. Collectively, this body of work spans roughly 10 to 60 GHz and demonstrates that a reconfigurable aperture can be built with far fewer active components than a conventional phased array of comparable size.

The frequency ranges covered by the prototypes in [38, 1, 125, 98, 126, 36], however,

are not yet aligned with the bands where commercial massive MIMO is deployed. The n77, n78, and n79 mid-bands span 3.3 to 5.0 GHz [127, 128], and major operators have rolled out 64-transmit, 64-receive massive MIMO arrays in these bands at scale [129]. The per-element cost and power consumption of 64 phase shifters and RF chains in a macrocell array is a strong driver for reconfigurable aperture alternatives such as the DMA, which moves the beamforming functionality into the radiating layer and eliminates per-element phase shifters entirely. A practical sub-6 GHz aperture must additionally provide high cross-polarization isolation, since modern base-station arrays use dual-polarized elements to double the number of independent spatial streams per user and to support orthogonal-polarization spatial multiplexing. Translating the DMA element down to sub-6 GHz, however, introduces problems that the X-band and millimeter-wave literature does not address. The meta-atom must be roughly twice the size of its 10 GHz counterpart, while the varactor diode package, which dictates the gap size, and readily-available substrate thicknesses, such as the 1.524 mm Rogers 4003C used here, remain unchanged. The resulting electrically smaller gap concentrates more of the resonant field, increasing the ohmic and dielectric losses, and the electrically thinner substrate strengthens the coupling between the meta-atom and the guided wave. Both effects degrade the radiation efficiency and realized gain at the array level.

Two recent DMA prototypes have begun to address the sub-6 GHz regime. The first is an 8 by 4 array of slot-shaped meta-atoms etched onto a substrate-integrated waveguide (SIW), demonstrating digital beamforming at 5.8 GHz [130]. The second uses a single-layer SIW with 12 square meta-atoms to generate three discrete beam directions at 5.1 GHz, achieving 5.6 dBi realized gain and roughly 45% simulated efficiency [131]. Both designs, however, are restricted to binary tuning states and a small set of predefined beam directions. To our knowledge, the closest continuously tunable DMA at any frequency reports a measured total efficiency between 5% and 11% across the scan range and a single 30 dB cross-polarization-isolation value without a cross-polarized pattern [1]. Beyond the frequency-band gap, no prior DMA prototype to our knowledge presents an element-level design methodology that jointly optimizes the radiation

efficiency, the peak co-polarized gain, and the cross-polarization isolation under the constraints imposed by sub-6 GHz operation.

In this chapter, we present the design, fabrication, and experimental characterization of a sub-6 GHz DMA with improved radiation efficiency, peak gain, and cross-polarization isolation over prior varactor-based designs. The contributions are summarized as follows. First, we propose a rotated elliptical meta-atom (REMA) whose slot orientation favors electric-dipole over magnetic-dipole radiation. This orientation improves the simulated cross-polarization isolation, peak co-polarized gain, and radiation efficiency over a square meta-atom baseline of comparable size and tuning range. Second, building on the tuning sensitivity metric and design optimization framework from our prior conference work [132], we apply a two-stage parametric design methodology that finalizes the elliptical dimensions and the SIW integration parameters from full-wave simulations. This methodology reveals a clear tradeoff between radiation efficiency and tuning sensitivity across the eight candidates and fixes the final design at around a 37% simulated radiation efficiency. Third, we fabricate an 8-element prototype on Rogers 4003C. We measure the realized gain and cross-polarization isolation across a $\pm 30^{\circ}$ scan range at 6 GHz. The prototype reaches a peak realized gain between 7.9 and 9.4 dBi and a cross-polarization isolation above 20 dB. The measured peak gain is comparable to the 7 to 10 dBi reported by the closest continuously tunable DMA [1]. Our prototype delivers this gain with only 8 elements rather than 96, and at a lower operating frequency where the substrate is electrically thinner and the varactor-imposed gap is electrically smaller, both of which tighten the element-level design constraints.

The rest of this chapter is organized as follows. Section 5.3 presents the DMA model and the parametric design methodology used to select the elliptical meta-atom. Section 5.4 specifies the final REMA geometry, compares it against a square baseline, and describes the 8-element array. Section 5.5 reports the fabrication, the single-element validation, the array beam patterns, the wideband measurements, and the comparison with prior-art DMAs. Section 5.6 concludes the chapter and outlines future work.

5.3 DMA architecture and meta-atom design methodology

This section develops the polarizability model for a single tunable meta-atom and applies a tuning-sensitivity figure of merit to compare eight elliptical candidate geometries. Fig. 5.1 shows a typical square meta-atom with a tunable varactor diode alongside the proposed REMA. The geometry is etched onto the upper conductor of a rectangular waveguide, and a varactor diode bridges the gap between the meta-atom and the outer conductor. When the waveguide is excited with the fundamental TE_{10} mode, the meta-atom couples to the guided fields and radiates with an amplitude and phase determined by the varactor state.

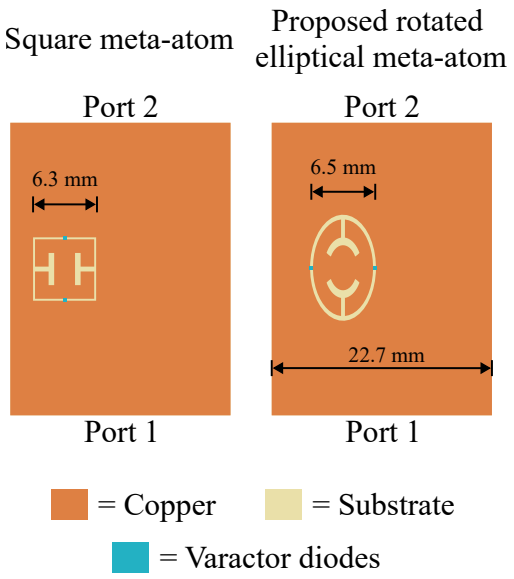


Figure 5.1. Topology of the typical square meta-atom and the proposed REMA. Both meta-atoms are etched onto the upper conductor of a substrate-integrated waveguide, with the guided TE_{10} mode propagating vertically in the figure. The varactor bridges the outer gap.

5.3.1 Polarizability and effective weight model

The REMA design and the array beamforming both rely on a model that links each meta-atom's varactor state to its contribution to the radiated field. This subsection develops that model in two steps. We first show how the effective beamforming weight of a meta-atom can be physically extracted from its polarizability, which lets us configure the fabricated array for

beamforming using only the simulated or measured scattering parameters of a single element. We then show that the polarizability follows a Lorentzian form set by the varactor capacitance, so that the varactor tuning range directly controls the range of accessible beamforming weights. This motivates the emphasis on tuning range in the design methodology in Section 5.3.2.

We model each meta-atom as a tunable dipole whose magnitude and phase are governed by a Lorentzian polarizability. Both the electric and magnetic polarizabilities of the meta-atom follow the same Lorentzian form. Let ω denote the angular operating frequency, $c_{\mathsf{var},n}$ the varactor capacitance of the nth element, $\omega_{\mathsf{r}}(c_{\mathsf{var},n}) = 2\pi f_{\mathsf{r}}(c_{\mathsf{var},n})$ the resonant angular frequency set by that capacitance with f_{r} as the corresponding resonant frequency, F_{coupl} a coupling factor, and Γ the resonator damping that captures the ohmic and dielectric losses. The polarizability is then [34]

$$\alpha(\omega, c_{\mathsf{var},n}) = \frac{F_{\mathsf{coupl}}\,\omega^2}{\omega^2 - [\omega_{\mathsf{r}}(c_{\mathsf{var},n})]^2 + \mathrm{j}\Gamma\omega}. \tag{5.1}$$

The varactor capacitance therefore acts as the single tuning variable in the model. Sweeping $c_{\mathsf{var},n}$ shifts $\omega_{\mathsf{r}}(c_{\mathsf{var},n})$, which changes the Lorentzian response as a function of the frequency. At a fixed operating frequency, this shift simultaneously varies the magnitude and phase of α, and therefore the magnitude and phase of the radiated dipole that determines the meta-atom's effective beamforming weight. This control of amplitude and phase is the fundamental mechanism that enables DMA beamforming.

To extract the polarizability of a specific meta-atom design, we use the simulated scattering parameters of the meta-atom. Sweeping $c_{\mathsf{var},n}$ in full-wave simulations modifies the meta-atom's reflection and transmission coefficients, which produces a set of polarizability values that lie on the Lorentzian curve in (5.1). Let $S_{11}(\omega, c_{\mathsf{var},n})$ and $S_{12}(\omega, c_{\mathsf{var},n})$ denote the reflection and transmission coefficients of the nth element for a given $c_{\mathsf{var},n}$, with a and b the waveguide width and height, β_{g} the guided propagation constant, and k_0 the free-space wavenumber. The magnetic

polarizability α_{m} and the electric polarizability α_{e} are then [42]

$$\alpha_{\mathsf{m}}(\omega, c_{\mathsf{var},n}) = \frac{\mathrm{j}ab}{2\beta_{\mathsf{g}}} \left(-S_{11}(\omega, c_{\mathsf{var},n}) + S_{12}(\omega, c_{\mathsf{var},n}) - 1\right), \tag{5.2}$$

$$\alpha_{\mathsf{e}}(\omega, c_{\mathsf{var},n}) = \frac{\mathrm{j}ab\beta_{\mathsf{g}}}{2k_0^2} \left(S_{11}(\omega, c_{\mathsf{var},n}) + S_{12}(\omega, c_{\mathsf{var},n}) - 1\right). \tag{5.3}$$

The orientation of the meta-atom determines whether the electric or magnetic polarizability dominates the radiated fields. For multiple meta-atoms tuned to different varactor capacitances, the resulting per-element variation in magnitude and phase allows the array to shape and steer the radiated beam.

Unlike a phased array, the DMA shares a single feed and a single traveling wave, so each slot radiates from a guided field that has already been perturbed by every preceding slot. We capture this effect through a transfer-matrix cascade along the waveguide [117]. Let x_n denote the position of the nth slot, and let F_n and B_n denote the forward and backward guided amplitudes and phases at that slot, referenced at the array input, obtained from the cascaded transfer matrices of all elements. We assume that F_n, B_n and the polarizability α_n are evaluated at a specific operating frequency and set of varactor capacitances as $\alpha_n \equiv \alpha_{\mathsf{e}}(\omega, c_{\mathsf{var},n})$. The effective beamforming weight of the nth element is then

$$w_n = \alpha_n \left(F_n + B_n e^{\mathrm{j}2\beta_{\mathsf{g}} x_n}\right), \tag{5.4}$$

where the exponential corrects for the phase of the backward-traveling contribution. Because F_n and B_n depend on the varactor states of all elements, changing a single capacitance alters the effective weights across the entire array.

5.3.2 REMA design methodology

With the DMA model established in Section 5.3.1, we now specify the REMA design. We identified the rotated elliptical topology through preliminary full-wave simulations of several

candidate sub-6 GHz meta-atom shapes. These simulations showed that rotating and elongating the standard square cELC consistently improved the simulated radiation efficiency and cross-polarization isolation. In this chapter, we apply the tuning-sensitivity design flow from our prior conference work [132] to select the specific elliptical dimensions.

The polarizability α_n traces a circular locus in the complex plane as the varactor capacitance sweeps the resonant frequency f_{r}, and a wider span of resonant frequencies allows a larger fraction of that locus to be used during beamforming. We define the tuning range of the meta-atom as the span of resonant frequencies accessible as the varactor capacitance c_{var} is swept over its full range. The tuning range therefore directly determines the range of polarizability values, and hence the range of beamforming weights, available to the array. The tuning range, however, depends jointly on the meta-atom geometry, the operating frequency, and the choice of varactor diode. Each varactor introduces a series ohmic loss into the resonator, which directly reduces the radiation efficiency. The varactor package also constrains the size of the outer capacitor gap, since the diode must physically bridge that gap when soldered onto the surface. This constraint becomes increasingly restrictive at sub-6 GHz, where the operating wavelength is roughly twice that of a 10 GHz design but the varactor package size is unchanged. The resulting electrically small gap concentrates more of the resonant electric field, which further increases both the ohmic and dielectric losses around the gap region. Designing a meta-atom that simultaneously achieves a wide tuning range and a high radiation efficiency at sub-6 GHz is therefore non-trivial without a quantitative comparison framework.

To compare different meta-atom designs, we use the tuning sensitivity S_{tune} from our prior work [132], defined as

$$S_{\mathsf{tune}} = \frac{\Delta f_{\mathsf{r}}}{\Delta c_{\mathsf{var}}} \frac{c_{\mathsf{var}}}{f_{\mathsf{r}}}. \tag{5.5}$$

The tuning sensitivity in (5.5) describes the shift in resonant frequency associated with a change in the varactor capacitance, which quantifies how sensitive a DMA design is to the tunable varactor diode. Designs with a higher magnitude of tuning sensitivity have a larger tuning range

and a greater range of beamforming weights. The factor $c_{\mathsf{var}}/f_{\mathsf{r}}$ normalizes the tuning sensitivity so that meta-atom designs with different nominal capacitances and resonant frequencies can be compared.

We evaluate eight REMA candidate designs at 6 GHz with the MACOM MAVR-011020 varactor fixed across all candidates, so that the comparison isolates the effect of the elliptical geometry. Fig. 5.2 shows the geometric variations across the different candidates. Here, we change the lengths, widths, and gaps between the various ellipses in the element design, while the substrate material and thickness remain constant. While the MAVR-011020 data sheet does not specify a parasitic resistance, its associated SPICE model gives $r_{\mathsf{var}} = 13.2\ \Omega$. We use this value to model the varactor in Ansys HFSS as a series RC circuit, and we sweep the varactor capacitance from 0.01 to 0.3 pF. This range extends beyond the varactor's actual 0.04 to 0.16 pF tuning range so that we can characterize the tuning sensitivity and radiation efficiency across a wider set of geometries, while the final design selection remains constrained to the actual varactor range.

The eight REMA candidates exhibit a clear tradeoff between radiation efficiency and tuning sensitivity. Fig. 5.3 shows the simulated resonances around 6 GHz for the eight candidates, where the meta-atom geometry directly sets the varactor capacitance required to resonate at 6 GHz. Fig. 5.4 then plots the resulting tradeoff between the tuning sensitivity and the simulated radiation efficiency. Across the eight candidates, the radiation efficiency varies from 15% to 43% and the tuning sensitivity magnitude varies from 0.03 to 0.22, where designs with higher efficiency have a narrower tuning range and fewer effective beamforming weights. The eight REMA candidates are representative examples that span the elliptical design space, and we find that the tradeoff curve in Fig. 5.4 is driven by the varactor rather than the elliptical geometry itself. Both the tuning range and the radiation efficiency are governed by how tightly the varactor is coupled to the meta-atom's resonance. Tighter coupling widens the tuning range, but also sends more of the resonant energy through the varactor's parasitic series resistance, which lowers the meta-atom's quality factor and radiation efficiency. As a result, further changes to the elliptical

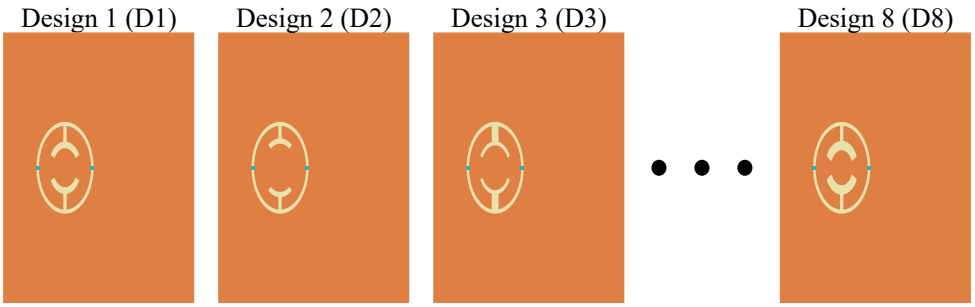


Figure 5.2. Examples for the different candidate DMA designs that we compare to finalize the REMA geometry with the best tradeoff between radiation efficiency and tuning range.

geometry would only move a candidate along the tradeoff curve without pushing it off. We select design 7 (D7) at a favorable point on the tradeoff curve, with a simulated radiation efficiency of 37% and a tuning sensitivity of -0.075, as the REMA design used for the remainder of the chapter.

In addition to the REMA geometry, the waveguide height and slot offset also play an important role in the element design. We first study the SIW height h, which impacts the resonant frequency, the strength of the resonance, and the cross-polarized radiation. Fig. 5.5(a) shows that increasing h from 1.5 mm to 4.5 mm shifts the resonance downward from 6.0 GHz to 5.27 GHz at the 0.10 pF reference capacitance, and Fig. 5.5(b) shows that the same sweep raises the $|S_{12}|$ dip from 0.41 to 0.54, which corresponds to weaker coupling between the slot and the guided wave. Fig. 5.6(a) further shows that the peak cross-polarized directivity drops by approximately 5 dB over the same sweep. The larger height therefore trades radiation strength for cross-polarization isolation. We are constrained to $h = 1.524$ mm by the standard thickness of the Rogers 4003C substrate that we use throughout the chapter, which corresponds to roughly $\lambda_0/33$ at 6 GHz. This is electrically thin and places our design at the strong-coupling, poor-cross-polarization end of the tradeoff. The same 1.524 mm substrate would be electrically thicker at higher operating frequencies and would offer a more favorable balance between coupling strength and cross-polarization isolation, but at sub-6 GHz we must accept the constraint set by the available substrate thicknesses.

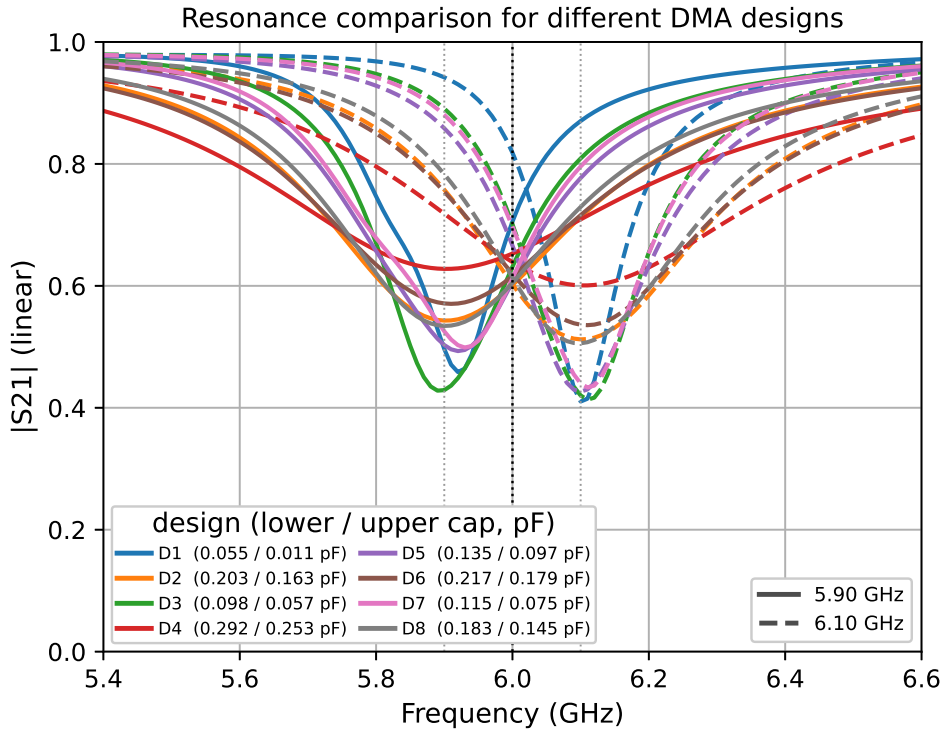


Figure 5.3. Simulated $|S_{12}|$ in linear scale for the eight REMA candidate designs, each tuned to land its resonance at 5.9 GHz (solid) and 6.1 GHz (dashed). The varactor capacitance spread required to achieve this detuning reflects each design's tuning sensitivity.

We next study the slot offset from the SIW centerline, which controls how strongly the slot perturbs the fields of the TE_{10} guided mode. Increasing the offset from 1 mm to 5 mm shifts the resonance upward from 5.64 GHz to 6.09 GHz, and lowers the $|S_{12}|$ dip from 0.75 to 0.42. The cross-polarized directivity in Fig. 5.6(b) also improves with offset for the two lower capacitances, but it does not improve at the largest capacitance, which sets the cross-polarization isolation floor across the tuning range. We select a slot offset of 4 mm, which places the resonance near 6 GHz under the 0.10 pF reference capacitance and maintains an acceptable cross-polarization isolation across the full varactor capacitance range. We adopt $h = 1.524$ mm and a 4 mm slot offset as the nominal operating point for the remainder of the chapter. While we show the general trends for the impact of the waveguide height and slot offset in Figs. 5.6(a) and Figs. 5.6(b), the final values were determined from a thorough, joint optimization between the REMA geometry and these parameters to obtain a high efficiency and cross-polarization isolation.

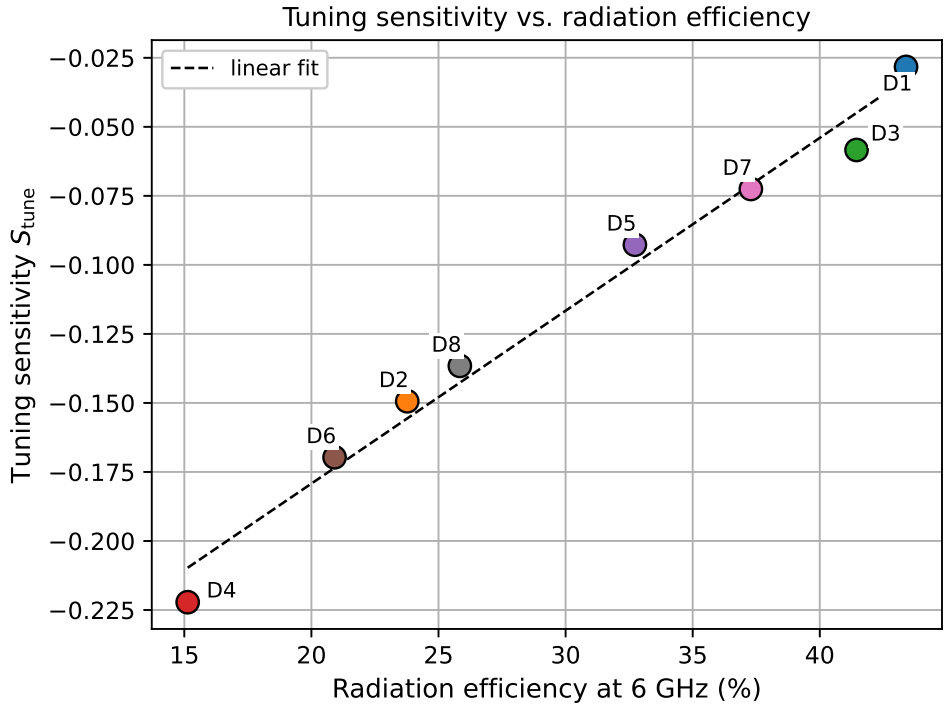
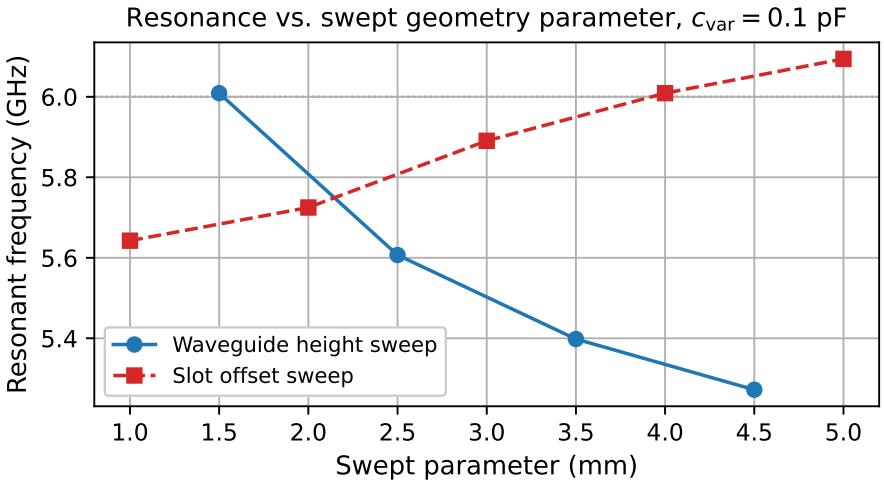


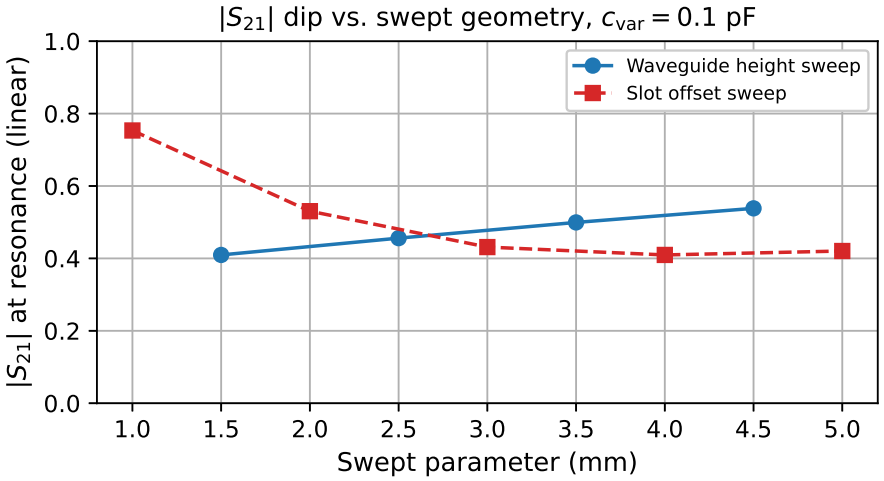
Figure 5.4. Tuning sensitivity S_{tune} versus radiation efficiency at 6 GHz for the eight candidate designs. We find that there is a distinct tradeoff between radiation efficiency and tuning sensitivity when we compare the eight designs. We choose design 7 (D7) for our final, proposed element due to its favorable radiation efficiency and sufficient tuning sensitivity with the selected varactor diode.

5.4 Final REMA design

With the parametric studies of the REMA geometry and SIW integration complete, we now specify the final design. Fig. 5.7 shows an outline of the REMA geometry, coplanar waveguide (CPW) feed and SIW. The corresponding numerical values are listed in Table 5.1. Here, $h = 1.524$ mm is the Rogers 4003C substrate height, and a_{ell} is the axial ratio shared by all four ellipses in the design. The CPW gap g_{cpw}, microstrip taper length t_{ms}, and via network dimensions were selected from a parametric sweep to minimize the insertion loss and provide a good impedance match, following the standard CPW-to-SIW transition design methodology [133]. As discussed in Section 5.3, the geometric values of the REMA were chosen to provide a favorable tradeoff between the tuning range and radiation efficiency while maintaining a low



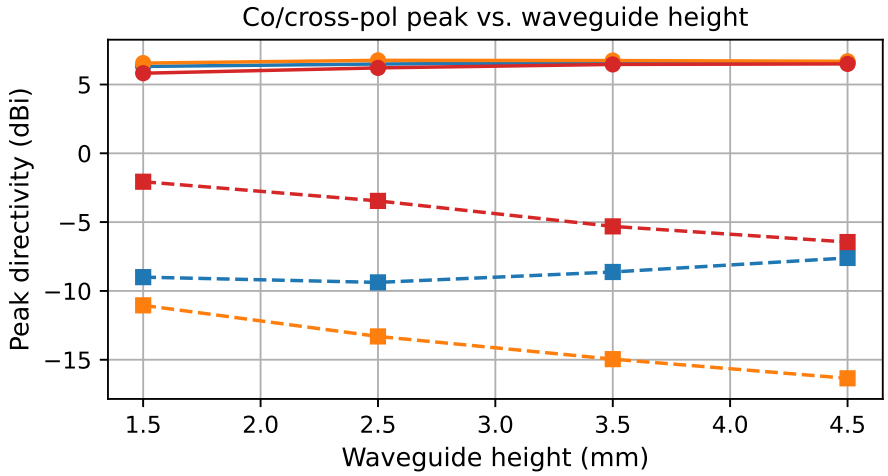
(a) Resonant frequency



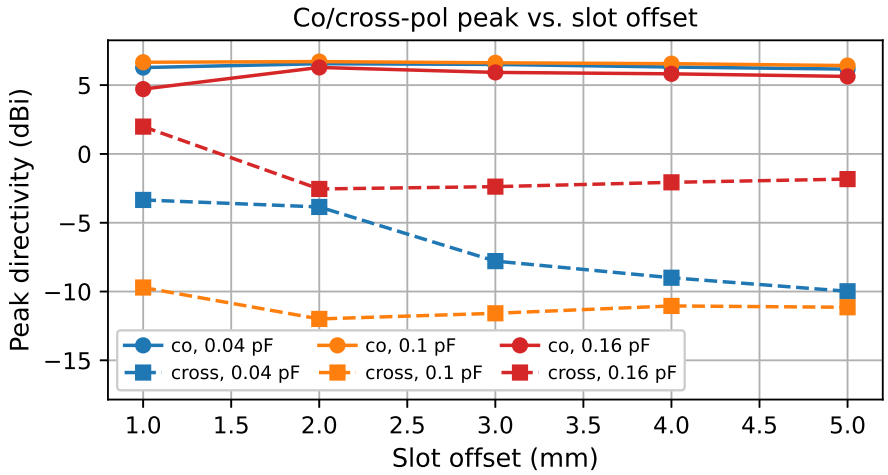
(b) $|S_{12}|$ dip at resonance

Figure 5.5. Element response versus waveguide height and slot offset at $c_{var} = 0.10$ pF, for (a) the resonant frequency and (b) the $|S_{12}|$ dip at each design's own resonance. Increasing the waveguide height lowers the resonant frequency and weakens the coupling between the REMA and the SIW, while increasing the slot offset raises the resonant frequency and strengthens the coupling.

cross-polarization. In the remainder of this section, we compare the REMA against a square meta-atom baseline and integrate the meta-atom into the proposed 8-element array.



(a) Vs. waveguide height



(b) Vs. slot offset

Figure 5.6. Peak co- and cross-polarized element directivity over $\theta \in [-40°, +40°]$ vs. waveguide height and slot offset at three swept varactor capacitances. Increasing the slot offset helps to improve the cross-polarization isolation at the lower varactor capacitance values.

5.4.1 Meta-atom comparison

By rotating the slot to favor electric-dipole over magnetic-dipole radiation and carefully designing the elliptical geometry, the REMA achieves a high radiation efficiency, peak co-polarized gain, and cross-polarization isolation. To highlight the contribution of the elliptical shape itself, we also design a square meta-atom baseline for comparison that uses the same MAVR-011020 varactor, the same Rogers 4003C substrate, and the same SIW cavity height. We

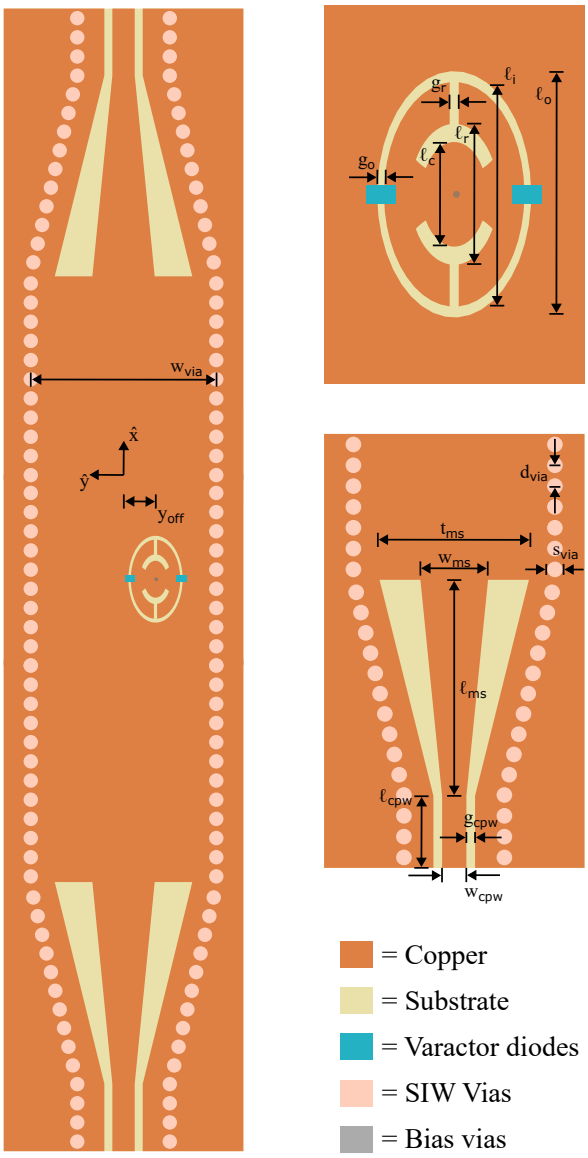


Figure 5.7. Geometry of the proposed REMA, the coplanar waveguide feed, and the substrate-integrated waveguide, with labeled dimensions corresponding to the values in Table 5.1.

size the square meta-atom so that it resonates at 6 GHz under the 0.10 pF reference capacitance and spans a similar simulated tuning range across the 0.04 pF to 0.16 pF varactor range. Thus, the comparison reflects the effect of the aperture shape rather than the underlying tuning behavior or integration parameters. The square meta-atom geometry follows the design from [1].

The REMA outperforms the square baseline on co-polarized directivity, cross-polarization isolation, and radiation efficiency across the full varactor range. Fig. 5.8 shows the simulated co-

Table 5.1. Geometric parameters of the proposed REMA and CPW-to-SIW feed.

(a) Elliptical element

Parameter	Value
ℓ_{o}	10.88 mm
ℓ_{i}	9.92 mm
ℓ_{r}	6.22 mm
ℓ_{c}	4.62 mm
a_{ell}	1.6
g_{r}	0.4 mm
g_{o}	0.2 mm
y_{off}	4.0 mm
d_{array}	21.6 mm
h	1.524 mm

(b) Feed and via network

Parameter	Value
w_{cpw}	2.8 mm
g_{cpw}	1 mm
ℓ_{cpw}	8.3 mm
ℓ_{ms}	24.9 mm
w_{ms}	7.8 mm
t_{ms}	17.22 mm
s_{via}	1.6 mm
d_{via}	2.4 mm
w_{via}	23.22 mm
ℓ_{bias}	4.9 mm

and cross-polarized element patterns for both designs at the lowest, the 6 GHz-resonant, and the highest swept varactor capacitances. Here, the co-polarized field is the ϕ-polarized component in the scan plane ($\phi = 90°$) for the REMA and the θ-polarized component in the same plane for the square meta-atom, reflecting the $90°$ rotation between the two slot orientations. The REMA achieves a peak co-polarized directivity of around 6.4 dBi at the 6 GHz-resonant capacitance with a cross-polarized directivity of -11.5 dBi, compared to 4.6 dBi for the square meta-atom with a cross-polarized directivity of -8.8 dBi. This trend continues across all swept capacitance values between 0.04 pF and 0.16 pF, where the average cross-polarization isolation is 15.1 dB for the REMA and 10.6 dB for the square meta-atom. Fig. 5.9 also shows the corresponding simulated radiation efficiency as a function of the varactor capacitance at 6 GHz. The REMA reaches a peak radiation efficiency of 46%, compared to 38% for the square meta-atom. The two designs span a similar simulated tuning range of approximately 600 MHz across the 0.04 pF to 0.16 pF varactor range. The REMA therefore improves the cross-polarization isolation, the peak co-polarized directivity, and the radiation efficiency over the square meta-atom without sacrificing tuning range.

Next, we plot the effective antenna weights for the square meta-atom and REMA, based

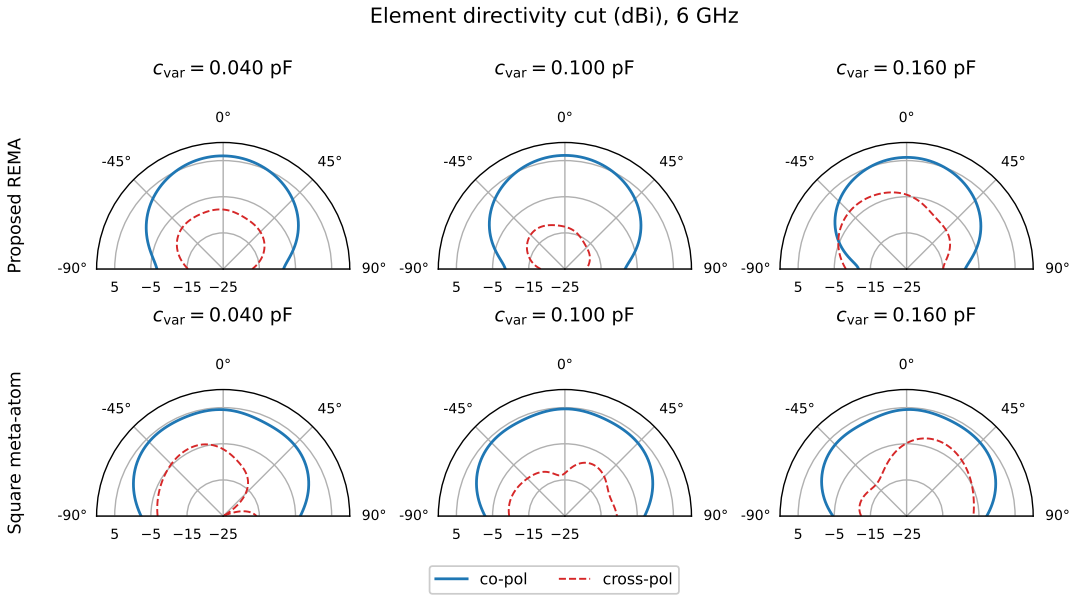


Figure 5.8. Simulated co- and cross-polarized element patterns at the lowest, 6 GHz-resonant, and highest swept capacitances for both the REMA and the square meta-atom. The REMA provides a higher co-polarized directivity compared with the square meta-atom, at the cost of a smaller beamwidth, and also yields better cross-polarization isolation.

on the polarizability, in Fig. 5.10. Due to the similar tuning range between both elements, we find that the available weights for beamforming are nearly identical as we vary the varactor capacitance from 0.04 pF to 0.16 pF. Thus, both elements can supply sufficient weights to steer beam patterns. Additionally, we find that the square meta-atom has a magnetic-dipole dominated radiation, while the REMA favors electric-dipole radiation. To understand why this is happening, we plot the surface currents and electric fields on both elements in Fig. 5.11. The REMA applies a $90°$ rotation to the orientation of the square element, causing the surface currents to also rotate in direction by $90°$. The rotation allows the REMA to be characterized by electric-dipole radiation rather than the typical magnetic-dipole radiation.

5.4.2 Array integration and beamsteering simulations

We now extend the single-element case to an array to determine the full benefits of the REMA design over the square meta-atom for beamforming. We arrange eight REMA elements into a 1-D array and compute the per-element beamforming weights from the extracted scattering

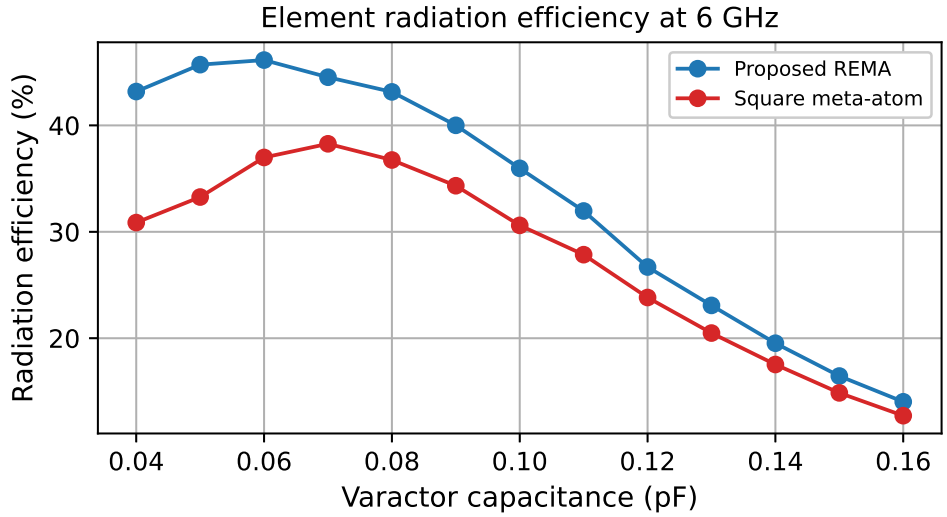
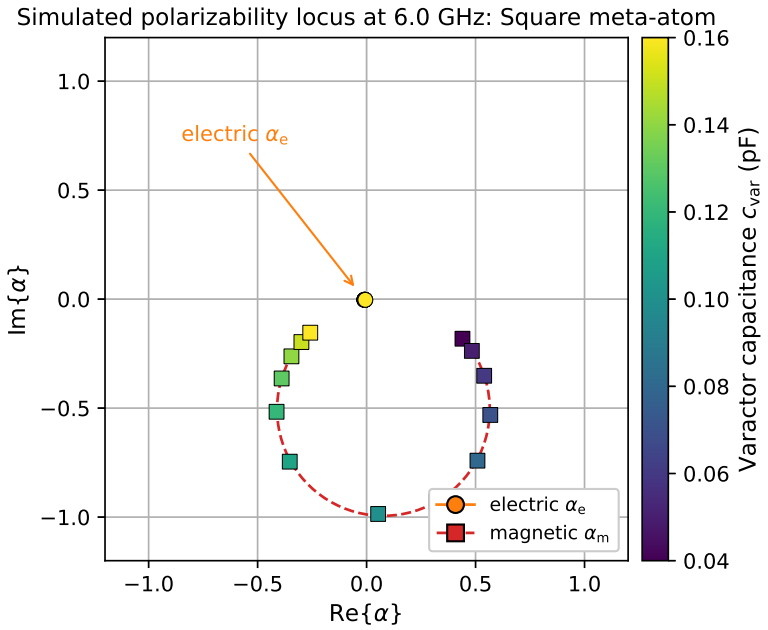


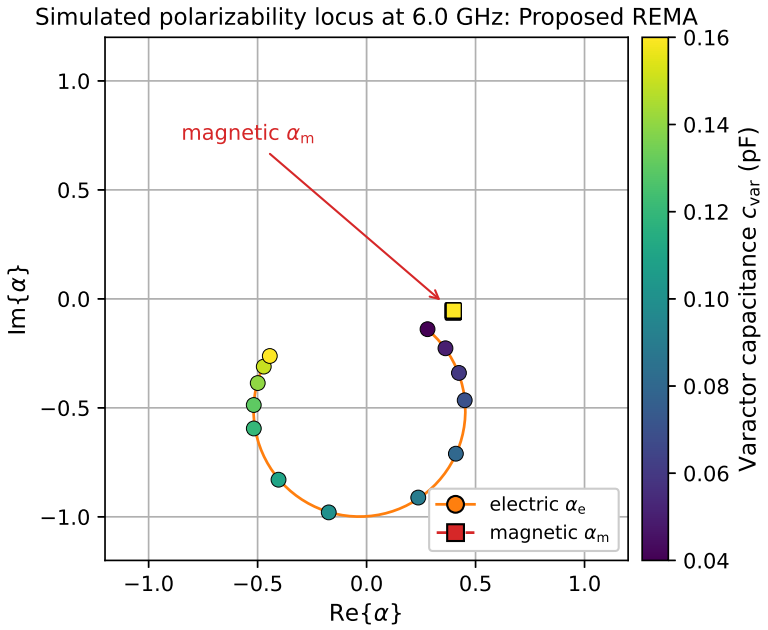
Figure 5.9. Simulated radiation efficiency versus varactor capacitance at 6 GHz for the REMA and the square meta-atom. The proposed REMA provides an increase in the overall radiation efficiency, especially at lower varactor capacitance values.

parameters and the polarizability equations from Section 5.3. Then, we use a genetic algorithm to obtain the optimized set of varactor capacitances that maximizes the realized gain of the DMA array at each target steering angle. Additional details for the genetic algorithm implementation can be found in our prior work [103]. We provide separate optimizations for the REMA and square meta-atom based on their Lorentzian weights, where the REMA is electric-dipole dominated and the square meta-atom is magnetic-dipole dominated. For both cases, the realized gain is maximized rather than the directivity or antenna gain, so that the comparison between the two element designs directly reflects which one radiates the most power at the target steering angle.

For both the square meta-atom and the REMA, we steer the beam pattern from -60° to 60° in electromagnetic simulations using Ansys HFSS. We show the beam pattern results for the square meta-atom array in Fig. 5.12a, the REMA in Fig. 5.12b and the co- and cross-polarized realized gain at the target steering angles for both arrays in Fig. 5.13. First, we find that the REMA can create reliable, steered beams from around -30° to 30°. Beyond 30°, the realized gain drops quickly because of the element pattern roll-off. In Fig. 5.13, we find that the REMA consistently achieves a higher realized gain than the square meta-atom between the -30° to

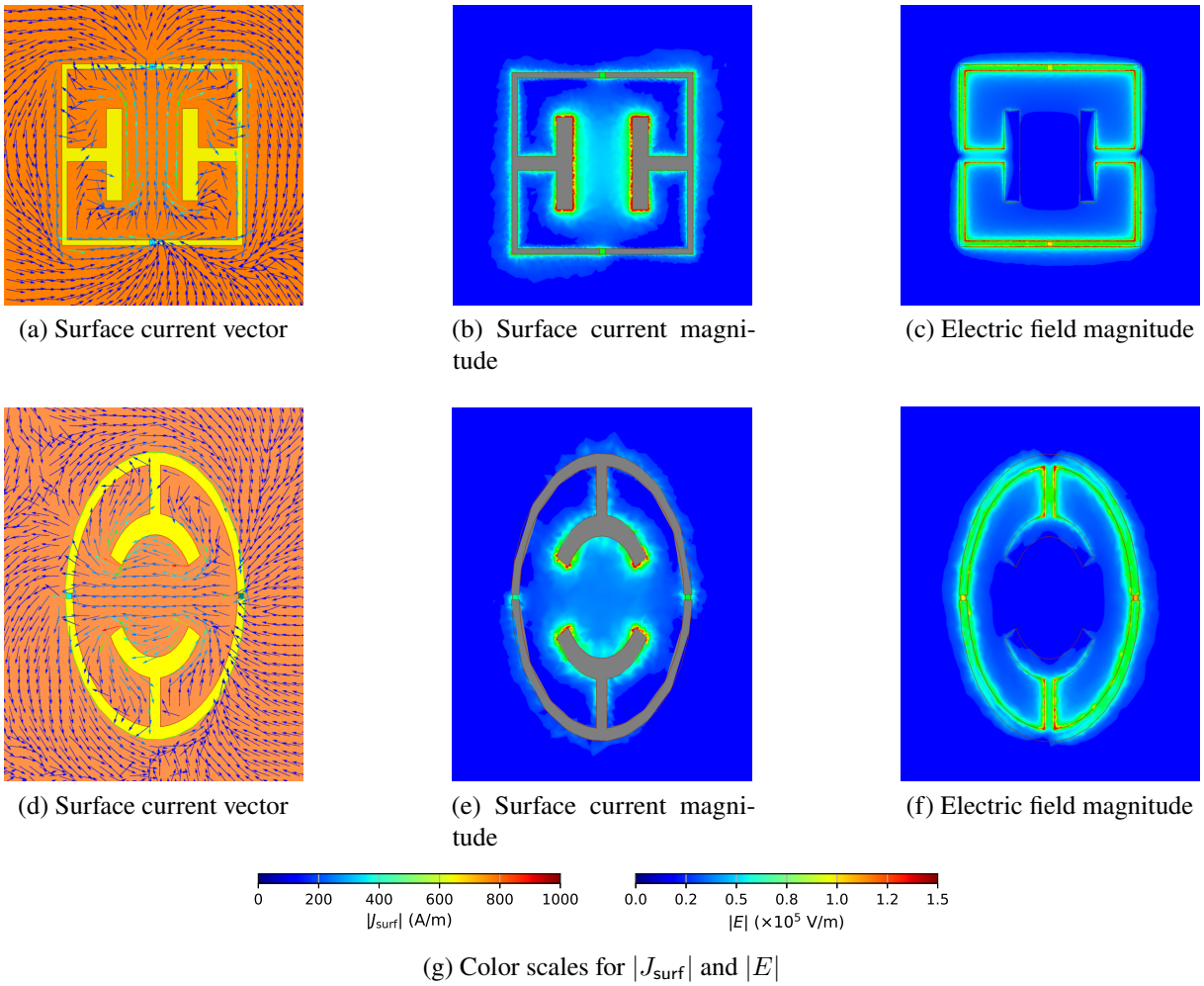


(a) Square meta-atom array



(b) REMA array

Figure 5.10. The simulated electric and magnetic polarizabilities for the (a) square meta-atom and the (b) proposed REMA. We find that the REMA favors electric-dipole radiation, while the square meta-atom favors magnetic-dipole radiation.



(a) Surface current vector

(b) Surface current magnitude

(c) Electric field magnitude

(d) Surface current vector

(e) Surface current magnitude

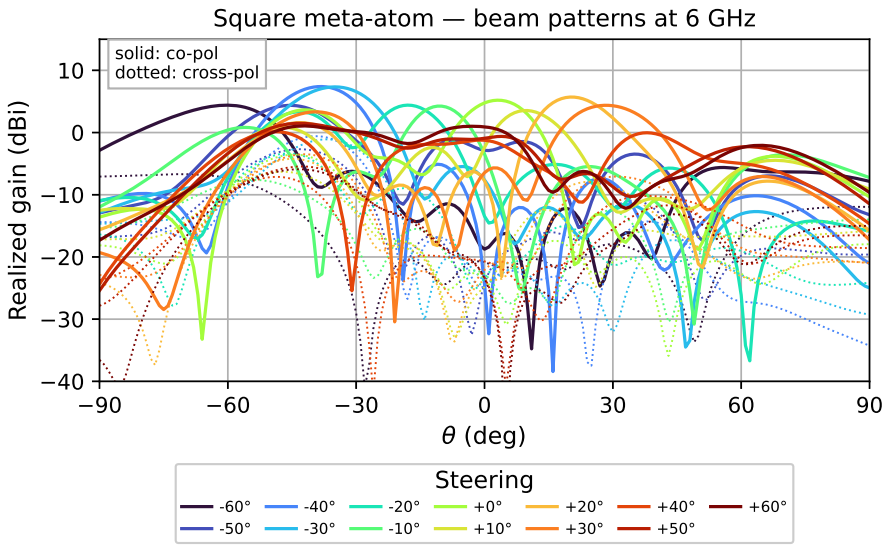
(f) Electric field magnitude

(g) Color scales for $|J_{\text{surf}}|$ and $|E|$

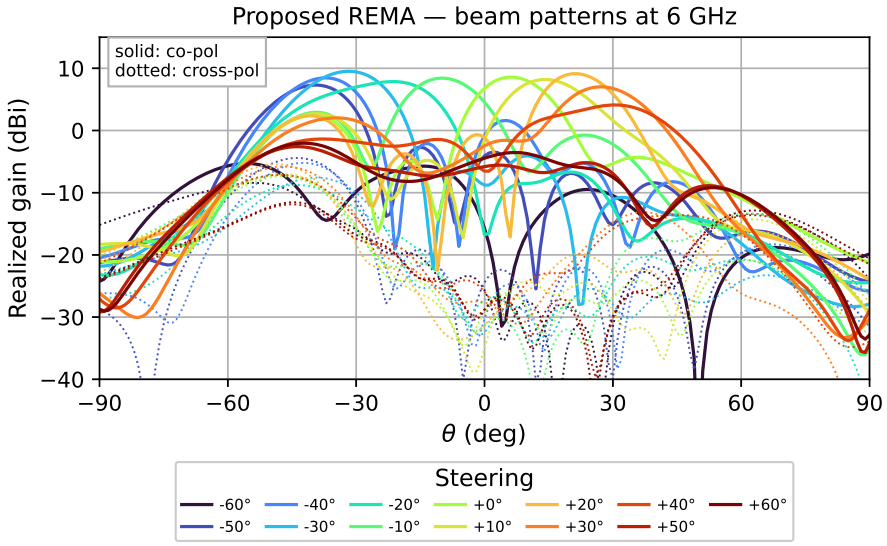
Figure 5.11. Comparison of the current densities and electric fields for the square meta-atom and proposed REMA.

30° steering angles, where the REMA averages an 8.0 dBi co-polarized gain and the square meta-atom averages a 4.8 dBi co-polarized gain. The average cross-polarization isolation over the same range is 27.8 dB for the REMA, compared with 16.6 dB for the square meta-atom. The simulated radiation efficiency of the REMA falls between 47% and 53% across the scan range, and the simulated total efficiency including the impedance mismatch at the array input falls between 43% and 51%. The close match between the two indicates that the input impedance is well matched across the steered beams. Overall, Figures 5.12b and 5.13 show the advantage of the proposed REMA in beamsteering, where the elliptical geometry provides a clear improvement

over the square meta-atom in terms of co-polarized gain and cross-polarization isolation.



(a) Square meta-atom array



(b) REMA array

Figure 5.12. Simulated co- and cross-polarized beam patterns of the 8-element (a) square and (b) REMA array at 6 GHz, steered from -60° to $+60^\circ$ in 10° steps. The REMA array sustains a higher co-polarized peak and a lower cross-polarized level within the $\pm 30^\circ$ scan range, while both arrays roll off beyond $\pm 30^\circ$ due to the element pattern.

For both meta-atom designs, we find that there is a visual lobe that occurs across every scan angle near $\approx -45^\circ$. To investigate why this lobe appears, we analyze the DMA array as a

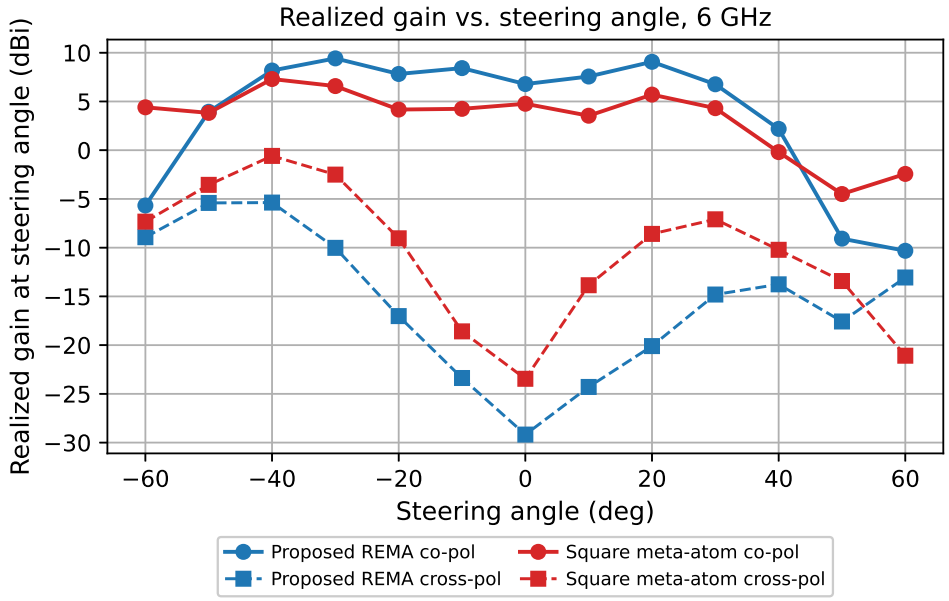


Figure 5.13. Simulated co- and cross-polarized realized gain at the desired steering angle for the REMA and square meta-atom arrays at 6 GHz. Within the -30° to 30° scan range, the proposed REMA provides an average co-polarized gain improvement of 3.2 dBi over the square meta-atom, and an average cross-polarization isolation improvement of 11.2 dB.

periodic leaky-wave antenna. Leaky-wave antennas with periodic spacing d create radiation at a specific angle θ_g due to the $n = -1$ space harmonic as [90]

$$\sin\theta_g \approx \frac{\beta_g}{k_0} - \frac{2\pi}{k_0 d}. \tag{5.6}$$

Substituting the values for $\beta_g = 189.4$ rad/m, $k_0 = 125.7$ rad/m, and $d = 21.6$ mm that correspond to the designs, we expect a lobe to appear at $\theta_g \approx -53.8^\circ$. This is very close to what we see visually in Fig. 5.12. Moreover, any discrepancies between the visual lobe and the predicted $\theta_g \approx -53.8^\circ$ angle can be accounted for due to the element pattern roll-off and variation in leakage between elements, as a typical leaky-wave antenna assumes uniform leakage. Thus, the lobe is an artifact of the DMA as a periodic leaky-wave antenna, and can be mitigated by selecting a smaller element spacing.

5.5 Prototype fabrication and measurement results

We fabricate both the full 8-element REMA array and a single-element REMA on Rogers 4003C using standard printed circuit board (PCB) processes. Fig. 5.14 shows an isometric view of the fabricated 8-element PCB, and Fig. 5.15 shows the fabricated REMA array and corresponding hardware in an anechoic chamber. In addition to the REMA elements, we design a CPW feed and tapered microstrip transition to bridge the end-launch SMA connector to the waveguide. We also convert a standard waveguide to a SIW for simple and cost-effective PCB fabrication [133]. Values for the CPW and SIW are listed in Table 5.1. We place vias within each REMA to apply a bias voltage to the varactor diodes. These bias vias connect down to layer 4, where they can be routed externally to a control board that generates 8 separate DC voltages. We design a radial bias stub to isolate any RF current from the biasing control hardware. The control hardware uses an Arduino-driven 8-channel digital-to-analog converter (DAC6578) and a set of LM358 amplifying stages to generate per-element bias voltages from 0 to 15 V, covering the full capacitance range of the MACOM MAVR-011020 varactor. All of the control hardware and fabricated REMA array are mounted on a custom 3D-printed structure.

5.5.1 REMA single-element measurements

We first validate the design at the single-element level, where the varactor bias sweep reproduces the simulated frequency tuning and Lorentzian weight locus. Using a Keysight P9371A network analyzer, we measure the S-parameters of the fabricated REMA as we sweep the DC bias voltage from 0 to 15 V. The resulting S_{12} parameters are shown in Fig. 5.16. We find that we can tune the resonant frequency of the fabricated REMA from approximately 5.5 GHz to 6.25 GHz, giving us a measured tuning range of around 750 MHz. We then extract the measured electric polarizability from the de-embedded S-parameters using (5.3) and plot the resulting Lorentzian-constrained locus at four frequencies in Fig. 5.17. The values in Fig. 5.17 are normalized to a magnitude of 1 for each frequency. The 750 MHz tuning range provides a

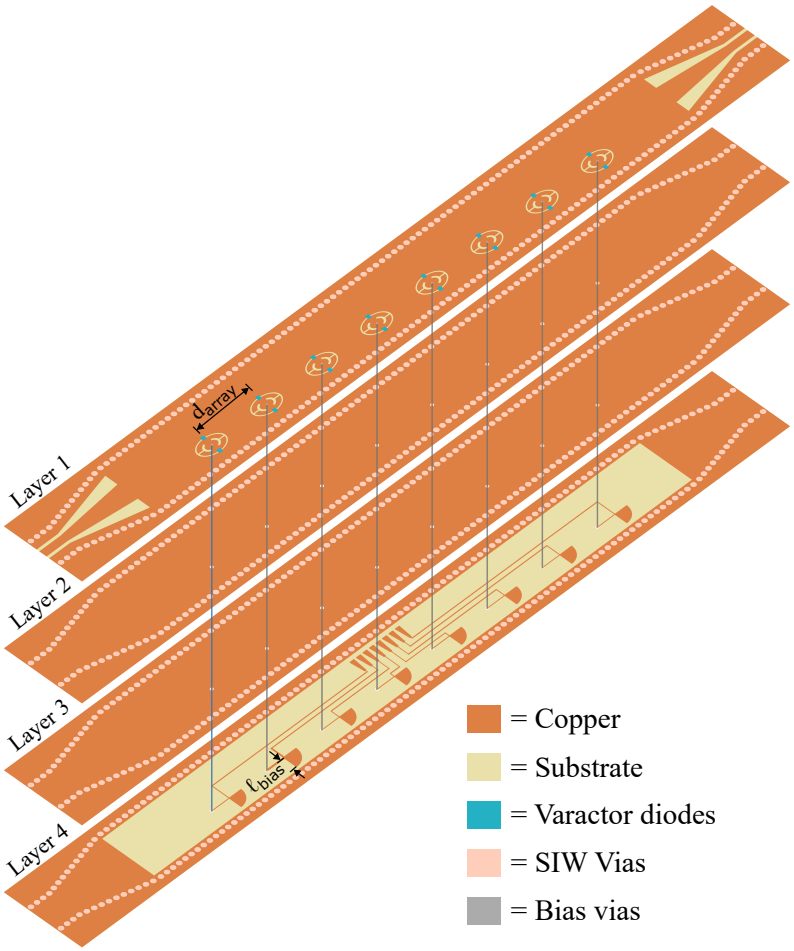


Figure 5.14. Isometric layout of the 4-layer printed circuit board for the fabricated REMA. Layers 1 and 2 consist of the REMA elements, CPW, and SIW, while layer 4 holds the biasing traces. A 1.524 mm thick Rogers 4003C substrate is used between layers 1 and 2, and layers 3 and 4, where pre-preg holds layers 2 and 3 together.

wide span of effective antenna weights at each target frequency, which gives the 8-element array enough degrees of freedom to steer the beam across the full scan range. Small oscillations in the measured $|S_{12}|$ are artifacts of the de-embedding procedure used to isolate the REMA response from the SIW and CPW feed.

We then measure the single-element REMA in an anechoic chamber using a Keysight E5071C network analyzer and an ETS-Lindgren Model 3119B horn antenna. Fig. 5.18 compares the measured single-element co-polarized realized gain at 6 GHz to the simulated pattern at the resonance-matched varactor capacitance, for five representative bias voltages spanning the

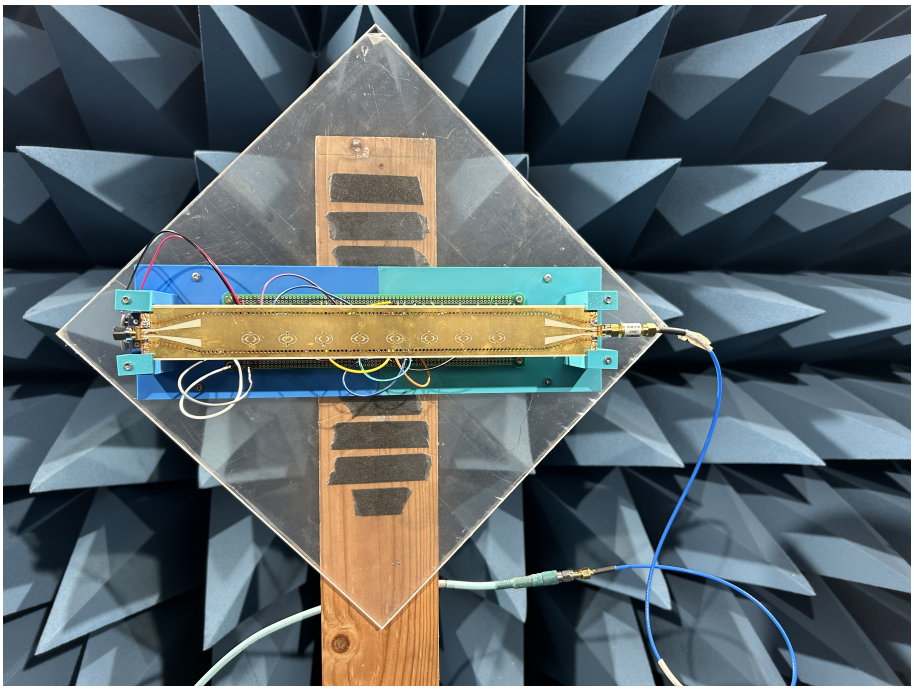


Figure 5.15. Fabricated 8-element DMA prototype mounted in the anechoic chamber. The array is fed through the CPW-to-microstrip-to-SIW transition, and the bias-stub network on the back side is connected to the control hardware.

tuning range. Each bias voltage corresponds to a point on the measured Lorentzian-constrained polarizability locus in Fig. 5.17, and the peak gain at each bias tracks the polarizability magnitude at that point, reaching its maximum when the resonance lands at 6 GHz. The close agreement between the measured and simulated patterns validates the Lorentzian polarizability model from Section 5.3.1 and the bias-voltage-to-capacitance mapping used to configure the array. Although the maximum per-element realized gain peaks around 0 dBi, each DMA element is designed to radiate only a fraction of the input power. Thus, while individual element gain is low, the overall array gain increases significantly.

5.5.2 Array beam pattern measurements

Next, we configure the full 8-element array at thirteen scan angles by setting the per-element bias voltages, and we measure the beam patterns in the anechoic chamber. Similar to the simulations for beamsteering, we implement the genetic algorithm with the measured

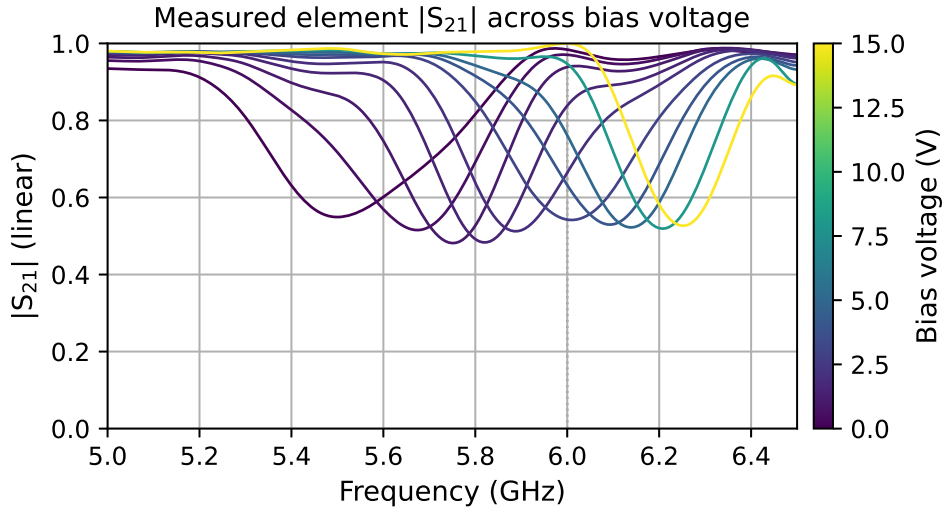


Figure 5.16. Measured, de-embedded $|S_{12}|$ of the fabricated REMA across the varactor bias voltage sweep (0–15 V). As we tune the varactor diodes with the bias voltage, the resonant frequency of the REMA varies between 5.5 and 6.25 GHz.

Lorentzian-constrained weights shown in Fig. 5.17 to calculate the bias voltages for steering beams from $-60°$ to $60°$ in $10°$ steps. Fig. 5.19 displays the measured beam patterns from the REMA array. The measured beam patterns match the simulation results closely. Within the $-30°$ to $30°$ angular range, the array delivers a realized gain of 7.9 to 9.4 dBi consistently, and the gain drops outside that range as the element pattern rolls off. Moreover, we also observe the same leaky-wave lobe near $-45°$ predicted by (5.6). Fig. 5.20 also shows the measured co-polarization and cross-polarization gain at the specified steering angles, where the REMA array achieves an average cross-polarization isolation of 24.7 dB within the $-30°$ to $30°$ range. Thus, despite ohmic and dielectric losses, potential varactor losses, and fabrication impairments or differences in the elements, the fabricated REMA array provides a high co-polarized gain and cross-polarization isolation. The beamsteering results further validate the polarizability model for the DMA element weights, where incorporating the measured Lorentzian constraint and scattering parameters yields accurate steering across the scan range.

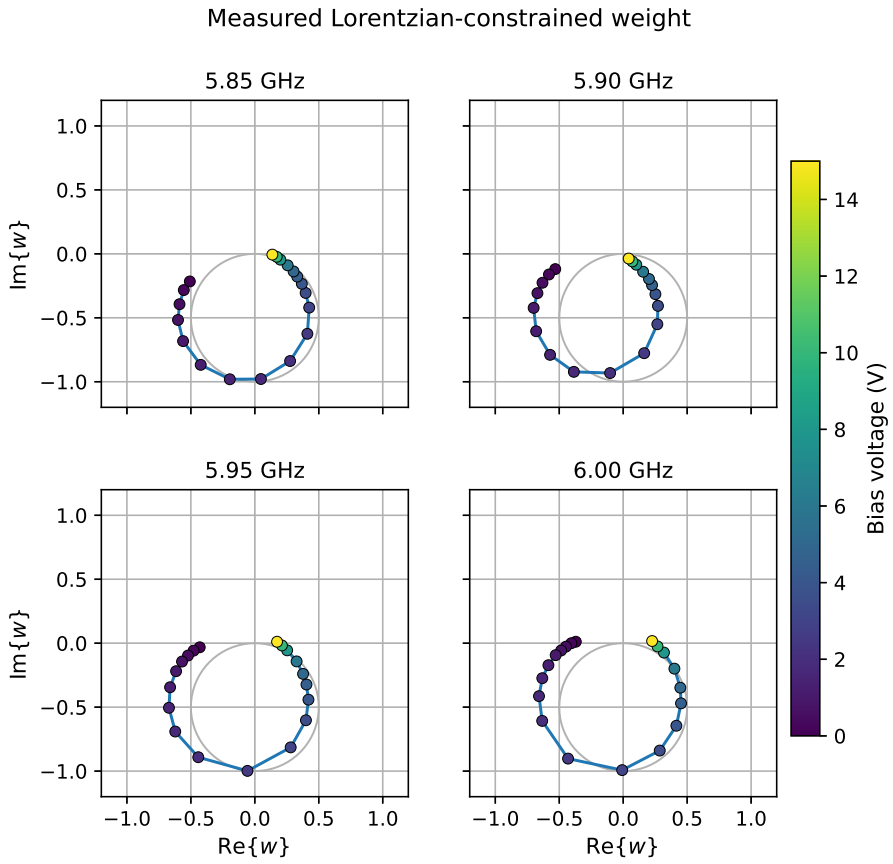


Figure 5.17. Measured Lorentzian-constrained beamforming weight using (5.3), drawn at four frequencies from 5.85 to 6 GHz with the bias voltage as the curve parameter. The measured Lorentzian constraint matches closely to the theoretical curve (grey), and the wide tuning range allows for a sufficient antenna weight range across multiple frequencies.

5.5.3 Wideband beam pattern measurements

Lastly, we measure the beam pattern of the REMA array at multiple target frequencies across a bandwidth of 150 MHz from 5.85 GHz to 6 GHz. We first test the wideband performance of the REMA array by modifying the genetic algorithm to maximize the realized gain at a 20° steering angle across all frequencies in the band, yielding a single configuration of varactor diodes for the entire bandwidth. Fig. 5.21(a) shows the results from the single beam pattern measurement across the frequencies. For 5.85 to 5.95 GHz, the realized gain remains between 7.8 and 8.8 dBi, but falls quickly to 5.7 dBi at 6 GHz. The REMA array therefore supports an instantaneous bandwidth of approximately 100 MHz under a single bias configuration, with

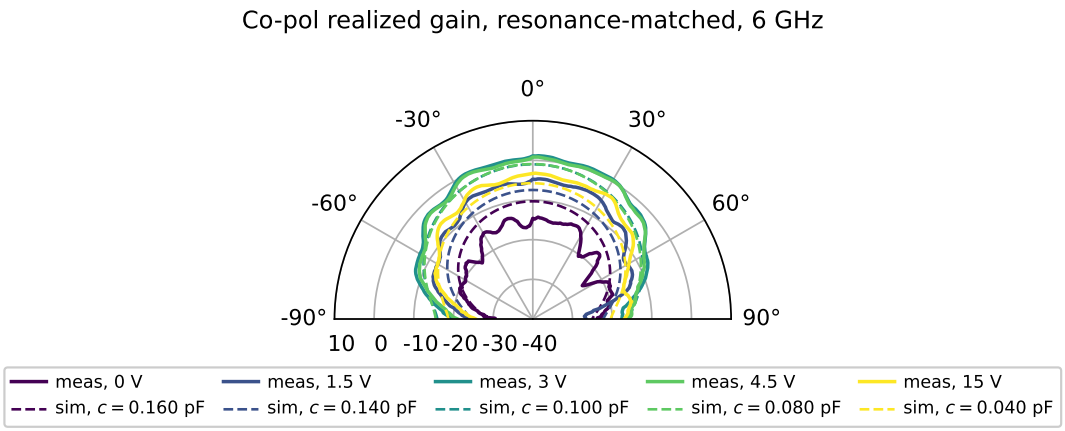


Figure 5.18. Simulated (dashed) and measured (solid) co-polarized element realized gain of the single-element REMA at 6 GHz, with the simulated varactor capacitance matched to the resonant frequency of each measured bias voltage by color. The measured patterns track the simulated patterns across the tuning range, which validates the Lorentzian polarizability model and the bias-voltage-to-capacitance mapping used to configure the array.

the realized gain degrading sharply at the band edges. To test the beamsteering capability at individual target frequencies, we also optimize the varactor configuration separately at 5.85, 5.90, 5.95, and 6.00 GHz to steer the pattern to $20°$. Fig. 5.21(b) shows the resulting four beam patterns. As expected, all four cases result in a directive beam at $20°$ at the desired frequencies. Compared to the wideband case, the per-frequency optimized beams only result in a maximum 0.9 dBi gain improvement over the wideband beam pattern across the 5.85 to 5.95 GHz frequency range. At 6 GHz, however, the gain improvement is 2.2 dBi, large enough to justify per-frequency bias updates near the band edge. These results indicate that single-bias operation suffices for typical 100 MHz channel bandwidths in sub-6 GHz operation, while per-frequency bias updates are needed to maintain peak gain across larger bandwidths.

5.5.4 Comparison with prior-art DMAs

Table 5.2 compares the proposed REMA array against the most relevant published DMA prototypes. The closest continuously-tunable comparator is the varactor-based 8×12 array at 10 GHz from [1], which achieves a measured realized gain between 7 and 10 dBi but reports

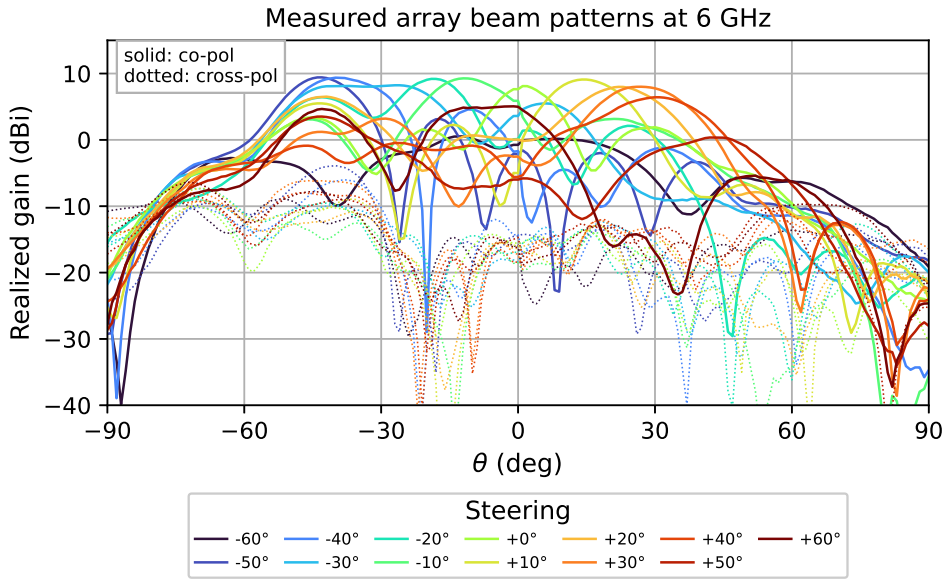


Figure 5.19. Measured co- (solid) and cross-polarized (dotted) beam patterns of the fabricated 8-element array at 6 GHz, steered from $-60°$ to $+60°$ in $10°$ steps. The measured realized gain stays between 7.9 and 9.4 dBi within the $\pm 30°$ scan range, and the cross-polarized level remains more than 20 dB below the co-polarized peak at each commanded angle.

Table 5.2. Comparison with prior-art DMA prototypes.

Reference	Year	Freq.	Elements	Tuning	Efficiency	X-pol iso.	Real. gain
Boyarsky *et al.* [1]	2021	10 GHz	96 (8×12)	varactor	5–11% (tot., meas.)	not reported	7–10 dBi (meas.)
Lin *et al.* [36]	2020	12.5 GHz	10 (1-D, sim.)	p-i-n	75% (rad., sim.)	not reported	10–14 dBi (sim.)
Li *et al.* [125]	2021	12 GHz	16 (1-D)	p-i-n	46–68% (rad., sim.)	not reported	4.3–7.3 dBi (meas.)
Li *et al.* [130]	2022	5.8 GHz	32 (8×4)	p-i-n	53.5% (rad., sim.)	not reported	15 dBi (sim.)
Jabbar *et al.* [98]	2024	60 GHz	16 (1-D)	p-i-n	∼70% (rad., sim.)	not reported	11.6 dBi (meas.)
Jain *et al.* [131]	2025	5.1 GHz	12 (1-D)	p-i-n	45% (rad., sim.)	not reported	4.7–6.7 dBi (meas.)
This work	**2026**	**6 GHz**	**8 (1-D)**	**varactor**	**43–51% (tot., sim.)**	**>20 dB (meas.)**	**7.9–9.4 dBi (meas.)**

a measured total efficiency between 5% and 11% across the scan range and a single 30 dB cross-polarization-isolation value without a cross-polarized pattern. Our 8-element prototype delivers a comparable measured realized gain of 7.9 to 9.4 dBi at 6 GHz and a measured cross-polarization isolation above 20 dB at every steering angle within the $\pm 30°$ scan range. The comparable peak gain is also delivered by an array with twelve times fewer radiating elements, and at a lower operating frequency where the substrate is electrically thinner and the varactor-imposed gap is electrically smaller, both of which tighten the element-level design constraints addressed

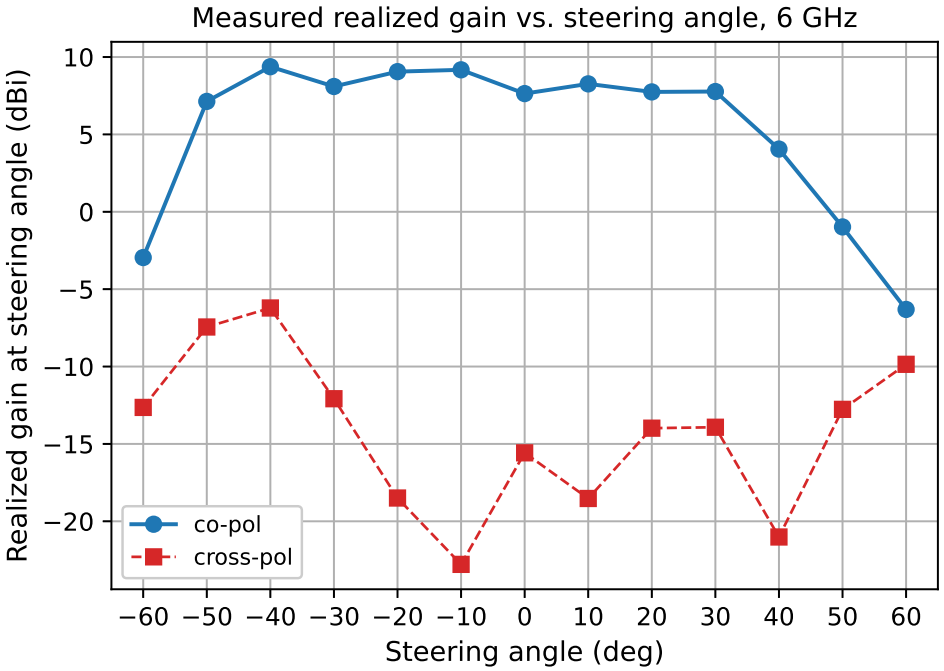
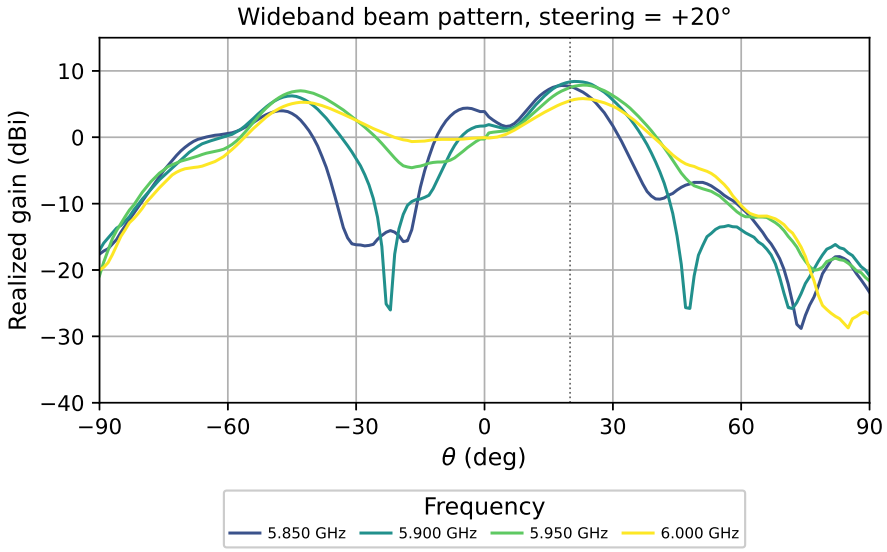


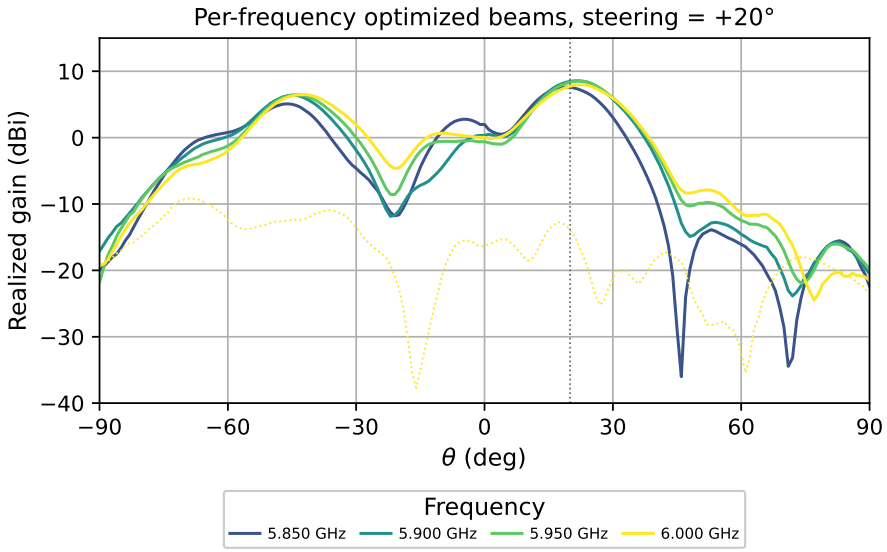
Figure 5.20. Measured co- and cross-polarized realized gain of the fabricated 8-element REMA array at 6 GHz versus commanded steering angle from $-60°$ to $+60°$. The array averages 24.7 dB of cross-polarization isolation within the $\pm 30°$ scan range and rolls off at wider angles due to the element pattern.

in Section 5.3. Although only the simulated total efficiency is reported for this work in Table 5.2, the measured realized gain agrees closely with simulations across the $\pm 30°$ scan range. Realized gain contains the total efficiency as a multiplicative factor, so this agreement indicates that the measured total efficiency is close to the simulated 43–51% range.

The remaining prior-art DMAs in Table 5.2 either operate at higher frequencies where the element-level design problem is less constrained, or rely on p-i-n diodes that restrict the array to a small set of binary-tuning states. The two recent sub-6 GHz designs in [130, 131] fall into the latter category, achieving discrete beam directions through digital coding rather than continuous beamsteering, and neither reports a measured cross-polarized pattern. The higher-frequency designs in [36, 125, 98] report higher simulated radiation efficiencies and, in the case of [98], a measured peak gain of 11.6 dBi at 60 GHz, but operate at frequencies where the electrically thicker substrate relaxes the tradeoffs identified in Section 5.3.2. To our knowledge, the proposed



(a) Single wideband bias



(b) Per-frequency optimized bias

Figure 5.21. Measured beam patterns of the fabricated array at four frequencies from 5.85 to 6.00 GHz, steered to $+20°$, with (a) a single bias configuration optimized for the full bandwidth and (b) a separate bias configuration optimized at each frequency. The dotted vertical line marks the commanded steering target. Single-bias operation maintains the peak gain over a roughly 100 MHz band, while per-frequency optimization recovers an additional 2.2 dBi at 6 GHz.

REMA is the first continuously-tunable sub-6 GHz DMA prototype, and the first DMA at any frequency to characterize cross-polarization isolation across its full scan range.

5.6 Conclusions and future work

In this chapter, we presented the design, fabrication, and experimental characterization of an 8-element sub-6 GHz dynamic metasurface antenna based on the proposed REMA. The element-level design followed a two-stage parametric methodology that selected the elliptical geometry from a tuning-sensitivity comparison across eight candidate designs, and then chose the SIW cavity height and slot offset to balance coupling strength against cross-polarization isolation. The fabricated array operates at 6 GHz with an average measured co-polarized gain of 8.5 dBi within the $\pm 30^{\circ}$ scan range, an average measured cross-polarization isolation of 24.7 dB, and a measured tuning range of 750 MHz. The wideband measurements further showed that a single bias configuration supports an instantaneous bandwidth of approximately 100 MHz. To our knowledge, the proposed REMA is the first continuously-tunable sub-6 GHz DMA prototype, and the first DMA at any frequency to characterize cross-polarization isolation across its full scan range. Future work will extend the REMA design to a two-dimensional aperture for elevation steering, and we plan to characterize the measured total efficiency through full 3D pattern integration. The measurements in this chapter characterize beamsteering only, so another direction is to place nulls with the fabricated array and measure the achievable null depth across the scan range. Demonstrating accurate nulls on hardware would show that the REMA supports interference mitigation in addition to beamsteering. A final step will also integrate the array with a software-defined radio testbed to demonstrate end-to-end DMA-based wireless communication.

Acknowledgment

The authors thank Prof. Daniel Sievenpiper of UC San Diego for access to the anechoic chamber, and Pratap Vangol and David Schwartz for their assistance with the measurement setup. The authors also used Anthropic Claude to assist with the preparation of the manuscript.

Publication Acknowledgment

Chapter 5, in full, has been submitted for publication of the material as it may appear in J. Carlson, S. Keshmiri, M. F. Imani and R. W. Heath, "A sub-6 GHz dynamic metasurface antenna design for improved gain and cross-polarization isolation," submitted to *IEEE Transactions on Antennas and Propagation*. The dissertation author was the primary investigator and author of this paper.

Chapter 6

Conclusions

In this chapter, we summarize the main insights of this dissertation and discuss directions for future work on DMAs.

6.1 Key takeaways

The goal of this dissertation is to establish the DMA as a feasible, energy-efficient alternative to conventional phased arrays. Across the four contributions, we found that the properties that appear to limit a DMA, such as the Lorentzian constraint and frequency selectivity, are better treated as design parameters. Once we model and account for them, the DMA becomes competitive with conventional arrays at a fraction of the power.

Chapter 2 shows that the Lorentzian constraint costs far less beamforming performance than it first appears. The zero-amplitude weight, which has no counterpart in a phase shifter, is what makes the wide beams of a hierarchical codebook possible, and the phase rotation optimization helps to overcome the limitations of the Lorentzian weights. With these two ideas, the DMA approaches the spectral efficiency of a phased array while using far less power, which makes it a viable replacement for conventional arrays.

Chapter 3 shows that the wideband behavior of a DMA is set by design choices rather than fixed by the hardware. The frequency selectivity of the elements causes the beamforming gain to fall away from the center frequency, but this loss depends directly on the element spacing

and the varactor tuning range, since a wider tuning range keeps the full set of Lorentzian weights available across the band. Modeling these effects also gives a closed-form approximation for the beamforming gain, which turns the wideband response into something predictable and controllable.

Chapter 4 shows that what limits advanced array processing with a DMA is the accuracy of its model rather than the Lorentzian constraint. Nulls are far more sensitive to modeling errors than main beams, and the analytical weight model cannot place them reliably because it does not capture the mutual coupling between elements. We found that a machine learning model trained on full-wave simulations does capture this coupling, which enables deep and accurate nullsteering with DMAs. We also found that the DMA can localize sources with a single RF chain by sweeping a null across multiple angles and measuring the received power, and reaches a DOA accuracy close to MUSIC without needing a covariance estimate or the number of sources in advance.

Chapter 5 shows that optimizing the DMA element itself leads to large gains in the performance of the array. A wide tuning range gives each element the range of weights needed for beamforming, but the coupling that widens it also sends more of the resonant energy through the varactor's series resistance. Thus, tuning range comes at the cost of radiation efficiency. By selecting a rotated elliptical geometry at a favorable point on this tradeoff, we improved both the radiation efficiency and the cross-polarization isolation over a conventional square element, and the resulting eight-element prototype matches the measured gain of a DMA with twelve times as many elements.

Together, these contributions take the DMA from a promising concept to an array that we have modeled, optimized, and measured in hardware.

6.2 Future work

Next, we discuss potential directions for future work based on the current contributions in Chapters 2–5.

6.2.1 Multi-user MIMO

While the current work largely considers communicating with a single user, multi-user communication is key in modern wireless systems. Moving to the multi-user setting with DMAs changes several of the assumptions behind the previous chapters. The first is the number of data streams. Each DMA waveguide is fed by a single RF chain and therefore carries one stream, so serving several users at once requires as many waveguides and RF chains as there are streams, and the array becomes a set of coupled subarrays rather than a single aperture. The second is the beamforming objective. Instead of maximizing the gain toward one user, the DMA must maximize the rates of all users together, which requires forming a beam toward each user while keeping the radiated power toward the others low. The nullsteering methods of Chapter 4 are a natural starting point here, since the nulls used to reject interference are the same mechanism needed to separate users. The third is power allocation. Each waveguide feeds a fixed set of elements, so the aperture is partitioned by the hardware and power is allocated per waveguide rather than per user, unlike a fully digital array that can devote any share of its power to any user. The Lorentzian constraint and waveguide scattering further limit the amplitude taper within each waveguide, so the power distribution across a single array is not freely chosen either. Together, these changes call for new DMA architectures, new multi-user beamforming algorithms, and new ways to estimate the user channels.

One direction for future work is to serve multiple users with multiple DMA arrays, where each array handles a different user or group of users. Since each DMA is frequency-selective, these arrays could also operate at slightly different resonant frequencies, which would help separate users in the frequency domain or increase the overall system bandwidth. Configuring

such a system, however, is harder than configuring a single array, since the arrays must be jointly optimized to manage inter-user interference under the Lorentzian-constrained weights. Determining how to design and configure these architectures, and quantifying the resulting gains in spectral and energy efficiency, remains an open problem.

Configuring the arrays in single- or multi-user cases also requires knowledge of the user channels, which is itself difficult to obtain with a DMA. Because each waveguide combines the signals from many elements into a single output, the array measures the combined channel rather than the response of each element. One way forward is to use the reconfigurability of the DMA itself, where sweeping the array through a set of configurations gives a sequence of measurements from which the user channels can be estimated, similar to how the null-scanning method of Chapter 4 estimates directions of arrival. The number of users that can be served at once is also limited by the number of waveguides and by how similar their channels are, so scheduling algorithms that decide which users to serve together would be needed alongside the beamforming.

6.2.2 Integration with the tri-hybrid architecture

While we have shown that a DMA alone can approach the performance of a phased array while consuming significantly less power, adding a small number of phase shifters and digital precoders can improve performance further [91, 134]. This is known as the tri-hybrid architecture, where the precoding and combining are split across a digital layer, an analog phase-shifter layer, and the DMA itself, as shown in Fig. 6.1 [101]. In our recent work, we developed the signal processing foundations for this architecture, including the channel and precoder models that describe how the three layers combine [135]. The tri-hybrid architecture offers more flexibility than a DMA-only system, since the three layers can compensate for one another's limitations while retaining much of the power savings of the DMA.

Extending the methods in this dissertation to the tri-hybrid architecture, however, is not trivial. The three layers are configured under three different sets of weight constraints, where the

digital precoder has unconstrained weights, the analog network has unit-modulus phase-shifter weights, and the DMA has Lorentzian-constrained weights. A beamformer designed for one layer cannot be applied to another. The layers are also physically coupled, since the analog network sets the field that excites the DMA. The three layers therefore cannot be configured one at a time, and the DMA beamforming algorithms from the earlier chapters do not extend directly to the joint problem.

One direction for future work is to develop joint precoding and combining algorithms for the tri-hybrid architecture, which would need to account for all three sets of weight constraints at once and to determine how much of the beamforming each layer should handle. It is also not clear how many phase shifters and RF chains are needed to maximize performance, where they should be placed within the array, or how to balance the added hardware against the resulting increase in power consumption. Answering these questions would also reveal whether the added layers can relax the limitations we found for the DMA alone and help to overcome the restrictions of the Lorentzian constraint.

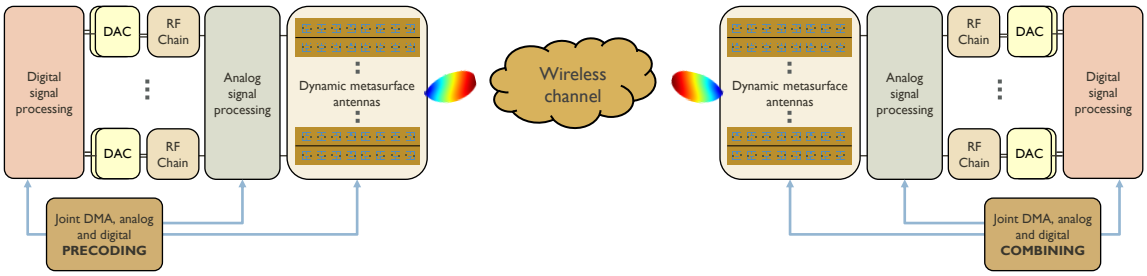


Figure 6.1. Overview of the tri-hybrid architecture using DMAs. To manage the signal processing with three layers of configuration, a joint analog, digital, and DMA precoder or combining algorithm is necessary.

6.2.3 Real-time wireless testbed

While several DMA prototypes have been fabricated, including the prototype in Chapter 5, most are evaluated through antenna measurements rather than in a working wireless link. Recent work has begun to build testbeds that integrate DMAs with radio hardware and demonstrate

communication over the air [104, 136, 137]. These demonstrations are an important first step, but they are limited in scale and do not yet validate the beamforming and array processing methods developed here. A natural next step is to incorporate a fabricated DMA array into a real-time testbed with software-defined radios, such as the USRP setup shown in Fig. 6.2, and to measure how well the DMA performs in a live link, including how reliably it recovers transmitted bits.

Building such a testbed introduces challenges that do not appear in simulation or in chamber measurements. The results in the earlier chapters were obtained with a static channel and a known source direction, whereas a live link must operate over a channel that changes with time and includes multipath. Real-time operation therefore requires channel estimation and synchronization algorithms that account for the structure of the DMA, where the signals received across many elements are combined into a single output through the waveguide. The way performance is measured also changes, from the beamforming gain and spectral efficiency used throughout this dissertation to the bit error rate over a live link, which depends on the entire transceiver chain rather than the antenna alone.

A live system would also expose hardware effects that a model does not capture. The most important is the speed of reconfiguration, since the varactors and their bias circuitry take time to settle, and this rate must be fast enough to update the beam as the channel changes, which sets a limit on how much user mobility the DMA can support. The elements of a fabricated array also vary slightly from one another because of fabrication tolerances, so a real system would need per-element calibration to map the bias voltages to the intended beamforming weights. Characterizing both effects would determine how well the methods developed in this dissertation hold up outside of a controlled setting.

6.2.4 The cost and benefit of DMAs

The preceding chapters establish that a DMA can beamform, steer nulls, and be built and measured in hardware. A separate question is whether the DMA is worth using in place of a conventional array. Answering this requires comparing the two architectures on the terms that

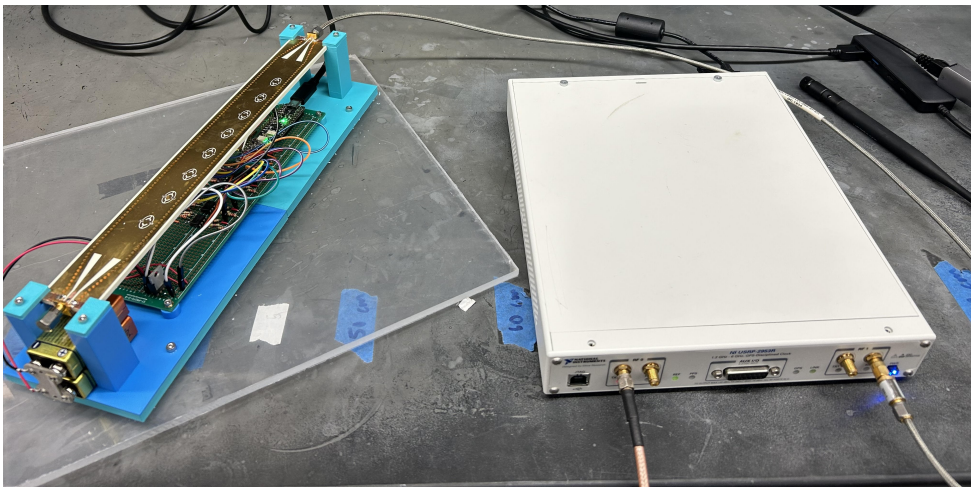


Figure 6.2. Hardware setup for a potential DMA-based wireless testbed with the fabricated DMA array on the left and a USRP radio on the right.

matter to a system designer, which are the loss through the beamforming network, the cost and area of the components, and the complexity of controlling them. We compare an eight-element DMA against an eight-element phased array at C-band using commercially available parts for both.

The clearest advantage of the DMA is that it removes the beamforming network entirely. A phased array needs one phase shifter per element, and a six-bit C-band phase shifter, such as the MACOM MAPS-010165, introduces roughly 5.5 dB of insertion loss [138] along with the power divider needed to feed it. The DMA replaces this network with varactors integrated into the radiating elements, so the guided wave is shaped as it propagates rather than being split, phase shifted, and recombined. Removing the network removes the dominant cost and area terms as well. The eight phase shifters cost roughly $\$855$ and occupy about 256 mm^2 together with their per-element amplifiers [139], compared with about $\$106$ of varactors for the DMA, which needs only 17 mm^2 because a single radio frequency chain requires a single amplifier. Component prices are taken from distributor listings and are intended to show the relative scale of the two architectures rather than exact system cost.

Accounting for all the losses, the DMA is competitive at C-band despite its lower radiation

efficiency. The DMA loses about $1 - 2$ dB in the substrate-integrated waveguide and radiates with roughly 50% efficiency, which together give about $4 - 5$ dB of loss from input to radiated field. The phased array loses about 5.5 dB in the phase shifters and 1 dB in the divider, and may radiate with around 95% efficiency, which gives about $6.5 - 7$ dB. The DMA therefore delivers slightly more radiated power than the phased array while using a fraction of the beamforming hardware.

The DMA also changes the nature of the control problem rather than simply reducing it. An eight-element phased array with six-bit phase shifters requires 48 digital control lines, whereas the DMA requires 8 analog bias voltages from a single digital-to-analog converter, such as the Texas Instruments DAC6578 [140]. The DMA needs far fewer connections, but it replaces discrete and repeatable phase states with continuous analog voltages whose mapping to beamforming weights depends on the varactor response. At millimeter wave the comparison changes again, since a beamforming integrated circuit such as the Renesas F5288 combines the phase shifters, amplifiers, and control into a single device addressed over a serial bus [141]. The trade-offs here, however, are more difficult to establish because the power consumption and cost of these parts are not readily available.

Overall, the case for the DMA is strongest where the array is large, and the cost and area per element matter. Establishing that case more firmly, however, requires answering several questions that this comparison leaves open. The numbers above are for an eight-element array, and the balance may shift as the array grows and the waveguide carries the guided wave over a longer distance. The power consumption of integrated beamforming hardware is not readily available, so the comparison at higher frequencies is unsettled. Settling these questions will require a systematic comparison of the two architectures across array sizes and frequency bands, built on measured power consumption rather than datasheet values. This is an important direction for future work, since the decision to adopt DMAs in a deployed system depends on these numbers.

Bibliography

[1] M. Boyarsky, T. Sleasman, M. F. Imani, J. N. Gollub, and D. R. Smith, "Electronically steered metasurface antenna," *Scientific Reports*, vol. 11, no. 1, p. 4693, Feb. 2021.

[2] F. Boccardi, R. W. Heath, A. Lozano, T. L. Marzetta, and P. Popovski, "Five disruptive technology directions for 5G," *IEEE Commun. Mag.*, vol. 52, no. 2, pp. 74–80, Feb. 2014.

[3] J. G. Andrews, S. Buzzi, W. Choi, S. V. Hanly, A. Lozano, A. C. K. Soong, and J. C. Zhang, "What will 5G be?" *IEEE J. Sel. Areas Commun.*, vol. 32, no. 6, pp. 1065–1082, Jun. 2014.

[4] W. Saad, M. Bennis, and M. Chen, "A vision of 6G wireless systems: Applications, trends, technologies, and open research problems," *IEEE Netw.*, vol. 34, no. 3, pp. 134–142, May 2020.

[5] E. Björnson, J. Hoydis, M. Kountouris, and M. Debbah, "Massive MIMO systems with non-ideal hardware: Energy efficiency, estimation, and capacity limits," *IEEE Trans. Inf. Theory*, vol. 60, no. 11, pp. 7112–7139, Nov. 2014.

[6] E. Björnson, E. G. Larsson, and T. L. Marzetta, "Massive MIMO: Ten myths and one critical question," *IEEE Commun. Mag.*, vol. 54, no. 2, pp. 114–123, Feb. 2016.

[7] F. Rusek, D. Persson, B. K. Lau, E. G. Larsson, T. L. Marzetta, O. Edfors, and F. Tufvesson, "Scaling up MIMO: Opportunities and challenges with very large arrays," *IEEE Signal Process. Mag.*, vol. 30, no. 1, pp. 40–60, Jan. 2013.

[8] T. L. Marzetta, "Noncooperative cellular wireless with unlimited numbers of base station antennas," *IEEE Trans. Wireless Commun.*, vol. 9, no. 11, pp. 3590–3600, Nov. 2010.

[9] E. G. Larsson, O. Edfors, F. Tufvesson, and T. L. Marzetta, "Massive MIMO for next generation wireless systems," *IEEE Commun. Mag.*, vol. 52, no. 2, pp. 186–195, Feb. 2014.

[10] X. Yang, M. Matthaiou, J. Yang, C.-K. Wen, F. Gao, and S. Jin, "Hardware-constrained millimeter-wave systems for 5G: Challenges, opportunities, and solutions," *IEEE Commun. Mag.*, vol. 57, no. 1, pp. 44–50, Jan. 2019.

[11] L. N. Ribeiro, S. Schwarz, M. Rupp, and A. L. de Almeida, "Energy efficiency of mmWave massive MIMO precoding with low-resolution DACs," *IEEE J. of Sel. Topics Signal Process.*, vol. 12, no. 2, pp. 298–312, Apr. 2018.

[12] H. Q. Ngo, E. G. Larsson, and T. L. Marzetta, "Energy and spectral efficiency of very large multiuser MIMO systems," *IEEE Trans. Commun.*, vol. 61, no. 4, pp. 1436–1449, Apr. 2013.

[13] R. W. Heath, N. González-Prelcic, S. Rangan, W. Roh, and A. M. Sayeed, "An overview of signal processing techniques for millimeter wave MIMO systems," *IEEE J. Sel. Topics Signal Process.*, vol. 10, no. 3, pp. 436–453, Apr. 2016.

[14] A. F. Molisch, V. V. Ratnam, S. Han, Z. Li, S. L. H. Nguyen, L. Li, and K. Haneda, "Hybrid beamforming for massive MIMO: A survey," *IEEE Commun. Mag.*, vol. 55, no. 9, pp. 134–141, Sep. 2017.

[15] I. Ahmed, H. Khammari, A. Shahid, A. Musa, K. S. Kim, E. De Poorter, and I. Moerman, "A survey on hybrid beamforming techniques in 5G: Architecture and system model perspectives," *IEEE Commun. Surveys Tuts.*, vol. 20, no. 4, pp. 3060–3097, 2018.

[16] O. El Ayach, S. Rajagopal, S. Abu-Surra, Z. Pi, and R. W. Heath, "Spatially sparse precoding in millimeter wave MIMO systems," *IEEE Trans. Wireless Commun.*, vol. 13, no. 3, pp. 1499–1513, Mar. 2014.

[17] A. Alkhateeb, J. Mo, N. Gonzalez-Prelcic, and R. W. Heath, "MIMO precoding and combining solutions for millimeter-wave systems," *IEEE Commun. Mag.*, vol. 52, no. 12, pp. 122–131, 2014.

[18] S. Han, C.-l. I, Z. Xu, and C. Rowell, "Large-scale antenna systems with hybrid analog and digital beamforming for millimeter wave 5G," *IEEE Commun. Mag.*, vol. 53, no. 1, pp. 186–194, Jan. 2015.

[19] M.-D. Tsai and A. Natarajan, "60GHz passive and active RF-path phase shifters in silicon," in *Proc. of 2009 IEEE RFIC Symp.*, Jun. 2009, pp. 223–226.

[20] X. Gao, L. Dai, S. Han, C.-L. I, and R. W. Heath, "Energy-efficient hybrid analog and digital precoding for mmWave MIMO systems with large antenna arrays," *IEEE J. Sel. Areas Commun.*, vol. 34, no. 4, pp. 998–1009, Apr. 2016.

[21] R. Méndez-Rial, C. Rusu, N. González-Prelcic, A. Alkhateeb, and R. W. Heath, "Hybrid MIMO architectures for millimeter wave communications: Phase shifters or switches?" *IEEE Access*, vol. 4, pp. 247–267, Jan. 2016.

[22] J. Brady, N. Behdad, and A. M. Sayeed, "Beamspace MIMO for millimeter-wave communications: System architecture, modeling, analysis, and measurements," *IEEE Trans. Antennas Propag.*, vol. 61, no. 7, pp. 3814–3827, Jul. 2013.

[23] S. Park, A. Alkhateeb, and R. W. Heath, "Dynamic subarrays for hybrid precoding in wideband mmWave MIMO systems," *IEEE Trans. Wireless Commun.*, vol. 16, no. 5, pp. 2907–2920, May 2017.

[24] R. L. Haupt and M. Lanagan, "Reconfigurable antennas," *IEEE Antennas Propag. Mag.*, vol. 55, no. 1, pp. 49–61, Feb. 2013.

[25] J. Costantine, Y. Tawk, S. E. Barbin, and C. G. Christodoulou, "Reconfigurable antennas: Design and applications," *Proc. IEEE*, vol. 103, no. 3, pp. 424–437, Mar. 2015.

[26] C. G. Christodoulou, Y. Tawk, S. A. Lane, and S. R. Erwin, "Reconfigurable antennas for wireless and space applications," *Proceedings of the IEEE*, vol. 100, no. 7, pp. 2250–2261, Jul. 2012.

[27] E. Basar, M. Di Renzo, J. De Rosny, M. Debbah, M.-S. Alouini, and R. Zhang, "Wireless communications through reconfigurable intelligent surfaces," *IEEE access*, vol. 7, pp. 116 753–116 773, Aug. 2019.

[28] M. Di Renzo, A. Zappone, M. Debbah, M.-S. Alouini, C. Yuen, J. de Rosny, and S. Tretyakov, "Smart radio environments empowered by reconfigurable intelligent surfaces: How it works, state of research, and the road ahead," *IEEE J. Sel. Areas Commun.*, vol. 38, no. 11, pp. 2450–2525, Nov. 2020.

[29] N. Shlezinger, G. C. Alexandropoulos, M. F. Imani, Y. C. Eldar, and D. R. Smith, "Dynamic metasurface antennas for 6G extreme massive MIMO communications," *IEEE Wireless Commun.*, vol. 28, no. 2, pp. 106–113, 2021.

[30] C. L. Holloway, E. F. Kuester, J. A. Gordon, J. O'Hara, J. Booth, and D. R. Smith, "An overview of the theory and applications of metasurfaces: The two-dimensional equivalents of metamaterials," *IEEE Antennas Propag. Mag.*, vol. 54, no. 2, pp. 10–35, Apr. 2012.

[31] N. Yu and F. Capasso, "Flat optics with designer metasurfaces," *Nature Materials*, vol. 13, no. 2, pp. 139–150, Feb. 2014.

[32] S. B. Glybovski, S. A. Tretyakov, P. A. Belov, Y. S. Kivshar, and C. R. Simovski, "Metasurfaces: From microwaves to visible," *Physics Reports*, vol. 634, pp. 1–72, 2016.

[33] T. J. Cui, M. Q. Qi, X. Wan, J. Zhao, and Q. Cheng, "Coding metamaterials, digital metamaterials and programmable metamaterials," *Light Sci. Appl.*, vol. 3, no. 10, p. e218, 2014.

[34] D. R. Smith, O. Yurduseven, L. P. Mancera, P. Bowen, and N. B. Kundtz, "Analysis of a waveguide-fed metasurface antenna," *Physical Review Applied*, vol. 8, no. 5, p. 054048, Nov. 2017.

[35] T. Sleasman, M. F. Imani, W. Xu, J. Hunt, T. Driscoll, M. S. Reynolds, and D. R. Smith, "Waveguide-fed tunable metamaterial element for dynamic apertures," *IEEE Antennas Wireless Propag. Lett.*, vol. 15, pp. 606–609, July 2016.

[36] M. Lin, X. Huang, B. Deng, J. Zhang, D. Guan, D. Yu, and Y. Qin, "A high-efficiency reconfigurable element for dynamic metasurface antenna," *IEEE Access*, vol. 8, pp. 87 446–87 455, May 2020.

[37] M. Boyarsky, T. Sleasman, L. Pulido-Mancera, T. Fromenteze, A. Pedross-Engel, C. M. Watts, M. F. Imani, M. S. Reynolds, and D. R. Smith, "Synthetic aperture radar with dynamic metasurface antennas: a conceptual development," *JOSA A*, vol. 34, no. 5, pp. A22–A36, May 2017.

[38] T. Sleasman, M. Boyarsky, L. Pulido-Mancera, T. Fromenteze, M. F. Imani, M. S. Reynolds, and D. R. Smith, "Experimental synthetic aperture radar with dynamic metasurfaces," *IEEE Trans. Antennas Propag.*, vol. 65, no. 12, pp. 6864–6877, Dec. 2017.

[39] N. Shlezinger, O. Dicker, Y. C. Eldar, I. Yoo, M. F. Imani, and D. R. Smith, "Dynamic metasurface antennas for uplink massive MIMO systems," *IEEE Trans. Commun.*, vol. 67, no. 10, pp. 6829–6843, Oct. 2019.

[40] H. Wang, N. Shlezinger, Y. C. Eldar, S. Jin, M. F. Imani, I. Yoo, and D. R. Smith, "Dynamic metasurface antennas for MIMO-OFDM receivers with bit-limited ADCs," *IEEE Trans. Commun.*, vol. 69, no. 4, pp. 2643–2659, Apr. 2021.

[41] L. You, J. Xu, G. C. Alexandropoulos, J. Wang, W. Wang, and X. Gao, "Energy efficiency maximization of massive MIMO communications with dynamic metasurface antennas," *IEEE Trans. Wireless Commun.*, vol. 22, no. 1, pp. 393–407, Jan. 2023.

[42] L. Pulido-Mancera, P. T. Bowen, M. F. Imani, N. B. Kundtz, and D. R. Smith, "Polarizability extraction of complementary metamaterial elements in waveguides for aperture modeling," *Physical Review B*, vol. 96, no. 23, p. 235402, Dec. 2017.

[43] Z. Xiao, T. He, P. Xia, and X.-G. Xia, "Hierarchical codebook design for beamforming training in millimeter-wave communication," *IEEE Trans. Wireless Commun.*, vol. 15, no. 5, pp. 3380–3392, May 2016.

[44] F. Gao, B. Wang, C. Xing, J. An, and G. Y. Li, "Wideband beamforming for hybrid massive MIMO terahertz communications," *IEEE J. Sel. Areas Commun.*, vol. 39, no. 6, pp. 1725–1740, June 2021.

[45] R. L. Haupt, "Phase-only adaptive nulling with a genetic algorithm," *IEEE Trans. Antennas Propag.*, vol. 45, no. 6, pp. 1009–1015, June 1997.

[46] R. O. Schmidt, "Multiple emitter location and signal parameter estimation," *IEEE Trans. Antennas Propag.*, vol. 34, no. 3, pp. 276–280, Mar. 1986.

[47] A. Mezghani and R. W. Heath, "The information and wave-theoretic limits of analog beamforming," in *Proc. of 2018 Inf. Theory Appl. Workshop (ITA)*, 2018, pp. 1–6.

[48] Z. Xiao, L. Zhu, Y. Liu, P. Yi, R. Zhang, X.-G. Xia, and R. Schober, "A survey on millimeter-wave beamforming enabled uav communications and networking," *IEEE Commun. Surveys Tuts.*, vol. 24, no. 1, pp. 557–610, 2022.

[49] N. Behdad and K. Sarabandi, "Dual-band reconfigurable antenna with a very wide tunability range," *IEEE Trans. Antennas Propag.*, vol. 54, no. 2, pp. 409–416, Feb. 2006.

[50] C. Panagamuwa, A. Chauraya, and J. Vardaxoglou, "Frequency and beam reconfigurable antenna using photoconducting switches," *IEEE Trans. Antennas Propag.*, vol. 54, no. 2, pp. 449–454, Feb. 2006.

[51] D. Piazza, N. J. Kirsch, A. Forenza, R. W. Heath, and K. R. Dandekar, "Design and evaluation of a reconfigurable antenna array for MIMO systems," *IEEE Trans. Antennas Propag.*, vol. 56, no. 3, pp. 869–881, Mar. 2008.

[52] S. J. Mazlouman, M. Soleimani, A. Mahanfar, C. Menon, and R. Vaughan, "Pattern reconfigurable square ring patch antenna actuated by hemispherical dielectric elastomer," *Electron. Lett.*, vol. 47, no. 3, pp. 164–165, Feb. 2011.

[53] L. Dixit and P. Pourush, "Radiation characteristics of switchable ferrite microstrip array antenna," *IEE Proceedings-Microwaves, Antennas Propag.*, vol. 147, no. 2, pp. 151–155, Apr. 2000.

[54] L. Liu and R. Langley, "Liquid crystal tunable microstrip patch antenna," *Electron. Lett.*, vol. 44, no. 20, pp. 1179–1181, Sept. 2008.

[55] P. T. Bowen, M. Boyarsky, L. M. Pulido-Mancera, D. R. Smith, O. Yurduseven, and M. Sazegar, "Optimizing polarizability distributions for metasurface apertures with lorentzian-constrained radiators," *arXiv preprint arXiv:2205.02747*, May 2022.

[56] M. Boyarsky, M. F. Imani, and D. R. Smith, "Grating lobe suppression in metasurface antenna arrays with a waveguide feed layer," *Optics Express*, vol. 28, no. 16, pp. 23 991–24 004, Aug. 2020.

[57] M. C. Johnson, S. L. Brunton, N. B. Kundtz, and J. N. Kutz, "Sidelobe canceling for reconfigurable holographic metamaterial antenna," *IEEE Trans. Antennas Propag.*, vol. 63, no. 4, pp. 1881–1886, Apr. 2015.

[58] W. Huang, H. Zhang, N. Shlezinger, and Y. C. Eldar, "Joint microstrip selection and beamforming design for mmwave systems with dynamic metasurface antennas," in *Proc. IEEE Int. Conf. Acoustics, Speech and Signal Process. (ICASSP)*, June 2023, pp. 1–5.

[59] D. Feng, C. Jiang, G. Lim, L. J. Cimini, G. Feng, and G. Y. Li, "A survey of energy-efficient wireless communications," *IEEE Commun. Surveys Tuts.*, vol. 15, no. 1, pp. 167–178, Feb. 2013.

[60] K. N. R. S. V. Prasad, E. Hossain, and V. K. Bhargava, "Energy efficiency in massive MIMO-based 5G networks: Opportunities and challenges," *IEEE Wireless Commun.*, vol. 24, no. 3, pp. 86–94, June 2017.

[61] D. Ha, K. Lee, and J. Kang, "Energy efficiency analysis with circuit power consumption in massive MIMO systems," in *Proc. of 2013 IEEE 24th Annu. Int. Symp. PIMRC*, Sept. 2013, pp. 938–942.

[62] S. Dong, Y. Wang, L. Jiang, and Y. Chen, "Energy efficiency analysis with circuit power consumption in downlink large-scale multiple antenna systems," in *Proc. of 2016 IEEE 83rd VTC*, May 2016, pp. 1–5.

[63] E. Björnson, L. Sanguinetti, J. Hoydis, and M. Debbah, "Optimal design of energy-efficient multi-user MIMO systems: Is massive MIMO the answer?" *IEEE Trans. Wireless Commun.*, vol. 14, no. 6, pp. 3059–3075, June 2015.

[64] L. Zhou and Y. Ohashi, "Efficient codebook-based MIMO beamforming for millimeter-wave WLANs," in *Proc. of 2012 IEEE 23rd Int. Symp. PIMRC*, 2012, pp. 1885–1889.

[65] A. N. Uwaechia and N. M. Mahyuddin, "A comprehensive survey on millimeter wave communications for fifth-generation wireless networks: Feasibility and challenges," *IEEE Access*, vol. 8, pp. 62 367–62 414, 2020.

[66] D. Pérez-Adán, Ó. Fresnedo, J. P. González-Coma, and L. Castedo, "Intelligent reflective surfaces for wireless networks: An overview of applications, approached issues, and open problems," *Electronics*, vol. 10, no. 19, p. 2345, 2021.

[67] R. W. Heath Jr and A. Lozano, *Foundations of MIMO communication*. Cambridge University Press, 2018.

[68] C. Beckman and B. Lindmark, "The evolution of base station antennas for mobile communications," in *Proc. of 2007 ICEAA*, Sept. 2007, pp. 85–92.

[69] C. A. Balanis, *Antenna theory: analysis and design*, 4th ed. John Wiley & Sons, 2016.

[70] F. Burkhardt, S. Jaeckel, E. Eberlein, and R. Prieto-Cerdeira, "QuaDRiGa: A MIMO channel model for land mobile satellite," in *Proc. of EuCAP 2014*, Apr. 2014, pp. 1274–1278.

[71] J. Wang, Y. Li, Z. H. Jiang, T. Shi, M.-C. Tang, Z. Zhou, Z. N. Chen, and C.-W. Qiu, "Metantenna: When metasurface meets antenna again," *IEEE Trans. Antennas Propag.*, vol. 68, no. 3, pp. 1332–1347, Mar. 2020.

[72] M. Faenzi, G. Minatti, D. González-Ovejero, F. Caminita, E. Martini, C. Della Giovampaola, and S. Maci, "Metasurface antennas: New models, applications and realizations," *Scientific reports*, vol. 9, no. 1, p. 10178, Jul. 2019.

[73] M. E. Badawe, T. S. Almoneef, and O. M. Ramahi, "A true metasurface antenna," *Scientific Reports*, vol. 6, no. 1, p. 19268, Jan. 2016.

[74] R. Deng, B. Di, H. Zhang, Y. Tan, and L. Song, "Reconfigurable holographic surface-enabled multi-user wireless communications: Amplitude-controlled holographic beamforming," *IEEE Trans. Wireless Commun.*, vol. 21, no. 8, pp. 6003–6017, Aug. 2022.

[75] R.-B. Hwang, "Binary meta-hologram for a reconfigurable holographic metamaterial antenna," *Scientific Reports*, vol. 10, no. 1, p. 8586, May 2020.

[76] S. Pan, D. Zhai, Y. Feng, L. Qi, and G. Li, "Design of a waveguide-fed dynamic reconfigurable metasurface element," in *Proc. of IEEE Int. Conf. Microwave Millimeter Wave Technol. (ICMMT)*, Sep. 2020, pp. 1–3.

[77] H. Wang, "Joint transmitter and receiver design for uplink MU-MIMO systems with dynamic metasurface antennas," in *Proc. IEEE 95th Veh. Technol. Conf. (VTC)*, June 2022, pp. 1–5.

[78] W. Huang, L. Xu, H. Zhang, C. Kai, C. Li, and Y. Huang, "Structured OFDM modulation for XL-MIMO system with dual-wideband effects," *IEEE Trans. Wireless Commun.*, vol. 24, no. 2, pp. 1510–1525, Feb. 2025.

[79] H. Zhang, N. Shlezinger, F. Guidi, D. Dardari, M. F. Imani, and Y. C. Eldar, "Beam focusing for near-field multiuser MIMO communications," *IEEE Trans. Wireless Commun.*, vol. 21, no. 9, pp. 7476–7490, Sept. 2022.

[80] S. Kimaryo and K. Lee, "Downlink beamforming for dynamic metasurface antennas," *IEEE Trans. Wireless Commun.*, vol. 22, no. 7, pp. 4745–4755, July 2023.

[81] A. Azarbahram, O. L. López, R. D. Souza, R. Zhang, and M. Latva-Aho, "Energy beamforming for RF wireless power transfer with dynamic metasurface antennas," *IEEE Wireless Commun. Lett.*, vol. 13, no. 3, pp. 781–785, Mar. 2024.

[82] A. D. Scher and E. F. Kuester, "Extracting the bulk effective parameters of a metamaterial via the scattering from a single planar array of particles," *Metamaterials*, vol. 3, no. 1, pp. 44–55, Feb. 2009.

[83] L. M. Pulido Mancera, "Analytical modeling of waveguide-fed metasurfaces for microwave imaging and beamforming," PhD Thesis, Duke University, 2018.

[84] J. Carlson, N. V. Deshpande, M. R. Castellanos, and R. W. Heath, "Analysis of dynamic metasurface antennas under matching network constraints," in *2024 58th Asilomar Conference on Signals, Systems, and Computers*, Oct. 2024, pp. 614–618.

[85] ——, "A wideband beamforming algorithm for dynamic metasurface antennas under realistic constraints," in *ICC 2025 - IEEE International Conference on Communications*, June 2025, pp. 3922–3927.

[86] J. Carlson, M. R. Castellanos, and R. W. Heath, "Hierarchical codebook design with dynamic metasurface antennas for energy-efficient arrays," *IEEE Trans. Wireless Commun.*, vol. 23, no. 10, pp. 14 790–14 804, Oct. 2024.

[87] N. V. Deshpande, J. Carlson, M. R. Castellanos, and R. W. Heath Jr, "Frequency-selective beamforming and single-shot beam training with dynamic metasurface antennas," arXiv preprint arXiv:2412.00215, 2024, https://arxiv.org/abs/2412.00215.

[88] I. Yoo, D. R. Smith, and M. Boyarsky, "Experimental characterization of a waveguide-fed varactor-tuned metamaterial element using the coupled dipole framework," *IEEE Antennas Wireless Propag. Lett.*, vol. 22, no. 2, pp. 387–391, Feb. 2023.

[89] N. Deshpande, M. R. Castellanos, S. R. Khosravirad, J. Du, H. Viswanathan, and R. W. Heath, "A wideband generalization of the near-field region for extremely large phased-arrays," *IEEE Wireless Commun. Lett.*, vol. 12, no. 3, pp. 515–519, Mar. 2023.

[90] A. A. Oliner and D. R. Jackson, "Leaky-wave antennas," in *Antenna Engineering Handbook*, 4th ed., J. L. Volakis, Ed. New York, NY, USA: McGraw-Hill, 2007, ch. 11.

[91] M. R. Castellanos, J. Carlson, and R. W. Heath, "Energy-efficient tri-hybrid precoding with dynamic metasurface antennas," in *2023 57th Asilomar Conf. Signals, Syst., Comput.*, Oct. 2023, pp. 1625–1630.

[92] C. Mack, *Fundamental Principles of Optical Lithography: the Science of Microfabrication*. John Wiley & Sons, 2007.

[93] D. R. Smith, M. Sazegar, and I. Yoo, "Equivalence of polarizability and circuit models for waveguide-fed metamaterial elements," *IEEE Trans. Antennas Propag.*, vol. 73, no. 1, pp. 7–21, Jan. 2025.

[94] H. L. Van Trees, *Optimum array processing: Part IV of detection, estimation, and modulation theory*. John Wiley & Sons, 2002.

[95] R. M. Davis, "Phase-only LMS and perturbation adaptive algorithms," *IEEE Trans. Aerosp. Electron. Syst.*, vol. 34, no. 1, pp. 169–178, Jan. 1998.

[96] Z. Zhao, H. Zhao, M. Zheng, and J. Tang, "Real-time phase-only nulling based on deep neural network with robustness," *IEEE Access*, vol. 7, pp. 142 287–142 294, Sep. 2019.

[97] T. Sleasman, M. F. Imani, J. N. Gollub, and D. R. Smith, "Dynamic metamaterial aperture for microwave imaging," *Applied Physics Letters*, vol. 107, no. 20, p. 204104, Nov. 2015.

[98] A. Jabbar, M. Elsayed, J. Ur Rehman Kazim, Z. Pang, J. Le Kernec, M. Ali Imran, Q. H. Abbasi, and M. Ur-Rehman, "60 GHz programmable dynamic metasurface antenna (DMA) for next-generation communication, sensing, and imaging applications: From concept to prototype," *IEEE Open J. Antennas Propag.*, vol. 5, no. 3, pp. 705–726, Jun. 2024.

[99] T. A. Sleasman, M. F. Imani, A. V. Diebold, M. Boyarsky, K. P. Trofatter, and D. R. Smith, "Implementation and characterization of a two-dimensional printed circuit dynamic metasurface aperture for computational microwave imaging," *IEEE Trans. Antennas Propag.*, vol. 69, no. 4, pp. 2151–2164, Apr. 2021.

[100] A. M. Molaei, V. Skouroliakou, V. Fusco, and O. Yurduseven, "Efficient 3D image reconstruction for near-field microwave imaging using dynamic metasurface antenna," *IEEE Access*, vol. 10, pp. 68 491–68 498, June 2022.

[101] R. W. Heath, J. Carlson, N. V. Deshpande, M. R. Castellanos, M. Akrout, and C.-B. Chae, "The tri-hybrid MIMO architecture," *IEEE Wireless Commun.*, vol. 33, no. 1, pp. 199–206, Feb. 2026.

[102] S. F. Kimaryo and K. Lee, "Weighted sum rate maximization for DMA-based MU-MIMO system," in *Proc. IEEE ICTC*, Oct. 2024, pp. 1171–1176.

[103] J. Carlson, N. V. Deshpande, and R. W. Heath, "Interference-resistant reconfigurable antenna arrays via dynamic metasurface antennas," in *Proc. IEEE Mil. Commun. Conf. (MILCOM)*, Oct. 2025, pp. 466–471.

[104] F. Yven, J. Tapie, J. Sol, and P. del Hougne, "End-to-end dynamic metasurface antenna wireless system: Prototype, opportunities, and challenges," *arXiv preprint arXiv:2506.09732*, Jun. 2025.

[105] J. H. Kim and S. W. Choi, "A deep learning-based approach for radiation pattern synthesis of an array antenna," *IEEE Access*, vol. 8, pp. 226 059–226 063, Dec. 2020.

[106] A. M. Montaser and K. R. Mahmoud, "Deep learning based antenna design and beam-steering capabilities for millimeter-wave applications," *IEEE Access*, vol. 9, pp. 145 583–145 591, Oct. 2021.

[107] Q. Wu, W. Chen, C. Yu, H. Wang, and W. Hong, "Machine learning-assisted array synthesis using active base element modeling," *IEEE Trans. Antennas Propag.*, vol. 70, no. 7, pp. 5054–5065, July 2022.

[108] K. Cao, C. Jin, B. Zhang, Q. Lv, and F. Lu, "Beam stabilization of deformed conformal array antenna based on physical-method-driven deep learning," *IEEE Trans. Antennas Propag.*, vol. 71, no. 5, pp. 4115–4127, May 2023.

[109] S. K. Patel, J. Surve, V. Katkar, and J. Parmar, "Machine learning assisted metamaterial-based reconfigurable antenna for low-cost portable electronic devices," *Scientific Reports*, vol. 12, no. 1, p. 12354, Jul. 2022.

[110] M. S. Yahya, S. Soeung, S. K. A. Rahim, U. Musa, S. S. B. Hashwan, and M. A. Haque, "Machine learning-optimized compact frequency reconfigurable antenna with RSSI enhancement for long-range applications," *IEEE Access*, vol. 12, pp. 10 970–10 987, Jan. 2024.

[111] A. Salisu, M. A. Elwanis, I. Elfergani, U. Musa, A. Alfares, I. Gharbia, J. Rodriguez, C. H. See, and R. Abd-Alhameed, "Machine learning-optimized compact wearable frequency reconfigurable antenna for sub-6 GHz/mm-wave 5G integration," *Scientific Reports*, vol. 15, no. 1, p. 44912, Dec. 2025.

[112] C. Plapous, J. Cheng, E. Taillefer, A. Hirata, and T. Ohira, "Reactance domain MUSIC algorithm for electronically steerable parasitic array radiator," *IEEE Trans. Antennas Propag.*, vol. 52, no. 12, pp. 3257–3264, Dec. 2004.

[113] E. Taillefer, A. Hirata, and T. Ohira, "Reactance-domain ESPRIT algorithm for a hexagonally shaped seven-element ESPAR antenna," *IEEE Trans. Antennas Propag.*, vol. 53, no. 11, pp. 3486–3495, Nov. 2005.

[114] S. Abielmona, H. V. Nguyen, and C. Caloz, "Analog direction of arrival estimation using an electronically-scanned CRLH leaky-wave antenna," *IEEE Trans. Antennas Propag.*, vol. 59, no. 4, pp. 1408–1412, Apr. 2011.

[115] S. Chen, B. Sima, F. Xi, W. Wu, and Z. Liu, "Super-resolution DOA estimation using dynamic metasurface antenna," in *Proc. European Conf. Antennas Propag. (EuCAP)*, Mar. 2020, pp. 1–4.

[116] L. Hou, L. Jin, K. Huang, S. Xiao, Y. Lou, and Y. Chen, "Beamspace spatial smoothing MUSIC DOA estimation method using dynamic metasurface antenna," *Entropy*, vol. 27, no. 4, p. 335, 2025.

[117] D. M. Pozar, *Microwave Engineering*, 4th ed. Hoboken, NJ, USA: John Wiley & Sons, 2011.

[118] B. Friedlander, "The extended manifold for antenna array calibration," in *Proc. Asilomar Conf. Signals, Syst., Comput.*, Oct. 2021, pp. 216–220.

[119] C. Zheng, H. Chen, and A. Wang, "A fast sparse covariance-based fitting method for DOA estimation via non-negative least squares," in *Proc. IEEE Int. Conf. Acoustics, Speech and Signal Process. (ICASSP)*, May 2020, pp. 4786–4790.

[120] J.-I. Oh, J.-W. Kim, S. H. Han, S. Kim, J.-W. Yu, and I.-J. Hwang, "Pattern reconfigurable dual-polarized dipole antenna with staggered parasitic elements," *IEEE Access*, vol. 10, pp. 93 773–93 784, Aug. 2022.

[121] J.-S. Row and C.-W. Tsai, "Pattern reconfigurable antenna array with circular polarization," *IEEE Trans. Antennas Propag.*, vol. 64, no. 4, pp. 1525–1530, Apr. 2016.

[122] A. Mansoul, F. Ghanem, M. R. Hamid, and M. Trabelsi, "A selective frequency-reconfigurable antenna for cognitive radio applications," *IEEE Antennas Wireless Propag. Lett.*, vol. 13, pp. 515–518, Mar. 2014.

[123] H. Zhu, X. Liu, S. Cheung, and T. Yuk, "Frequency-reconfigurable antenna using metasurface," *IEEE Trans. Antennas Propag.*, vol. 62, no. 1, pp. 80–85, Jan. 2014.

[124] N. Nguyen-Trong, L. Hall, and C. Fumeaux, "A frequency- and polarization-reconfigurable stub-loaded microstrip patch antenna," *IEEE Trans. Antennas Propag.*, vol. 63, no. 11, pp. 5235–5240, Nov. 2015.

[125] S. Li, F. Xu, X. Wan, T. J. Cui, and Y.-Q. Jin, "Programmable metasurface based on substrate-integrated waveguide for compact dynamic-pattern antenna," *IEEE Trans. Antennas Propag.*, vol. 69, no. 5, pp. 2958–2962, May 2021.

[126] I. Yoo, M. F. Imani, T. Sleasman, and D. R. Smith, "Efficient complementary metamaterial element for waveguide-fed metasurface antennas," *Optics Express*, vol. 24, no. 25, pp. 28 686–28 692, Dec. 2016.

[127] 3GPP, "NR; Base Station (BS) radio transmission and reception," 3rd Generation Partnership Project (3GPP), Technical Specification TS 38.104, 2024, version 18.5.0.

[128] ——, "NR; User Equipment (UE) radio transmission and reception; Part 1: Range 1 Standalone," 3rd Generation Partnership Project (3GPP), Technical Specification TS 38.101-1, 2024, version 18.5.0.

[129] E. Björnson, L. Sanguinetti, H. Wymeersch, J. Hoydis, and T. L. Marzetta, "Massive MIMO is a reality—what is next?: Five promising research directions for antenna arrays," *Digital Signal Processing*, vol. 94, pp. 3–20, Nov. 2019.

[130] H. Li, S. Li, B. Hou, X. Zhang, W. Wen, and C. Hu, "A digital SIW-slot antenna array with FPGA implementation of beamforming," *Scientific Reports*, vol. 12, no. 1, p. 8927, May 2022.

[131] P. Jain, S. Ghosh, S. Cotton, and O. Yurduseven, "Single-layer sub-6 GHz leaky dynamic metasurface antenna with wide beam coverage," *IEEE Antennas Wireless Propag. Lett.*, vol. 24, no. 11, pp. 4323–4327, Nov. 2025.

[132] J. Carlson, S. Keshmiri, M. F. Imani, and R. W. Heath, "Design optimization of dynamic metasurface antenna elements for beamforming capabilities," in *Proc. IEEE Eur. Conf. Antennas Propag. (EuCAP)*, Dublin, Ireland, Apr. 2026, to be published.

[133] D. Deslandes and K. Wu, "Accurate modeling, wave mechanisms, and design considerations of a substrate integrated waveguide," *IEEE Trans. Microw. Theory Techn.*, vol. 54, no. 6, pp. 2516–2526, Jun. 2006.

[134] J. Carlson and R. W. Heath, "Tri-hybrid combining for interference mitigation in mobile ad hoc networks," in *2025 59th Asilomar Conference on Signals, Systems, and Computers*, Oct. 2025, pp. 599–603.

[135] N. V. Deshpande, J. Carlson, S. Yang, M. Akrout, A. Gonzalez, M. R. Castellanos, T. Ratnarajah, C.-B. Chae, and R. W. Heath, "Signal processing foundations of reconfigurable antennas in the tri-hybrid MIMO architecture," submitted to npj Wireless Technology.

[136] A. Jabbar, M. Elsayed, J. U.-R. Kazim, Z. Pang, J. L. Kernec, M. Imran, H. Larijani, M. Ur-Rehman, Q. Abbasi, and M. Usman, "Millimeter-wave communication testbed using digital coding dynamic metasurface antenna: Practical design and implementation," *IEEE J. Sel. Topics Electromagn. Antennas Propag.*, vol. 2, pp. 307–319, July 2026.

[137] A. Bautista, R. Stevenson, M. Sazegar, T. Schlichter, and T. Heyn, "Dynamically reconfigurable metasurface antennas for mobile connectivity in 5G non-terrestrial networks," in *2022 IEEE/MTT-S International Microwave Symposium - IMS 2022*, June 2022, pp. 994–997.

[138] MACOM Technology Solutions, "MAPS-010165 6-bit digital phase shifter, 3.5–6.0 GHz," Datasheet.

[139] Qorvo, "QPA9501 5.1–5.9 GHz power amplifier," Datasheet.

[140] Texas Instruments, "DAC6578 digital-to-analog converter," Datasheet.

[141] Renesas Electronics, "F5288 Ka-band 8-channel beamformer," Datasheet.